Université Fédérale
Toulouse Midi-Pyrénées

THÈSE

En vue de l'obtention du

DOCTORAT DE L'UNIVERSITÉ DE TOULOUSE

Délivré par l'Université Toulouse 3 - Paul Sabatier

Présentée et soutenue par

Juliana BARROS BARBOSA

Le 16 Septembre 2020

Matériaux 2D TMDC pour la génération d'Hydrogène par Photo-décomposition de l'eau

Ecole doctorale : **SDM - SCIENCES DE LA MATIERE - Toulouse**

Spécialité : **Sciences et Génie des Matériaux**

Unité de recherche :

CIRIMAT - Centre Interuniversitaire de Recherche et d'Ingénierie des Matériaux

Thèse dirigée par :

Jean-Yves CHANE-CHING et Pierre-Louis TABERNA

Jury :

M. Frédéric SAUVAGE	Laboratoire de Réactivité et Chimie des Solides	Rapporteur
Mme. Sophie CASSAIGNON	Sorbonne Université	Rapporteur
M. Vincent PAILLARD	Université Toulouse 3 - Paul Sabatier	Examinateur
M. Bruno JOUSSELME	CEA Paris-Saclay	Examinateur
M. Jean-Yves CHANE CHING	CIRIMAT	Directeur de thèse
M. Pierre-Louis TABERNA	CIRIMAT	Co-directeur de thèse
M. Andrea BALOCCHI	Laboratoire de Physique et Chimie des Nano-objets	Invité

Remerciements

Tout d'abord et avant tout, je remercie Dieu de m'avoir toujours béni avec les bonnes opportunités que la vie m'a offertes et pour sa guidance, me donnant la force de surmonter tous mes défis.

Cette thèse a été réalisée au sein de l'Institut Carnot CIRIMAT (Centre Interuniversitaire de Recherche et d'Ingénierie des MATériaux) de l'Université Paul Sabatier dans les équipes Oxydes à Valence Mixte et Revêtements et Traitement de Surface. Mes premiers remerciements vont à mes encadrants de thèse : M. Jean-Yves Chane Ching et M. Pierre-Louis Taberna, directeurs de recherche du CNRS au CIRIMAT. Merci de m'avoir guidé et enseigné pendant ces 4 années, de m'avoir donné toute l'aide et l'opportunité de terminer ce doctorat et surtout d'avoir cru en moi. Je remercie également M. Andrea Balocchi, maître de conférences à l'INSA Toulouse, pour toute l'assistance et l'enseignement. De plus, je suis reconnaissant à Lucianna Gama, qui m'a aidé avec l'opportunité de poursuivre un doctorat en France.

Je remercie les deux rapporteurs de mon jury de thèse; Mme Sophie Cassaignon, professeur à l'Université de Sorbonne et M. Frédéric Sauvage, directeur de recherche au Laboratoire de Réactivité et Chimie des Solides, pour leurs commentaires et remarques pertinentes. Je remercie également M. Bruno Jousselme, directeur de recherche au CEA Paris-Saclay et M. Vincent Paillard, professeur à l'Université Paul Sabatier, d'avoir accepté de participer à ce jury de thèse.

Je remercie et salue également l'aide apportée par le Conseil national du développement scientifique et technologique - CNPq (agence brésilienne pour la promotion de la science) qui m'a accordé les moyens financiers pour réaliser mon doctorat en France et pour encourager le développement de la recherche scientifique au Brésil.

Je remercie également le laboratoire CIRIMAT de m'avoir accueilli et de m'offrir un environnement agréable et convivial pour mener à bien mes travaux. Je suis particulièrement reconnaissant à Jean Jacques, Marie Claire, Pauline, Vincent, Pierre, Benjaman, Abde, Nabila, Jessie et Murielle qui m'ont aidé pendant ces années et qui ont contribué d'une manière ou d'une autre avec la réalisation de mon travail. Pourtant, j'ai rencontré de chers amis et collègues sur le labo qui m'ont aussi aidé et encouragé, avec qui j'ai échangé des idées et des bonnes soirées pendant ces 4 années: Dasha, Itchy, Xue, Marie, Inthuga, Candida, Romain, Quentin, Assane, Hue, Justine, Marco, Julien, Anthony, Clément et Andreas.

Je remercie à toute ma famille, mes parents et ma sœur Izabelle, qui m'ont toujours et tout le temps soutenu dans tous mes choix et dans les moments difficiles, et qui ont tout fait pour garantir mon bonheur et ma réussite.

Certainement, je suis également reconnaissant à ma famille *brésilienne-toulousaine*. Mes chers amis qui m'ont encouragé et m'ont donné le sentiment d'être chez moi même loin de la famille: Patricia, Lilaine, Leticia, Paulo, Hans, Gustavo, Natalia, Juliano, Giovanna et tout la troupe brésilienne. Je remercie Violette, avec qui j'ai partagé le lieu que j'ai appellé chez moiet vécu à Toulouse pendant ces 4 années. Je remercie également mes chers amis brésiliens, qui même de loin, étaient présents sur ce parcours, me conseillant et croyant en moi: Roberta, Luanna, Raquel et Gabriela. Et à mes cousines-sœurs Priscila et Samara qui m'ont toujours conseillé et qui sont une de mes sources d'inspiration depuis que je suis petite.

Enfin, je suis extrêmement reconnaissant envers tous ceux qui m'ont aidé direct ou indirectement et qui ont fait partie de mon cheminement vers l'obtention de mon doctorat. Merci beaucoup à tous.

Table of Content

List of Abbreviations

HER	*Hydrogen Evolution Reaction*
PEC	*Photoelectrochemical*
NHE	*Normal Hydrogen Electrode*
2D	*Two-dimensional*
TMDC	*Transition Metal Di-Chalcogenide*
rGO	*Reduced Graphene Oxide*
Mo_xS_y	*Thio, oxo-thio Mo Complexes*
FTO	*Fluor doped Thin Oxide*
XRD	*X-Ray Diffraction*
XPS	*X-Ray Photoelectron Spectroscopy*
ESI-MS	*Electrospray Ionization Mass Spectrometry*
HRTEM	*High Resolution Transmission Electron Microscope*
SEM-FIB	*Focused Ion Beam Scanning Electron Microscope*
HAADF-STEM	*High-angle annular dark-field - Scanning transmission electron microscopy*
BET	*Brunauer-Emmett-Teller*
PL	*Photoluminescence*
NMR	*Nuclear Magnetic Resonance*
LSV	*Linear Sweep Voltammetry*
EIS	*Electrochemical Impedance Spectroscopy*
IMPS	*Intensity Modulated Photocurrent Spectroscopy*
IPCE	*Incident Photon-to-electron Conversion Efficiency*
DFT	*Density Functional Theory*

List of Figures

List of Tables

Introduction

The accelerated global warming and the world's high energy demand have led the scientific community to focus on the development of clean and renewable energy source [1]. Among the new alternatives, hydrogen is one of the most promising energy carriers. Its utilization as fuel is free of toxic gas formation and CO_2 emission, where the only product is water vapor [2]. However, hydrogen does not exist freely in nature and its production is still fossil-based [3]. With the global interest in solar energy research, clean hydrogen production can be accomplished making use of sustainable resources such as the sun and the water. For this purpose, semiconductor-based materials have been envisioned for solar energy harvesting, allowing for the conversion of photons to chemical compounds – hydrogen and/or oxygen – through charge separation [4], often denoted as solar-to-fuel conversion.

Among other possibilities, solar-to-fuel conversion can be achieved using a photoelectrochemical (PEC) device consisting of a semiconductor electrode in direct contact with a liquid electrolyte. The use of photoelectrochemical (PEC) for water splitting has received attention for being cost-competitive with fossil-based technologies in the techno-economic evaluation of hydrogen generation [5][6]. Indeed, for the realization of this hydrogen economy, the scientific community has been actively searching for efficient PEC cells composed of semiconductor photocatalysts earth-abundant and inexpensive [7].

Most of the studies are reported on n-type semiconductors [8]–[11], but the development of promising p-type semiconductor materials, exhibiting decent photocatalytic performances, were reported using photocathodes including p-type gallium indium phosphide (p-$GaInP_2$), p-type silicon (p-Si), p-type (p-Cu_2O), such as CZTS (copper zinc tin sulfide, p-Cu_2ZnSnS_4) and CIGS (copper indium gallium selenide, p-$CuInGaSe_2$). However, their low stability and the manufacturing high cost for large-scale still limit the use of these materials as photocathode devices [4]. To face this challenge, the development of new photocatalyst materials has been targeted to enable practical direct solar-to-hydrogen conversion, and so the realization of PEC involving low-cost, robust and high-performance semiconductor materials [5][7].

New opportunities have shown up with the emerging of 2D materials, displaying of unique optoelectronic properties and high specific surface areas that are important for catalysis and energy storage applications [12][13]. The layered structure of 2D materials favors maximum solar harvesting and decreases charge carrier pathways. Despite being graphene the most well-known layered material, transition metal di-chalcogenides (TMDC) also represents an interesting class of photoactive materials with the ability to be exfoliated into atomically thin 2D sheets. Their

structure and unique absorption properties provide tunable band-gap characteristics corresponding to the number of atomic layers [14] and strong light-matter interactions that offer outstanding performances in solar energy conversion [15]. Besides, viable routes for suitable economical production of large-area photocatalyst devices have been explored for further development of solar energy conversion procedures using these materials [15]–[17].

The 2D TMDCs have, however, a high concentration of surface defects that can act as efficient charge carrier traps (recombination sites) and are one of the most common scattering centers limiting the electron mobility [18]. The surfaces of the TMDCs have many electronic defects as unsaturated di-chalcogenides atoms on the edges. Previous works suggest that edges sites are detrimental to the photon-to-electron conversion efficiency, because the under-coordinated atoms on the edges are reactive toward surface corrosion processes and act as sites for charge carrier recombination [19].

Since the electrochemical reactions proceed at the electrode/electrolyte interface, at the semiconductor are generally complex, multistep and proton and electron transfer processes, which physically transpire on catalytic surface sites [4]. Therefore, rational control of the interface is required to adjust the semiconductor properties. As being one of the most important issues in photocatalysis [20], various strategies have been proposed to remove or neutralize these surface defects and thus, improve their performances in photocatalysis.

The main strategies involve surface treatments that include passivation of surface states, the addition of protection layers and co-catalysts – usually noble metals; and still p/n heterojunctions and doping [21]. For instance, HER was considerably improved on 2D WSe_2 under visible irradiation with an optimized Pt-Cu co-catalyst combined with a defect passivation treatment [22]. Nevertheless, to make feasible a large-scale development of this technology, it is mandatory to replace the precious metal catalysts used with a more earth-abundant material.

To perfectly suit the use in layered 2D materials, molecular co-catalysts can be very promising because they have ideal size matching, so they can easily be infiltrated into the layered structure and their thin films can minimize shielding [23]. MoS_2-based nanomaterials were previously proposed as earth-abundant alternative HER catalysts, such as the molecular Mo complexes including Mo_3S_4 [24], $(Mo_2S_{12})^{2-}$[25], $(Mo_3S_{13})^{2-}$ [26]. Their promising catalytic efficiency, comparable with the one of Pt [27], make them ideal candidates for use onto 2D photoactive materials such as the 2D TMDCs [28]. Also, as the defect sites found on the 2D TMDCs are very reactive [29], chemical bonding via ligand interactions at the surface of these

photocathodes could be seen as another interesting use of these molecular complexes to passivate surface defects.

Another important aspect is the morphology of the semiconductor and its nanostructuration. It is seen as an effective way to enhance the reaction kinetics thanks to both a more efficient charge transfer at the photoelectrode/electrolyte interface and a more efficient charge collection. Optical absorption is also supposed to benefit from a fine control of the photoelectrode material morphology [30]-[32]. However, morphology optimization techniques usually require heat treatments at high temperatures (> 400 °C) and these conditions are not suitable for many non-oxide semiconductors like chalcogenides or the processability into large-area of thin films [7]. Nevertheless, in a recent report [33] enhanced photoelectrochemical performance was achieved after a low-temperature nanostructuring technique for the obtention of mesoporous films exhibiting high surface area.

To some point, the high surface area can lead to poor effective charge mobility and the use of carbon-based nanojunctions, such as the graphene due to their metallic-like conductivity, is expected to allow for facile electron injection/collection within photoelectrode material [34]. Such kind of nanojunction has proven to lead to a superior photocatalytic activity for H_2 evolution [35].

Among the challenges to fully take benefit of the layered morphology of the 2D materials, optimization of both the film microstructure and the charge collection towards the electrodes are highly desirable to significantly increase the access to catalytic sites, since packing of TMDC layers can occur with substantial restacking [36]. A relevant strategy may involve the design and fabrication of layered hetero-structures composed of interconnected nanoporous TMDC with high specific surface area, combined with carbon-based nanojunctions. In this context, the transition metal di-chalcogenides are promising candidates because of their good light absorption properties and are highly tunable: their number of layers can be tweaked to modify noticeably their properties.

Motivated by these reasons, the present work will be dedicated to the use of a 2D TMDC materials as photocatalyst for the hydrogen generation through solar water splitting and the application of potential strategies to improve its photocatalytic properties.

This thesis manuscript is divided into six chapters summing up all the important information and results that allowed for the accomplishment of this research work for 4 years.

The first chapter is focused on the presentation and contextualization of essential information about the hydrogen generation through solar water splitting. Basic notions of

semiconductors and their use in photocatalysis will also be discussed. Then, after a brief presentation of the suitable photoelectrode materials, this chapter will be dedicated to the use of 2D TMDC materials as photocatalysts, presenting their properties, their synthesis methods, based on what has been previously reported in the literature. After presenting the main bottlenecks of such materials, it will be present the strategies used in this work to achieve higher conversion efficiencies.

The second chapter will be devoted to the experimental methods used and developed all along this work: the semiconductor and co-catalyst synthesis, the electrode fabrication, the surface treatments, the thin film characterizations, the photoelectrochemical analyses and hydrogen measurements.

The third chapter will be focused on the exfoliated 2D p-WSe_2 photoelectrode characterizations achieved obtained *via* a simple synthesis route: such as optoelectronic characterizations and photoelectrochemical assessment. A comparison will be done after the electrodeposition of Pt co-catalyst together with the surface passivation, both inspired from previous works.

The fourth chapter will be dedicated to the development of cost-effective surface treatment of the exfoliated 2D p-WSe_2. Water-stable Mo thio complexes as molecular co-catalysts anchored onto the WSe_2 photoelectrode *via* a solvent-free film-forming process will be presented here. A proper complex selection upon deposition allows achieving both a defect healing and more efficient charge transfer, leading to improve significantly the photocatalytic performance of the p-WSe_2 photoelectrode. Besides, these results will be supported by density functional theory calculations that provide further insights into the interactions developed between the surface defects of the 2D photocathode and the Mo thio complex film catalyst, as well as the thermodynamics of H^+ adsorption and H_2 desorption on the thio, oxo-thio complexes.

Within the fifth chapter is addressed the design and elaboration of nanostructured WSe_2 photoelectrode with optimized morphology and conductivity property. It will be detailed the obtention of a 3D nanoporous network made of TMDC building blocks using a colloidal self-assembling process involving a post-etchable template and graphene oxide nanosheets. The experimental results will show that this nanostructuration procedure shows no chemical degradation of the TMDC materials while improving the photocatalytic performance, which is assured after deposition of Mo_xS_y co-catalyst thin film. Further insights will demonstrate that this approach leads to the elaboration of a photocathode with faster charge carrier collection and transfer as well as good results of incident photon-to-current conversion efficiency.

Finally, a last chapter in outlook will redirect the application of nanostructuring using the same colloidal self-assembly procedure, and defect passivation treatment with the use of thio, oxo-thio complexes catalysts for another TMDC material, the p-WS_2. The preliminary results will show that the approaches developed in this work are suitable for other 2D photocathode. Lastly, the perspectives for further development and evolution of this class of materials as photocatalyst for the construction of a photoelectrochemical system to afford efficient and economical conversion of solar energy into chemical fuel are highlighted.

BIBLIOGRAPHIC REFERENCES

[1] N. Z. Muradov and T. N. Veziroğlu, "'Green' path from fossil-based to hydrogen economy: An overview of carbon-neutral technologies," *Int. J. Hydrogen Energy*, vol. 33, no. 23, pp. 6804–6839, 2008.

[2] S. E. Hosseini and M. A. Wahid, "Hydrogen production from renewable and sustainable energy resources: Promising green energy carrier for clean development," *Renew. Sustain. Energy Rev.*, vol. 57, pp. 850–866, 2016.

[3] N. Armaroli and V. Balzani, "The hydrogen issue," *ChemSusChem*, vol. 4, no. 1, pp. 21–36, 2011.

[4] K. Sivula and R. van de Krol, "Semiconducting materials for photoelectrochemical energy conversion," *Nat. Rev. Mater.*, vol. 1, pp. 15010, 1–16, 2016.

[5] B. A. Pinaud *et al.*, "Technical and economic feasibility of centralized facilities for solar hydrogen production via photocatalysis and photoelectrochemistry," *Energy Environ.Sci.*, vol. 6, no. 7, pp. 1983–2002, 2013.

[6] C. Ding, J. Shi, Z. Wang, and C. Li, "Photoelectrocatalytic Water Splitting: Significance of Cocatalysts, Electrolyte, and Interfaces," *ACS Catal.*, vol. 7, no. 1, 2017.

[7] K. Sivula, "Advancing materials and methods for photoelectrochemical energy conversion," *Chimia (Aarau).*, vol. 71, no. 7–8, pp. 471–474, 2017.

[8] M. S. Prévot, N. Guijarro, and K. Sivula, "Enhancing the Performance of a Robust Sol-Gel-Processed p-Type Delafossite CuFeO2 Photocathode for Solar Water Reduction," *ChemSusChem*, vol. 8, no. 8, pp. 1359–1367, 2015.

[9] C. Jiang, S. J. A. Moniz, A. Wang, T. Zhang, and J. Tang, "Photoelectrochemical devices for solar water splitting-materials and challenges," *Chem. Soc. Rev.*, vol. 46, no. 15, pp. 4645–4660, 2017.

[10] P. Luan and J. Zhang, "Stepping towards Solar Water Splitting: Recent Progress in Bismuth Vanadate Photoanodes," *ChemElectroChem*, vol. 6, no. 13, pp. 3227–3243, 2019.

[11] K. Sivula, F. Le Formal, and M. Grätzel, "Solar water splitting: progress using hematite (α-Fe 2O3) photoelectrodes," *ChemSusChem*, vol. 4, no. 4, pp. 432–449, 2011.

[12] J. N. Coleman *et al.*, "Two-dimensional nanosheets produced by liquid exfoliation of layered materials," *Science (80-.).*, vol. 331, no. 6017, pp. 568–571, 2011.

[13] Q. H. Wang, K. Kalantar-Zadeh, A. Kis, J. N. Coleman, and M. S. Strano, "Electronics and optoelectronics of two-dimensional transition metal dichalcogenides," *Nat. Nanotechnol.*, vol. 7, no. 11, pp. 699–712, 2012.

[14] K. F. Mak, C. Lee, J. Hone, J. Shan, and T. F. Heinz, "Atomically thin MoS2: A new direct-gap semiconductor," *Phys. Rev. Lett.*, vol. 105, no. 13, pp. 2–5, 2010.

[15] X. Yu, M. S. Prévot, N. Guijarro, and K. Sivula, "Self-assembled 2D WSe2 thin films for photoelectrochemical hydrogen production," *Nat. Commun.*, vol. 6, no. May, 2015.

[16] V. Nicolosi, M. Chhowalla, M. G. Kanatzidis, M. S. Strano, and J. N. Coleman, "Liquid exfoliation of layered materials," *Science (80-.).*, vol. 340, no. 6139, pp. 72–75, 2013.

[17] Y. Li, Y. L. Li, B. Sa, and R. Ahuja, "Review of two-dimensional materials for photocatalytic water splitting from a theoretical perspective," *Catal. Sci. Technol.*, vol. 7, no. 3, pp. 545–559, 2017.

[18] W. Zhu *et al.*, "Electronic transport and device prospects of monolayer molybdenum disulphide grown by chemical vapour deposition," *Nat. Commun.*, vol. 5, pp. 1–8, 2014.

[19] J. M. Velazquez *et al.*, "A Scanning Probe Investigation of the Role of Surface Motifs in the Behavior of p-WSe 2 Photocathodes," *Energy Environ. Sci.*, vol. 9, pp. 164–175, 2015.

[20] J. Lu *et al.*, "Atomic healing of defects in transition metal dichalcogenides," *Nano Lett.*, vol. 15, no. 5, pp. 3524–3532, 2015.

[21] N. Guijarro, M. S. Prévot, and K. Sivula, "Surface modification of semiconductor photoelectrodes," *Phys. Chem. Chem. Phys.*, vol. 17, no. 24, pp. 15655–15674, 2015.

[22] M. Johnson and K. Sivula, "Defect Mitigation of Solution-Processed 2D WSe 2 Nano fl akes for Solar-to-Hydrogen Conversion," 2018.

[23] C. G. Morales-Guio and X. Hu, "Amorphous molybdenum sulfides as hydrogen evolution catalysts," *Acc. Chem. Res.*, vol. 47, no. 8, pp. 2671–2681, 2014.

[24] Y. Hou *et al.*, "Bioinspired molecular co-catalysts bonded to a silicon photocathode for solar hydrogen evolution," *Nat. Mater.*, vol. 10, no. 6, pp. 434–438, 2011.

[25] Z. Huang *et al.*, "Dimeric [Mo2S12]2- Cluster: A Molecular Analogue of MoS2 Edges for Superior Hydrogen-Evolution Electrocatalysis," *Angew. Chemie - Int. Ed.*, vol. 54, no. 50, pp. 15181–15185, 2015.

[26] J. Kibsgaard, T. F. Jaramillo, and F. Besenbacher, "Building an appropriate active-site motif into a hydrogen-evolution catalyst with thiomolybdate [Mo3S13]2- clusters," *Nat. Chem.*, vol. 6, no. 3, pp. 248–253, 2014.

[27] T. F. Jaramillo, K. P. Jørgensen, J. Bonde, J. H. Nielsen, S. Horch, and I. Chorkendorff, "Identification of Active Edge Sites for Electrochemical H2 Evolution from MoS2 Nanocatalysts," *Science (80-.).*, vol. 317, no. 5834, pp. 100–102, 2007.

[28] A. B. Laursen, S. Kegnæs, S. Dahl, and I. Chorkendorff, "Molybdenum sulfides—efficient and viable materials for electro - and photoelectrocatalytic hydrogen evolution," *Energy Environ. Sci.*, vol. 5, no. 2, p. 5577, 2012.

[29] S. S. Chou *et al.*, "Ligand conjugation of chemically exfoliated MoS2," *J. Am. Chem. Soc.*, vol. 135, no. 12, pp. 4584–4587, 2013.

[30] Y. Liu, Y. X. Yu, and W. De Zhang, "MoS2/CdS heterojunction with high photoelectrochemical activity for H2 evolution under visible light: The role of MoS2," *J. Phys. Chem. C*, vol. 117, no. 25, pp. 12949–12957, 2013.

[31] T. W. Kim and K.-S. K.-S. Choi, "Nanoporous BiVO4 Photoanodes with Dual-Layer Oxygen Evolution Catalysts for Solar Water Splitting," *Science (80-.).*, vol. 343, no. 6174, pp. 990–994, 2014.

[32] K. Sivula *et al.*, "Photoelectrochemical water splitting with mesoporous hematite prepared by a solution-based colloidal approach," *J. Am. Chem. Soc.*, vol. 132, no. 21, pp. 7436–7444, 2010.

[33] N. Guijarro, M. S. Prévot, X. A. Jeanbourquin, X. Yu, and K. Sivula, "Autodecomposition Approach for the Low-Temperature Mesostructuring of Nanocrystal Semiconductor Electrodes," *Chem. Mater.*, vol. 27, no. 18, pp. 6337–6344, 2015.

[34] S. J. A. Moniz, S. A. Shevlin, D. J. Martin, Z.-X. Guo, and J. Tang, "Visible-light driven heterojunction photocatalysts for water splitting – a critical review," *Energy Environ. Sci.*, vol. 8, no. 3, pp. 731–759, 2015.

[35] Z. Liu, H. Zhao, N. Li, Y. Zhang, X. Zhang, and Y. Du, "Assembled 3D electrocatalysts for efficient hydrogen evolution: WSe_2 layers anchored on graphene sheets," *Inorg. Chem. Front.*, vol. 3, no. 2, pp. 313–319, 2016.

[36] D. Gerchman and A. K. Alves, "Solution-processable exfoliation and suspension of atomically thin WSe2," *J. Colloid Interface Sci.*, vol. 468, pp. 247–252, 2016

CHAPTER I

A Solar Water Splitting for Hydrogen Evolution

A.1 Context

The urgency in finding new alternative clean, renewable energy supplies has origin from the increasing global reliance on non-renewable, geopolitically sensitive sources of energy such as natural gas and coal, coupled with highly volatile crude oil prices. According to Moniz *et al.* [1], global primary energy consumption in 2013 was about 17 TW, and is predicted to at least double by 2050. In this post-fossil fuel era, our society will require routes to efficiently convert renewable energy into chemical feedstocks and fuels using abundant starting materials like CO_2, N_2, and water. The efficient electrochemical reduction of these starting materials into CO, CH_3OH, NH_3, and H_2 can potentially form the basis for a sustainable chemical network supplying the manufacturing, agriculture, and transportation industries [2].

Hydrogen-based energy systems have attracted extensive attention because of their environmentally clean nature. The chemical energy stored in the H-H bond easily released when it combines with oxygen, yields only water as a reaction product. Accordingly, a future energy infrastructure based on hydrogen has been perceived as an ideal long-term solution to energy-related environmental problems [3],[4]. Hydrogen production is still based on raw fossil materials and only 4% is produced through water electrolysis [5]. Because of the increasing interest of producing hydrogen driven by the current concern about global climate change, new alternatives have been developed to produce hydrogen from environmentally friendly energies sources. Photocatalytic water splitting using solar energy for hydrogen production has become a challenging and attractive subject to work on [6].

In the past two decades, solar energy utilization has been the subject of intense research, development, and deployment efforts have been accelerated [7]. Engineering artificial photosynthetic systems to afford the efficient and economical conversion of abundant solar energy into chemical fuel on a scale in accordance with global energy demand (tens of terawatts) is an important step towards the realization of a sustainable carbon-neutral society. Electricity produced from solar energy has advantages over wind power and hydropower, since the latter two need turbines with moving parts that are both noisy and require much maintenance. However, the major disadvantage of solar energy is its intermittent nature. That is, the amount of sunlight a location receives varies greatly depending on the geographical location, time of day, season, and even clouds [8].

The photocatalytic production of hydrogen from natural resources such as water and solar energy has a lighter environmental footprint than fossil fuels and is a part of sustainable development; their conversion to hydrogen has been described as an ideal solution to counter environmental issues associated with fossil fuels [9].

Hydrogen production from solar water-splitting processes generally can be categorized into thermochemical water splitting, photo-biological water splitting and photocatalytic water splitting. According to C. Liao *et al.*, the photocatalytic water splitting, if compared with thermochemical and photo-biological water-splitting techniques, has the following advantages: (a) reasonable solar-to-hydrogen efficiency; (b) low process cost; (c) the ability to achieve separate hydrogen and oxygen evolution during reaction; and (d) small reactor systems suitable for household applications, thus providing for a huge market potential [8].

Hydrogen production via water splitting was first reported in 1972 with TiO_2 as the photo-catalyst. The concept of water decomposition using solar energy was demonstrated by Fujishima and Honda using a Photo-Electrochemical Cell (PEC) [10].

In the nearly 40 years, the approach for solving the water splitting problem has been focused on evaluating new materials for both anodic/cathodic processes and integrating configurations that utilize photovoltaic cell junctions, to increase the obtainable voltage for a single or dual band gap device. Now, the efforts have been redirected to afford efficient solar-to-fuel conversion identifying ideal semiconductors for the economically viable PEC tandem cell [2]. Despite the large number of materials that possess suitable band gap potentials, there are few materials that can function as a photocatalyst due to structural and electronic dependence. The development of promising materials for economically viable solar-to-chemical conversion is an on-going challenge with the attempt to prepare a photocatalyst with efficient optoelectronic properties and intrinsic stability under visible light [11].

B Principles of Solar Water Splitting

Photocatalytic systems for overall water splitting can be divided into two primary approaches. One approach is to split water into H_2 and O_2 using a single visible-light-responsive photocatalyst with a sufficient potential to achieve overall water splitting. The second approach is to apply a two-step excitation mechanism using two different photocatalysts [12]. In this system, the photocatalyst should have a suitable thermodynamic potential for water splitting, a sufficiently narrow band gap to harvest visible photons, and stability against photo-degradation [13]. This photocatalytic system is considerably dependent on the physicochemical properties of a photocatalyst, the nature of the active sites, and the reaction conditions [14].

B.1 Processes in the photocatalytic water splitting

The overall water splitting reaction on a semiconductor photocatalyst is depicted in **Figure I - 1**. It occurs through three main steps: (I) the semiconductor absorbs light photons and generates excited electrons and holes; (II) the excited electrons and holes can migrate to the surface of the semiconductor or recombine again; (III) at the surface, holes can oxidize water to O_2 and electrons can reduce protons to H_2 [15].

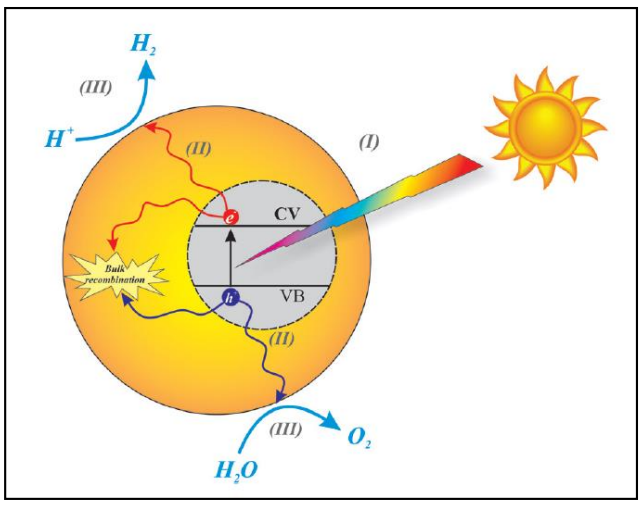

Figure I - 1: *Schematic of the fundamental mechanisms of photocatalytic water splitting [15].*

More precisely, the light-driven water splitting is initiated when a photo-semiconductor absorbs light photons with energies greater than its band gap energy (E_g). This light absorption creates excited photoelectrons in the conduction band (CB) and holes in the valence band (VB) of the semiconductor, as schematically presented in **Figure I - 1**. After that, the second step in photochemical water splitting consists of charge separation and the migration of

photogenerated electron–hole pairs from the bulk of the semiconductor towards the reaction sites on the photocatalyst surface. The final step of the photocatalytic process involves the surface chemical reactions [3]. The photo-generated electrons (e^-) and holes (h^+) that migrate to the surface of the photocatalyst without recombination can reduce (Equation I - 1) or oxidize (equation I - 2), respectively.

$$H_2O + e^- \rightarrow \frac{1}{2}H_2 + OH^- \qquad \text{(I - 1)}$$

$$H_2O + 2h^+ \rightarrow \frac{1}{2}O_2 + 2H^+ \qquad \text{(I - 2)}$$

According to **Figure I - 2** (Pourbaix diagram of water), at least 1.23V is needed to split water. So, to perform water reduction the bottom of the conduction band of the photocatalyst must be located at more negative potentials than the proton reduction potential (H^+/H_2 = 0 V *vs.* the Normal Hydrogen Electrode (NHE) at pH 0). To perform water oxidation, the valence band edge of the photocatalyst must exceed the oxidation potential of water (H_2O/O_2 = +1.23V vs. NHE at pH 0).

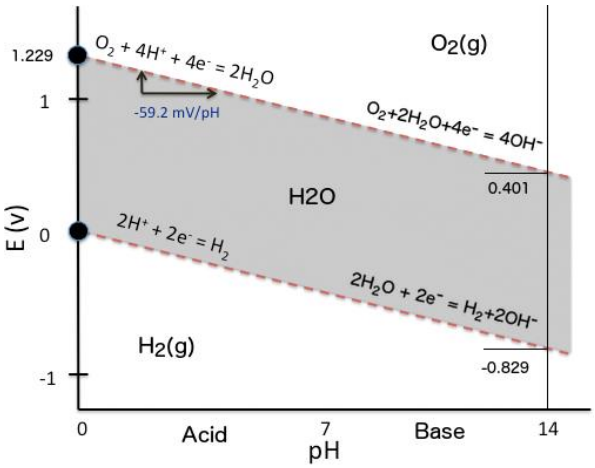

Figure I - 2: *Pourbaix diagram for water, including equilibrium regions for water, oxygen and hydrogen [16].*

B.2 Solar-to-Chemical Using Semiconductors

B.2.1 Some fundamentals about semiconductors

Semiconductors exhibit an intermediate behavior between insulators and metals in term of conductivity; conductivity activated by thermal energy oppositely to metals. They are called intrinsic semiconductors. Among others, a great interest of semiconductors is their ability to generate electron-hole pairs under ionizing radiation which confers photoelectrochemical properties to semiconductor [17]. These peculiar properties can be understood by examining the

electronic structures of semiconductor materials. Due to the essentially infinite number of atoms that must be considered, the electronic structure of these solids is typically discussed in terms of energy bands, which are made up of the atomic orbitals of the individual atoms [18].

As a result of the large number of orbitals, the difference in energy between adjacent molecular orbitals within a given energy band is so small that the band can be effectively considered a continuum of energy levels (**Figure I - 3**). The highest and lowest energy levels of a band are referred to as the band edges. As with molecular orbitals, the energy bands of interest are the highest occupied (called valence band) and the lowest unoccupied (called conduction band). It is the energy gap (band gap - E_g) between these bands (i.e., the difference in energy between the upper edge of the valence band and the lower edge of the conduction band) that determines the properties of the material [17].

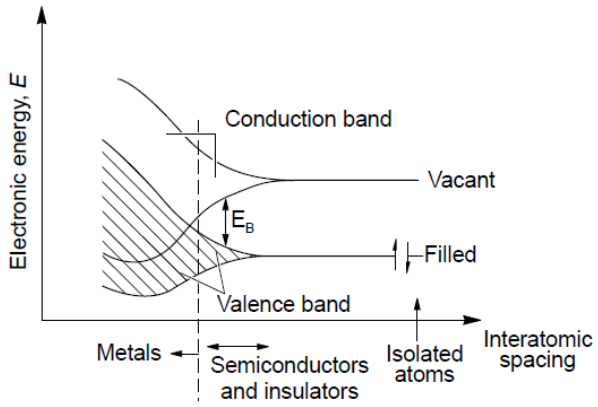

Figure I - 3: *Generation of bands in solids from atomic orbitals of isolated atoms [17].*

To increase the free charge carrier density within a semiconductor, different elements are introduced into a semiconductor material, referred to as doping. In the latter case, they are called extrinsic semiconductors. The addition of different elements can lead to vacant or occupied energy levels, which allows facile promotion of holes in the valence band or electrons into the conduction band [17]. Thus, doped semiconductors in which dominant charge carriers are electrons are referred to as n-type semiconductors, whereas those in which holes are the majority charge carriers are referred to as p-type semiconductors (see **Figure I - 4**).

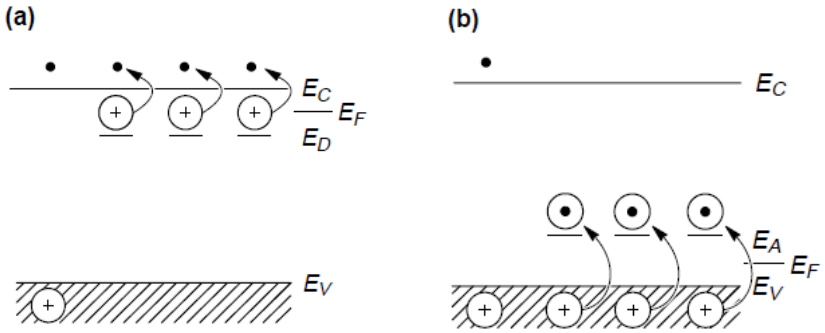

Figure I - 4: *Schematic diagram of the energy levels of an (a) n-type semiconductor and a (b) p-type semiconductor [17].*

Another important concept to consider in the semiconductors is the Fermi level (E_F). In band structure theory, this is defined as the energy level at which the probability of occupation by an electron is 1/2. For an intrinsic semiconductor, the Fermi level lies at the mid-point of the band-gap. Since doping changes the distribution of electrons within the solid, it affects the Fermi level position: for a n-type semiconductor, the Fermi level lies just below the bottom of CB; whereas for a p-type semiconductor, it lies just above top of the VB, as presented in **Figure I-4**. The Fermi level (can also be defined using the equation I - 3):

$$E_F = \tilde{\mu}_e^S \qquad \text{(I - 3)}$$

Where, $\tilde{\mu}_e^S$ is the electrochemical potential of the electron in the material (in J) defined as:

$$\tilde{\mu}_e^S = \mu_e^S - e\Delta\phi_S \qquad \text{(I - 4)}$$

Where, μ_e^S is the chemical potential (in J) of the electron; $\Delta\phi_S$ is the Galvani potential (in V); and e is the electron charge ($1.602\ 10^{-19}$ C).

B.2.2 The semiconductor – electrolyte interface

Fundamental studies have explored the semiconductor - electrolyte junction including the kinetics and energetics of electron transfer across the interface. The interface of the semiconductor/liquid electrolyte is the most critical point for photoelectrochemical catalysis presenting alluring scientific issues, thus challenges related to their physical chemistry and complexity must be given attention [19].

Without any illumination, when a semiconductor is placed in contact with an electrolyte, after charge transfer an equilibrium is reached, the electrochemical potential of electrons in a redox system is equivalent to the E_F leading to:

$$E_F = \tilde{\mu}_e^{el} = \tilde{\mu}_e^{el0} + kTln\left(\frac{C_{ox}}{C_{red}}\right) = E_{redox} \qquad \text{(I - 5)}$$

In which C_{ox} and C_{red} are the concentrations of the oxidized and reduced species of the redox system, respectively.

$$E_F = \mu_e^S - e\Delta\phi_S = \mu_e^{el} - e\Delta\phi_{el} \qquad \text{(I - 6)}$$

Where, $\tilde{\mu}_e^{el}$ is electrochemical potential of the electron in the electrolyte (in J); $\tilde{\mu}_e^{el0}$ is the standard electrochemical potential which can be expressed as:

$$\tilde{\mu}_e^{el0} = E_{NHE} - eU_{redox}^0 \qquad \text{(I - 7)}$$

Where, E_{NHE} is the energy of an electron at the standard hydrogen potential in the absolute scale, e the electron charge and U_{redox}^0 is the standard redox potential of an electron in the solution in the hydrogen electrochemical potential scale.

So, the semiconductor/electrolyte potential is equilibrated *via* an equalization of Fermi level with the electrochemical potential of the electron in the solution, which operates through a charge transfer across the interface [17] (**Figure I-5**). As a result, on each side of the interface there are charge distributions that differ from the bulk which in turn lead at equilibrium to a Galvani potential ($\Delta\phi$) across the interface leading to:

$$\Delta\phi = \Delta\phi_{SC} + \Delta\phi_{edl} \qquad \text{(I - 8)}$$

Where $\Delta\phi_{SC}$ and $\Delta\phi_{edl}$ are respectively the Galvani potentials across the space charge region and the electrochemical double layer. Eventually, it is related to the Electrode potential ($U_{electrode}$) by:

$$U_{electrode} = \Delta\phi + const \qquad \text{(I - 9)}$$

Where, *const* depends on the choice of the reference electrode. In usual experimental condition, the charge density in the electrolyte is a lot more superior to the one in the semiconductor resulting in potential drop mainly occurring in the space charge region.

$$U_{electrode} = \Delta\phi_{SC} + const' \qquad \text{(I - 10)}$$

Where, $const' = const + \Delta\phi_{edl}$.

As a result, the Fermi level of a semiconductor electrode can be potentially driven by applying an external voltage. Different situations can take place depending on the initial relative position of the Fermi level respect to the electrochemical potential of the electrolyte [20].

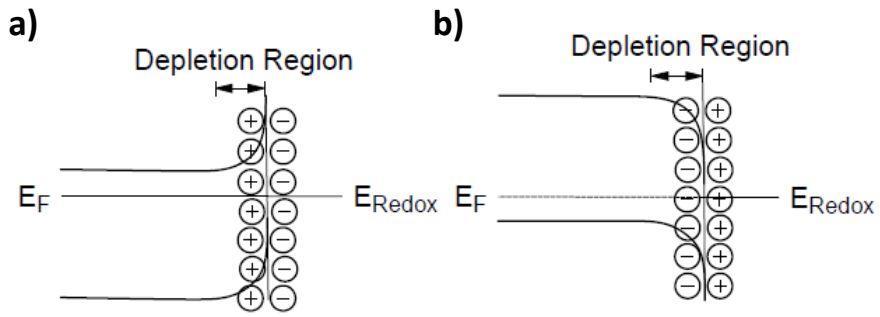

Figure I - 5: *Band bending for an (a) n-type semiconductor and a (b) p-type semiconductor in equilibrium with an electrolyte [17][17].*

A typical situation for a n-type semiconductor electrode can be depicted assuming that the Fermi level is higher than the electrochemical potential of an electron in the electrolyte. Hence, electrons will be transferred from the electrode into the solution. Therefore, there is a positive charge associated with the space charge region, and this is reflected in an upward bending of the band edges (**Figure I - 5a**). The region where the majority charge carrier of the semiconductor has been removed from space charge region is referred to as a depletion layer [17].

For a p-type semiconductor, the Fermi level is expected to be lower than the electrochemical potential of an electron in the electrolyte, and hence electrons must transfer from the solution to the electrode to attain equilibrium. This generates a negative charge in the space charge region, which causes a downward bending in the band edges (**Figure I - 5b**). Since this process removes the holes in the space charge region, this region is also called a depletion layer.

Bott explains that as the Fermi level shifts, the band edges in the interior of the semiconductor varies with the applied potential [17]. However, the band edges energies at the interface are not affected by changes with the applied potential. Therefore, the changes in the energies of the band edges on going from the interior of the semiconductor interface, and hence the magnitude and direction of band bending, varies with the applied potential.

According to the applied potential, there are three different situations to be considered between the semiconductor and the electrolyte interface: flat band, depletion and accumulation.

At a certain potential, when $\Delta\phi_{SC} = 0$, (**Figure I - 6 in I and II**) there is no band bending. This potential is therefore referred as the flatband potential (E_{fb}). Depletion regime arises at potentials positive of the flat band potential for an n-type semiconductor – at potentials negative of the flatband potential for a p-type semiconductor (**Figure I - 6 in III and IV**). In these aforementioned situations the space charge region can be under inversion regime: minor charge carriers take over. At potential negative of the flatband potential for an n-type semiconductor, there is an excess of the majority charge carrier (electrons) in this space charge region, which is referred to as an accumulation region (**Figure I - 6 in V**). An accumulation region arises in a p-type semiconductor at potentials more positive than the flatband potential (**Figure I - 6 in VI**). Thus, the accumulation and depletion layers formed according with the applied biases drives the charge transfer abilities of the semiconductors [17].

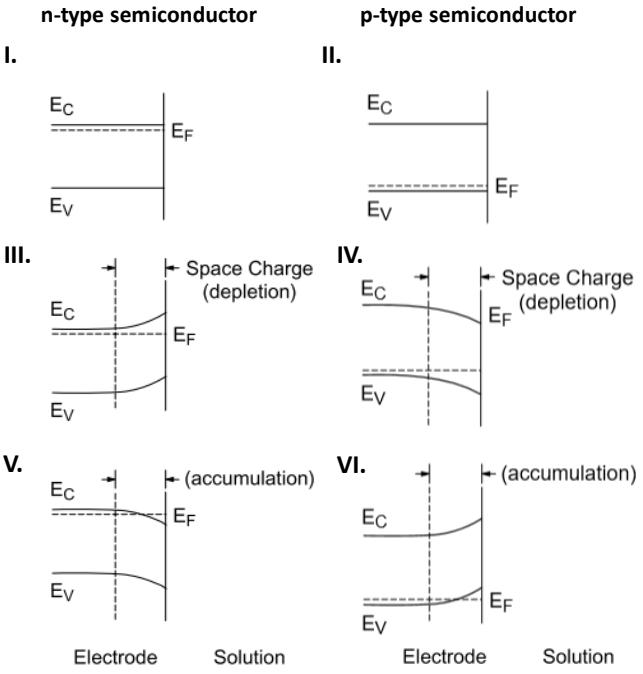

***Figure I - 6**: Effect of varying the applied potential (E) on the band edges in the interior of an n-type and p-type semiconductors [17].*

B.2.2.1 Semiconductor behavior under irradiation

When the semiconductor is exposed to irradiation of sufficient energy, electrons can be driven to the conduction band leading to an electric field. In the semiconductor bulk, recombination of the promoted electron can occur; however, in the space charge region, the electric field will cause the separation of generated electron-hole pairs (excitons). For a n-type semiconductor at positive potentials, the band edges curve upwards (**Figure I - 7**) - the holes

move towards the interface, and the electrons moves to the bulk of the semiconductor [20]. The same occurs for the p-type semiconductor, but in analogue way.

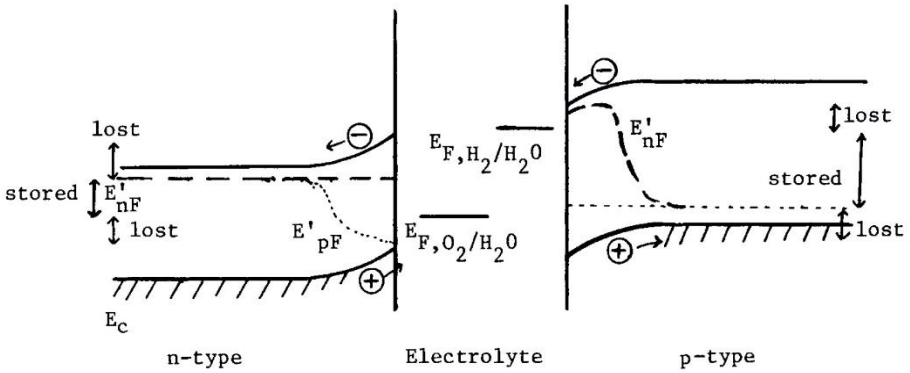

***Figure I - 7**: Energy bands in a system of two semiconductors chosen to generate opposite photovoltages [21].*

Then, photogenerated electron-hole pairs lead to an excess concentration which impact mainly the minor-carrier distribution – holes for n-type and electrons for p-type – leading to a hole quasi-Fermi level shift for n-type semiconductors and an electron quasi-Fermi level shift for p-type semiconductors. As a result, anodic photocurrent can be measured for n-type semiconductors; cathodic one, for p-type semiconductors.

B.2.3 Light absorption properties of semiconductors

In a photoelectrochemical cell at least one of the electrodes is a semiconductor material. The semiconductor must have a band gap energy (E_g) which is suitable to promote visible light absorption. In theory, a semiconductor band-gap energy of 1.23 eV is required to drive the overall water-splitting reaction in a PEC cell, as presented in the Pourbaix diagram (**Figure I - 2**). As a remind, the energy of a photon is inversely proportional to the wavelength of a photon, thus, to perform water-splitting in a PEC cell the required energy is equivalent to the energy of a photon with a wavelength of around 1010 nm ($E = \frac{hc}{\lambda} \rightarrow 1.23 = \frac{1240}{\lambda} \rightarrow \lambda \approx 1010\, nm$) – hence ca. 70% of all solar photons are theoretically available for water splitting.

However, all solar photonic processes have unavoidable energy losses (e.g. thermodynamic losses, electron/hole transport) that in practice involve per-photon energy values higher than the theoretical limit of 1.23 eV [3]. The existence of energy losses associated with solar energy conversion on photocatalysis increases the optimal band-gap for high performance photocatalysts from the theoretical value of 1.23 eV to 2.0-2.2 eV. Therefore, the basic parameter that governs the light-harvesting ability of the photocatalyst is its electronic

structure, which determines its band gap energy. **Figure I - 8** illustrates the band positions of various semiconductors regarding the potentials (NHE) for water-oxidation/reduction processes [22].

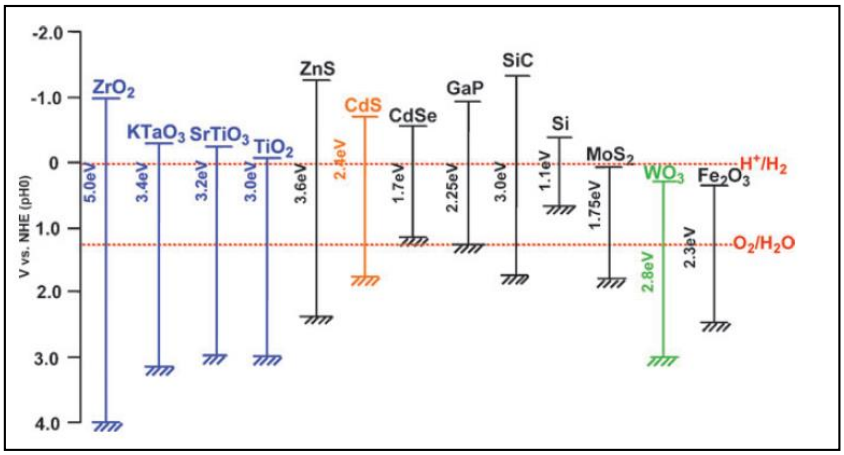

Figure I - 8: *Band-gap energies and relative band positions of different semiconductors relative to the water oxidation/reduction potential (vs. NHE) [14].*

Upon the absorption of a solar photon with energy $h\nu > E_g$ (the semiconductor band gap energy), this space-charge field can separate photo-generated electrons in the semiconductor's conduction band from their corresponding holes in the valence band, to directly drive an electrochemical solar fuel production reaction [23].

B.2.3.1 Indirect and direct band-gap of semiconductors

Light absorption and emission in a semiconductor are known to be heavily dependent on the detailed band structure of the semiconductor. Thus, the band gap of a semiconductor can be of two basic types: indirect band gap or direct band gap.

Direct band gap semiconductors, *i.e.* semiconductors for which the lowest energy state of the conduction band occurs at the same wave vector, k, as the highest energy state of the valence band and have a strong absorption of light as characterized by a larger absorption coefficient (**Figure I - 9a**). In contrast, in the case of an indirect bandgap semiconductor, since the conduction minimum and the valence band maximum does no exhibit the same k-vector (crystal momentum) the photon absorption involves the contribution of the lattice (phonons) which hampers the process and so indirect bandgap semiconductors have a smaller absorption coefficient (**Figure I - 9 b**) [24]. As a consequence, in the direct band semiconductors the electron makes a direct transition from conduction to valence band emitting a photon. In an indirect semiconductor, the electrons make transition from conduction to valence band passing

through intermediate states giving up its energy to the crystal lattice, causing rise in crystal temperature.

Some semiconductors have electronic structure transitions from an indirect band-gap to direct band-gap, making these particular materials very interesting for the use as photo-catalysts devices. Layered materials which can exfoliate into ultrathin monolayers are able to tune their band-gap from indirect to direct in order to absorb significant part of the visible spectra, particularly in longer wavelengths [25].

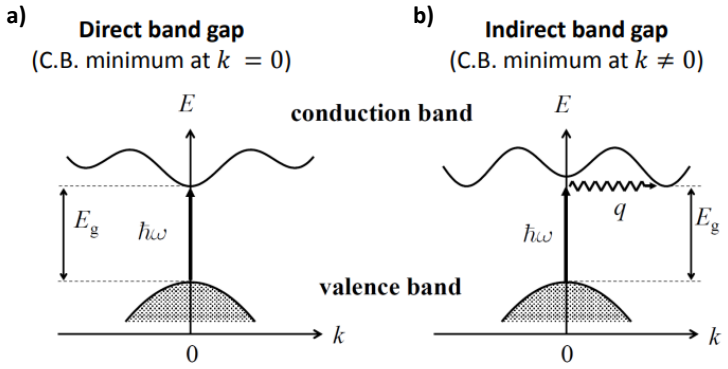

Figure I - 9: *Energy vs. crystal momentum for a semiconductor with (a) direct bandgap, (b) indirect band gap, showing that an electron cannot shift from the highest-energy state in the valence band to the lowest-energy state in the conduction band. Here, almost all of the energy comes from a photon (vertical arrow), while almost all of the momentum comes from a phonon (horizontal arrow) [26].*

B.3 Photoelectrochemical Cell

Compared to the photovoltaics and electrolysis approaches, a more straightforward path to light-driven chemical transformations is to directly interface a semiconductor and the electrolyte in a photoelectrochemical (PEC) device. It does not only eliminate the need for a separate electrolyzer (reducing system complexity), reducing the number of potential loss channels in the system [23]. A defining characteristic of a PEC cell is the direct interface between the semiconductor and the liquid electrolyte. This process results in a PEC diode owing to the Schottky-type electronic junction formed as a result of the development of a region in the semiconductor that is depleted of free charge carriers [27].

B.3.1 PEC Cells Configurations

The direct conversion of solar energy into chemical fuels can be achieved by a basic photoelectrochemical device, which can be constructed from a semiconductor electrode in direct contact with a liquid electrolyte, as a single band gap device (**Figure I - 10**) and connected

to a metallic counter electrode – Pt for instance. However, such kind of device configuration has not turned out so far to reach high solar to hydrogen conversion efficiencies [28], since it often requires an additional bias voltage to overcome the low photovoltage cell. Instead, the use of two semiconductors can form multi-junction configurations with p- and n-type semiconductors connected in series, as a dual band gap device [20]. In this tandem cell approach, the solar photons not absorbed by the top cell are transmitted and absorbed by the cell underneath. In this configuration the cells can generate sufficient photo-potential and harvest a significant portion of the solar-to-hydrogen conversion efficiency [2], without the need of any bias voltage.

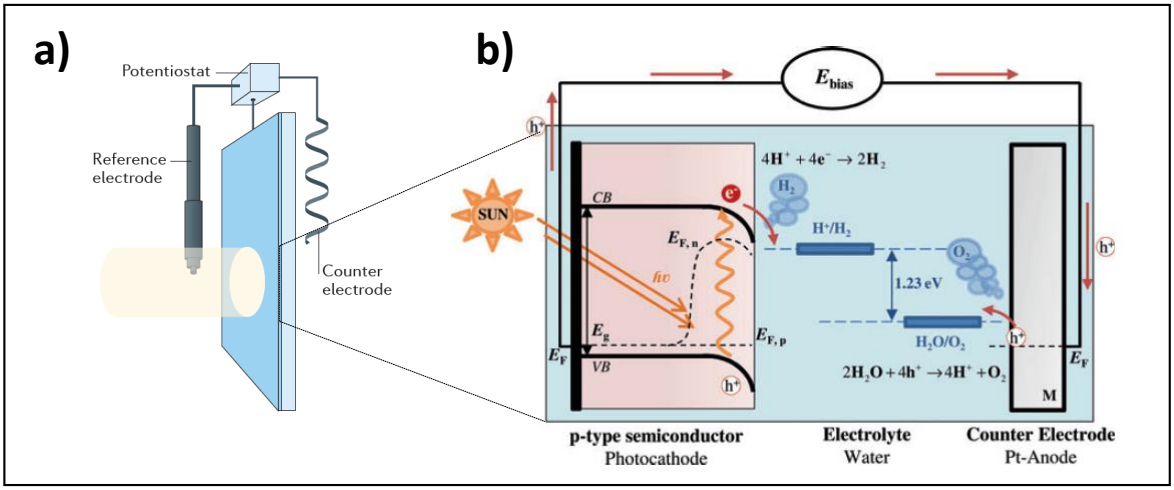

Figure I - 10: *(a) Schematic of a single-type PEC cell for water splitting with incident solar illumination [27]. (b) Working principle of single-type PEC using a photoelectrode with a single bandgap energy (E_g) under illumination* [29] *(adapted image).*

No semiconductor has been identified to provide sufficient photo-potential, while harvesting a sufficient portion of the solar spectrum to afford efficient solar-to-fuel conversion. Since two electrodes are required for any complete electrochemical operation, a tandem cell employing a photoanode and a photocathode that harvests complimentary portions of the solar spectrum is envisioned as a more viable device design. A schematic of a photoelectrochemical (PEC) tandem cell for water splitting is shown in **Figure I - 11.**

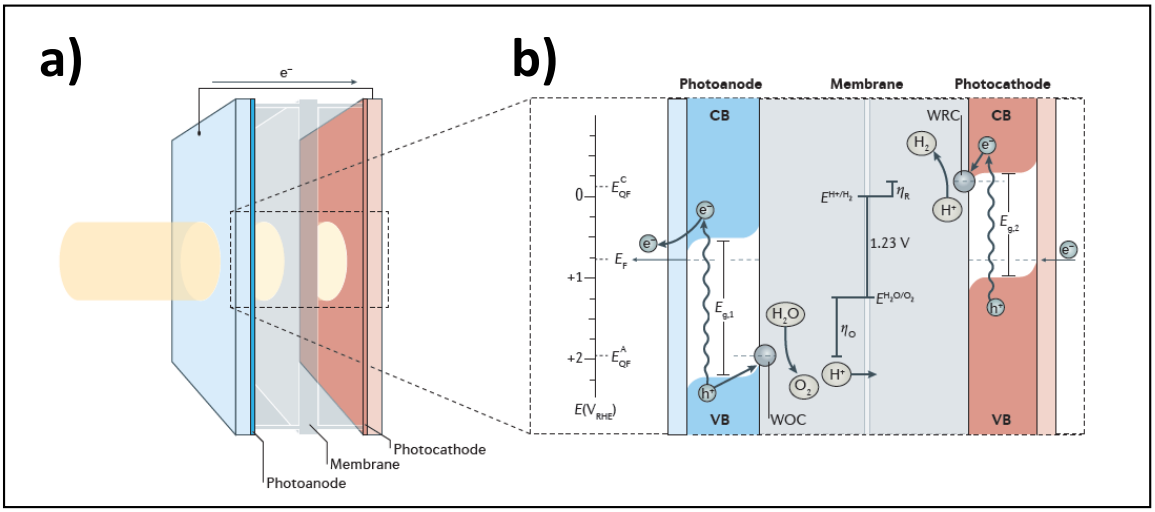

Figure I - 11: *(a) Schematic of a 'wired'-type tandem cell for water splitting with incident solar illumination striking the photoanode and transmitting to the photocathode. (b) Working principle of the tandem cell using a photoanode with bandgap energy E_{g1} and a photocathode with E_{g2} (where $E_{g,1} > E_{g,2}$) [27].*

Since only 1.23V are needed for water splitting under standard conditions from a thermodynamic standpoint, one could believe that a semiconductor with a minimum band-gap (E_g) of 1.23 eV (an absorption wavelength cut-off of ≈ 1010 nm) could be effective [30]. However, significant loss processes are involved. According to Sivula *et al.* [30], there is an entropic energy loss resulting from the amount of work that must be done to extract the excited states. The chemical potential of the excited state, $\Delta\mu_{ex}$, represents the maximum amount of energy available to do the work, and is necessarily significantly less than E_g, as illustrated in **Figure I-12**. These loss processes imply that a semiconductor with E_g greater than 1.23 eV must be used to realize a PEC cell, in order to generate the onset potential (V_{oc}) necessary to split the water.

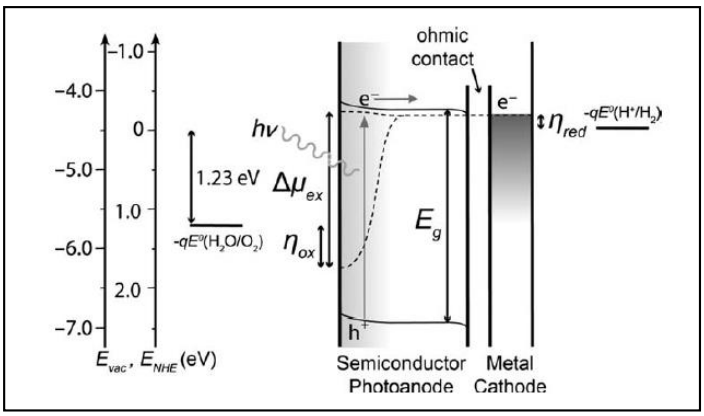

Figure I - 12: *Electron energy scheme of single PEC water splitting using a photoanode. The absorption of a photon (hν) by the semiconductor with a band-gap (E_g) creates an electron-hole pair with free energy of $\Delta\mu_{ex}$ [30].*

Based on the standard AM 1.5G solar spectrum (1000 W m^{-2}), a semiconductor with 1.23 eV band-gap would operate at a maximum overall solar-to-hydrogen conversion efficiency (η) of about 47%, assuming no other losses [31]. Whereas, the efficiency of conversion of incident solar radiant energy to chemical potential energy stored as H_2 is given by $\eta = J_{ph}(mA\ cm^{-2})\ x\ 1.23\ eV/100\ (mW\ cm^{-2})$. However, the significant loss processes involved are unavoidable in any energy conversion process. Despite the ideal solar energy conversion limit using one single device is 34% for AM1.5G irradiation, Bolton et al. [32] analyzed the upper limit for η_{STH} using one absorber material with realistic losses and reported maximum values of 11.6% using E_g = 2.2 eV and 17% using E_g = 2.03 eV. Moreover, if materials with band gaps greater than 3.0 eV are employed, limiting η_{STH} to less than 2% can be reached. **Figure I - 13** presents the Shockley and Queisser efficiency limit for an ideal solar cell versus band gap energy.

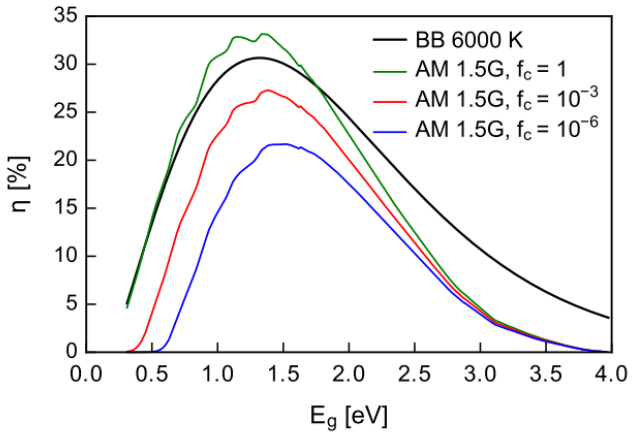

Figure I - 13: *Shockley–Queisser limit for a solar cell with a cell temperature at 300 K illuminated by a black body with a surface temperature of 6000 K (black curve) compared to the detailed balance limit for standard solar cell test conditions (Tc = 298.15 K, AM 1.5G). Considering only radiative recombination (green curve), non-radiative recombination that is 10-3 (red curve) and 10-6 (blue curve) times stronger than radiative recombination [33].*

A comparison with the detailed balance limit for single junction cells under standard test conditions (AM 1.5G, 25 °C) reveals that higher conversion efficiencies can be reached with the AM 1.5G spectrum for band gap energies between 0.6 and 1.7 eV [33]. The effect of non-radiative recombination is also considered for different factors (f_c) that describes the fraction of radiative recombination. If (f_c) = 1, then there are no non-radiative recombination paths and the calculated efficiency corresponds the green curve (**Figure I - 13**). One should note that window where the highest efficiencies can be reached (e.g. 90% of η_{max}) is moving toward higher band gap energies with increasing recombination. In fact, while a semiconductor can only harvest photons with energy greater than E_g, the requirement to use a material with a larger band-gap also implies a lower possible solar-to-hydrogen conversion efficiency (η_{STH}) [30].

By employing multiple light absorbers in tandem, dual-PEC systems can both harvest a significant portion of the solar spectrum and provide enough energy to afford water splitting. This approach to PEC water splitting increases system complexity, but also energy conversion efficiencies. Moreover, both compounds must be able to support rapid charge transfer at the interface, must exhibit long-term stability, and must efficiently harvest a large portion of the solar spectrum, which transforms absorbed solar photons into excited electronic states (both electrons and holes) [23].

B.3.2 Main requirements to perform solar water splitting

In this section, important requests necessaires to perform solar water splitting were discussed. The following table (**Table I - 1**) summarizes the main characteristics and important considerations to achieve significant solar-to-chemical conversion efficiencies.

Table I - 1: *summary of main requirements for solar water splitting.*

Photocatalysis – principal characteristics	
Semiconductor as photoelectrode	p-type as photocathode and n-type as photoanode
Photocathode	Hydrogen evolution reaction (0V vs NHE, pH0)
Photoanode	Oxygen evolution reaction (+ 1.23 eV vs NHE, pH0)
Band-gap Energy (E_g)	1.2 eV (≈ 1010 nm) < E_g < 3.1 eV (≈ 400 nm)
PEC Cell	Single device Double device – Tandem Cells

Nevertheless, it is also essential to understand the fundamental device physics of semiconductors, the thermodynamic and kinetic parameters of semiconductor-liquid contacts, and the function of surface electrocatalysts. The electric field developed in equilibrium with a redox couple and the photoelectrode results in band banding, that directs photogenerated free minority charge carriers (holes for n-type semiconductors and electrons for p-type semiconductors) to move from the semiconductor surface into the solution. In addition, the efficiency of a photoelectrode is determined by the energy that can be extracted from the photogenerated electron-hole pairs.

B.4 Emerging p-type Semiconductors as Photocathodes

While numerous n-type semiconductors has been well-studied as a photoanode for water oxidation; comparatively p-type semiconductors has been less extensively studied as a photocathode for water reduction [23]. Indeed, it is still necessary to find materials with suitable

band gap energy to harvest significant portions of the visible light, adding to the fact that the search of efficient photocathodes is not limited to oxide materials, in the case of the photoanodes, since the reductive side of the cell is not submitted to oxidative conditions, as discussed by Prévot *et al.* [23]. As this study will focus on the photoelectrochemical production of hydrogen, the present section will present several works that have been related to the development of stable photocathodes, as well as low-cost and efficient photocathodes for water reduction.

Photocathodes used for a water splitting cell need to supply sufficient cathodic potential to reduce water to H_2 and must be stable in aqueous environments. The latter has been reported to be less problematic than photoanodes of the cathodic polarization under operation [20] The first p-type semiconductor reported as photocathode was a single crystal of GaP with a band gap of 2.38 eV, reported by Yoneyama *et al.* in 1975 [34]. Since then, many different p-type semiconductors have been studied as a photocathode for water photo-reduction. Here, we will present emerging materials used as photocathodes for hydrogen evolution, divided in different classes of semiconductor materials.

B.4.1 p-type Metal Oxides

The variety of p-type oxides provided a large amount of work for the study of its performance in water splitting. The metal oxide semiconductors have the advantage of simple synthesis procedure. Several metal oxide semiconductors, such as binary oxide Cu_2O (2.0 eV) [35][36], ternary oxides $CaFe_2O_4$ (1.9 eV) [37], $CuNb_3O_8$ (1.5 eV) [38] and $CuFeO_2$ (1.5eV) [39] have been investigated as photocathodes. Special attention has been paid to p-Cu_2O. Paracchino *et al.* reported a highly efficient electrodeposited p-Cu_2O electrode, protected by nanolayers of Al-doped ZnO and TiO_2, and coated with electrodeposited platinum [35], making this photocathode one of the most promising low-cost materials reported so far.

The chemical stability, abundance and low-cost of the oxides give a promising type of material for large-scale device production. However, they usually have modest optical absorption coefficients, poor charge-carrier mobility and short charge-carrier lifetime [40]. Further research efforts are aimed at increasing its overall efficiency and stability, such as by increasing the dopant concentration, adjusting particle sizes and surface modification.

B.4.2 p-type Silicon

p-Si makes one of the best photocathodes for use in a tandem cell, due to its abundance and low cost. However, its small band gap energy (Eg = 1.12 eV) limits the conversion efficiency, requiring an n-type photoanode to work together to achieve overall water splitting [23]. Even so, a lot of effort has been placed into improving performances of p-Si photocathode for HER [41]–[46], since the first report about p-Si electrodes in NaCl [47]. The diversity of reported works demonstrates the silicon performances as photocathodes using several approaches such as morphology control and surface treatments, and its high abundance makes the p-Si one of the most promising materials. However, it presents high efficiency only in red and infrared light.

B.4.3 p-type Metal Chalcogenides

Chalcogenide p-type materials are also considered potential photocathodes for water reduction. Sulfur and selenium have higher-lying p-band energy levels than oxygen and considering choices of other chemical elements, they can have a wider tunable bandgap values (E_g = 1.0 – 2.4 eV) [27]. The first reports showed that binaries chalcogenides, such as ZnTe (E_g = 2.25 eV) was unstable, and single-crystalline CdTe showed a relatively low band gap (E_g = 1.5 eV) and good stability at cathodic potentials under acidic conditions [48]. The chalcopyrite-type semiconductors (CIGS), such as $CuIn_xGa_{(1-x)}S(Se)_2$, has shown that tuning its bandgap energy can shift valence and conduction band edges of semiconductor towards the suitable position for water splitting [49]. Other chalcogenides such as p- Cu_2ZnSnS_4 (E_g = 1.5 eV) [50], p- $CuInS_2$ (E_g = 1.5 eV) [51], p-Cu(In,Ga)S_2 (Eg = 1.5 eV) [52] and p-$CuGaSe_2$ (E_g = 1.65 eV) [53] also have been investigated as photocathodes, with the these two last as being one of the most performants photocathodes modified with a CdS layer and Pt nanoparticles. However, it must be noted that the enhanced photoactivity of these materials comes often from the resulting p–n junction using n-type overlayers (commonly CdS) [27]. Note that the long-term stability of the bare CdS–electrolyte junction will require further investigation.

B.4.4 p-type Phosphides

p-GaP, p-InP and p-$GaInP_2$ are single-crystals with good visible light absorption properties with relatively low band gap energy and have been previously investigated as photocathodes [54]–[58]. p-type InP (E_g = 1.3 eV) showed comparable photocatalytic activity with the one of noble metals by using MoS_3 nanoparticles as co-catalyst [59]. p-type $GaInP_2$ (E_g = 1.8 eV) also demonstrated good conversion efficiencies, however, the energetics of its band

edges are not well aligned with water redox potential levels and requires an additional induced bias for water splitting [60][61]. Despite the high efficiencies of gallium and indium phosphides, they are not ideal for inexpensive large-scale production, due to the scarcity of their components and the need for them to be single-crystalline.

B.4.5 Carbon-based semiconductors

Carbon-based semiconductors such as graphitic carbon (IV) nitride polymer ($g\text{-}C_3N_4$) is an attractive metal-free semiconductor that can be used in photocatalytic water splitting and dye degradation and optoelectronic conversion under visible light without photo-corrosion [62]. g-CN is a low-cost material with a band gap of approximately 2.7 eV [63]. Several works have been reported about graphitic carbon nitride which demonstrated visible-light hydrogen evolution and stability as p-type photocathode [63]–[65]. One challenge for g-CN is that the conversion efficiency of pristine g-CN solids in sunlight is low, due to limited visible light absorption ($\lambda < 400$ nm), low surface area and grain boundary effects. For optimizing light absorption, there has been intensive investigation of various ionic, covalent and non-covalent chemical dopants [62][66].

As previously reported, solar-to-hydrogen efficiencies are mainly governed by band gap of the photoactive materials (**Figure I - 13**). Another figure of merit largely reported to describe PEC devices performances is the Incident Photon-to-Current Efficiency (IPCE). Although IPCE under applied bias is not considered as a valid estimate, it is a useful tool to get insights into the material properties. An overview of several photocathode materials discussed in this section reported over less than the last 10 years with relevant conversion efficiencies is presented in the **Figure I - 14**. A remarkable observation is the relation between the bandgap energy and photocathode performance, which shows that the semiconductor should be visible-light responsive to make best use of the solar radiation in order to increase the solar energy conversion efficiency as high as possible [40].

In the metal oxide group, Cu_2O nanowires was reported with incident photon-to-current conversion efficiencies about 70% for $\lambda > 550$ nm by Luo and co-workers [36] and $CuFeO_2$ revealed IPCE up to 10% in smaller wavelengths ($\lambda < 450$ nm) [39]. Metal chalcogenides such as the CIGS are considered the as one of the best photocathodes for the HER, achieving IPCE up to 30, 50% for $\lambda < 700$ nm after deposition layer of CdS and Pt nanoparticles [52][53]. For the silicon-based photocathodes multi-junction amorphous silicon (a-Si), which has a tunable bandgap, was reported with IPCE of 80% with a protective layer of TiO_2 and Ni–Mo alloy [46]. As for the

phosphide-based photocathodes, conversion efficiencies of about 6% was obtained for p-InP nanowires with MoS_3 catalyst [59].

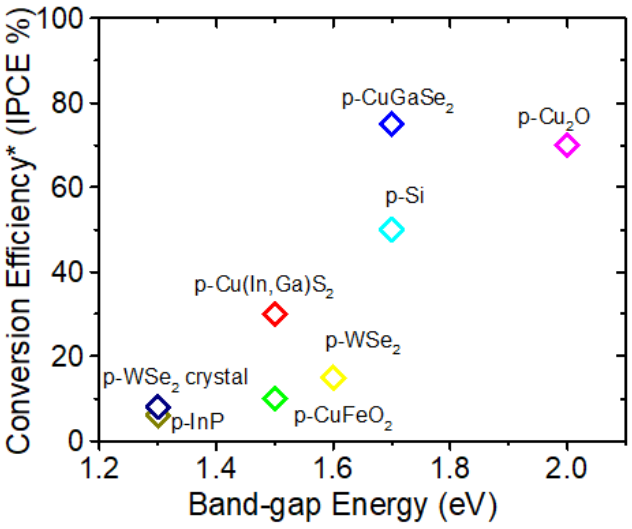

Figure I - 14: *The relation between the semiconductor bandgap and the obtained photocurrent under AM 1.5G illumination and IPCE conversion efficiency. *The collected data was based on experimental results of previous works [36], [39], [46], [52], [53], [59], [67], [68].*

Lastly, not very far from the metal chalcogenide group, the transition-metal di-chalcogenides such as p-WSe_2 have been investigated, but not as much as other photocathode semiconductors, for the HER. The layered crystal structure have recently attracted attention due to their ability to be exfoliated into atomically thin 2D sheets [27], resulting in unique optoelectronic properties with high interfacial exchanges, and allows the bandgap to be tuned according to the number of atomic layers. Previous studies revealed higher conversion efficiencies from WSe_2 crystal [67] to few layered [68] photocathodes, tuning the bandgap energy and achieving improved photoelectrochemical performance. These studies previously reported have given encouraging results for further development as photocathodes for hydrogen generation.

B.5 2D TMDCs as promising materials for Solar Water Splitting

The TMDC materials have been reported as photoelectrodes to the solar water splitting. As the graphene, these materials exist in bulk form as a stack of layers with weak interlayer attraction, allowing exfoliation into individual atomic thin layers [25]. Although the overall structure is similar for all TMDCs, the material properties can be significantly changed depending on the cation (W, Mo) and anion (S, Se). There is an engineering interest in TMDCs

in their atomically thin 2D forms because they can display of various hydrogen evolution onset potentials and tune band-gaps around 1-2 eV [69].

Interestingly, the semiconducting properties of these materials can be tuned by altering the chemical composition as well as the doping preference [70]. Besides the well-suited band-gap values, alteration of their conduction and valence band positions could be exploited for the fabrication of tandem cells [71]. The band offsets provide different electronic structures and preference. The higher or lower positions of the conduction or valence bands give doping preference for n- or p- type semiconductor. Thus, TMDCs materials such as WSe_2 has p-type doping preference due to the high values of the conduction and valence band. Differently of the MoS_2 that the doping preference is n-type [72]. The band alignment for MX_2 monolayers is shown in **Figure I - 15**.

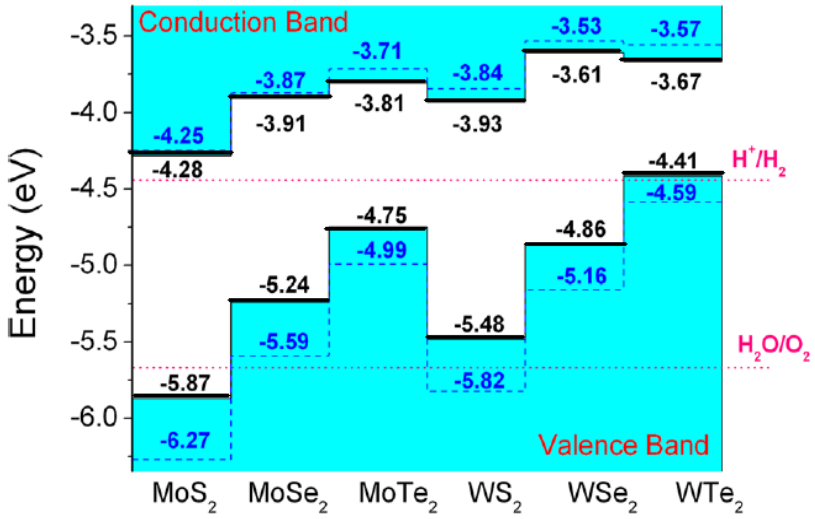

Figure I - 15: *Calculated band alignment for MX_2 monolayers. The dotted lines indicate the water reduction (H^+/H_2) and oxidation (H_2O/O_2) potentials. The vacuum level is taken as zero reference [71].*

As a matter of fact, the surfaces of TMDC thin sheets consist in multiple terraces separated of edge sites. Besides, these edge sites have been demonstrated as deleterious to the photo-conversion efficiency because the under-coordinated atoms on the edges are reactive toward surface corrosion processes [73] and additionally act as sites for charge-carrier recombination [74]. The photocatalytic activity of the TMDCs has been commonly showed to be increased after surface modification by deposition of co-catalysts [75] or/and surface passivation treatments [68]. Strategies developed to control the surface defects present on TMDC thin films have been an attractive challenge for improvement of the photoactivity of this class of materials.

The structural tunability of the TMDCs allows their large applicability in electrochemical fields for energy conversion and storage; and the remaining challenges in finding strategies to decrease surface defect has motivated the present work to focus on the TMDC materials as photocathode for the HER. Therefore, the next section will be focusing in this class of semiconductor materials, presenting more precise information about their structure, their optoelectronic properties and the present challenges to improve their solar-to-energy conversion efficiency.

C Two-dimensional TMDCs for HER Evolution

Historically, first-row transition metal chalcogenides were mainly the center of focus due to the elemental abundance and low cost. In general, this class of material displays of a wide range of optical, electronic, chemical, mechanical and thermal properties and when exfoliated into thin films, they can exhibit different properties from that of the bulk material.

C.1 Crystalline Structure

TMDCs are a class of materials with the generalized formula of MX_2, whereby M represents a transition metal element from group 4, 5 or 6 (Mo, W) and X represents a chalcogen (Se, S or Te). WSe_2, $MoSe_2$, WS_2, and MoS_2 crystallize in a layered structure such that the chalcogen atoms are arranged in close-packed hexagonal layers in the form X-M-X, with the chalcogen atoms in two hexagonal planes separated by a plane of metal atoms arranged periodically (**Figure I-16**). Precisely, the monolayer of TMDC materials is constituted by a plane of metal atoms sandwiched by two hexagonal planes of chalcogen atoms, which are covalently bonded to the metal atoms. On the other hand, adjacent layers are weakly held together by van der Waals interactions to form the 3D bulk structure [69].

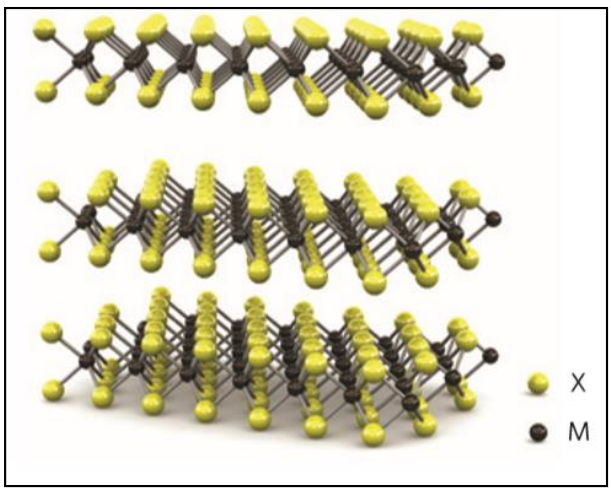

***Figure I-16**: Three-dimensional schematic representation of a typical MX_2 structure, with the chalcogen atoms (X) in yellow and the metal atoms (M) in grey [69].*

The weak van der Waals interactions between the layers, as being a strongly distance-dependent ($E_{van\ der\ Waals} \propto r^{-6}$) and do not result from a chemical electronic bond make possible to split such kind of materials into individual atomic layers, which can be achieved *via* mechanical cleavage, liquid exfoliation or ion intercalation methods [76].

The adjacent layers are weakly held together to form the bulk crystal in a variety of polytypes, which vary in stacking orders and metal atom coordination. The overall symmetry of TMDC is hexagonal or rhombohedral and the metal atoms have octahedral or trigonal prismatic coordination. depending on the metal atom coordination by the six chalcogen atoms, the electronic properties can range from metallic to semiconducting [69]. In the 2H structure the metal atom coordination is trigonal prismatic, and the material is semiconducting, being this one the most occurring. In the 1T structure, the metal coordination is trigonal anti-prismatic (or octahedral) inferring to the material a metal character, as represented in **Figure I - 17** [77].

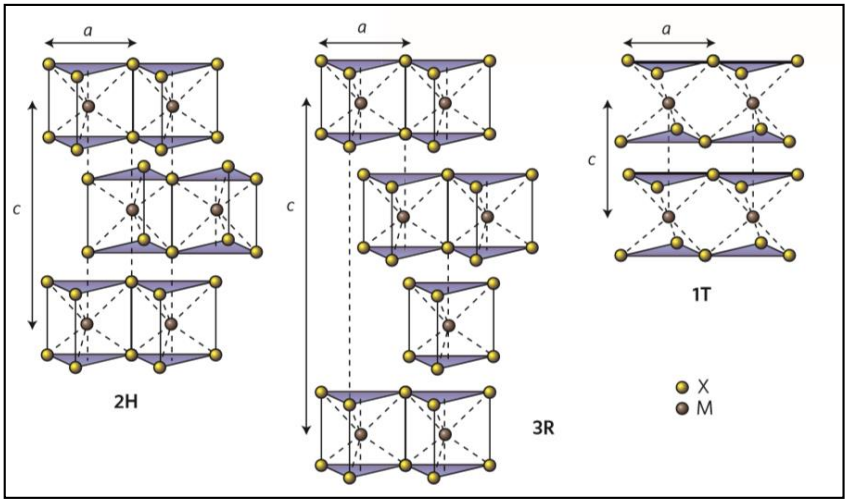

Figure I - 17: *Schematics of the structural polytypes: 2H (hexagonal symmetry, two layers per repeat unit, trigonal prismatic coordination), 3R (rhombohedral symmetry, three layers per repeat unit, trigonal prismatic coordination) and 1T (tetragonal symmetry, one layer per repeat unit, octahedral coordination) [69].*

The layers perpendiculars to the axe c defined as the plan (002) is called basal plane. The basal surfaces are constituted of an atomically thin extern layer. If the chalcogen atom bindings on the surface/edges are saturated, the surfaces are low chemically reactive. However, if there is presence of unsaturated bindings in the nanosheets edges, the surfaces are chemically reactive [78].

C.2 Synthesis routes: bulk to ultrathin films of TMDCs

The characteristic structure of 2D flat sheet is essentially required in electrochemical or photocatalytic applications, because of the high specific surface area promoted by these structures. Another advantage of exfoliation into 2D nanosheets is the quantum confinement of electrons in two dimensions, transforming the electron band structure to yield new types of electronic and magnetic materials. Different methods of exfoliation have been developed to yield

semiconducting 2D flakes of stable dispersions with high concentrations and processing them into uniform thin films without layer restacking. There three main ways to achieve 2D structure from exfoliation: the mechanical exfoliation, the chemical exfoliation and liquid exfoliation

C.2.1 The mechanical exfoliation process

The earlier reports described graphite mechanically exfoliated into graphene flakes consisting of tens and hundreds of layers [25]. There are two kinds of mechanical exfoliation, normal force which one can exert normal force to overcome Van der Waals attraction when peeling two layers apart, such as the Scotch tape (**Figure I-18**) and lateral force, where one can exert lateral force to promote the relative motion between the layers [79].

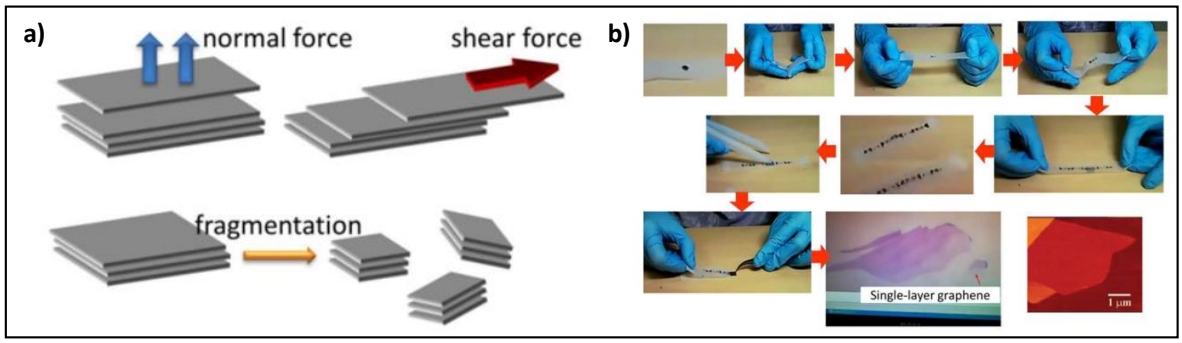

Figure I-18: *(a) Two kinds of mechanics routes for exfoliating graphite into graphene flakes and the auxiliary route for fragmentation, (b) illustrative procedure of Scotch-tape based micromechanical cleavage of HOPG [79].*

Despite the selectivity of the mechanical method, the main shortcoming is the difficulty to go for large scale production. For development of solar energy conversion devices, a controllable method to fabricate large-area and continuous thin films with controllable layer orientation and suitable contact to a conducting substrate is demanded. Though substantial efforts have been made to improve the yield and degree of exfoliation, the yield of monolayer graphene is still quite low [79]. Moreover, a large majority of graphite is not exfoliated, and centrifugation is needed.

C.2.2 The chemical-exfoliation process

Layered materials can also strongly adsorb guest molecules into the spacing between layers. The intercalation, often of ionic species, increases the layer spacing, weakening the interlayer adhesion and reducing the energy barrier to exfoliation. One well-known class of intercalants is the organo-lithium compounds. MoS_2 can be intercalated with lithium to give the reduced Li_xMX_n phase (X = Se, S) with expanded lattice, then, this can be exfoliated in a second

step into single-layer sheets by ultrasound-assisted hydration process [80]. Intercalants such as n-butyl-lithium can transfer charge to the layers [81], where a redox reaction occurs, resulting in the formation of octane from two butyl radicals and in the reduction of interlayer binding. **Figure I - 19** presents a schematic of the ion intercalation.

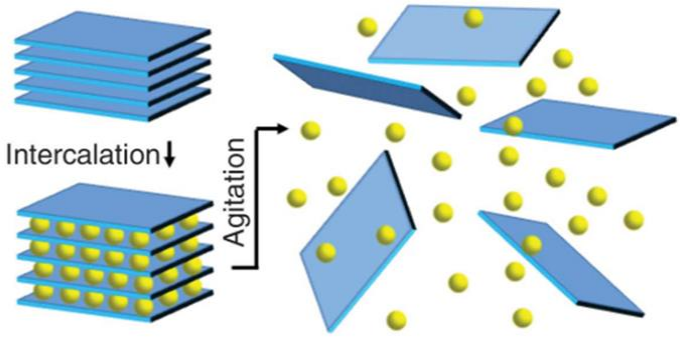

Figure I - 19: *Ions (yellow spheres) are intercalated between the layers in a liquid environment, swelling the crystal and weakening the interlayer attraction. Then, agitation can completely separate the layers, resulting in an exfoliated dispersion [81].*

The chemical exfoliation of TMDCs using lithium intercalation has been reported affordable stable dispersions of 2D flakes for homogeneous film formation [82][83]. However, in this kind of exfoliation the semiconducting 2H-phase of the TMDC reduces to the metallic 1T-phase causing a loss in the photo-activity properties [84]. In addition, the exfoliated nanosheets sometimes need to be stabilized in case of highly exfoliated nanosheets, due to their sensitivity to ambient conditions. Despite the low cost and high monolayer selectivity, the complexity and use of toxic chemicals limit the adoption of this exfoliation process [85].

C.2.3 The solvent-exfoliation process

Another strategy of exfoliation process has been developed to provide single or multilayer nanosheets that are then stabilized by interaction with the solvent or a surfactant. The strategy for solvent-assisted exfoliation is to find a solvent displaying of dispersive, polar and H bonding components suitable with the materials to be exfoliated. In addition, the material is exposed to ultrasonic waves in a solvent. Such waves generate cavitation bubbles that collapse into high-energy jets, breaking up the layered crystallites and producing exfoliated nanosheets [86].

This method is known to be of extreme simplicity, and it results in high-quality exfoliated nanosheets, which can then be fabricated into films or composite materials [87] and is suitable for the economical production of large-area solar energy conversion devices. Resulting in usually

few-layer nanosheets (typically ~1–10 stacked monolayers), with individualized monolayer contents that are low compared to other methods, as the ones described above [85].

After exfoliation, the dispersion is usually submitted to centrifugation to remove unexfoliated material and perform size selection. This step is especially necessary for those applications requiring the direct band gap luminescence properties that are conferred only by monolayers, as in the case of TMDCs [88]. Therefore, to acquire the full potential of nanosheet materials in applications it is clear that size selection must be an integral part of the material production process [85].

Several works were dedicated to study the exfoliation of different TMDC materials (WS_2, MoS_2, $MoSe_2$ and $MoTe_2$) and the dispersibility in different solvents, as well as the control of the surface nature. As the exfoliated material is two-dimensional with lateral size of hundreds of nanometers, it is assumed that the solvent-nanosheet interaction occurs primarily at the basal plane surface. It was reported that high dispersion concentrations are achieved with solvents having high surface energies. Thus, the surface energy can be used as a dispersion parameter for these materials [81]. TMDCs and other materials as graphene have been exfoliated by ultrasonication using surfactant or polymer solution that are electrostatically or sterically stabilized [89]. Dispersions of MoS_2, WS_2, $MoSe_2$ and others were obtained at concentrations higher than 4 mg/mL [85].

C.2.3.1 Step process of liquid exfoliation

According to Backes and co-workers, liquid exfoliation is considered as a three-step process [85]. The **Figure I-20** presents the full-steps process of liquid exfoliation. First, the weak interlayer attractions between adjacent sheets need to be overcome by imparting energy during the actual exfoliation process. Second, the nanosheets need to be stabilized against re-aggregation by suitable solvents or surfactants. They play a dual role as they minimize the net energy cost of the exfoliation while also adsorbing to the nanosheet surface, shielding them from restacking in the liquid. Third, size-selection is often required. This is because the as-produced dispersions are highly poly-disperse (**Figure I-20B**), containing nanosheets with a range of sizes and thicknesses (**Figure I-20C**). Equally, such dispersions typically display low monolayer contents.

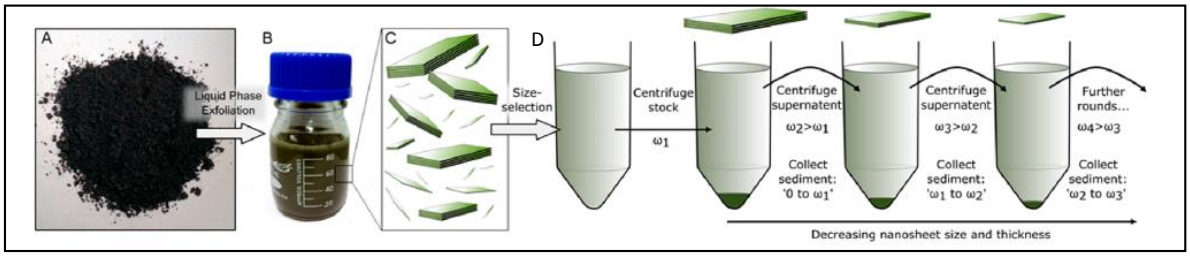

Figure I - 20: *Liquid exfoliation and size selection. (A) Photograph of a typical starting material, WS_2 powder, yielding (B) colloidal stable colored dispersions after the exfoliation containing (C) a mixture of nanosheets with varying lateral sizes and thicknesses. (D) Schematic of the liquid cascade centrifugation with subsequently increasing rotational speeds ω. The supernatant after each step is subjected to another centrifugation at higher centrifugal acceleration. Size-selected nanosheets are collected as sediments [85].*

The use of additive-free solvents provides efficient stabilization or dissolution. Typical solvents that are known to give stable dispersions include N-methyl-2-pyrrolidone (NMP), N-cyclo-2-pyrrolidone, dimethyl-formamide (DMF), dimethyl-sulfoxide (DMSO) and isopropyl alcohol (IPA). Moreover, there are two types of sonication, one is the ultrasonic tip that is positioned in the dispersion media and the other is called bath sonication, whereas a vial containing the material to be dispersed is itself immersed in a water bath that is perturbed by ultrasonic vibrations. In general, bath sonication may offer lower-cost alternative to tip sonication [85]. However, longer processing times are required to achieve an equivalent concentration of dispersed material and the process can be less reproducible.

Among the TMDC materials, the exfoliation of WSe_2 seemed not to be sufficiently explored. WSe_2 was previously reported using the sono polymer-assisted exfoliation method. Obtaining 2D sheet size (200–1000 nm) and thickness of monolayer and few layer flakes in 1,2-dichlorobenzene (DCB) [90]. Giving stable dispersions of high-concentration and continuous thin-film formation. Despite the development of liquid exfoliation and size selection, several challenges are remaining. The quality control of the exfoliated nanosheets involves lateral size, thickness, monolayer content and the defectiveness of the nanosheets [85].

C.3 Optoelectronic Properties of 2D TMDCs

C.3.1 Band gap and visible light absorbance

Interestingly, TMDCs materials usually exhibit an indirect band gap transition but as a monolayer it turns to direct bandgap transition, which was pointed out in the literature by an enhanced photoluminescence intensity [91]. In the same line, a systematic study on MoS_2 crystals reported the change of both the indirect and direct band gaps of the material as a

function of layer thickness [88]. Also, the results have shown a blue-shift in the indirect bandgap, depending on the layer number, from the bulk value of 1.29 eV to over 1.90 eV (**Figure I - 21**).

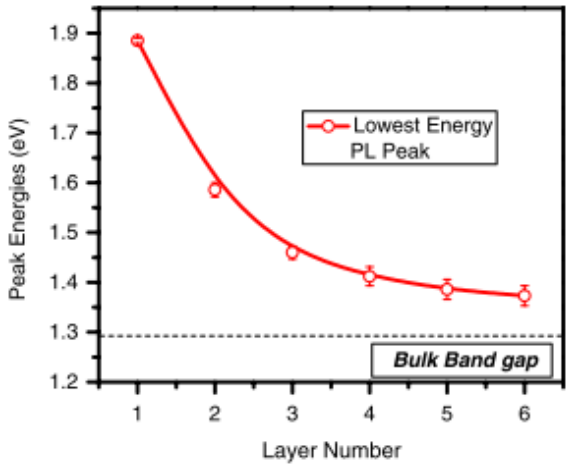

***Figure I - 21**: Band-gap energy of thin layers of MoS2. The dashed line represents the indirect band-gap energy of bulk MoS2 [88].*

The aforementioned experimental study has been also supported by a published density-functional theory calculation results [92][93]. Interestingly, it has been reported for MoS_2 [88], the decrease of layer number makes the Quantum Yield (QY) – the number of photons that the material emits over the number of absorbed photons [94] – increase dramatically together with an important increase of the photoluminescence intensity, as presented in **Figure I - 22**. QY values ranging from 0.01 to 6% have been reported, indicating high density of defected states and poor electronic quality [87].

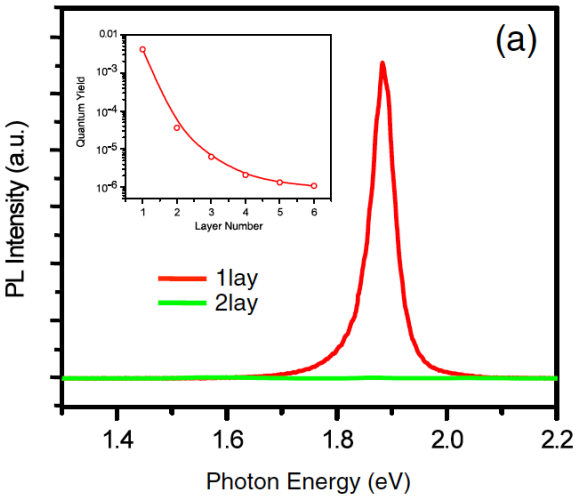

***Figure I - 22:** PL spectra for mono- and bilayer MoS_2 samples in the photon energy range from 1.3 to 2.2 eV. Inset: PL QY of thin layers for N = 1–6 [88].*

The achievement of high PL QY demonstrated by this work and other previous works indicates that the TMDC monolayers are well suited for high-performance optoelectronics at the atomically thin limit, including photocatalysis [94]–[96].

Besides, absorption properties also show sensitivity to the layer number (N); band gap decreases with increasing N. Indirect-gap optical transitions is limited by the sensitivity of absorption measurements, due to weak exciton binding. For MoS_2 thin crystals, it was demonstrated that the photoconductivity increases with photon energy towards the direct band gap. As presented in the **Figure I - 23**, for MoS_2 bilayer the onset photoconductivity occurs around 1.6 eV. For a monolayer, the photoconductivity occurs at 1.8 eV and is enhanced significantly, with an absorption rate of 10%. Corresponding to the optical absorption in the direct band gap edge.

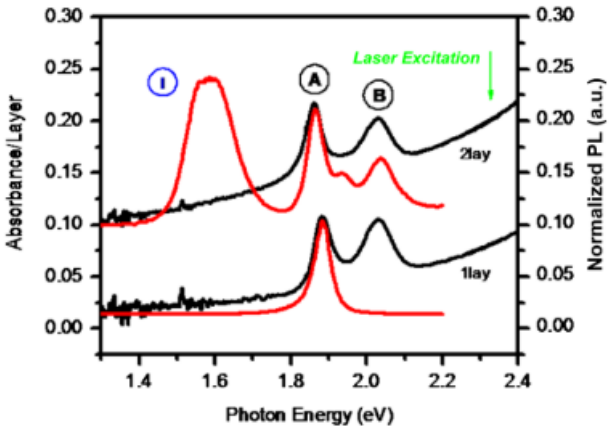

Figure I - 23: *Absorption spectra and the PL spectra for a mono and bi-layer of MoS_2 [88].*

C.3.2 Influence of the type of the elements and their size

Although the overall structure is similar for all TMDCs, the material properties can also change depending on the size and charge of both elements. Heavier chalcogens provide better electrical conductivity, critical for optoelectronic applications. For this aspect, the tungsten di-chalcogenides (WS_2 or WSe_2) have attracted considerable attention because of larger W size, which can alter the 2D structure [72]. Although W is a heavier element, its natural abundance is similar to that of Mo [97]. What makes W commercially more favorable for future industrial applications.

As discussed in this section, the properties of the TMDC materials are usually related to their layered structure. Likely to the graphite, they are very anisotropic. As the evolution of

optical properties and electronic structure can vary according to the number of layers, the control of the active sites formation is highly influenced by synthesis routes. All the applications of 2D TMDCs depends on the arrangements of active sites (whether edge sites of basal plane). Hence, the material properties significantly change with these arrangements [72]. Liquid exfoliation approaches of TMDC is being more considerable synthesis route, since it is more easily up-scalable, resulting in differences in the electronic properties of the material.

D Design of High Performance Photocathode for HER

There are many strategies to advance the development of new semiconductor materials for photoelectrochemical cells. The electrochemical reactions at the semiconductor are generally complex, multistep and proton-coupled electron transfer processes, which physically depends on catalytic surface sites. These sites can originate from the surface of the semiconductor itself or from a catalyst deposited [27]. Therefore, the intrinsic properties of the semiconductor materials still limit the maximum quantum yield – here the number of generated electrons or the number of hydrogen moles as a fraction of the absorbed photon number. Charge separation strategies to avoid recombination have primarily centered on the use of semiconductor/electrolyte interfaces under the application of electrical bias [1].

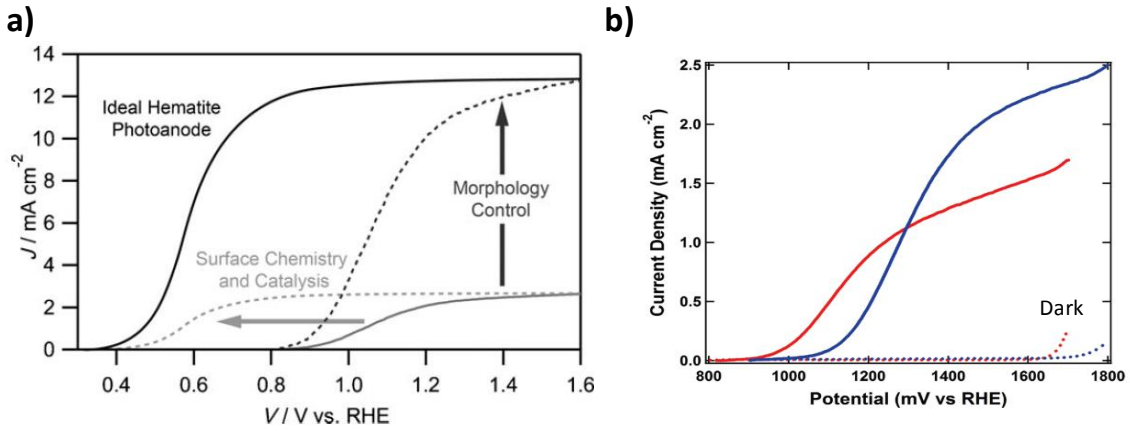

Figure I-24: *(a) Strategy for improving hematite performance photocurrent density for an idealized hematite photoanode (solid black trace) compared to the typical performance (solid grey trace) under simulated sunlight, and the expected effects of improving the surface chemistry and the morphology [98]; (b) Photocurrent (solid lines) and dark current (dotted lines) vs. applied voltage curves of control (red) and encapsulated (blue) hematite photoanodes after annealing step under simulated solar light in 1M NaOH electrolyte [99].*

Optimizing the electrode morphology and surface modifications, such as the deposit of relevant co-catalysts, have been reported to be key parameters to improve photocatalyst performances. A specific example for hematite based photoelectrode is depicted in **Figure I-24** [98][99]. Selection of desired feature size by the ability to anneal hematite films at high temperature showed effectiveness in the solar water-splitting capability of the electrodes. Recent works have demonstrated important aspects in the development of more efficient photoelectrodes, consisting in morphology modification, surface treatments, or still

nanojunctions with other efficient materials to ameliorate performance, and it will be further discussed further in this chapter.

There is a great need for nanostructuring the photoelectrocatalyst to optimize the absorption properties and perhaps tailor the band gap, size, and/or band edge position using quantum confinement [57]. Eventually, nano-structuration would promote the enhancement of visible light absorption and of the photogenerated charge carrier transfer efficiency [100]. Depending on the material properties, better performance maybe realized with a single crystalline thin film, or a film with a very high surface area. For materials with a very small photogenerated carrier diffusion length, larger interfacial areas between the semiconductor and the electrolyte will benefit the charge transfer kinetic [2].

Nevertheless, the interface of the semiconductor and liquid electrolyte is the most critical point in photoelectrochemical applications; the interface is the location where occur the charge separation, the charge transfer and large part of the charge recombination. Thus, to reduce charge carrier recombination or boost the charge extraction it is often necessary applying a co-catalyst and/or a passivation overlayer to improve performance. Much research efforts have been focused on understanding and controlling the quality of the interfaces in PEC cells through surface modifications. According to Guijarro [101], these surface treatments can improve drastically the energy conversion efficiency through distinct mechanisms: (i) surface state passivation, by acting over the surface with reagents that strongly bind the dangling atoms; (ii) charge transfer enhancement, by employment of materials that are known to work as efficient catalysts to provide effective attachment/reaction sites for the initial species and also release the final products, creating islands of these materials onto the photoactive semiconductor surface and promote favorable channels for charge transfer and surface reactions [102]. On top of that, an increase of the band bending, thanks to an adequate material deposition, is intended to improve charge separation [103][104]. The bottom line is those strategies are somehow in the direction of the formation of a heterojunction at the surface of the semiconductor to improve its overall quantum yield.

What is more, a proper charge collection is required and high pathways for charge transport within the material are to be developed. As an example, carbon nanotube and/or graphene [105]–[108] can optimize the electrical conductivity. As a popular graphite-based material, graphene exhibits superior electron mobility and good electronic behavior [109]. Previous studies have suggested that graphene-modified materials can show enhanced

electrocatalytic properties and, particularly, the combination of graphene with TMDCs appears to be a promising way to improve their HER performance [110]–[113], attributed to the contact between the layered structure of the TMDCs and the highly conductive graphene nanosheets. Each nanostructuring is widely used to overcome the trade-off between optical absorption, minority-carrier diffusion length and to increase the catalytic activity through an increased surface area.

D.1 Morphology optimization to obtain high surface area photocathodes

Some strategies have been recently proposed to construct photocatalysts based of high surface area. Solution-based colloidal methods for preparing oxide semiconductor electrodes has allowed the use of inexpensive processing techniques and displaying of mesoporous films with a morphology placing all of the material [114]. A morphology more adapted would promote a sufficient thickness to absorb all possible solar irradiation. This optimization, to obtain nanoparticle high surface area, has gained attention with recent studies, which have demonstrated improvement in the electronic transport properties. Such a novel architecture should provide an intimate and large contact interface for fast interfacial charge separation.

The application of nanostructuring techniques to PEC solar hydrogen production has led to advances with many materials [98][114]. Guijarro et al. [115] employed nitrocellulose as a low-temperature auto-decomposing porogen for the formation of mesostructured CdS and CZTS semiconductor thin films. Colloidal dispersions of CdS and CZTS nanocrystals previously prepared were mixed up with the nitrocellulose solution forming stable solutions. The films were obtained by doctor blading the solution and annealing in air (CdS) or under argon (CZTS) at 300°C. SEM images demonstrated controlled morphology with formation of pores, as presented in **Figure I - 25**. In addition, smaller pore sizes were obtained with further increase of the porogen content with an optimum loading to not result in poor adhesion of the thin films. The mesostructured thin films achieved photocurrents increase over compact nanocrystal films and an incident photon-to-electron conversion efficiency over 70% in the case of the CdS thin films, after control over surface areas and pore sizes.

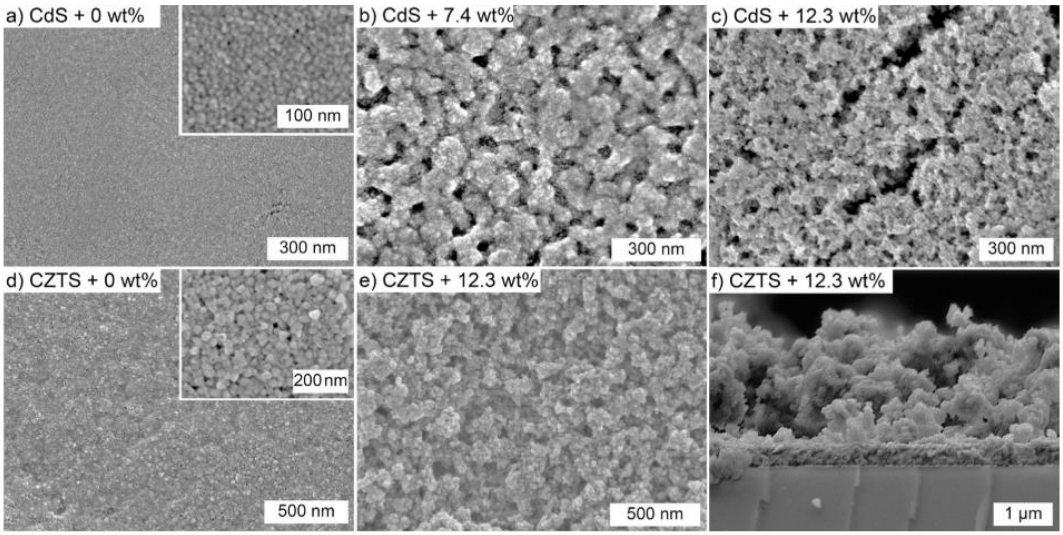

Figure I - 25: *Top view SEM images for air-annealed CdS (a,b,c) and Argon-annealed CZTS (d,e) nanoparticle thin films prepared from solutions containing nitrocellulose weight fractions (wt) as indicated. (f) shows a cross section image of the film in (e). All films were annealed at 300°C [115].*

In another work, bismuth vanadate ($BiVO_4$) with high surface area demonstrated outstanding photocatalytic performance with morphology optimization [116]. To improve the electron-hole separation yield, Kim and co-workers reported high-surface area nanoporous $BiVO_4$ electrode achieved by using simple, unmodified $BiVO_4$ with no extrinsic doping and no composition tuning [116]. The nanoporous films was obtained by using a vanadium source solution that could easily wet the BiOI surface, resulting in manifested porosity after heating in air at 450°C. The mesoporous morphology obtained (**Figure I - 26 a and b**) with specific surface area of about 30 $m^2\ g^{-1}$ effectively increased the photocurrent without additional doping. In addition, to maximize photocurrent generation, two different catalysts, FeOOH and NiOOH layers were deposited onto the resulting $BiVO_4$ photoanode achieving a photocurrent density of 2.7 mA cm^{-2}, as presented.

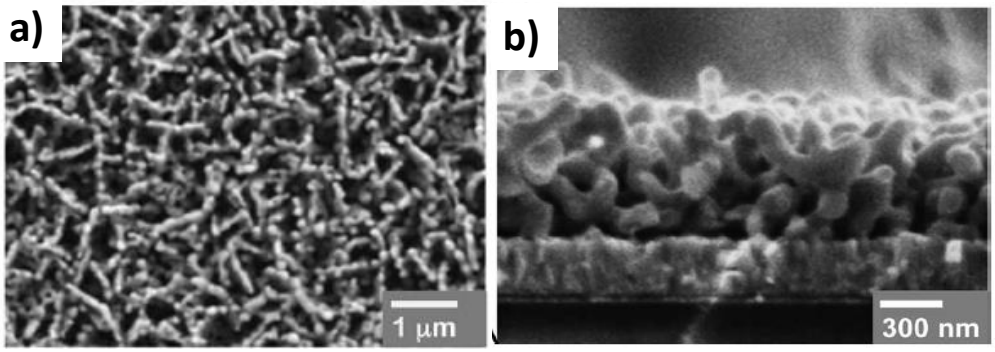

Figure I - 26: *(a) Top-view and (b) side-view SEM images of nanoporous $BiVO_4$ prepared using DMSO/$VO(acac)_2$ [116].*

These strategies of morphology control and formation of structured nanoporous materials, as discussed above, give a semiconductor material with considerable internal surface area. Mesoporous oxides such as TiO_2 and ZnO have been already reported [117][118]. The structure interconnected allow electronic conduction to take place, whereas the mesoporous are filled with an electrolyte. As previously discussed by Grätzel [119], the result is a junction of extremely large contact area between two interpenetrating, individually continuous networks. In this case, charge carriers could percolate across the mesoscopic particle network, making the huge internal surface area electronically addressable. Although still in development, the nanostructured cells offer potentiality for the improvement of the photoelectrochemical activity, by giving more accessible internal surfaces where the redox reaction can take place.

Even though morphology is an important feature, but it is both the antidote and the poison. Surface area enhancement comes with surface defect enhancement and poorer charge percolation. Thus, surface modifications must be performed to reach better solar to hydrogen efficiency. Hierarchical nanostructures have turned out to be favorable for photocatalyst design, because they combine reactive nanoscale architectures with high surface areas [120], but surface tuning with photocatalysts enhances performances either via stabilization of surfaces with optimal catalyst-reactant interactions, through optimization of their light absorption properties [121] and/or by taking away surface recombination (surface defects, surface states…) [122]. The latter being emphasized while specific surface of the material is increased.

D.2 Surface defects – Main Challenges of the 2D TMDC Materials

When reporting about the 2D materials, a comprehensive understanding is still lacking about the quality of the exfoliated nanosheets. The small flake size having high specific surface areas of the liquid-phase exfoliated TMDCs can result in large concentration of surface defects. The concentration of different structural defects in their crystal lattices, significantly alter their physico-chemical properties [123]. These structural defects are known to be either dangling bonds in the edge of the nanoflakes or punctual defects due to non- stoichiometry in the "bulk" of the flake [68].

Besides *in situ* generation of defects during materials synthesis, recent progress also highlights the possibility of post-synthesis defect engineering [124]. Corrosions on the photoactive semiconductor can also lead to a high surface defect density, because of instability in the electrolyte and the surface of the photoelectrode is oxidized [104]. Studies have been developed to better understand the surface defects and the reports indicated that chalcogenides vacancies are the most abundant defects [125][126]. These defects create deep trap states to recombine photogenerated charge carriers, changing optoelectronic properties and thus, interfering in the photocatalytic activity of the 2D materials.

Surface defects either generated *in situ* or *ex situ* significantly alter the original electrical, optical and chemical properties of materials. However, the effects of structural imperfections in 2D TMDCs are not necessarily detrimental. In certain cases, defects provide benefits to material properties, enhancing device performance, as it is in the case of MoS_2 for electrocatalysis [127]. In case of photocatalysis, experimental and computational results focusing on 2D TMDCs have indicated that point defects such as chalcogenide vacancies, can create deep trap states, perjuring light harvesting and decreasing charge carrier transfer [68].

D.2.1 Classification of surface defects in TMDCs

A work review dedicated to the defects in TMDCs classified them according to their dimensionality: as zero-dimensional (point defects, dopants or 'non-hexagonal' rings), one-dimensional (grain boundaries, edges, and in-plane heterojunctions) and two-dimensional (layer stacking of different layers or van der Waals solids, wrinkling, folding, and scrolling [123]. These defects are represented in the **Figure I - 27**.

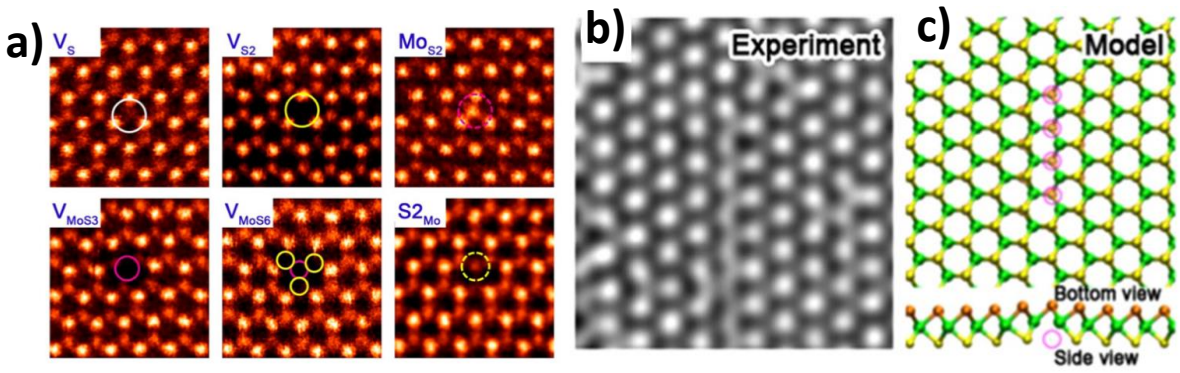

Figure I - 27: *(a) Atomic-resolution annular dark field (ADF) images showing different types of vacancy and vacancy complexes in MoS_2 monolayers* [126]. *(b) High-resolution transmission electron microscopy (HRTEM) image and (c) structural model showing a single vacancy line in MoS_2 monolayers [128]. Via [123]*

The zero-dimensional are the most common defect given their relatively low formation energy. The vacancies showed to be intrinsic point defects observed with regularity. In a precise investigation on MoS_2 monolayer, six varieties of intrinsic point defects were observed with regularity (**Figure I - 27** a): single sulfur vacancies (V_S), double sulfur vacancies (V_{S2}), a vacancy of a Mo atom and a triad of its bonded S within one plane (V_{MoS3}), a pair of S atoms occupying a Mo position ($S2_{Mo}$) and others [126]. Foreign atoms can also be adsorbed to the crystal surface and form anti-sites.

Single- and double-line vacancies of sulfur were observed experimentally also in a MoS_2 monolayer [128]. For the one-dimensional defects (**Figure I - 27:** b), the situation becomes more complex, because it starts to involve grain boundaries and the dislocation cores. As for example, when atoms are removed from a monolayer of MoS_2, the structure relaxes in three dimensions, to form dreidel shaped dislocations with a variety of ringed motifs that are dependent on the grain boundary angle [129]. Another type included on the one-dimensional defects is the single islands presents in the edges that can form triangular shapes.

The two-dimensional defects in TMDCs occurs in the interfaces between vertical hetero-layers of p-n junctions when there is lattice mismatch between layers results in different optoelectronic properties that have not been very well explored yet. Experimental evidences about the various defects present in the 2D materials demonstrated to be in agreement with DFT calculations performed and it could indicate defect formation energies of vacancies. Further understanding about the defects in TMDC are required to gain more control of the presence of defects and its tuning properties.

D.2.2 Effects of the defects onto TMDC properties

The point defects in semiconductors can trap free charge carriers and localize excitons – electron-hole pairs. In such case, the photo-generated excitons would bind with excess electrons or holes originated by the defects to form trions (with lower formation energy), instead of neutral excitons (with higher formation energy) [130]. Therefore, the lifetimes of electrons and holes are very influenced by these formations, being critical for optoelectronic devices. The interaction between these defects and charge carriers becomes stronger at reduced dimensionalities. Its existence mostly results in the degradation of the photocatalytic performance or poor luminescence quantum yields (QY) of the TMDC nanosheets.

Their performances are highly influenced by these defects because they leave dangling bonds at the vdW surface that may affect the crystal in two ways. Firstly, such regions can act as active precursors in chemical reactions such as chemisorption of atoms, corrosion, or etching; second, the electronic states due to the unsaturated or reconstructed bonds are located within the band gap and serve as recombination centers [131]. Since the early studies on TMDCs for solar electrocatalysis, exposed edges on the surface perpendicular to the C axis act as recombination centers for the photogenerated carriers or as sites for back-reaction of photogenerated products, thus decreasing efficiencies dramatically [132].

D.2.3 Strategies for defect passivation – Applications to 2D TMDCs

Performances relative to surface defects and the development of strategies for defect passivation are still under progress. A single surface treatment can yield more than one surface engineering effects, and it may be co-related. Passivation of defects in few-layer LPE TMDC nanoflakes using techniques compatible with the solution-based processing is a remaining challenge. To passivate defect states, the surface treatment should deactivate only the defect states without a permanent change in the intrinsic crystal and electronic structure of TMDCs. Moreover, the adsorbed molecules should be chemically and thermally stable on TMDCs. Consequently, they should not decompose or desorb during the fabrication processes [133].

D.2.3.1 Defect passivation using adsorption of molecules or surface treatments

Since the atomic orbitals of the surface atoms can no longer interact efficiently with their neighbors, which remains instead as dangling bonds, it can act over the surface with reagents that strongly bind these "dangling" atoms and suppress these surface states [101]. In presence of passivation layers there will be passivated surface trap states and fast interfacial charge-transfer

rate. The photo-generated carrier near the surface are in competition between trap sites induced recombination with majority-carrier electrons and charge-transfer to the surface layer [104]. By passivating the surface, the surface recombination rate (k_{re}) and charge recombination are suppressed and the interfacial charge-transfer rate (k_{HER}) is improved (see **Figure I - 28**). This straightforward involves coating the surface with a thin layer of material possessing energy levels adequately positioned for selectively accepting one of carriers. The extracting layer accepts one of the carriers, leaving the other in the semiconductor.

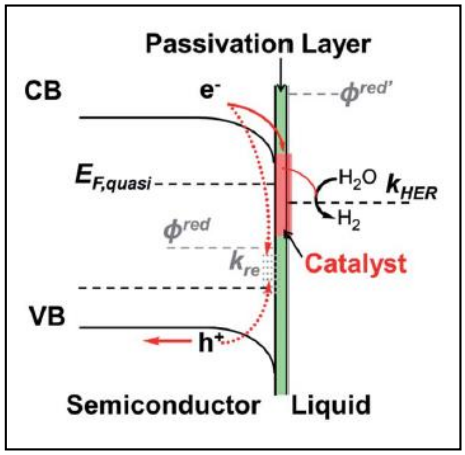

***Figure I - 28**: Schematic illustration of the band structure for a surface passivation layer onp-type semiconductor [104].*

Nagasubramanian and co-workers [134] firstly demonstrated the surface adsorption of halide ions into p-WSe_2 photocathodes which provided the efficient passivation of recombination centers located at exposed edges. Recently, Yu and co-workers [68] have tackled this issue on exfoliated 2D nanosheets of WSe_2 applying a two steps strategy: defects healing thanks to pre-annealing powder and surface treatment based on a Hexyl-Trichlorosilane (HTS) deposition, see **Figure I - 29**; then an optimized Pt–Cu co-catalyst deposition, for enhanced charge transfer. It was attributed that with reduced concentration of active surface, HTS can hinder the access to edge and surface defects (**Figure I - 29 c** and **d**).

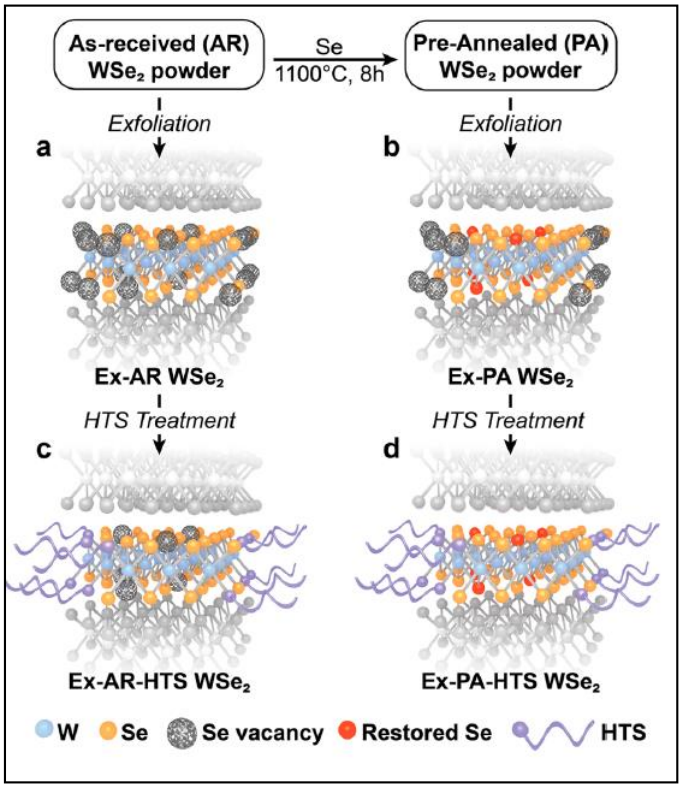

Figure I - 29: *(a) WSe_2 prepared by exfoliating as-received power, which likely contains Se vacancies both at the exposed flake edges and internally in the few-layer flakes. (b) WSe_2 prepared by exfoliating pre-annealed powder; Treatment with hexyl-trichlorosilane (HTS) surfactant is suggested for the filling of the exposed edge vacancies to give the WSe_2 samples (panels c and d) [68].*

The reported works about surface defects and defect site passivation of 2D TMDC materials have demonstrated the strong association between the surface defects and the performance on the photocatalytic activity. Photoluminescence analysis can be performed to evaluate defect sites and to indicate defect-mediated non-radiative recombination, where strong PL must be observed. Surface treatments and doping onto the crystal layers of TMDCs to passivate the surface defects have been already reported [94][95], but the structural defect implication is still in development and most of the work reported corresponds to MoS_2. Therefore, further investigations about defects and passivation treatments onto other TMDC materials such as WSe_2 and WS_2 remains necessary to develop further this kind photoactive materials. Since these materials have high potentialities for the water reduction, attention and development of defects passivation treatments are required to enhance the performance of solution-processed TMDC semiconductors for solar energy conversion.

D.2.3.2 Defect passivation using deposition of catalyst thin layer

High density of surface defect states contributes to slower charge transfer kinetics caused by charge recombination at the surface. Deposition of thin layers can passivate surface charge recombination and avoid formation of the surface defect states, promoting the desired chemical reaction by catalyzing faster charge transfer to the redox species [104]. The effects of surface recombination passivation using co-catalysts can result in improvement in charge transfer kinetics and chemical stabilization leading to a catalytic effect. Several works reported in the literature have designed photocathodes with deposition of catalyst thin layers and passivation treatments to combine these properties and improve the conversion efficiency [135][136].

According to Liu and co-workers, the design of passivation layers has attracted big interest, because it can improve the efficiency of PEC cells by the inhibition of deleterious reactions and catalyzing beneficial ones. These layers are usually very thin (typically <100 nm, often only 1–2 nm) thus preventing parasitic light absorption or charge-transfer inhibition and can be incorporated onto high surface area or high aspect ratio nanostructures [104][137].

D.2.3.3 Effect of Catalyst Particles on Semiconductors Surface

The HER overpotential can be understood as the voltage applied to the electrode relatively to the redox potential of the relevant couple (H^+/H_2 or H_2O/O_2) in the electrolyte of interest. Generally, the adsorption/desorption at the surface of bare semiconductors of intermediate species is responsible for a large overpotential to perform the reactions [104]. Thus, it limits the efficiency of these reactions even if the band edges positions are appropriate for the water splitting [20].

Due to this issue, a common, and often necessary, strategy to improve the kinetics of photoelectrochemical devices is the deposition of a co-catalyst at the surface of the semiconductor [20]. The catalysts are deposited as thin layers or as nanoparticles to avoid excessive light absorption or reflection; but results in a better the light harvesting thanks to improved charge separation (longer exciton life time), while lowering activation barriers for H_2 or O_2 evolution [138].

In a PEC water splitting, the onset potential (V_{on}), relates to the photovoltage (V_{ph}), the redox potential (E_{redox}) of the considered electrochemical reaction and the kinetic overpotential (η) – negative for cathodic and positive for anodic – as in the Equation 1 - 11 [139].

$$V_{on} = E_{redox} + \eta - V_{ph} \qquad (1 - 11)$$

The challenge is to minimize η and maximizeV_{ph}. To do so, the introduction ofa surface layer changes the semiconductor surface environment and can reduce the surface recombination (higher V_{ph}) or the catalytic overpotential (lower η). In case of a photocathode, an anodic shift is expected. The photovoltage (V_{ph}), generated by the semiconductor, significantly influences the onset potential. Catalyst particles at the semiconductor surface lead to a lower overpotential reducing the activation energy, as illustrated in **Figure I - 30.** Also, by facilitating the charge transfer lead to a lower recombination rate is usually observed [140].

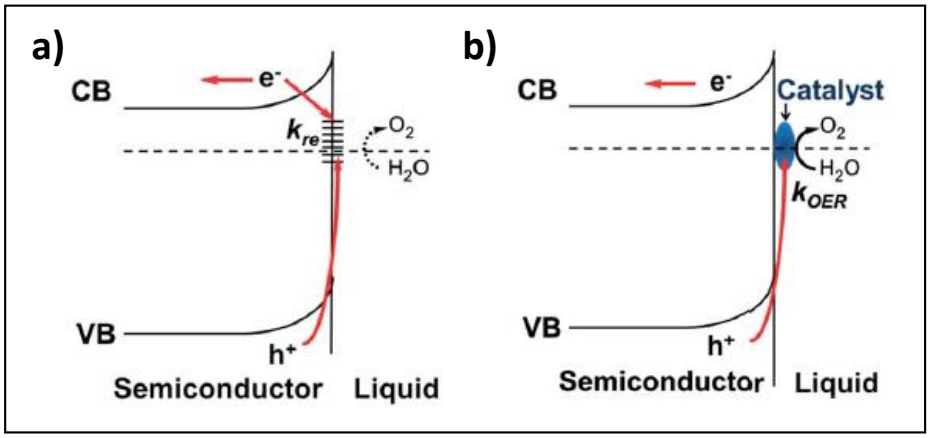

Figure I - 30: *Comparison of an n-type semiconductor photoanode with (a) surface defect states in the band structure, which lead to high charge recombination and inefficient water oxidation by the photogenerated holes; (b) application of an OER catalyst layer, which promotes facile hole transfer across the interface to the catalyst for improving water oxidation [104].*

Metal nanoparticles are very commonly used as catalyst on the semiconductor surface. A metal has a continuum of energetic states, so there is higher concentration of majority carriers than in the semiconductor. This facilitates the transport of minority carriers into the metal [20]. Deposition of Platinum layer is very common on the surface of photocathodes to the HER. Lewis and co-workers have reported crystals of WSe_2, already discussed in this work, with Ru/Pt catalyst electrochemically deposited onto its surface [67]. The catalytic performance of the photocathode is largely increased compared to the bare material and the onset potential was shifted to +0.6 V vs RHE, as presented in **Figure I - 31**.

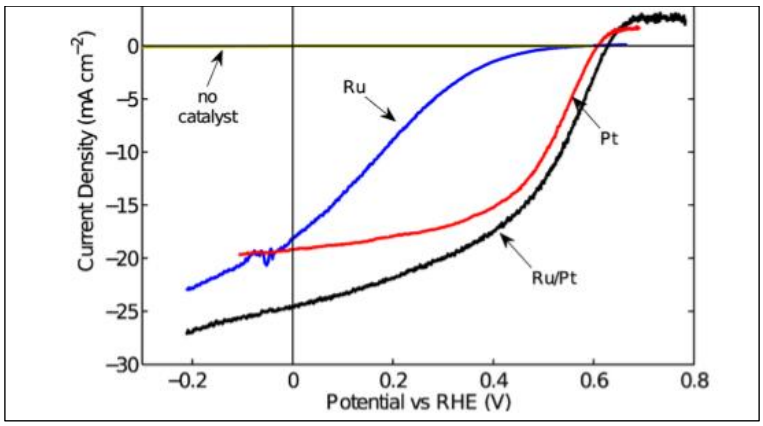

Figure I - 31: *J–E behavior of p-WSe_2 photoelectrodes from aqueous pH 4.2 electrolyte without catalyst coating and with Ru, Pt, or Ru/Pt coatings, respectively [67].*

D.2.3.4 Fermi level pinning

The origin of the band bending lies in the so-called band edge pinning and it refers to the effect that the electron affinity (A) of the semiconductor on the surface remains unchanged relative to the electrochemical potential (E_{redox}) of the solution before and after contact [139]. Semiconductors that are coated with discontinuous films of metal nanoparticles behave essentially like the semiconductor alone in contact with a redox couple, albeit with the catalytic activity of the metal coating [20].

However, different behavior can be observed from a continuous metal film on a semiconductor surface, which forms a Schottky barrier whose height is determined by the metal/semiconductor interface and whose energetics are independent of the solution. In this case, the semiconductor-metal Schottky junction exhibit Fermi-level pinning. Similar behavior is observed when a high surface state density is present at the surface of the semiconductor. In both cases the applied potential does not modify anymore the band bending in space charge of the semiconductor. Instead, the voltage drop is reported to the electrochemical double layer; as it happens for metal electrodes (as the black and gray lines indicated in (**Figure I - 32**). This effect participates to reduce the photo-voltage (V_{ph}) [104][139].

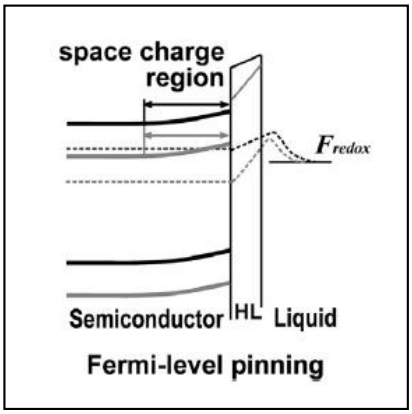

Figure I - 32: *Band structure under Fermi-level pinning, where the applied bias is dropped across the Helmholtz layer instead of the semiconductor (the black and gray lines are under different bias and the bumps between semiconductor and liquid represent potential drop in HL) [139].*

In an ideal photo-electrode system, foreign material on the semiconductor surface influences the charge transfer at the solid–liquid interface leading to a reduced overpotential. On the other hand, surface defect states can be passivated or generated at the interface between the semiconductor and this surface layer (**Figure I - 33**). Thus, the photo-voltage generated in the semiconductor is modulated from the interlayer side. Practical devices often exhibit a combination of partial band-edge pinning and partial Fermi level pinning, thus an evaluation of the influence of surface layer on both sides is suggested to balance these contributions, especially when their contributions are conflicted to each other [104].

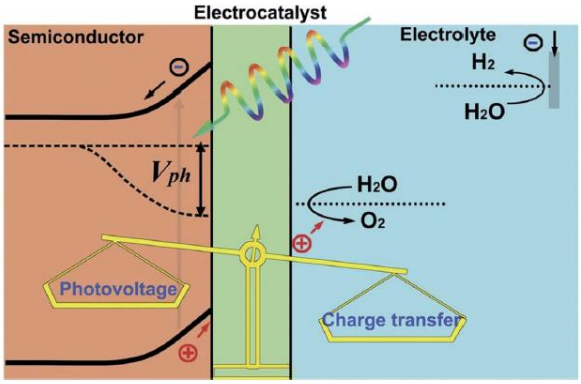

Figure I - 33: *schematic of the interfacial energetics with a catalytic passivation layer present, demonstrating the dual influence on both of the semiconductor side and electrolyte side [104].*

The understanding and deconvolution of the multiple effects of a single surface layer on a semiconductor is complex. The contributions can include surface state passivation, enhanced interfacial charge-transfer kinetics, suppression of corrosion reactions, buried junction effects and surface band position shifts relative to the solution [104]. However, it is difficult for a single layer material to provide all the benefits for efficient water-splitting applications. Thus, to

achieve optimal results, composite layers containing both inert passivating and catalytic material may be a promising option.

For water splitting applications, metal nanoparticles are almost always used for their catalytic properties towards water reduction or water oxidation. In the case of hydrogen evolution, the good catalyst will bind hydrogen strongly enough to allow for the adsorbed protons to react together, but weakly enough to easily release the resulting hydrogen molecule (Sabatier principle) [101]. However, most efficient HER metal catalysts are scarce and can negatively impact the cost. Therefore, alternative cheaper and more abundant catalysts have been developed, in particular, molybdenum sulfide [141][142], cobalt sulphide [143] and nickel phosphide [144] have shown promising performances.

Besides surface charge transfer enhancement, another issue to be addressed is the charge collection from photo-electroactive material to the current collector. Nanostructuration of the material comes with a degradation of the charge percolation within the material, because of a higher grain boundaries resistance respect to sintered materials. The outcome is a lower efficiency because of a higher Ohmic drop and a higher recombination rate since the free mean path of charge carriers is shorter than the mean charge transfer path. A strategy is to develop semiconductor-carbon assembly.

D.3 Nanojunctions formed by semiconductor-carbon self-assembly

The 2D layered materials exhibit high anisotropy in material properties because of the large difference between intra- and interlayer bonding. This feature presents opportunities to engineer materials whose properties strongly depend on the orientation of the layers relative to the substrate [145]. In fact, the high contact resistance at the place of attachment of the nanoplates to the substrate promotes low conductivity of the TMDC materials themselves, giving limitation of access to active sites [146]. Nevertheless, their large surface area and large amount of coordination-unsaturated surface atoms, can promote the adsorption of reactants and thus improve catalytic properties [147].

This feature makes suitable for the 2D materials to form hybrid nanojunctions, taking advantage of the geometry and electronic properties of the involved materials to improve catalytic properties. Thus, this section brings some approaches previous reported concerning enhanced HER activity acquired by morphology control and interactions between TMDC materials and carbon-based materials, such as graphene oxide.

D.3.1 Interest of building TMDC- carbon nanojunctions

Nanojunctions formed between a semiconductor and carbon have attracted attention and graphene is one of the commonly used due to their metallic-like conductivity, high electron mobility and high surface area, allowing for facile electron injection from the light absorbing semiconductor [1]. In addition, nanosheets of graphene have increased attention to their incorporation into nanoelectronic and energy storage devices thanks to their unique chemical properties [148]. Multiples studies have shown monolayer and multilayers of graphene acquired by different methods exhibiting high conductivity and large surface area [149][150]. This good property has attracted much interest in photocatalysis, facilitating electron transfer with improved electrical properties. Several works about nanojunctions involving TMDC materials have been reported and have been demonstrated as promising in the catalytic activity.

The combination of reduced graphene oxide (rGO) and TMDC materials to form nanocomposites has showed good catalytic activity which is associated with the increased number of exchanged electrons [145][151]. The association of the two materials possessing mesoporous structures facilitates interfacial reactions and charge transport through the network. The morphology of the nanocomposite showed to not change after combining with the reduced graphene oxide. Moreover, the obtention of these nanojunctions can be achieve simply using routes, such as colloidal synthesis method at low temperature in situ self-assembly [152] [109].

D.3.2 Previous works of TMDC-carbon based for HER

In one approach, 3D hybrids were produced by growing WSe_2 thin layers vertically on 2D reduced graphene oxide nanosheets for electrocatalysis of HER (**Figure I - 34 a and b**) [152]. The electrocatalytic performance of pure WSe_2 layers and WSe_2/rGO hybrid, investigated in 0.5M H_2SO_4, electrolyte gave higher current value with improved electrode/electrolyte interactions, as showed in **Figure I - 34 c**. Compared to the pure WSe_2 the onset potential of the WSe_2/rGO hybrid shifted from –160 mV to –100 mV. The increased catalytic activity of the 3D hybrid was explained by the improved charge transfer efficiency between the WSe_2 layers and rGO nanosheets. The Nyquist plots of the referred samples revealed the decrease of the charge transfer resistance for the WSe_2/rGO sample (**Figure I - 34 d**). According to the authors, WSe_2 layers grown on rGO could effectively expose the active edges, reducing the agglomeration of WSe_2 layers and the charge transfer efficiency was promoted through combining the high electro-conductivity of rGO.

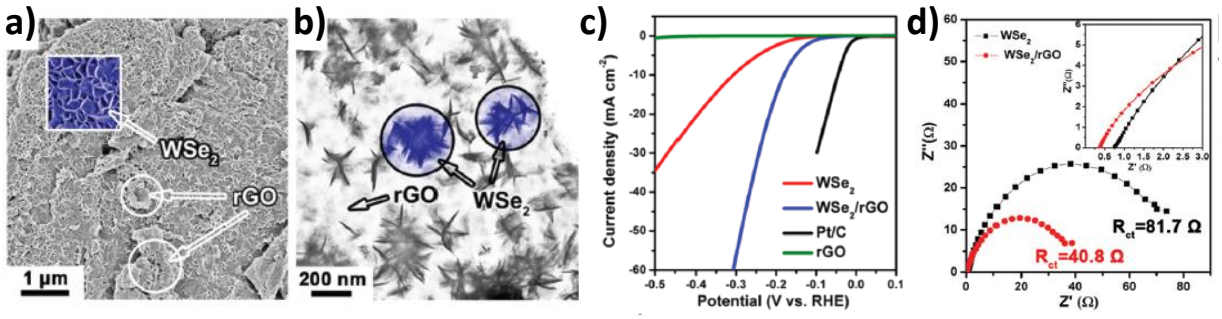

Figure I - 34: *(a) SEM and (b) TEM images of the WSe_2/rGO hybrid. The square inset of (a) is the enlarged SEM image and the circular insets in (d) show the TEM image of WSe_2 grown on rGO sheets, (c) Polarization curves of the WSe_2 layers, the WSe_2/rGO hybrid, pure rGO and Pt/C are given as reference, (d) EIS Nyquist plots of pure WSe_2 and WSe_2/rGO hybrid [152].*

In another similar approach, a hybrid network is constructed with few-layered WSe_2 nanoflowers anchored on graphene nanosheets to obtain photocathode for HER electrocatalysis [109]. Compared with the relatively poor HER performance of bare WSe_2 nanoflowers, the rGO/WSe_2 sample demonstrated a highly effective and stable electrocatalytic performance, with current density of 38 $mAcm^{-2}$ (**Figure I - 35 a**). The superior HER performance of RGO/WSe_2 hybrid was attributed to the WSe_2-anchored-on-graphene structure, which ensures the robust contact between the few-layered WSe_2-nanoflowers catalyst and the highly conductive graphene matrix, leading to enhance the charge transfer kinetics between the catalytic edge sites and the graphene nanosheets.

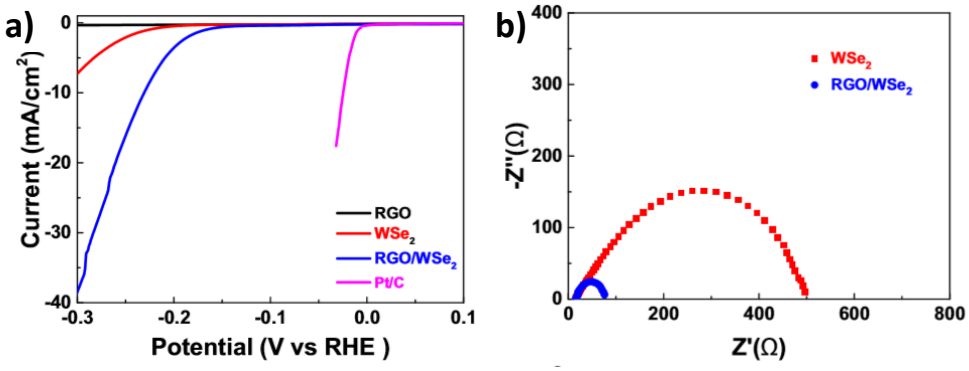

Figure I - 35*: (a) Polarization curves of RGO/WSe_2 composite, bare WSe_2, RGO and commercial Pt/C catalyst samples added as references, (b) Nyquist plots of RGO/WSe_2 hybrid and bare WSe_2 samples [153].*

To obtain effective self-assembly in abundance of accessible edges, it is important to highlight that the atomic ratio and particle size of the involved materials is an important parameter to obtain rGO sheets uniformly distributed onto the TMDC network.

MoS_2 nanoparticles also has been reported grown on rGO nanosheets, synthetized by solvothermal reaction and demonstrated higher HER electroactivity for the resulting MoS_2/rGO hybrid [151]. According to the authors, the interactions between functional groups on GO sheets and Mo precursors in a suitable solvent environment allows the growth on GO sheets (**Figure I-36 a and b**). In addition, the high performance in the HER is attributed to strong chemical and electronic coupling between the GO sheets and MoS_2. The electrical coupling in an interconnected conducting network can afford rapid electron transport from the less-conducting material to the electrodes.

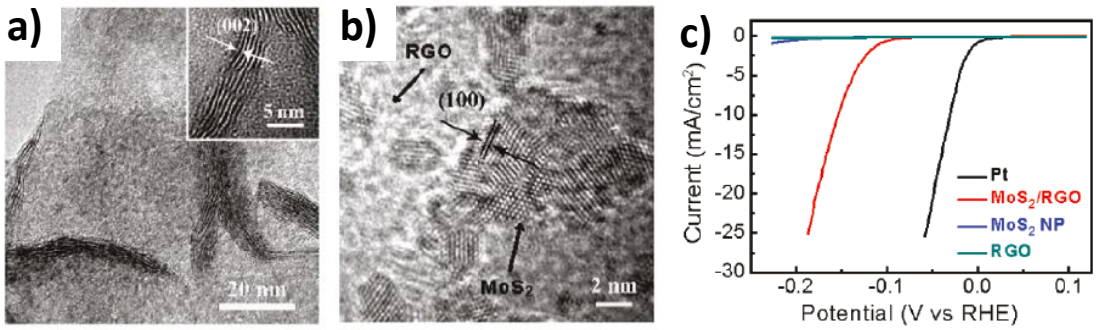

Figure I-36: *(a) TEM image showing folded edges of MoS_2 particles on RGO in the hybrid. The inset shows a magnified image of the folded edge of a MoS_2 nanoparticle. (b) HRTEM image showing nanosized MoS_2 with highly exposed edges stacked on a RGO sheet. (c) Polarization curves obtained with several catalysts as indicated recorded on glassy carbon electrodes with a catalyst loading of 0.28 mg cm^{-2} [151].*

The reports existents in the literature have suggested that TMDC semiconductors combined with graphene show enhanced electrochemical properties and shows to be a promising way to improve their HER performance. The principal advantage of introducing rGO is the improvement of the electrical conductivity, leading to the reduction of charge transfer resistance (R_{ct}) at the electrode-electrolyte interface [154]; these junctions minimize parasitic ohmic losses and improve the electrical contact at the material/current collector interface which leads to higher charge transfer efficiency.

The outstanding catalytic performance places these nanojunctions very competitive compared with the state-of-the-art Pt layered TMDC HER catalysts. With a proper structure engineering, the catalyst performance can be further enhanced [154]. Furthermore, the preparation of these hybrids based on facile and scalable ways motivates the development of this kind of composites. Although, highly applied in the HER electrocatalysis, promising performances can be expected assembling different properties in the HER photocatalysis. The optoelectronic properties offered for the TMDC materials, with graphene nanosheets

introduction to improve electrical conductivity shows to be a potential strategy for overall enhanced catalytic activity.

D.4 Previous works of TMDC materials for solar water splitting

Herein previous works reported about TMDC materials for HER are presented. Some of them have been evaluated as promising photocathodes for solar water splitting. Still to achieve a proper efficiency they require the use of co-catalysts. Usually noble metals are used for this purpose [52], [67], [68], [90], [155], [156] and the challenge is to develop low cost material for large scale applications. Among others, Mo_xS_y-based TMDCs have been envisioned to be a good candidate as a co-catalyst for HER [41], [141], [157]–[159].

D.4.1 TMDC employed as photocathodes for HER

D.4.1.1 Tungsten Diselenide (WSe_2)

Tungsten diselenide was earlier studied as photoanode material, due to its high light absorption coefficient, small band gap energy (E_g = 1.4 eV) and anisotropic properties [131]. Crystalline n-type WSe_2 has been reported to reach a photoelectrochemical energy conversion efficiency higher than 17%. Since the conduction band position is suitable respect to water reduction, the development of p-type WSe_2 is appealing. First works reported an energy conversion efficiency equivalent to 8.6 and 14% respectively for photovoltaique (PV) and photoelectrochemical (PEC), thanks to surface passivation [132]. Since then, WSe_2 has been spotted as very promising for direct hydrogen production.

Lewis and co-workers reported a Pt-Ru coated crystalline p-type WSe_2 photocathode with 7% of conversion efficiency achieved in acidic electrolyte [67]. Crystals of WSe_2 were grown by a chemical vapor transport technique and the photoelectrochemical revealed photocurrent up to 24 mA cm^{-2} after Pt/Ru co-catalyst deposition, achieving 7.2% conversion efficiency.

In another important work Yu and co-workers described solution-processed WSe_2 thin film electrodes with an optimum photocurrent of approximately 1 mA cm^{-2} after Pt deposition in acidic media and solar-to-hydrogen conversion efficiency gave 20% at λ = 400 nm [90]. Few years later, the same group examined the surface defects role on the performance of the p-WSe_2 photocathode by applying a pre-exfoliation annealing and a post-deposition surfactant attachment, designed to target intraflake and passivate edge defects, respectively [68]. After Pt deposition, the photoelectrochemical results revealed photocurrent up to 4 mA cm^{-2} in 1M

H_2SO_4 with passivation and surface treatment. Conversion efficiency resulted in ≈ 17% at λ < 500 nm. **Table I - 2** summarizes important results reported for p-WSe_2 as photocathode.

***Table I - 2**: p-WSe_2 PEC performances previous reported in the literature for HER.*

Photocathode Material	***Strategy***	***Photocathode Performance for HER***	***Ref.***
p-WSe_2	*Addition of Pt-Ru catalyst*	*24.5 mA cm^{-2}| 7% in 0.5 M K_2SO_4*	[67]
	Addition of Pt catalyst	*1 mA cm^{-2}| 20% at λ < 600 nm in 1.0M H_2SO_4*	[90]
	Pre-annealing + HTS treatment + Pt-Cu catalyst	*4 mA cm^{-2}| 17% at λ < 500 nm in 1.0M H_2SO_4*	[68]

WSe_2 is among the rising stars in the family of TMDC with high potentialities for the photocatalysis. The larger W size can alter the 2D structure and its natural abundance is similar to that of Mo. However, the industrial consumption of Mo is currently higher while having a lower amount of mineral resources. Making W commercially more favorable for future industrial applications [72]. Furthermore, p-type doping is dominant for WSe_2 because of the high positions of the conduction band minimum (CBM) and the VBM in comparison with common TMDCs such as MoS_2 as the doping preference is n-type [71].

D.4.1.2 Tungsten Disulfide (WS_2)

Primary studies on bulk p-WS_2 achieved 7% conversion efficiency by deposition of platinum or palladium layers in acidic media, at λ = 630 nm to improve the overall interfacial electron-transfer kinects of H_2 evolution [160]. Indeed, WS_2 has not been well investigated yet as photocathode for the photocatalytic HER activity, being a popular member of the TMDC family in others optoelectronic applications, such as photodetectors [161] and field effect transistors [162]. However, WS_2 has been recently considered as a potential alternative for strong visible light photocatalytic due to its capability to work in the full solar light spectrum [163].

The recent developments show promising performances and could lead to significant improvements in solar to hydrogen conversion [142]. To take benefit of the conduction band maximum (CBM) position of WS_2 – higher than the water reduction potential [71] – for direct water reduction, the WS_2 must be doped to tune into p-type material. For this aspect, Sobczynski *et al.* synthesized Ni-doped WS_2 by calcining tungsten trioxide and nickel (II) supported on

silica. They successfully made WS_2/SiO_2 behave as a photocathode with enhanced catalytic properties [164].

D.4.1.3 Molybdenum Disulfide (MoS_2)

In the first reports of MoS_2, studied by Tributsch and co-workers, the photo-electrocatalytic activity of natural crystals of n and p MoS_2 was investigated. For p-type, photocurrent observed were of ≈ 0.5 mA cm^{-2} [165]. Although not too much work has been reported about MoS_2-base PEC, this TMDC material can be regarded as a promising approach in the photocatalytic performance of MoS_2-based systems [166]. As reported by Liu *et al.* [100], MoS_2 loaded on the CdS film, forming a p-n heterojunction, showed high photocatalytic performance and achieved conversion efficiencies of 28% at λ = 420 nm. Where the role of MoS_2 was to promote charge injection from one semiconductor into another, leading to efficient charge separation. Several other works have been explored MoS_2-based photocathodes with different approaches [167]–[170], due to the good electrocatalytic properties offered by the MoS_2 that will be further discussed in the next section.

D.4.1.4 Molybdenum Diselenide ($MoSe_2$)

As well as in the WSe_2, the size and the electrical conductivity of $MoSe_2$, the unsaturated Se atoms at the edge or those at defective points or altered basal plane have superior electrocatalytic activity toward hydrogen evolution reaction (HER) [171]. First optical emission studies of single-layer and few-layer $MoSe_2$ was reported displaying of good thermal stability with a 1.55 eV direct bandgap. The results revealed temperature dependence of the photoluminescence in few-layer $MoSe_2$ and the PL enhancement to the bandgap crossover going from the bulk to the quantum limit, giving promise applications in energy conversion involving solar spectrum [172].

For being considered as an alternative to the popular MoS_2, no attention has been paid yet to the mechanisms or fundamental understanding of the electrochemical behaviors at an atomic scale, as available knowledge of MoS_2-based systems has been granted as reliable references. According to Eftekhari, despite a considerable number of works devoted to $MoSe_2$, this attractive material is still in its infancy, and subtle studies are still required to understand its behaviors for electrochemical performance [171].

D.4.2 TMDC and Mo_xS_y molecular mimics complexes as a co-catalyst for HER

D.4.2.1 Molybdenum Disulfide (MoS_2)

Molybdenum disulfide has been demonstrated as a good catalyst for water reduction in acidic media with activities on a per site basis that approach those of the noble metals [173]. With a direct band gap around 1.7 eV and the conduction band slightly more positive than that for the HER, it has been demonstrated that the MoS_2 may function as both the semiconductor and the catalyst material. According to Laursen and co-workers [173], there are two possible applications of MoS_2 in photo-electrocatalytic water splitting: (i) the use of MoS_2 as both the semiconductor and the HER catalyst and (ii) the use of an alternative semiconductor in combination with MoS_x as the HER catalyst.

D.4.2.1.1 <u>MoS_2 and molecular mimics as electrocatalysts for the HER</u>

First fundamental works reported active edge sites of MoS_2 nanoparticles and DFT-calculated free energy of adsorption of hydrogen results (Δ_{GH} = +0.08 eV) indicated that the edges of MoS_2 nanoparticles are active for hydrogen evolution [174]. This value lies just below those of the precious Pt-group metals (**Figure I - 37**). Several works showed MoS_2 nanoparticles with high electrochemical activity to yield high hydrogen production rates. Where edge sites of MoS_2 nanoparticles in different sizes, mimicking the active sites, provides high catalytic activity for hydrogen evolution [41], [142], [173]–[176].

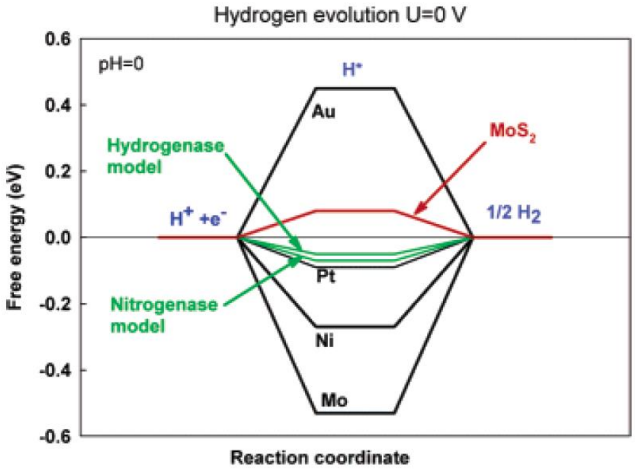

Figure I - 37: *Calculated free energy diagram for hydrogen evolution at a potential V = 0 V relative to the standard hydrogen electrode at pH 0. The free energy of $H^+ + e^-$ is by definition the same as that of 1/2 H_2 at standard conditions [176].*

The exchange current density referred to the edge active sites were also suggested as in agreement with the volcano relation between the HER exchange current density developed by Nørskov [177], where values of hydrogen binding energies (ΔG_H) approaches to zero. Therefore, to search for methods to obtain MoS_2 with more exposed edge sites with ΔG_H closer to zero, many works have been performed in order to better understand the HER activity offered by the nanoparticles of MoS_2.

Molecular mimics of MoS_2, such as $[MoS_3]^{2+}$ [178], cubane-type $[Mo_3S_4]^{4+}$ [157], $[Mo_3S_{13}]^{2-}$ [141][159] and $[Mo_2S_{12}]^{2-}$ [158] nanoclusters (**Figure I - 38**) have showed high catalytic activities and low cathodic overpotentials for the hydrogen evolution, similar as the MoS_2 crystals. These nanoclusters can be obtained by reacting tetramolybdate salt - $(NH_4)_2[MoS_4]\cdot 2H_2O$ in ammonium polysulfide or aqueous solutions. The deposition of these nanoclusters on a substrate were related to the formation of nanoparticles or amorphous thin films [159][178], where the clusters could be arranged as a coordination polymer. The electrocatalytic evaluation of the thin films revealed pre-catalytic reduction through hydrogen evolution conditions, indicating possible transformation of the MoS_x film into a novel HER catalyst.

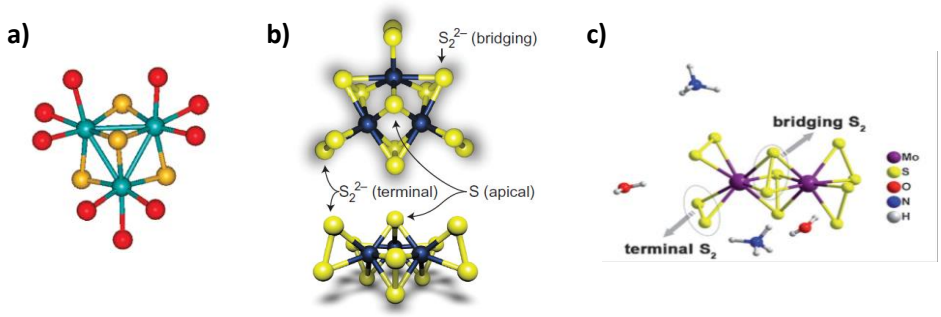

***Figure I - 38**: (a) Molecular structure of $[Mo_3S_4]^{4+}$. Blue (Mo), yellow (S), and red (O from water ligands) [157], (b) Model of a single $[Mo_3S_{13}]^{2-}$ cluster, top and side views [141], (c) structure of $[Mo_2S_{12}]^{2-}$, determined by synchrotron-radiated single-crystal XRD [158].*

In these previous reports, XPS analysis identified different chemical states of sulfur, showing three different types of sulfur ligands for $[Mo_3S_{13}]^{2-}$, such as terminal S_2^{2-} ligands, S^{2-} ligands and bridging S_2^{2-} ligands, as presented in **Figure I - 39:**, where all is located intrinsically in the edges, and the Mo 3d region showed molybdenum formal 4^+ oxidation state [157][159]. In another report, synchrotron-radiated single-crystal XRD analysis showed its structure with Mo centers coordinated to four S_2 units, with two bridging S_2 having a short average S-S bond length and two terminal S_2 having a long average S-S bond length [158]. Besides, Raman spectrum have demonstrated that the structure or composition of the clusters do not change during the HER [141][159].

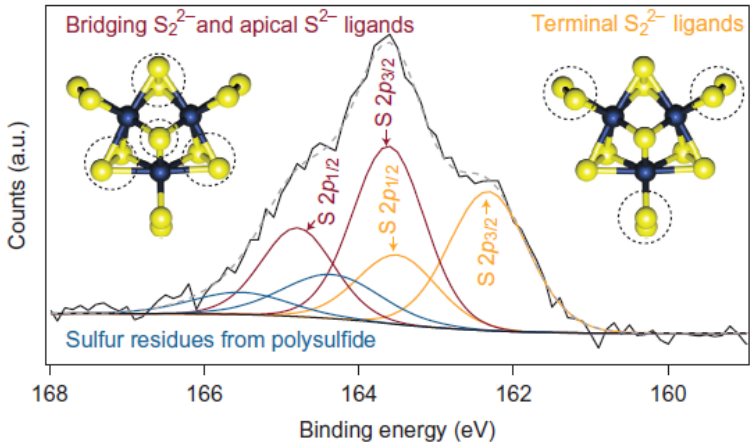

Figure I - 39: *XPS spectra of $[Mo_3S_{13}]^{2-}$ showing the Sulfur 2p region deconvolution showing the different doublets [141].*

Performed DFT calculations suggested unsaturated catalytic Mo centers for the H_2 evolution from active sites presents in Mo^{IV} sites [159], while other studies have assigned the preferred hydrogen binding position to bridging S_2^{2-}, with ΔG_H = -0.05 eV, being the best value among non-metallic HER catalysis evaluated [158]. Moreover, a new family of molecular MoS_2 edge-site mimics made of tetragonal Mo(VI) complex $[MoOS_3]^{2-}$ for homogeneous HER was recently reported [179]. The theoretical calculations found the most thermodynamically favored pathway as being the protonation of the Mo=O moiety. From this result, the authors suggested that Mo=O acts as a proton relay that may be extended to a-MoS_x.

D.4.2.1.2 Promising use of Mo-S based clusters in Photocathodes as co-catalysts

There is a big interest in the utilization of these Mo-S based complexes as co-catalysts for photocatalytic hydrogen generation. Motivated by the scarceness of Pt and the necessity of a co-catalyst to perform effective photocatalytic activity, since large areas need to be covered with the catalyst to sustain the energy demand [173].

Molecular mimics of MoS_2 has already been reported as co-catalyst for photocatalytic HER. Colloidal MoS_2 nanoparticles coupled on a transition metal complex Ruthenium tri-bispyridine ($Ru(bpy)_3^{2+}$) obtained higher efficiency in photocatalytic HER [175]. Regarding the conception of using molecular mimics, Hou and co-workers coupled cubane-like clusters $[Mo_3S_4]^{4+}$ catalysts on a p-type Si semiconductor for efficient photocatalysis [41]. To prepare the new photocathodes, solution of Mo_3S_4 in organic solvent was drop-casted onto p-Si photoelectrodes. Photocatalytic activity of the photocathode resulted in 47% conversion efficiency, for $\lambda > 620$ nm, see **Figure I - 40**. p-InP nanowire arrays also was reported with higher

photocatalytic activity using MoS_3 nanoparticles deposited by photochemical deposition, achieving photocathodes efficiencies of 6.4% [59].

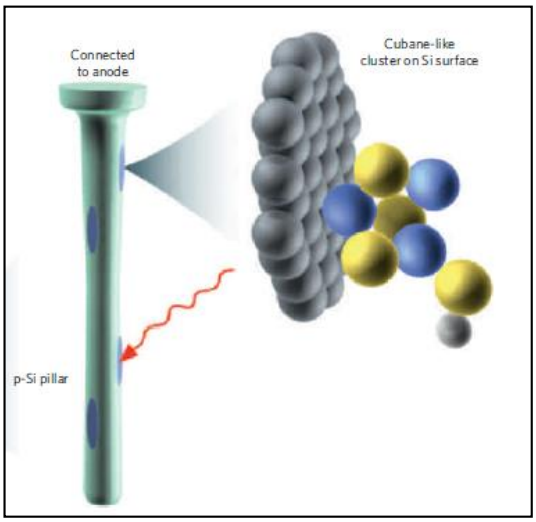

Figure I-40: *Schematic Mo_3S_4 clusters adsorbed on the Si pillars. Inset: Mo_3S_4 model cluster on H-Si (100); (Mo blue, S yellow, Si grey and H white) [41].*

The use of Mo-S based complexes as HER electrocatalysts counts with a diversity of clusters with active sites of efficient catalytic activity. The potentiality offered by the amount of edges present in the layered MoS_2 demonstrated these molecular mimics as being suitable candidates for the replacement of Pt in acidic solutions. Therefore, the use of the MoS_x clusters are promising for photocatalysis, because it can offer a structure consisting of only surface atoms/edge sites, and thus has a very small electrode footprint using the electrocatalytic HER activity together with a good photon absorber.

Summary and Work Strategies

This bibliographic review had as objective to transmit the mains ideas concerning the solar water splitting and to show the important points to be considered in the process of water reduction and oxidation using visible light. It was discussed about the requirements necessaries to perform the solar water splitting, such as a semiconductor of high crystallinity with suited band-gap energy to absorb in the visible light and energetic levels of conduction and valence bands well placed to achieve the redox reactions. The p-type semiconductors are responsible to carry out the photoelectrochemical reduction of water and various materials have been demonstrated to have interesting photocatalytic properties and efficient solar-to-hydrogen conversion, such as p-GaP, p-InP, CdS and p-Si, as discussed in section B.4. However, factors such as scarcity of elements, instability, degradation in aqueous media and lack of controllable method of fabrication limit the use of these materials for photocatalytic HER and for high-scale production. These limitations took to the advance in the research and development of other efficient photocathodes.

The 2D materials have been demonstrated with immense potential for application in solar cells and optoelectronic devices in reason of their unique structure disposing of atomic thin layers with high surface areas and optical properties that enables outstanding performances for interfacial reactions. Among the 2D materials, there is the transition metal di-chalcogenides. As presented in section C, the TMDCs are layered materials that can be exfoliated into ultrathin 2D nanosheets preserving their properties and are direct-gap semiconductors whose bandgap energy varies between compounds depending on their composition, structure and dimensionality, which can be used as the active layer in ultrathin solar cells.

Attracted by the chemistry and optoelectronic properties of MX_2 compounds, this chapter was mostly dedicated to present a literature review with insights necessaries to the development and application of these materials as photocathodes to the HER. Although, the high concentration of optical surface defects is still a remaining challenge for the 2D TMDCs, as presented in the section D.2. Several works in the literature have focused on the study of two different approaches to increase the photocatalytic performance of these materials: treatments for surface defect passivation or the deposition of catalyst layer.

Among the TMDCs materials, MoS_2 have been the most explored in catalytic applications. What gives space to the investigation and development of other TMDCs. Moreover,

the major challenge of finding new strategies to decrease or eliminate surface defects consequences and increase conversion efficiency still requires more efforts. In order to replace the use of noble-metals catalysts or to find another alternative of passivation treatment.

Motivated by the unique combination of atomic-scale thickness, direct band gap and favorable electronic properties given to the 2D nature of TMDC materials, added to the factors mentioned just above, here, we will focus into explore the photoelectrochemical properties of 2D tungsten di-chalcogenides (WSe_2 and WS_2), and into the development new strategies to improve their photocatalytic activity. Thus, two strategies will be considered to design a p-WSe_2 photocathode with improved photoelectrochemical performance to be, in a longer term, configured in a Tandem Cell approach:

Strategy 1

The first strategy concerns the deposition of a catalyst layer onto the surface of the 2D material in order to increase the presence of active sites and passivate surface defects, simultaneously. To obtain our catalyst, we will be inspired in the high HER performance demonstrated using molecular mimics of Mo-S, discussed in the section D.4. We will apply these Mo - S complexes as catalysts to enhance the photocatalytic performance of WSe_2. As the development of free-noble metal catalyst is of big interest, we want to elaborate a water-soluble catalyst solution deposited by facile methods that could encourage the large-scale production of these photocathodes. All the elaboration, study and evaluation of p-WSe_2 photocathode with Mo-S complexes catalyst will be discussed in the chapters III and IV.

Strategy 2

The second strategy turned to the nanostructure optimization of p-WSe_2 to obtain a 3D nanosheets network of anisotropic morphology and high conductivity. Morphology control and optimization can lead to an increase in the electrode/electrolyte interface and gain more exposed catalytic sites. For that, a self-assembly process is stablished involving the TMDC material, an adapted colloidal template and graphene oxide (GO) nanosheets, to form nanojunctions for improvement of the electrical conductivity of the system. To design a photocathode with improved nanostructure and conductivity, we were stimulated by previous reports mentioned in the section D.1 and D.3 of this chapter. Thereafter, Mo-S complexes catalyst layer will be deposited onto the surface of the modified films to promote even higher

photocatalytic performances. The design and evaluation of the new WSe_2 photoelectrode of optimized nanostructure will be reported in chapter V.

Lastly in outlook, our self-assembly process performed for the p-WSe_2 will be applied to form optimized microstructures of p-MoS_2 and p-WS_2 materials of high surface areas. The optoelectronic properties will be investigated and compared to consider their potentialities, in a long-term perspective, for the design of tandem cells. As photoelectrodes based on TMDC nanosheets are interesting candidates, offering tunable band-gap (E_g) values and hydrogen onset potentials. To support the development and the achievement of the two strategies presented above, we counted with several route synthesis, material characterizations and photoelectrochemical evaluations that will be detailed in the following chapter.

BIBLIOGRAPHIC REFERENCES

[1] S. J. A. Moniz, S. A. Shevlin, D. J. Martin, Z.-X. Guo, and J. Tang, "Visible-light driven heterojunction photocatalysts for water splitting – a critical review," *Energy Environ.Sci.*, vol. 8, no. 3, pp. 731–759, 2015.

[2] K. Sivula, "Advancing materials and methods for photoelectrochemical energy conversion," *Chim. Int. J. Chem.*, vol. 71, no. 7, pp. 471–474, 2017.

[3] R. M. Navarro Yerga, M. Consuelo Álvarez Galván, F. del Valle, J. A. Villoria de la Mano, and J. L. G. Fierro, "Water splitting on semiconductor catalysts under visiblelight irradiation," *ChemSusChem*, vol. 2, no. 6, pp. 471–485, 2009.

[4] J. O. M. Bockris and T. N. Veziroglu, "Estimates of the price of hydrogen as a medium for wind and solar sources," *Int. J. Hydrogen Energy*, vol. 32, no. 12, pp. 1605–1610, 2007.

[5] G. L. Chiarello, M. H. Aguirre, and E. Selli, "Hydrogen production by photocatalytic steam reforming of methanol on noble metal-modified TiO2," *J. Catal.*, vol. 273, no. 2, pp. 182–190, 2010.

[6] H. Ahmad, S. K. Kamarudin, L. J. Minggu, and M. Kassim, "Hydrogen from photo-catalytic water splitting process: a review," *Renew. Sustain. Energy Rev.*, vol. 43, pp. 599–610, 2015.

[7] Lewis S. Nathan, "Research opportunities to advance solar energy utilization," *Science*, vol. 351, no. 6271, pp. aad1920-1–9, 2016.

[8] C. H. Liao, C. W. Huang, and J. C. S. Wu, "Hydrogen production from semiconductor-based photocatalysis via water splitting," *Catalysts*, vol. 2, no. 4, pp. 490–516, 2012.

[9] S. E. Hosseini and M. A. Wahid, "Hydrogen production from renewable and sustainable energy resources: promising green energy carrier for clean development," *Renew. Sustain. Energy Rev.*, vol. 57, pp. 850–866, 2016.

[10] L. Finegold and J. L. Cude, "Biological sciences: one and two-dimensional structure of alpha-helix and beta-sheet forms of poly(L-Alanine) shown by specific heat measurements at low temperatures (1.5-20 K)," *Nature*, vol. 238, no. 5358, pp. 38–40, 1972.

[11] F. Le Formal, W. S. Bourée, M. S. Prévot, and K. Sivula, "Challenges towards economic fuel generation from renewable electricity: the need for efficient electro-catalysis," *Chimia (Aarau).*, vol. 69, no. 12, pp. 789–798, 2015.

[12] A. J. Bard, "Photoelectrochemistry and heterogeneous photo-catalysis at semiconductors," *J. Photochem.*, vol. 10, no. 1, pp. 59–75, 1979.

[13] K. Maeda and K. Domen, "Photocatalytic water splitting: recent progress and future challenges," *J. Phys. Chem. Lett.*, vol. 1, no. 18, pp. 2655–2661, 2010.

[14] A. Kudo and Y. Miseki, "Heterogeneous photocatalyst materials for water splitting," *Chem. Soc. Rev.*, vol. 38, no. 1, pp. 253–278, 2009.

[15] M. Reza Gholipour, C.-T. Dinh, F. Béland, and T.-O. Do, "Nanocomposite heterojunctions as sunlight-driven photocatalysts for hydrogen production from water splitting.," *Nanoscale*, vol. 7, no. 18, pp. 8187–8208, 2015.

[16] "Electrolysis of water - Wikiwand." [Online]. Available: https://www.wikiwand.com/en/Electrolysis_of_water. [Accessed: 16-Feb-2020].

[17] A. W. Bott, "Electrocthemistry of semiconductors," *Curr. Sep.*, vol. 76, no. 9, pp. 87–91, 1998.

[18] A. J. Bard and L. R. Faulkner, *Electrochemical Methods: Fundamentals and Applications*, vol. 2. 2001.

[19] A. J. Nozik and R. Memming, "Physical chemistry of semiconductor-liquid interfaces," *J. Phys. Chem.*, vol. 100, no. 31, pp. 13061–13078, 1996.

[20] M. G. Walter *et al.*, "Solar water splitting cells," *Chem. Rev.*, vol. 110, no. 11, pp. 6446–6473, 2010.

[21] A. F. Janzen, "Photoelectrochemistry.- I Photoelectrolysis" in *Solar Energy Conversion*, pp. 905–921, 1979.

[22] X. Yong and M. A. A. Schoonen, "The absolute energy positions of conduction and valence bands of selected semiconducting minerals," *Am. Mineral.*, vol. 85, no. 3–4, pp. 543–556, 2000.

[23] M. S. Prévot and K. Sivula, "Photoelectrochemical tandem cells for solar water splitting," *J. Phys. Chem. C*, vol. 117, no. 35, pp. 17879–17893, 2013.

[24] "Direct and indirect band gaps - Wikipedia." [Online]. Available: https://en.wikipedia.org/wiki/Direct_and_indirect_band_gaps. [Accessed: 21-Feb-2020].

[25] K. S. Novoselov *et al.*, "Two-dimensional atomic crystals," *Proc. Natl. Acad. Sci. U. S. A.*, vol. 102, no. 30, pp. 10451–10453, 2005.

[26] M. Fox, *Optical properties of solids*, Oxford University Press, 2003.

[27] K. Sivula and R. van de Krol, "Semiconducting materials for photoelectrochemical energy conversion," *Nat. Rev. Mater.*, p. 15010, 2016.

[28] P. Bornoz *et al.*, "A bismuth vanadate-cuprous oxide tandem cell for overall solar water splitting," *J. Phys. Chem. C*, vol. 118, no. 30, pp. 16959–16966, 2014.

[29] P. Dias and A. Mendes, "Hydrogen Production from Photoelectrochemical Water Splitting" in *Encyclopedia of Sustainability Science and Technology*, Springer, 2018.

[30] K. Sivula and M. Grätzel, "Tandem photoelectrochemical cells for solar water splitting," in *Photoelectrochemical Water Splitting: Materials, Processes and Architectures*, , pp. 83–108, 2013.

[31] M. F. Weber and M. J. Dignam, "Splitting water with semiconducting photoelectrodes - efficiency considerations," *Int. J. Hydrogen Energy*, vol. 11, no. 4, pp. 225–232, 1986.

[32] J. R. Bolton, S. J. Stricklert, and J. Connolly, "Limiting and realizable efficiencies of solar photolysis of water," *Nature*, vol. 316, pp. 5–10, 1985.

[33] S. Rühle, "Tabulated values of the Shockley-Queisser limit for single junction solar cells," *Sol. Energy*, vol. 130, pp. 139–147, 2016.

[34] H. Yoneyama, H. Sakamoto, and H. Tamura, "A photo-electochemical cell with

production of hydrogen and oxygen by a cell reaction," *Electrochim. Acta*, vol. 20, no. 5, pp. 341–345, 1975.

[35] A. Paracchino, V. Laporte, K. Sivula, M. Grätzel, and E. Thimsen, "Highly active oxide photocathode for photoelectrochemical water reduction," *Nat. Mater.*, vol. 10, no. 6, pp. 456–461, 2011.

[36] J. Luo, L. Steier, M. K. Son, M. Schreier, M. T. Mayer, and M. Grätzel, "Cu2O nanowire photocathodes for efficient and durable solar water splitting," *Nano Lett.*, vol. 16, no. 3, pp. 1848–1857, 2016.

[37] S. Ida, K. Yamada, T. Matsunaga, H. Hagiwara, Y. Matsumoto, and T. Ishihara, "Preparation of p-type CaFe2O4 photocathodes for producing hydrogen from water," *J. Am. Chem. Soc.*, vol. 132, no. 49, pp. 17343–17345, 2010.

[38] U. A. Joshi and P. A. Maggard, "CuNb3O8: a p-type semiconducting metal oxide photoelectrode," *J. Phys. Chem. Lett.*, vol. 3, no. 11, pp. 1577–1581, 2012.

[39] M. S. Prévot, N. Guijarro, and K. Sivula, "Enhancing the performance of a robust sol-gel-processed p-type delafossite CuFeO2 photocathode for solar water reduction," *ChemSusChem*, vol. 8, no. 8, pp. 1359–1367, 2015.

[40] Q. Huang, Z. Ye, and X. Xiao, "Recent progress in photocathodes for hydrogen evolution," *J. Mater. Chem. A*, vol. 3, no. 31, pp. 15824–15837, 2015.

[41] Y. Hou *et al.*, "Bioinspired molecular co-catalysts bonded to a silicon photocathode for solar hydrogen evolution," *Nat. Mater.*, vol. 10, no. 6, pp. 434–438, 2011.

[42] D. C. Bookbinder, J. A. Bruce, R. N. Dominey, N. S. Lewis, and M. S. Wrighton, "Synthesis and characterization of a photosensitive interface for hydrogen generation: chemically modified p-type semiconducting silicon photocathodes," *Proc Natl Acad Sci USA*, vol. 77, no. 11, pp. 6280–6284, 1980.

[43] S. W. Boettcher *et al.*, "Photoelectrochemical hydrogen evolution using Si microwire arrays," *J. Am. Chem. Soc.*, vol. 133, no. 5, pp. 1216–1219, 2011.

[44] Y. Nakato, Y. Egi, M. Hiramoto, and H. Tsubomura, "Hydrogen evolution and iodine reduction on an illuminated n-p junction silicon electrode and its application to efficient solar photoelectrolysis of hydrogen iodide," *J. Phys. Chem.*, vol. 88, no. 19, pp. 4218–4222, 1984.

[45] B. Seger *et al.*, "Hydrogen production using a molybdenum sulfide catalyst on a titanium-protected n+p-silicon photocathode," *Angew. Chemie - Int. Ed.*, vol. 51, no. 36, pp. 9128–9131, 2012.

[46] Y. Lin *et al.*, "Amorphous Si thin film based photocathodes with high photovoltage for efficient hydrogen production," *Nano Lett.*, vol. 13, no. 11, pp. 5615–5618, 2013.

[47] R. M. Candea, M. Kastner, R. Goodman, and N. Hickok, "Photoelectrolysis of water: Si in salt water," *J. Appl. Phys.*, vol. 47, pp. 2724–2726, 1976.

[48] K. Ohashi, K. Uosaki, and J. O. Bockris, "Cathodes for photodriven hydrogen generators: ZnTe and CdTe," *Energy Reseach*, vol. 1, pp. 25–30, 1977.

[49] D. Yokoyama *et al.*, "Photoelectrochemical water splitting using a Cu(In,Ga)Se2 thin film," *Electrochem. commun.*, vol. 12, no. 6, pp. 851–853, 2010.

[50] D. Yokoyama *et al.*, "H2 evolution from water on modified Cu2ZnSnS4 photoelectrode under solar light," *Appl. Phys. Express*, vol. 3, no. 10, pp. 12–15, 2010.

[51] J. Zhao *et al.*, "Enhancement of solar hydrogen evolution from water by surface modification with CdS and TiO2 on porous CuInS2 photocathodes prepared by an electrodeposition-sulfurization method," *Angew. Chemie - Int. Ed.*, vol. 53, no. 44, pp. 11808–11812, 2014.

[52] W. Septina *et al.*, "Photosplitting of water from wide-gap Cu(in,ga)S2 thin films modified with a CdS layer and pt nanoparticles for a high-onset-potential photocathode," *J. Phys. Chem. C*, vol. 119, no. 16, pp. 8576–8583, 2015.

[53] M. Moriya, T. Minegishi, H. Kumagai, M. Katayama, J. Kubota, and K. Domen, "Stable hydrogen evolution from cds-modified CuGaSe2 photoelectrode under visible-light irradiation," *J. Am. Chem. Soc.*, vol. 135, no. 10, pp. 3733–3735, 2013.

[54] E. Aharon-Shalom and A. Heller, "Efficient p - InP (Rh - H alloy) and p - InP (Re - H alloy) Hydrogen Evolving Photocathodes," *J. Electrochem. Soc.*, vol. 129, no. 12, pp. 2865–2866, 1982.

[55] S. S. Kocha, J. A. Turner, and A. J. Nozik, "Study of the Schottky barrier and determination of the energetic positions of band edges at the n- and p-type gallium indium phosphide electrode |electrolyte interface," *J. Electroanal. Chem.*, vol. 367, no. 1–2, pp. 27–30, 1994.

[56] O. Khaselev and J. A. Turner, "A monolithic photovoltaic-photoelectrochemical device for hydrogen production via water splitting," *Science*, vol. 280, no. 5362, pp. 425–427, 1998.

[57] M. H. Lee *et al.*, "P-Type InP nanopillar photocathodes for efficient solar-driven hydrogen production," *Angew. Chemie - Int. Ed.*, vol. 51, no. 43, pp. 10760–10764, 2012.

[58] M. Hettick, M. Zheng, Y. Lin, C. M. Sutter-Fella, J. W. Ager, and A. Javey, "Nonepitaxial thin-film InP for scalable and efficient photocathodes," *J. Phys. Chem. Lett.*, vol. 6, no. 12, pp. 2177–2182, 2015.

[59] L. Gao *et al.*, "Photoelectrochemical hydrogen production on InP nanowire arrays with molybdenum sulfide electrocatalysts," *Nano Lett.*, vol. 14, no. 7, pp. 3715–3719, 2014.

[60] O. Khaselev and J. A. Turner, "Electrochemical stability of p-GaInP2 in aqueous electrolytes toward photoelectrochemical water splitting," *J. Electrochem. Soc.*, vol. 145, no. 10, pp. 3335–3339, 1998.

[61] M. M. May, H. J. Lewerenz, D. Lackner, F. Dimroth, and T. Hannappel, "Efficient direct solar-to-hydrogen conversion by in situ interface transformation of a tandem structure," *Nat. Commun.*, vol. 6, pp. 4–10, 2015.

[62] Y. Zhang *et al.*, "Biopolymer-activated graphitic carbon nitride towards a sustainable photocathode material," *Sci. Rep.*, vol. 3, pp. 1–5, 2013.

[63] Y. Zhang, T. Mori, J. Ye, and M. Antonietti, "Phosphorus-doped carbon nitride solid: enhanced electrical conductivity and photocurrent generation," *J. Am. Chem. Soc.*, vol. 132, no. 18, pp. 6294–6295, 2010.

[64] X. Wang *et al.*, "A metal-free polymeric photocatalyst for hydrogen production from water under visible light," *Nat. Mater.*, vol. 8, no. 1, pp. 76–80, 2009.

[65] Y. Hou, Z. Wen, S. Cui, X. Guo, and J. Chen, "Constructing 2D porous graphitic C3N4 nanosheets/nitrogen-doped graphene/layered MoS2 ternary nanojunction with enhanced photoelectrochemical activity," *Adv. Mater.*, vol. 25, no. 43, pp. 6291–6297, 2013.

[66] G. Liu *et al.*, "Unique electronic structure induced high photoreactivity of sulfur-doped graphitic C3N4," *J. Am. Chem. Soc.*, vol. 132, no. 33, pp. 11642–11648, 2010.

[67] J. R. McKone, A. P. Pieterick, H. B. Gray, and N. S. Lewis, "Hydrogen evolution from Pt/Ru-coated p-type WSe2 photocathodes," *J. Am. Chem. Soc.*, vol. 135, no. 1, pp. 223–231, 2013.

[68] X. Yu, N. Guijarro, M. Johnson, and K. Sivula, "Defect mitigation of solution-processed 2D WSe2 nanoflakes for solar-to-hydrogen conversion," *Nano Lett.*, vol. 18, no. 1, pp. 215–222, 2018.

[69] Q. H. Wang, K. Kalantar-Zadeh, A. Kis, J. N. Coleman, and M. S. Strano, "Electronics and optoelectronics of two-dimensional transition metal dichalcogenides," *Nat. Nanotechnol.*, vol. 7, no. 11, pp. 699–712, 2012.

[70] G. Wang *et al.*, "Spin-orbit engineering in transition metal dichalcogenide alloy monolayers," *Nat. Commun.*, vol. 6, pp. 1–7, 2015.

[71] J. Kang, S. Tongay, J. Zhou, J. Li, and J. Wu, "Band offsets and heterostructures of two-dimensional semiconductors," *Appl. Phys. Lett.*, vol. 102, no. 1, 2013.

[72] A. Eftekhari, "Tungsten dichalcogenides (WS2, WSe2, and WTe2): materials chemistry and applications," *J. Mater. Chem. A*, vol. 5, no. 35, pp. 18299–18325, 2017.

[73] Z. Chen, A. J. Forman, and T. F. Jaramillo, "Bridging the gap between bulk and nanostructured photoelectrodes: the impact of surface states on the electrocatalytic and photoelectrochemical properties of MoS2," *J. Phys. Chem. C*, vol. 117, no. 19, pp. 9713–9722, 2013.

[74] H. J. Lewerenz, "Charge collection microscopy on p-WSe2: recombination sites and minority carrier diffusion length," *J. Electrochem. Soc.*, vol. 129, no. 2, p. 418, 1982.

[75] J. M. Velazquez *et al.*, "A scanning probe investigation of the role of surface motifs in the behavior of p-WSe2 photocathodes," *Energy Environ. Sci.*, vol. 9, pp. 164–175, 2015.

[76] A. H. Loo, A. Bonanni, Z. Sofer, and M. Pumera, "Exfoliated transition metal dichalcogenides (MoS2, MoSe2, WS2, WSe2): an electrochemical impedance spectroscopic investigation," *Electrochem. commun.*, vol. 50, pp. 39–42, 2015.

[77] A. Ambrosi, Z. Sofer, and M. Pumera, "2H → 1T phase transition and hydrogen evolution activity of MoS_2, $MoSe_2$, WS_2 and WSe_2 strongly depends on the MX_2 composition," *Chem. Commun.*, vol. 51, no. 40, pp. 8450–8453, 2015.

[78] M. Chhowalla, H. S. Shin, G. Eda, L.-J. Li, K. P. Loh, and H. Zhang, "The chemistry of two-dimensional layered transition metal dichalcogenide nanosheets," *Nat. Chem.*, vol. 5, p. 263-275, 2013.

[79] M. Yi and Z. Shen, "A review on mechanical exfoliation for the scalable production of graphene," *J. Mater. Chem. A*, vol. 3, no. 22, pp. 11700–11715, 2015.

[80] J. Zheng *et al.*, "High yield exfoliation of two-dimensional chalcogenides using sodium naphthalenide," *Nat. Commun.*, vol. 5, pp. 1–7, 2014.

[81] V. Nicolosi, M. Chhowalla, M. G. Kanatzidis, M. S. Strano, and J. N. Coleman, "Liquid exfoliation of layered materials," *Science*, vol. 340, no. 6139, pp. 72–75, 2013.

[82] P. Joensen, R. F. Frindt, and S. R. Morrison, "Single-layer MoS2," *Mater. Res. Bull.*, vol. 21, no. 4, pp. 457–461, 1986.

[83] W. M. R. Divigalpitiya, R. F. Frindt, and S. R. Morrison, "Oriented films of molybdenum trioxide," *Thin Solid Films*, vol. 188, no. 1, pp. 173–179, 1990.

[84] D. Voiry *et al.*, "Covalent functionalization of monolayered transition metal dichalcogenides by phase engineering," *Nat. Chem.*, vol. 7, no. 1, pp. 45–49, 2015.

[85] C. Backes *et al.*, "Guidelines for exfoliation, characterization and processing of layered materials produced by liquid exfoliation," *Chem. Mater.*, vol. 29, no. 1, pp. 243–255, 2017.

[86] W. Qiao *et al.*, "Effects of ultrasonic cavitation intensity on the efficient liquid-exfoliation of MoS2 nanosheets," *RSC Adv.*, vol. 4, no. 92, pp. 50981–50987, 2014.

[87] G. Cunningham *et al.*, "Solvent exfoliation of transition metal dichalcogenides: dispersibility of exfoliated nanosheets varies only weakly between compounds," *ACS Nano*, vol. 6, no. 4, pp. 3468–3480, 2012.

[88] K. F. Mak, C. Lee, J. Hone, J. Shan, and T. F. Heinz, "Atomically thin MoS2: a new direct-gap semiconductor," *Phys. Rev. Lett.*, vol. 105, no. 13, pp. 2–5, 2010.

[89] R. J. Smith *et al.*, "Large-scale exfoliation of inorganic layered compounds in aqueous surfactant solutions," *Adv. Mater.*, vol. 23, no. 34, pp. 3944–3948, 2011.

[90] X. Yu, M. S. Prévot, N. Guijarro, and K. Sivula, "Self-assembled 2D WSe 2 thin films for photoelectrochemical hydrogen production," *Nat. Commun.*, vol. 6, no. 7596, pp. 1-8,2015.

[91] J. Xi, T. Zhao, D. Wang, and Z. Shuai, "Tunable electronic properties of two-dimensional transition metal dichalcogenide alloys: a first-principles prediction," *J. Am. Chem. Soc.*, 2014.

[92] T. Li and G. Galli, "Electronic Properties of MoS2 Nanoparticles," vol. 12, pp. 16192–16196, 2007.

[93] R. Roldán, J. A. Silva-Guillén, M. P. López-Sancho, F. Guinea, E. Cappelluti, and P. Ordejón, "Electronic properties of single-layer and multilayer transition metal dichalcogenides MX2 (M = Mo, W and X = S, Se)," *Ann. Phys.*, vol. 526, no. 9–10, pp. 347–357, 2014.

[94] M. Amani *et al.*, "Near-unity photoluminescence quantum yield in MoS2," *Science*, vol. 350, no. 6264, pp. 1065–1068, 2015.

[95] A. Splendiani *et al.*, "Emerging photoluminescence in monolayer MoS2," *Nano Lett.*, vol. 10, no. 4, pp. 1271–1275, 2010.

[96] H. Kim *et al.*, "Emerging photoluminescence in monolayer MoS2," *Sci. Adv.*, vol. 5, no. 1, pp. 1–8, 2019.

[97] A. A. Yaroshevsky, "Abundances of chemical elements in the Earth's crust," *Geochemistry Int.*, vol. 44, no. 1, pp. 48–55, 2006.

[98] K. Sivula, F. Le Formal, and M. Grätzel, "Solar water splitting: progress using

hematite (α-Fe 2O3) photoelectrodes," *ChemSusChem*, vol. 4, no. 4, pp. 432–449, 2011.

[99] J. Brillet, M. Grätzel, and K. Sivula, "Decoupling feature size and functionality in solution-processed, porous hematite electrodes for solar water splitting," *Nano Lett.*, vol. 10, no. 10, pp. 4155–4160, 2010.

[100] Y. Liu, Y. X. Yu, and W. De Zhang, "MoS2/CdS heterojunction with high photoelectrochemical activity for H2 evolution under visible light: The role of MoS2," *J. Phys. Chem. C*, vol. 117, no. 25, pp. 12949–12957, 2013.

[101] N. Guijarro, M. S. Prévot, and K. Sivula, "Surface modification of semiconductor photoelectrodes," *Phys. Chem. Chem. Phys.*, vol. 17, no. 24, pp. 15655–15674, 2015.

[102] F. Le Formal, K. Sivula, and M. Grätzel, "The transient photocurrent and photovoltage behavior of a hematite photoanode under working conditions and the influence of surface treatments," *J. Phys. Chem. C*, vol. 116, no. 51, pp. 26707–26720, 2012.

[103] F. F. Abdi, L. Han, A. H. M. Smets, M. Zeman, B. Dam, and R. Van De Krol, "Efficient solar water splitting by enhanced charge separation in a bismuth vanadate-silicon tandem photoelectrode," *Nat. Commun.*, vol. 4, pp. 1–7, 2013.

[104] R. Liu, Z. Zheng, J. Spurgeon, and X. Yang, "Enhanced photoelectrochemical water-splitting performance of semiconductors by surface passivation layers," *Energy Environ. Sci.*, vol. 7, no. 8, pp. 2504–2517, 2014.

[105] J. Young Kim, J. W. Jang, D. Hyun Youn, J. Yul Kim, E. Sun Kim, and J. Sung Lee, "Graphene-carbon nanotube composite as an effective conducting scaffold to enhance the photoelectrochemical water oxidation activity of a hematite film," *RSC Adv.*, vol. 2, no. 25, pp. 9415–9422, 2012.

[106] Y. Ouyang, Q. Li, L. Shi, C. Ling, and J. Wang, "Molybdenum sulfide clusters immobilized on defective graphene: a stable catalyst for the hydrogen evolution reaction," *J. Mater. Chem. A*, vol. 6, no. 5, pp. 2289–2294, 2018.

[107] S. Das, D. Pandey, J. Thomas, and T. Roy, "The role of graphene and other 2D materials in solar photovoltaics," *Adv. Mater.*, vol. 31, no. 1, pp. 1–35, 2019.

[108] Y. Yuan *et al.*, "Excellent photocatalytic performance of few-layer MoS2/graphene hybrids," *J. Alloys Compd.*, vol. 700, pp. 12–17, 2017.

[109] X. Wang *et al.*, "Few-layered WSe2 nanoflowers anchored on graphene nanosheets: a highly efficient and stable electrocatalyst for hydrogen evolution," *Electrochim. Acta*, vol. 222, pp. 1293–1299, 2016.

[110] K. Chang, Z. Mei, T. Wang, Q. Kang, S. Ouyang, and J. Ye, "MoS2/graphene cocatalyst for efficient photocatalytic H2 evolution under visible light irradiation," *ACS Nano*, vol. 8, no. 7, pp. 7078–7087, 2014.

[111] H. Zhou *et al.*, "Highly active and durable self-standing WS2/graphene hybrid catalysts for hydrogen evolution reaction," *J. Mater. Chem. A*, vol. 4, pp. 9472–9476, 2016.

[112] Z. Pu, Q. Liu, A. M. Asiri, A. Y. Obaid, and X. Sun, "Graphene film-confined molybdenum sulfide nanoparticles: Facile one-step electrodeposition preparation and application as a highly active hydrogen evolution reaction electrocatalyst," *J. Power Sources*, vol. 263, pp. 181–185, 2014.

[113] E. G. S. Firmiano, M. A. L. Cordeiro, A. C. Rabelo, C. J. Dalmaschio, A. N. Pinheiro, and E. C. Pereira, "Graphene oxide as a highly selective substrate to synthesize a layered MoS2 hybrid electrocatalyst," *Chem. Commun.*, vol. 48, no. 62, pp. 7687–7689, 2012.

[114] K. Sivula *et al.*, "Photoelectrochemical water splitting with mesoporous hematite prepared by a solution-based colloidal approach," *J. Am. Chem. Soc.*, vol. 132, no. 21, pp. 7436–7444, 2010.

[115] N. Guijarro, M. S. Prévot, X. A. Jeanbourquin, X. Yu, and K. Sivula, "Autodecomposition approach for the low-temperature mesostructuring of nanocrystal semiconductor electrodes," *Chem. Mater.*, vol. 27, no. 18, pp. 6337–6344, 2015.

[116] T. W. Kim and K.-S. Choi, "Nanoporous $BiVO_4$ photoanodes with dual-layer Oxygen evolution catalysts for solar water splitting," *Science*, vol. 343, no. 6174, pp. 990–994, 2014.

[117] A. Hagfeldt and M. Grätzel, "Molecular photovoltaics," *Acc. Chem. Res.*, vol. 33, no. 5, pp. 269–277, 2000.

[118] M. Hilgendorff, L. Spanhel, C. Rothenhäusler, and G. Müller, "From ZnO colloids to nanocrystalline highly conductive films," *J. Electrochem. Soc.*, vol. 145, no. 10, pp. 3632–3637, 1998.

[119] M. Grätzel, "Photo-electrochemical cells," *Nature*, vol. 414, no. 15 November 2001, 2001.

[120] D. Ressnig, R. Kontic, and G. R. Patzke, "Morphology control of $BiVO_4$ photocatalysts: PH optimization vs. self-organization," *Mater. Chem. Phys.*, vol. 135, no. 2–3, pp. 457–466, 2012.

[121] G. Liu, J. C. Yu, G. Q. Lu, and H. M. Cheng, "Crystal facet engineering of semiconductor photocatalysts: Motivations, advances and unique properties," *Chem. Commun.*, vol. 47, no. 24, pp. 6763–6783, 2011.

[122] N. S. Lewis, "Chemical control of charge transfer and recombination at semiconductor photoelectrode surfaces," *Inorg. Chem.*, vol. 44, no. 20, pp. 6900–6911, 2005.

[123] Z. Lin *et al.*, "Defect engineering of two-dimensional transition metal dichalcogenides," *2D Mater.*, vol. 3, no. 2, 2016.

[124] J. Hong *et al.*, "Exploring atomic defects in molybdenum disulphide monolayers," *Nat. Commun.*, vol. 6, no. 6293, pp. 1–8, 2015.

[125] S. Kc, R. C. Longo, R. Addou, R. M. Wallace, and K. Cho, "Impact of intrinsic atomic defects on the electronic structure of MoS 2 monolayers," *Nanotechnology*, vol. 25, no. 37, 2014.

[126] W. Zhou *et al.*, "Intrinsic structural defects in monolayer molybdenum disulfide," *Nano Lett.*, vol. 13, no. 6, pp. 2615–2622, 2013.

[127] J. Xie *et al.*, "Controllable disorder engineering in oxygen-incorporated MoS2 ultrathin nanosheets for efficient hydrogen evolution," *J. Am. Chem. Soc.*, vol. 135, no. 47, pp. 17881–17888, 2013.

[128] H. P. Komsa, S. Kurasch, O. Lehtinen, U. Kaiser, and A. V. Krasheninnikov, "From point to extended defects in two-dimensional MoS2: evolution of atomic structure under

electron irradiation," *Phys. Rev. B - Condens. Matter Mater. Phys.*, vol. 88, no. 3, pp. 1–8, 2013.

[129] X. Zou, Y. Liu, and B. I. Yakobson, "Predicting dislocations and grain boundaries in two-dimensional metal-disulfides from the first principles," *Nano Lett.*, vol. 13, no. 1, pp. 253–258, 2013.

[130] H. Nan *et al.*, "Strong photoluminescence enhancement of MoS2 through defect engineering and oxygen bonding," *ACS Nano*, vol. 8, no. 6, pp. 5738–5745, 2014.

[131] A. Jakubowicz, D. Mahalu, M. Wolf, A. Wold, and R. Tenne, "WSe2: Optical and electrical properties as related to surface passivation of recombination centers," *Phys. Rev. B*, vol. 40, no. 5, pp. 2992–3000, 1989.

[132] H. D. Abruna and A. J. Bard, "Semiconductor Electrodes. 44. Photoelectrochemistry at Polycrystalline p-Type WSe2 Films," *J. Electrochem. Soc.*, vol. 129, no. 3, pp. 673–676, 1982.

[133] J. H. Park *et al.*, "Defect passivation of transition metal dichalcogenides via a charge transfer van der Waals interface," *Sci. Adv.*, vol. 3, no. 10, pp. 1–7, 2017.

[134] G. Nagasubramanian and A. J. Bard, "Photoelectrochemistry of p-Type WSe2 in Acetonitrile and the p-WSe2 -Nitrobenzene Cell," *J. Electrochem. Soc.*, vol. 128, no. 5, pp. 1055–1060, 1981.

[135] F. Le Formal, N. Tétreault, M. Cornuz, T. Moehl, M. Grätzel, and K. Sivula, "Passivating surface states on water splitting hematite photoanodes with alumina overlayers," *Chem. Sci.*, vol. 2, no. 4, pp. 737–743, 2011.

[136] L. Badia-Bou *et al.*, "Water oxidation at hematite photoelectrodes with an iridium-based catalyst," *J. Phys. Chem. C*, vol. 117, no. 8, pp. 3826–3833, 2013.

[137] Y. J. Hwang, C. Hahn, B. Liu, and P. Yang, "Photoelectrochemical properties of TiO2 nanowire arrays: a study of the dependence on length and atomic layer deposition coating," *ACS Nano*, vol. 6, no. 6, pp. 5060–5069, 2012.

[138] Y. Hou *et al.*, "Layered nanojunctions for hydrogen-evolution catalysis," *Angew. Chemie - Int. Ed.*, vol. 52, no. 13, pp. 3621–3625, 2013.

[139] X. Yang, C. Du, R. Liu, J. Xie, and D. Wang, "Balancing photovoltage generation and charge-transfer enhancement for catalyst-decorated photoelectrochemical water splitting: a case study of the hematite/MnOx combination," *J. Catal.*, vol. 304, pp. 86–91, 2013.

[140] O. Krüger, C. N. Kenyon, M. X. Tan, and N. S. Lewis, "Behavior of Si photoelectrodes under high level injection conditions. 2. Experimental measurements and digital simulations of the behavior of quasi-Fermi levels under illumination and applied bias," *J. Phys. Chem. B*, vol. 101, no. 15, pp. 2840–2849, 1997.

[141] J. Kibsgaard, T. F. Jaramillo, and F. Besenbacher, "Building an appropriate active-site motif into a hydrogen-evolution catalyst with thiomolybdate [Mo3S13]2⁻ clusters," *Nat. Chem.*, vol. 6, pp. 248–253, 2014.

[142] J. Kibsgaard, Z. Chen, B. N. Reinecke, and T. F. Jaramillo, "Engineering the surface structure of MoS 2 toÂ preferentially expose active edge sites forÂ electrocatalysis," *Nat. Mater.*, vol. 11, no. 11, pp. 963–969, 2012.

[143] E. J. Popczun, C. G. Read, C. W. Roske, N. S. Lewis, and R. E. Schaak, "Highly

active electrocatalysis of the hydrogen evolution reaction by cobalt phosphide nanoparticles," *Angew. Chemie - Int. Ed.*, vol. 53, no. 21, pp. 5427–5430, 2014.

[144] E. J. Popczun *et al.*, "Nanostructured nickel phosphide as an electrocatalyst for the hydrogen evolution reaction," *J. Am. Chem. Soc.*, vol. 135, no. 25, pp. 9267–9270, 2013.

[145] J. Guo, Y. Shi, X. Bai, X. Wang, and T. Ma, "Atomically thin MoSe2/graphene and WSe2/graphene nanosheets for the highly efficient oxygen reduction reaction," *J. Mater. Chem. A*, vol. 3, no. 48, pp. 24397–24404, 2015.

[146] V. Y. Fominski, S. N. Grigoriev, R. I. Romanov, M. A. Volosova, A. I. Grunin, and G. D. Teterina, "The formation of a hybrid structure from tungsten selenide and oxide plates for a hydrogen-evolution electrocatalyst," *Tech. Phys. Lett.*, vol. 42, no. 6, pp. 555–558, 2016.

[147] Y. Sun, F. Lei, S. Gao, B. Pan, J. Zhou, and Y. Xie, "Atomically thin tin dioxide sheets for efficient catalytic oxidation of carbon monoxide," *Angew. Chemie - Int. Ed.*, vol. 52, no. 40, pp. 10569–10572, 2013.

[148] K. S. Kim *et al.*, "Large-scale pattern growth of graphene films for stretchable transparent electrodes," *Nature*, vol. 457, no. 7230, pp. 706–710, 2009.

[149] A. T. Najafabadi and E. Gyenge, "High-yield graphene production by electrochemical exfoliation of graphite: Novel ionic liquid (IL)-acetonitrile electrolyte with low IL content," *Carbon N. Y.*, vol. 71, no. Il, pp. 58–69, 2014.

[150] T. T. Dang, V. H. Pham, S. H. Hur, E. J. Kim, B. S. Kong, and J. S. Chung, "Superior dispersion of highly reduced graphene oxide in N,N-dimethylformamide," *J. Colloid Interface Sci.*, vol. 376, no. 1, pp. 91–96, 2012.

[151] Y. Li, H. Wang, L. Xie, Y. Liang, G. Hong, and H. Dai, "MoS2 nanoparticles grown on graphene: an advanced catalyst for the hydrogen evolution reaction," *J. Am. Chem. Soc.*, vol. 133, no. 19, pp. 7296–7299, 2011.

[152] Z. Liu, H. Zhao, N. Li, Y. Zhang, X. Zhang, and Y. Du, "Assembled 3D electrocatalysts for efficient hydrogen evolution: WSe_2 layers anchored on graphene sheets," *Inorg. Chem. Front.*, vol. 3, no. 2, pp. 313–319, 2016.

[153] X. Wang *et al.*, "Few-layered WSe 2 nano fl owers anchored on graphene nanosheets : a highly ef fi cient and stable electrocatalyst for hydrogen evolution," *Electrochimica Acta*, vol. 222, pp. 1293–1299, 2016.

[154] S. oriented M. nanosheets as advanced electrocatalysts for hydrogen evolution Mao, Z. Wen, S. Ci, X. Guo, K. Ostrikov, and J. Chen, "Perpendicularly oriented MoSe2/graphene nanosheets as advanced electrocatalysts for hydrogen evolution," *Small*, vol. 11, no. 4, pp. 414–419, 2015.

[155] N. Cheng *et al.*, "Platinum single-atom and cluster catalysis of the hydrogen evolution reaction," *Nat. Commun.*, vol. 7, pp. 1–9, 2016.

[156] H. Yan *et al.*, "Visible-light-driven hydrogen production with extremely high quantum efficiency on Pt-PdS/CdS photocatalyst," *J. Catal.*, vol. 266, no. 2, pp. 165–168, 2009.

[157] T. F. Jaramillo *et al.*, "Hydrogen Evolution on Supported Incomplete Cubane-type [Mo 3 S 4] 4+ Electrocatalysts," *J. Phys. Chem. C*, vol. 112, no. 45, pp. 17492–17498, 2008.

[158] Z. Huang *et al.*, "Dimeric [Mo2S12]2- cluster: a molecular analogue of MoS2 edges

for superior hydrogen-evolution electrocatalysis," *Angew. Chemie - Int. Ed.*, vol. 127, no. 50, pp. 15396–15400, 2015.

[159] P. D. Tran *et al.*, "Coordination polymer structure and revisited hydrogen evolution catalytic mechanism for amorphous molybdenum sulfide," *Nat. Mater.*, vol. 15, no. 6, pp. 640–646, 2016.

[160] E. Kamieniecki *et al.*, "Electrochemical characterization of p-type semiconducting tungsten disulfide photocathodes: efficient photoreduction processes at semiconductor/liquid electrolyte interfaces," *J. Am. Chem. Soc.*, vol. 105, no. 8, pp. 2246–2256, 1983.

[161] L. Zeng *et al.*, "High-responsivity UV-Vis photodetector based on transferable WS2 film deposited by magnetron sputtering," *Sci. Rep.*, vol. 6, no. October 2015, pp. 1–8, 2016.

[162] H. M. W. Khalil, M. F. Khan, J. Eom, and H. Noh, "Highly stable and tunable chemical doping of multilayer WS2 field effect transistor: reduction in contact resistance," *ACS Appl. Mater. Interfaces*, vol. 7, no. 42, pp. 23589–23596, 2015.

[163] Y. Sang, Z. Zhao, M. Zhao, P. Hao, Y. Leng, and H. Liu, "From UV to near-infrared, WS2 nanosheet: a novel photocatalyst for full solar light spectrum photodegradation," *Adv. Mater.*, vol. 27, no. 2, pp. 363–369, 2015.

[164] A. Sobczynski *et al.*, "Catalytic hydrogen evolution properties of nickel-doped tungsten disulfide," *J. Phys. Chem.*, vol. 93, no. 1, pp. 401–403, 1989.

[165] H. Tributsch and J. C. Bennett, "Electrochemistry and photochemistry of MoS2 layer crystals," *J. Electroanal. Chem.*, vol. 81, no. 1, pp. 97–111, 1977.

[166] Z. Li, X. Meng, and Z. Zhang, "Recent development on MoS2-based photocatalysis: A review," *J. Photochem. Photobiol. C Photochem. Rev.*, vol. 35, pp. 39–55, 2018.

[167] J. Zhang, Z. Zhu, and X. Feng, "Construction of two-dimensional MoS2/CdS p-n nanohybrids for highly efficient photocatalytic hydrogen evolution," *Chem. - A Eur. J.*, vol. 20, no. 34, pp. 10632–10635, 2014.

[168] F. A. Frame and F. E. Osterloh, "CdSe-MoS2: a quantum size-confined photocatalyst for hydrogen evolution from water under visible light," *J. Phys. Chem. C*, vol. 114, no. 23, pp. 10628–10633, 2010.

[169] X. Zong *et al.*, "Photocatalytic H2 evolution on MoS2/CdS catalysts under visible light irradiation," *J. Phys. Chem. C*, vol. 114, no. 4, pp. 1963–1968, 2010.

[170] X. Guo, X. Tong, Y. Wang, C. Chen, G. Jin, and X. Y. Guo, "High photoelectrocatalytic performance of a MoS2-SiC hybrid structure for hydrogen evolution reaction," *J. Mater. Chem. A*, vol. 1, no. 15, pp. 4657–4661, 2013.

[171] A. Eftekhari, "Molybdenum diselenide (MoSe2) for energy storage, catalysis, and optoelectronics," *Appl. Mater. Today*, vol. 8, pp. 1–17, 2017.

[172] S. Tongay *et al.*, "Thermally driven crossover from indirect toward direct bandgap in 2D Semiconductors: MoSe2 versus MoS2," *Nano Lett.*, vol. 12, no. 11, pp. 5576–5580, 2012.

[173] A. B. Laursen, S. Kegnæs, S. Dahl, and I. Chorkendorff, "Molybdenum sulfides—efficient and viable materials for electro - and photoelectrocatalytic hydrogen evolution," *Energy Environ. Sci.*, vol. 5, no. 2, p. 5577, 2012.

[174] T. F. Jaramillo, K. P. Jørgensen, J. Bonde, J. H. Nielsen, S. Horch, and I. Chorkendorff, "Identification of active edge sites for electrochemical H2 evolution from MoS2 nanocatalysts," *Science*, vol. 317, no. 5834, pp. 100–102, 2007.

[175] X. Zong *et al.*, "Visible light driven H2 production in molecular systems employing colloidal MoS2 nanoparticles as catalyst," *Chem. Commun.*, no. 30, pp. 4536–4538, 2009.

[176] B. Hinnemann *et al.*, "Biomimetic hydrogen evolution: MoS2 nanoparticles as catalyst for hydrogen evolution," *J. Am. Chem. Soc.*, vol. 127, no. 15, pp. 5308–5309, 2005.

[177] J. K. Nørskov *et al.*, "Trends in the exchange current for hydrogen evolution," *J. Electrochem. Soc.*, vol. 152, no. 3, pp. 26–29, 2005.

[178] C. G. Morales-guio and X. Hu, "Amorphous Molybdenum Sul fi des as Hydrogen Evolution Catalysts," 2014.

[179] B. R. Garrett, S. M. Polen, M. Pimplikar, C. M. Hadad, and Y. Wu, "Anion-redox mechanism of MoO(S2)2(2,2′-bipyridine) for electrocatalytic hydrogen production," *J. Am. Chem. Soc.*, vol. 139, no. 12, pp. 4342–4345, 2017.

CHAPTER II

Materials and Experimental Methods

Introduction

During this thesis work, several experimental techniques were used to develop and to study the morphology, microstructure, optical, electrical, and photoelectrochemical properties of the 2D TMDC photoelectrodes. The different analysis and characterizations were realized in the CIRIMAT laboratory, and also in collaboration with other laboratories (LPCNO, CEMES, ICT, Raimond Castaing Microcaraterization Center and Nagasaki University). For this second chapter, all the development and characterization techniques used will be detailed in the following sections.

II.1 Material Synthesis and Elaboration

II.1.1 TMDC Nanoflakes Fabrication

II.1.1.1 2D p-WSe_2 nanoflakes fabrication by solvent exfoliation

The WSe_2 powder from Alfa Aesar (99.8%) was exfoliated in dichlorobenzene solvent (DCB, Sigma Aldrich) using an ultrasonicator 750W (Biobloc Scientific). 3g of WSe_2 was exfoliated at 40% amplitude (6 sec on/4 sec off) for 16h in a 4°C bath in 30 ml of DCB. After exfoliation, a size selection was performed through an ultracentrifugation at various rpm – from 600 to 1500 rpm – during 10 min; the supernatant phase was then collected. Removal of soluble impurities and transfer in dimethylformamide solvent (DMF, Sigma Aldrich) of the WSe_2 nanosheets were carried out by a series of ultracentrifugation/re-dispersion. The DCB dispersion containing the WSe_2 nanosheets was ultracentrifuged at 15.300 rpm and the solid redispersed in 20 ml of DMF. This sequence was repeated twice. The WSe_2 nanosheets were re-dispersed in a final DMF volume adjusted to a concentration of 8.0 g l^{-1}.

II.1.1.2 Self-assembly of p-WSe_2/Graphene oxide nanosheets fabrication in DMF

Preparation of Sn (IV)-SbS_3 (Sb = 0.5 molar) colloids

A metallic cation stock liquor was prepared by addition of $SbCl_3$ (Sigma, 1.83g – 8 mmol) and $SnCl_4.5H_2O$ (Sigma, 2.8g – 8 mmol) dissolved in 32 ml DMSO. A $(NH_4)_2S$ aqueous solution (denoted diluted S^{2-} solution) was prepared by adding 128 ml H_2O to 19.8 ml of a 3.2 M S^{2-} Sigma

commercial solution. Precipitation of a brown solid was observed after the instantaneous addition of the DMSO metallic salts solution to the sulfide solution. The reaction mixture was aged at 30°C until complete solubilization to a clear yellow limpid solution containing the anionic metallic chalcogenide species. After dilution of the freshly prepared anionic metallic chalcogenide solution, thermal-activated polycondensation of the soluble anionic species was performed in a pre-heated constant temperature bath at 65°C. When the solution turned (after 2 hours) to yellow-green turbid, the reaction was immediately quenched by addition of 200 ml H_2O to the solution. After aging for one night at room temperature, the colloidal solution was washed on a 3 KD membrane by 200 ml H_2O and finally post concentrated by ultrafiltration yielding an orange colloidal dispersion, as shown in **Figure II - 1**. The transfer in DMF was performed by adding DMF into the aqueous dispersions and slow evaporation during 16 hours in Air atmosphere at 65°C.

Figure II - 1: *Template colloidal dispersion of $Sn_xSb_yS_z$ in DMF.*

Preparation of Graphene Oxide in DMF solvent

Graphene oxide (GO) was synthesized according to the Hummers' method [1]. Concentrated H_2SO_4 (2 x 25mL, 95%, Sigma Aldrich) was added to a mixture of graphite flakes (2 x 0.5 g, 1 wt. equiv) and $NaNO_3$ (2 x 0.5 g, 1 wt. equiv). The mixture was cooled using an ice bath to 4°C. $KMnO_4$ (2 x 3.0 g, 6 wt. equiv) was added slowly in portions to keep the reaction temperature below 20 °C. The reaction was warmed and stirred for 10 min and closed in a reactor

at 45°C during 48 hours. Then, 2 x 40 ml of H_2O was added slowly to the mixture reaction heating up to 95 °C – exothermic reaction –, stirred for 1h until cooled down at room temperature. More 2 x 100 mL of H_2O and 2 x 8mL of H_2O_2 (30%, Sigma Aldrich) was added into the reaction mixture and stirred for 2 hours. The mixture was then centrifuged (4.500 rpm for 10min), and the supernatant was decanted away. The remaining solid material was then re-dispersed with NaOH solution (120-140 ml, 1M) for pH shifting (pH = 8.5, 9.0) and washed 4 times in succession with distilled water to eliminate the impurities. Once the mixture is purified, it was re-dispersed into 400 mL of DMF and ultrasonicated at 750 W (Biobloc Scientific) 40% amplitude (6 sec on/4sec off) for 16. The dispersion of GO in DMF was reduced at 200°C during 4 hours with hydrazine (H_4N_2). A concentration of 1 g l^{-1} was determined after a selection of 15.300 rpm, 10 min.

Self-assembly of Sb_2S_3 –SnS_2 template and rGO-WSe_2 nanosheets

Our self-assembly process involves in a first step the mixing of the Sb_2S_3 –SnS_2 template (100 g l^{-1}) and concentrated WSe_2 (40 g l^{-1}) colloidal dispersions stabilized in DMF. The WSe_2 volume fraction was $\Phi_{V\,WSe_2} = V_{WSe_2}/(V_{WSe_2} + V_{SnSbS}) = 0.1$. Then, 1 ml of graphene oxide dispersion (1 g l^{-1}) was added to the previous mixture with $\Phi_{V\,GO} = V_{GO}/(V_{WSe_2} + V_{GO}) = 0.1$. The resulting solution was poured in a large surface open reactor (S = 314 cm^2) and evaporated at room temperature under a hood equipped with Air flow. The dried solid mixture was collected and calcined at 200°C for one hour under Argon atmosphere. Dissolution of the template from the co-textured powder was performed at room temperature by adding 20 ml of $(NH_4)_2S$ 1.5M solution. This operation was done three times and the powder was finally washed with H_2O to obtain the final product. **Figure II - 2** illustrates the self-assembly process described just above.

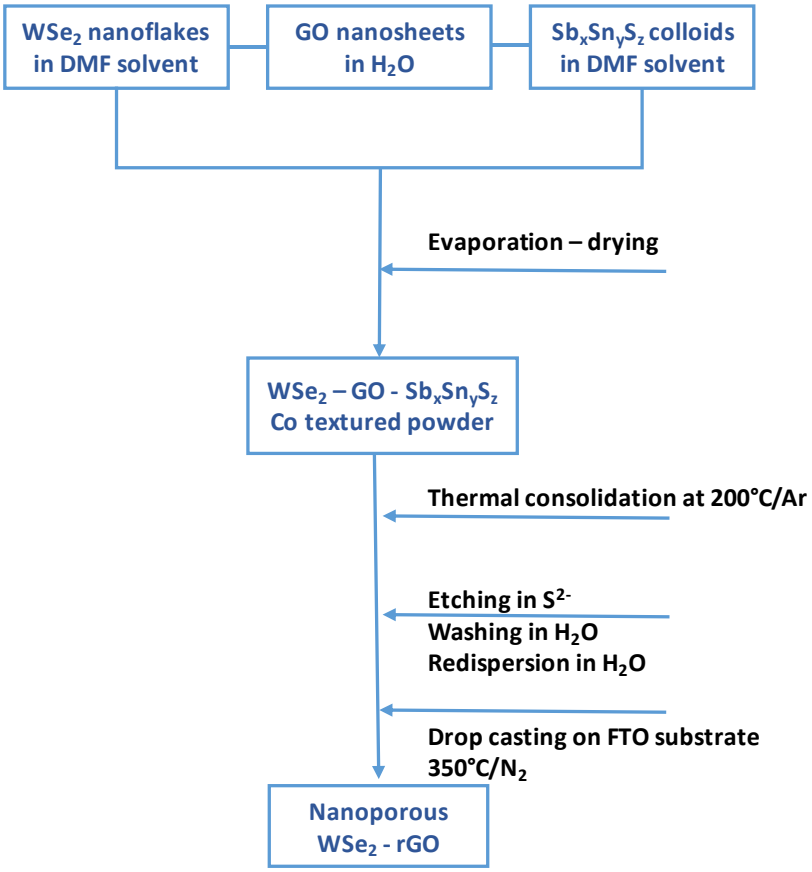

Figure II - 2: *Scheme of self-assembly process of $Sn_xSb_yS_z$ colloid template and rGO-WSe_2 nanosheets.*

II.1.2 TMDC photo-electrodes fabrication

A simple procedure was used to fabricate all the TMDC films. All the dispersions were deposited by drop casting on F: SnO_2-coated glass substrate (SOLEMS, France), 3.0 cm x 1.5 cm for the small and 3.0 cm x 3.0 cm for the large electrodes. The electrodes were made of 3-4 layers of the active material, with solvent evaporation between the layer depositions. An overall active layer thickness of ≈ 2 to 3 µm was achieved, which corresponded to a mass loading of about 1.0 – 1.5 mg for electrodes with geometric surface of 1 cm^2 or 3 - 4 mg for electrode with geometric surface of 4 cm^2 (**Figure II - 3**). After deposition, the electrodes underwent a heat treatment in a PYROX VK90 controlled atmosphere of N_2: under a low heating rate (0.5°C. min^{-1}) to get a dwell temperature of 350°C during 2 hours. The low heating rate was used to perform the heat treatment without degradation of the TMDC films, either in case of remaining oxygen in the furnace system or from carbon monoxide degassing in the case of self-assembled rGO-WSe_2 electrodes.

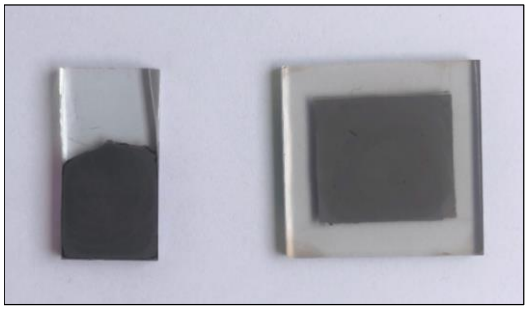

Figure II - 3: *Drop-casted WSe_2 films onto FTO substrate after heat treatment at 350°C, under N_2 atmosphere.*

II.1.3 Mo_xS_y-based co-catalyst fabrication and deposition

II.1.3.1 Mo thio and oxo thio complexes aqueous solution preparation

Ammonium tetrathiomolybdate ($(NH_4)_2MoS_4$) from Sigma Aldrich (0.65g – 2.5mM) was dissolved in 24 ml of a 0.31M aqueous ammonium sulfide solution, prepared from $(NH_4)_2S$ 20% wt. in H_2O (Sigma Aldrich), (8ml, 2.5mM). To ensure reproducibility of the prepared solutions, complete initial depolymerisation of the species in the solution was achieved by aging the solution during 4 hours. Subsequent polycondensation of the species was performed by pH adjustment of pH from pH 12.0 to 9.0 by addition of 4.5-5.0 ml of HCl (0.5M) and then the solution was extended to 250 ml (Mo = 0.1 M) with distilled H_2O. After 2h aging at 25°C, the solution was further diluted to 250ml with distilled H_2O. A molar ratio of S^{2-} to Mo was S/Mo = 5 and the Mo concentration is Mo = 0.01M. After aging for 1h, the solid precipitate was removed by ultracentrifugation at 15.300 rpm/10 min and the molecular Mo thio complexes were collected in the supernatant. The solutions were aged 24h at 25°C before being used. **Figure II - 4** shows the final aqueous dispersions of Mo thio, oxo-thio complexes with different pHs.

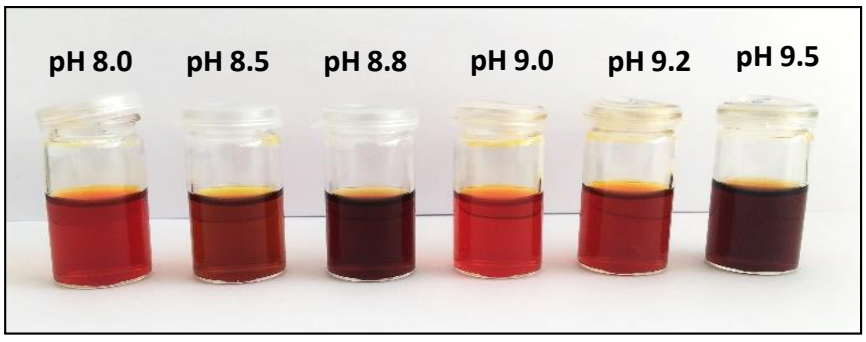

Figure II - 4: *Aqueous dispersions of Mo thio, oxo-thio complexes 0.01M with pH range 8.0 < pH < 9.5 from the left to the right, S/Mo = 5.*

II.1.3.2 $(Mo_2S_{12})^{2-}$ DMF solution preparation

$(Mo_2S_{12})^{2-}$ DMF ink was prepared by a method previously reported in the literature. Briefly, a red solution of ammonium polysulfide was first prepared by adding 7.1g of sulfur powder to 30 ml of ammonium sulfide at 50°C. To this solution, 30 ml of an aqueous solution containing 2g of ammonium molybdate tetrahydrate $(NH_4)_6Mo_7O_{24}$. 4 H_2O and 1.5g of hydroxylamine hydrochloride (NH_2OH HCl) was added and it was stirred for 2h at 50°C. Then, the solution was centrifuged at 4.500 rpm/10 min and the supernatant was stirred at 90°C for another 4 hours. The solution was cooled down to room temperature, filtered again and mixed with 20ml of ammonium polysulfide and allowed to stand overnight in argon atmosphere. The black crystals formed in solution were collected and washed as previously described. These black crystals were dissolved in DMF to form a DMF ink at the required concentration (0.01M).

II.1.3.3 Mo thio, oxo-thio complexes catalyst deposition

Co-catalyst deposition by drop casting

The Mo thio complexes or $(Mo_2S_{12})^{2-}$ co-catalyst was deposited on FTO or FTO/WSe_2 electrodes by drop casting from the solutions prepared at 0.01M Mo, aged 24h at 25°C, with pH range of 8.0 < pH < 9.5 as previously described. After drying evaporation at room temperature, the electrodes were heat treated at 110°C/10min in Air, before photoelectrochemical evaluation. **Figure II - 5** shows Mo thio, oxo-thio films dispersions of different pHs drop-casted onto FTO substrate.

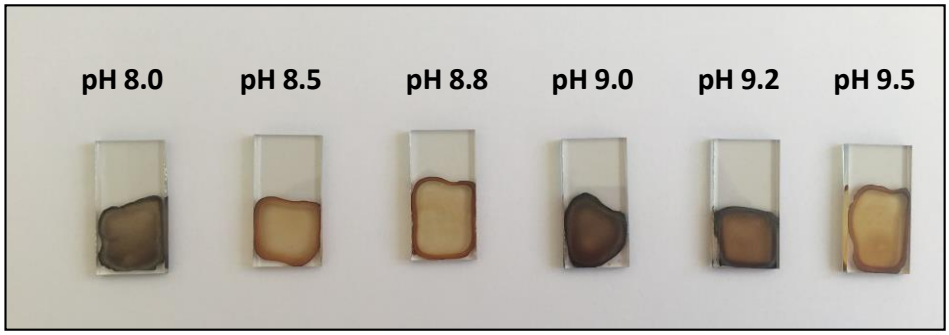

Figure II - 5: *Mo thio oxo-thio films with different pH deposited on FTO substrate and dried at 110°C, 10 min in Air.*

Co-catalyst deposition by selective dip coating impregnation

The selective dip coating of the co-catalyst was performed by vertically immersing the WSe_2-FTO electrode into the Mo thio complexe solution. The electrode was in contact with the

co-catalyst solution for 2 x 16h (sometimes additional 6 hours) under gentle stirring (≈100 rpm) at room temperature. Then, the electrode was washed/rinsed by dropping the electrode into distilled water without stirring for 5 minutes. This rising time was optimized to ensure removal of the less interactive species before the following impregnation. After the rinsing stage, the electrode was dried with compressed air at room temperature and heat treated at 110°C/10 min under Air. Afterwards, the WSe_2 electrode + co-catalyst was evaluated electrochemically by Linear Scanning Voltammetry.

A typical impregnation sequence included the three following steps:

a. 16 h impregnation – 5 min washing – 10 min heat treatment at 110°C
b. 6 h impregnation – 5 min washing – 10 min heat treatment at 110°C
c. 6 h impregnation – 5 min washing – 10 min heat treatment at 110°C

II.1.3.4 Surface treatment with Hexyl-trichlorosilane (HTS) on WSe_2 electrodes

The procedure was applied according to a previous reported work [2]. WSe_2 electrodes were immersed in a solution of Hexyl-trichlorosilane (Sigma Aldrich, 97%) in Hexane (Sigma Aldrich, 95%). The solution was prepared with 5% wt. HTS (m = 128 mg) in 20 mL of Hexane. After 10 minutes of stirring, the electrodes were rinsed with absolute Ethanol and dried at 70°C in air.

II.1.3.5 Platinum-Cupper co-catalysts electrodeposition on WSe_2 electrodes

Inspired by a method described by McKone *et al.* [3], WSe_2 electrodes were immersed in a mixed solution containing 0.96 mM $H_2PtCl_4.6H_2O$ [5g/L] and 0.15 mM (m = 3.6 mg)/0.25 mM (m = 6 mg) $Cu(NO_3)_2$ in distilled H_2O (V_T = 100 mL). Applying chronocoulommetry, the electrodes were polarized under constant potential −0.3 V vs Ag/AgCl until 100 $mCcm^{-2}$ were deposited. The electrodes were then removed, thoroughly rinsed and dried with compressed air. Then, the WSe_2 electrodes are evaluated using both electrochemical and photoelectrochemical characterization techniques.

II.2 Material Characterizations

II.2.1 Characterizations of Solids

II.2.1.1 Brunauer-Emmett-Teller (BET) surface area analysis

The surface area and pore size distribution of the TMDCs were measured by nitrogen adsorption/desorption isotherms using a Micrometrics ASAP 2000 system at 77K. Prior each analysis, samples were degassed at 473K under vacuum for 8 hours. The surface area (in $m^2.g^{-1}$) was calculated using the Brunauer-Emmett-Teller equation (Equation $(II-1)$, for relative pressure in the range 0.05-0.30. The Pore Size Distributions (PSD) were calculated using Barret-Joyner-Halenda (BHJ) model.

$$\frac{1}{V_a\left[\frac{P_0}{P}-1\right]}=\frac{c-1}{V_m c}\left(\frac{P}{P_0}\right)+\frac{1}{V_m c} \qquad (II-1)$$

Where, V_a is the total volume of adsorbed gas (in m^3); $\frac{P}{P_0}$ is the relative pressure with P_0 as the saturation pressure of the gas – the adsorbate –, and P the actual equilibrium pressure (both in bar, c is the BET constant ($c=\exp(\frac{E_1-E_L}{kT})$, with E_1 and E_L respectively the heat of adsorption of the first adsorbate layer and the heat of liquefaction) and V_m is the monolayer volume of adsorbed gas (in m^3).

From the BET equation, V_m is obtained and the specific surface area (S_{sp}) is calculated according to Equation $II-2$.

$$S_{sp}=\frac{V_m\cdot N_A\cdot s}{V\cdot m} \qquad (II-2)$$

Where, V_m is the monolayer volume, V is the molar volume of nitrogen, s is the nitrogen section, m is the mass weight of the sample and N_A is the Avogadro number.

II.2.1.2 Microstructural Characterizations of thin films

X-Ray Diffraction (XRD)

The XRD acquisitions were performed at room temperature, provided by a BRUKER AXS D4 ENDEAVOR diffractometer operating in the Bragg-Brentano geometry with a Bruker LynxEye position sensitive detector. The radiation source was an anticathode of copper (λK_{α} =

1.5405 Å and λ $K_{\alpha 2}$ = 1.5443 Å). The acquisition conditions of the diffractograms were collected from: 2θ = 0° to 100° at a scanning rate of 0.69° per minute with a step size of 0.01°. The irradiated zone of the sample was 20 mm.

X-Ray Diffraction (XRD) measurements were performed mainly for phase identification of crystalline structures. In this work XRD diffraction was also used get crystallographic information of TMDC nanosheets after solvent exfoliation and to calculate the size of the crystallites from the Scherer and Williamson Hall models [4].

Scanning Electron Microscope (SEM)

Cross-sectioned and topography images of nanoflakes films were obtained by a JEOL 6500 and a JEOL 6400 instruments with accelerate voltages ranging from 20 to 30 kV. Images were recorded using Secondary Electron detector.

Energy-dispersive X-ray analysis (EDX)

The analyzed surfaces by EDX, using a JEOL 6500 and a JEOL 6400 instruments, were around 120 µm x 100 µm. The acceleration voltage of the electrons was 20-30 kV. Under this voltage, the penetration depth of the beam (interaction pear) is around 1 µm. The counting time of the X-ray signals were between 60 and 120 seconds. The chemical analyzes present are in the average of 3 measurements made randomly on the samples.

Focused Ion Beam Scanning Electron Microscope (SEM – FIB)

The observations of the films morphology were also performed using a Focused Ion Beam (FIB) coupled to the FEI Model HELIOS 600i MEB. The sample cutting was performed using a gallium ion beam after platinum deposition to protect the surface. To facilitate the displacement of the cut slice, at the half of the cut, samples were welded with platinum to the microscopy grid which was molybdenum. Once placed on the grid, a carbon deposit was made to make the sample conductive.

Transmission Electron Microscope (TEM)

Transmission Electron Microscopy (TEM) images were obtained in collaboration with Dr. Antoine Barnabé (CIRIMAT, MicroCharacterization Center Raimond Castaing, Toulouse)

on a JEOL 2100F field emission gun electron microscope operating at 100-200 kV equipped with a side entry single tilt specimen holder.

II.2.1.3 Surface Characterizations of thin films

X-Ray Photoelectron Spectroscopy (XPS)

TMDC thin films were analyzed before and after electrochemical evaluation to gain further insights about the surface composition and oxidation state of the films. The analysis was realized XPS analysis were performed in collaboration with Mr. Jérôme Esvan (CIRIMAT, Toulouse), using a Thermo Scientific K-Alpha system with monochromatic Al Kα (hv = 1486.6 eV). All the XPS spectra were calibrated with C 1s at 284.6 eV (± 0.1 eV).

Raman Spectroscopy

In this study, Raman analysis were performed to provide structural and electronic information and to identify functional groups and chemical modifications on our photoelectrodes after deposition of Mo thio, oxo-thio complexes. The Raman spectrums given in this work were achieved in collaboration with Dr. Pascal Puech, from CEMES – Toulouse. The micro-Raman measurements of samples were performed using a Horiba Jobin Yvon XPlora equipped with an Olympus microscope. A 50x objective and low laser power (0.01 P0, P0 = 40mW at 785 nm) have been used to avoid any thermal effects due to laser heating. The focused spot diameter on the samples was ~1µm leading to an excitation power of 0.5mW/µm² with the reported spectra.

Photoluminescence (PL)

Continuous wave PL was performed on bare WSe_2 photoelectrodes and on WSe_2 films after Mo thio, oxo-thio complexes deposition. The analysis was achieved in collaboration with Dr. Andrea Balocchi from the Laboratory of Physics and Chemistry of Nano-objects (LPCNO, Toulouse).

The samples were mounted on an AttoCube atto 700 cryostat and excited with a He-Ne laser (excitation 632.8nm) with 1.2 pulse duration and 80 MHz repetition frequency with wavelength (λ) = 760 nm and various average power between 25-500 µW. The laser light was focused on the sample using a high numerical aperture lens (NA = 0.55) to a ~ 2 µm spot-size. The PL signal, collected from the sample in backscattering mode, was dispersed by an imaging monochromator and the spectrum recorded using a liquid nitrogen-cooled silicon charge

coupled device (CCD camera). After irradiation the Photoluminescence intensity originates from the electronic relaxation gives insight regarding the relative rates of radiative and non-radiative recombination, giving information regarding the defect content of the samples under analysis.

II.2.1.4 Optical and Electrical Characterizations

Absorption Spectroscopy

Transmission and optical reflection of thin films, deposited on glass substrate by drop cast, were measured with a BENTHAM PVE300 UV-visible spectrometer to obtain the absorption spectra. The measurements were made between 300 and 1100 nm. The device is equipped with a dual source Xe/QH (Hydrogen Quartz), TMc 300 triple network monochromator and an integrating sphere for total or diffuse measurements of transmission and reflection. **Figure II - 6** illustrates the incident light on a material surface that can be reflected, transmitted, or absorbed.

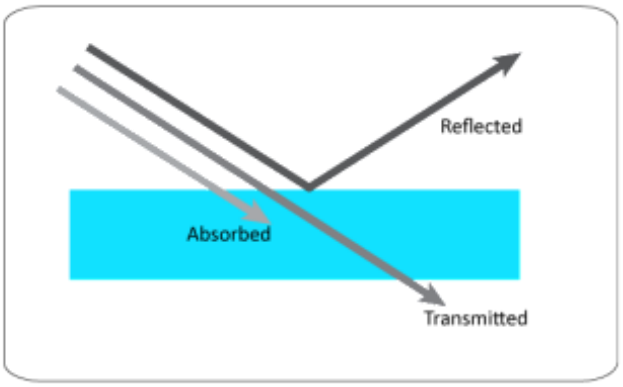

Figure II - 6: *The light that encounters a material can be reflected, transmitted, or absorbed [5].*

The absorbance of the TMDC films was calculated using the Kirchhoff's law which dictates that the power continuity expression is:

$$A(\nu) = 1 - [T(\nu) + R(\nu)] \qquad (II - 3)$$

Where ν is the wave frequency (Hz); A, the absorptance; T, the transmittance; and R, the reflectance. Absorbance of the different tested materials were calculated from the measured Transmittances and Reflectance after removing the contribution of the glass substrate. This equation gives the absorption, which is the part of the irradiance that is not reflected or transmitted.

For layered materials as the TMDCs, absorption resonances can vary in function of the number of layers (N) in a broader energy range, which reflects the changes in the strength of excitonic binding and the character of excitonic states, from 1 monolayer to bulk [6]. This means that the magnitude of absorptance tends to differ within the number of layers. Thus, the absorbance of thin TMDC films is as a function of the thickness above their ground exciton energy, which is approximated with the differential transmission [7].

Thus, the absorbance spectra of the TMDC films could be attributed using the Beer-Lambert Law:

$$A = -log_{10}(I/I_0) \qquad (II-4)$$

Or still, the Beer-Lambert Law gives the linear relationship between absorbance and the concertation of the absorbing species with an apparent thickness [8]:

$$I = I_0\, e^{-\alpha x} \qquad (II-5)$$

Where, α is the absorption coefficient, I_o is the intensity of the incident beam, I is the intensity of the light after a distance x in the sample, and x is the sample thickness.

The above calculations are dependent on the incident photon energy and thickness of the material [8]. Thus, the indirect/direct band gap transitions could be assigned from the resulted absorbance spectra, obtained by calculating the absorption coefficient using the equations $II-4$) and $II-5$. **Figure II - 7** presents the absorbance spectra obtained from the absorption coefficient.

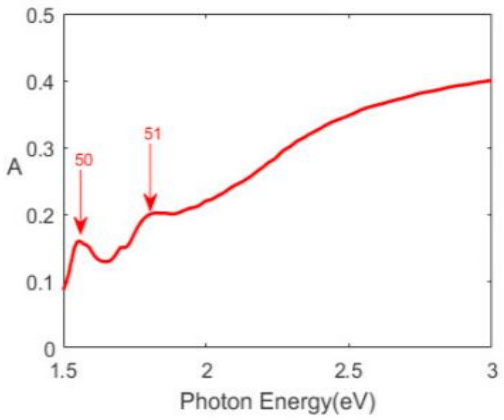

Figure II - 7: *Absorbance spectra of atomically thin layer as a function of the photon energy [8].*

For the catalyst thin film, the band gap energy was determined according to the Tauc law, whereas the absorption coefficient, α, due to an interband transition is near the band-gap [9]. It is described as:

$$(\alpha h\nu)^{1/r} = A(\nu)\left(h\nu - E_g\right) \qquad (II-6)$$

$$\alpha h\nu^{1/r} = A\left(h\nu - E_g\right) \qquad (\text{II}-7)$$

Where, $h\nu$ is the photon energy at a specific frequency (ν), E_g is the optical band gap (in eV). The value of the exponent r denotes the nature of the transition: r = 1/2 for direct transitions and r = 2 for indirect transitions.

Tauc plot shows the quantity $h\nu$ (the energy of the light) on the abscissa and the quantity $(\alpha h\nu)^{1/r}$ on the ordinate, where α is the absorption coefficient of the material. E_g was determined from the linear extrapolation to zero. **Figure II - 8** presents the Tauc plots for direct and indirect bandgap.

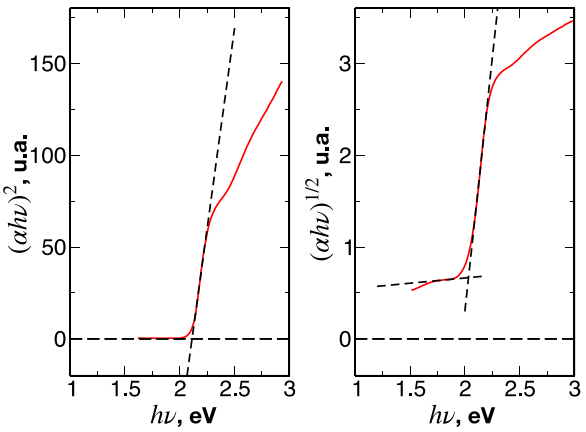

Figure II - 8: *Tauc plots for (a) direct and (b) indirect bandgaps. Figures are adapted from [10].*

D.4.2.2 Electrical Conductivity measurements

In plane resistivity – also known as sheet resistance – measurements were perfomed using a four-points set-up. This method is commonly used in the characterization of ultra thin films (few tens of nanometers) [11]. The probes that monitor the current and the voltage were point contacts, usually mounted on a special bracket with the probe tips arranged in line at an equivalent distance from each other. At the outer ends a dc current source was connected to apply a constant current (i) between these ends. At the inner ends was connected a voltmeter (10 MΩ of internal resistance) that monitored the voltage drop (V) between them [12]. Such

configuration allows nulling any series resistances. **Figure II - 9** illustrates in-plane conductivity measurements using a four-point set-up.

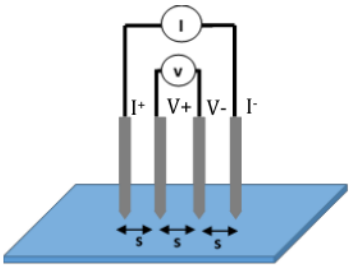

Figure II - 9: *Schema of the in plane electrical conductivity measurement using the four point probe technique [13].*

The Resistance of the active layer (R_L, in Ω) becomes:

$$R_L = \frac{R_M}{1 - R_M / R_V} \qquad (II - 8)$$

Where R_M the measured resistance (in Ω) is calculated from the division of the voltage drop by the applied current; R_V is the internal resistance of the used voltmeter.

Since the four-point measuring device consisting of a KEITHLEY 237 generator/meter was exhibiting an internal resistance of 10 MΩ (R_V), R_L was considered to be equal to R_M. Thus, the sheet resistance, R_S, (in Ω/□) can be calculated from R_L using Equation $II - 9$:

$$R_S = R_L \cdot C \qquad (II - 9)$$

Where, R_L is the measured resistance of the layer and C is the correction factor. Being the distance between the contact points (s) equidistant and the sample thickness negligible, a value of 4,532 is considered as the correction factor, given as coefficient K – typical in 2D geometry [14].

In our case, the distance between the points is 1.6 mm and the dimension of samples is 20x20 mm². The measurements were performed on 2D WSe_2, free-rGO WSe_2 3D and 3D WSe_2-rGO films drop casted on a glass substrate. After heat treatment at 350°C/2h in N_2 atmosphere, the films, with thickness of ≈ 2µm were submitted to resistivity measurements.

If the sample thickness is known, the resistivity can be calculated from Equation $II - 8$:

$$\rho_L = R_S \cdot e \qquad (II - 10)$$

Where e is the thickness (in cm); and ρ_L is the resistivity of the layer (in Ω.cm).

II.2.2 Characterizations of Solutions

II.2.2.1 Electrospray Ionization Mass Spectrometry (ESI-MS)

Mass spectrometry is an analytical technique that can provide both qualitative (structure) and quantitative (molecular mass or concentration) information on analytic molecules after their conversion to ions. The molecules of interest are first introduced into the ionization source of the mass spectrometer, where they are first ionized to acquire positive or negative charges. The ions then travel through the mass analyzer and arrive at different parts of the detector according to their mass/charge (m/z) ratio. After the ions make contact with the detector, useable signals are generated and recorded by a computer system. The computer displays the signals graphically as a mass spectrum showing the relative abundance of the signals according to their m/z ratio [15]. In this work, species formed on each solution of aqueous Mo thio and oxo thio complexes were identified by ESI-MS.

The analysis of electrospray ionization mass spectrometry was performed in collaboration with Valerie Bourdon from Toulouse Institute of Chemistry (ICT). The analysis data were collected using a XEVO G2 Q TOF MS instrument equipped with an electrospray (ESI) source supplied by Waters. The detector is an electron multiplier and all the data were processed using the Masslynx 4.1 software. For the analysis, 2 µL of the sample was introduced into the MS using flow injection analysis. Nitrogen was employed as the drying and nebulizing gas at a temperature of approx. + 350°C. The cone voltage was set at low value of 20 V order to minimize fragmentation. All the MS data were collected in negative ion mode on the as-synthesized solutions (0.01 Mo) after dilution 20x. The spectrometer was calibrated to give a precision of 3.0 ppm in the region of 100-2000 m/z.

II.2.2.2 Nuclear Magnetic Resonance (NMR) Spectroscopy

NMR experiments were performed in collaboration with Mr. Pierre Lavedan (ICT, Toulouse). The analysis was carried out using an AVANCE III HD BRUKER NMR liquid spectrometer operating at 500.13 MHz for 1H and equipped with a 5mm BBFO ATMA Prodigy cryoprobe. This cryoprobe delivers a sensitivity enhancement over room temperature probes of a factor of 2 to 3 for X-nuclei from 15N to 31P. NMR experiments were recorded at 298K using the zgig30 pulse sequence. The recycle delay was adjusted to 2s. Experimental time was between 2 and 18 hours for the acquisition of ^{119}Sn spectrum. Topspin 3.2 software was used to acquire and process all NMR experiments.

II.3 Electrochemical Characterizations

II.3.1 Photoelectrochemical (PEC) Measurements

All the photoelectrodes were tested in a three-electrode set-up in a Gamry Interface 1010E potentiostat, with a Pt wire counter electrode and an Ag/AgCl 1M KCl (sat) reference electrode. The electrolytes used were 0.5M H_2SO_4 solution (pH 0), 0.1M Na_2SO_4 solution (pH 6.7) and 0.2M Na_2SO_4 coupled with 100mM of Potassium Ferri/Ferro cyanide ($Fe^{2+/3+}$), all in distilled water.

Two different electrochemical cells were used in this work: a typical electrochemical glass cell (**Figure II - 10a**) and a specially tailored cell for PEC measurements from Zähner – elektrik (**Figure II - 10b**). The intermittent illumination for photoelectrochemical analysis was provided by a LCS – 100 Oriel 100W power Xe lamp with integrated reflector, AM 1.5 operation at 1 sun output (**Figure II - 10c**).

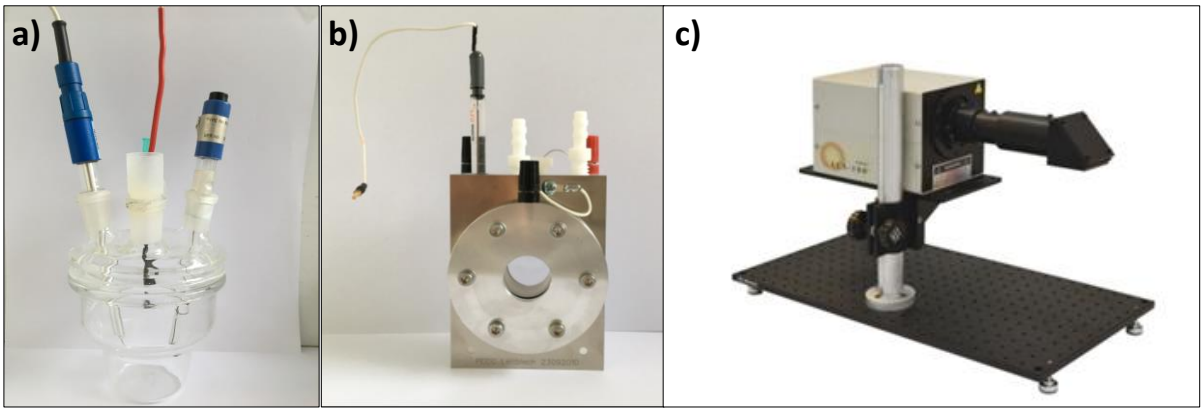

Figure II - 10: *(a) and (b) photoelectrochemical cells in three-electrode configurations used for PEC and hydrogen measurements, (c) visible-light simulator.*

II.3.2 Linear Sweep Voltammetry

Linear Sweep Voltammetry (LSV) under light illumination analysis provided the photocurrent measurement of the photoelectrodes, consisting of a single unidirectional voltage sweep to examine the photoelectrochemical (PEC) performance of the films deposited on the conductive substrates.

In a typical LSV acquisition, the voltage applied to the working electrode was swept cathodically from 0.2 to - 0.6V versus Ag/AgCl, scan rate of 10mV.s^{-1}, either in 0.5M H_2SO_4 or 0.1M Na_2SO_4 electrolytes. The intermittent illumination was 5 seconds light on and 4 seconds light off, provided by the Xe Arc Lamp sunlight simulator.

II.3.3 Chronoamperometry

Stability measurements were conducted by applying a constant voltage to the working electrode and recording the evolution of the photocurrent over time. To our electrodes of 2D WSe_2 a voltage of -0.4V versus Ag/AgCl (-0.2V versus NHE) was applied during 300 seconds under intermittent illumination (5 sec on, 4 sec off), in 0.5M H_2SO_4 electrolyte.

II.3.4 Electrochemical Impedance Spectroscopy (EIS)

Electrochemical Impedance Spectroscopy is a stationary technique where a sinusoidal signal of either current or voltage of a small amplitude is applied to the system, within a wide frequency range from megahertz to millihertz. The system being measured must be at a steady state throughout the time required to measure the EIS spectrum. Electrochemical impedance is normally measured using a small excitation signal. This operational method allows a linearization of the ratio between the current and the tension [16].

According to Euler's formula, when a voltage V_0 is applied to the system with a sinusoidal variation ΔV of low amplitude, we obtain:

$$V(\omega) = \delta V e^{j\omega t} \qquad (II-11)$$

And the resulting current:

$$I(\omega) = \delta I e^{j\omega t+\phi} \qquad (II-12)$$

So, come the impedance expressed as a complex function, which is:

$$Z(\omega) = \frac{V(\omega)}{I(\omega)} = \frac{\delta V}{\delta I} e^{-j\phi} \qquad (II-13)$$

Where, ω is the angular frequency (in rad.s^{-1}); $V(\omega)$ is the voltage applied in sinusoidal signal (in V) and $I(\omega)$ is the measured current (in A), ϕ is the phase angle (in rad)

EIS data are commonly analyzed by fitting to an equivalent electrical circuit model. The electrical circuit model used in this study was the simplified Randles cell, where the diffusion is neglected. It includes a solution resistance (R_U), a double layer capacitance (C_{dl}) and a charge transfer (or polarization) resistance (R_P). The double-layer capacitance is in parallel with the charge-transfer resistance (**Figure II - 11**).

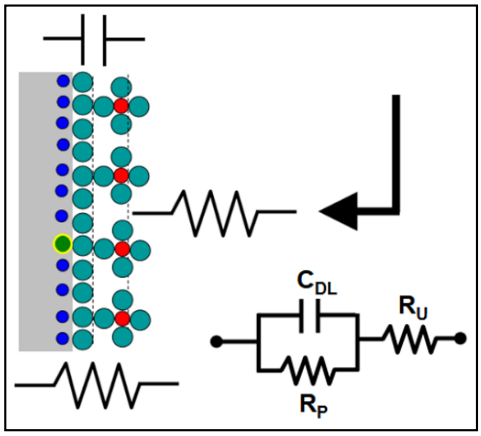

Figure II - 11: *Simplified Randles Cell Schematic Diagram. Source: Gamry Electrochemistry.*

The impedance of a resistor is independent of frequency and has no imaginary component.

$$Z = R \qquad (\mathrm{II} - 14)$$

The capacitor's impedance decreases as the frequency is raised. Capacitors also have only an imaginary impedance component.

$$Z = \frac{1}{jC\omega} \qquad (\mathrm{II} - 15)$$

One of the most usual way to present impedance data is the Nyquist Plot, presenting the imaginary part as function of the real part. The Nyquist Plot for a Simplified Randles cell is always a semicircle representing the composition of the real and the imaginary part of Z (ω). In this plot, each point is the impedance at one frequency: the low frequency data is on the right side of the plot and higher frequencies are on the left, as represented in **Figure II - 12**. The real axis value at the other (low frequency) intercept is the sum of the polarization resistance and the solution resistance. The diameter of the semicircle is therefore equal to the polarization resistance.

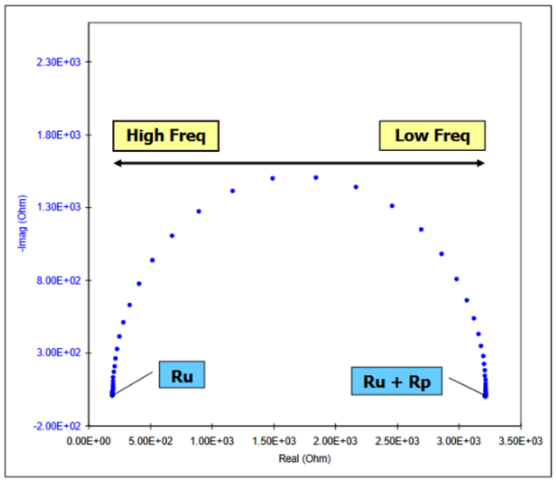

Figure II - 12: *Nyquist Plot for a typical Simplified Randles cell. Source: Gamry Electrochemistry.*

The electrochemical impedance measurements on TMDC films deposited on FTOwere carried out in the dark in a typical 3-electrode configuration, with Pt foil and Ag wire collated by Ag/AgCl (KCl, sat) as the counter electrode and the reference electrode, respectively. The WSe_2 layers were measured in 0.1 M Na_2SO_4 and 0.5M H_2SO_4 aqueous electrolyte between 0V and 0.4V vs Ag/AgCl.The frequencies were varied from 100 kHz to 100 mHz for each potential. The amplitude of the AC signal was 10mV. According to an established procedure. Measurements in presence of light were provided by a light-emitting diode with wavelengthof 450 nm, 1300 W m^{-2} power.

II.3.5 Mott-Schottky model

The Mott-Schottky model is traditionally used to measure the flat band potential of a semiconductor material, to identify the nature of the charge carriers and to determine the charge carrier densities of semiconductors in contact with the electrolyte. It is a complementary tool to further understand the mechanisms of specific faradaic reactions, the electrode reactivity and the changes in its conductivity. By varying the potential at the electrode-electrolyte interface, the space-charge capacitance within the semiconductor is measured. As consequence, the location of the energy levels in the electrode-electrolyte junction, the flat band potential E_{FB}, the conduction band edge E_c and the valence band edge E_v can be studied.

The variation of the capacitive response ($1/C^2$) with potential is how the Mott-Schottky plot is presented. Higher values of C^{-2} are recorded for a sample when the potential changes in the cathodic and anodic ranges. In specific potential ranges, the C^{-2} vs. E follows a straight line,

with either a negative slope indicating a p-type semiconductor behavior or a positive slope indicating a n-type semiconductor behavior.

According to the semiconductor theory, the capacitance of the space-charge region of a p-type semiconductor is given by:

$$\frac{1}{C^2} = \frac{2}{\epsilon_{SC}\epsilon_0 e A^2 N_a}\left(E - E_{fb} - \frac{kt}{e}\right) \qquad (II-16)$$

Where ε is the dielectric constant, ε_0 refers to vacuum permittivity, e is the charge of the electron, N_a is the acceptor concentration E is the applied potential and E_{fb} is the flat band potential. By means of this equation, the flat band potential of the material can be determined by evaluating the interception of the linear region with the axis representing the applied potential. In addition, the doping agent concentration Na can be worked out of the slope of that linear relation [17].

The Mott-Schottky model was used in this work to measure the flat band potential, to identify the semiconducting behavior and to calculate the charge carrier density of WSe_2, WS_2 and Mo-S catalysts.

As mentioned before, TMDC films were prepared by drop cast deposition of as-exfoliated nanosheets on FTO substrate, followed by a heat treatment at 350°C under N_2 atmosphere during 2h. EIS of the as-prepared films was done in a three-electrode cell configuration, using a Pt wire as counter-electrode and standard Ag/AgCl in 1M KCl as reference electrode, in 0.1M Na_2SO_4 electrolyte. EIS spectra was obtained with a Metrohm Autolab PGSTAT-204 potentiostat. The range of potential used was between 0 and +0.6 V vs Ag/AgCl, the frequency range was from 100 kHz to 100 mHz and the AC voltage amplitude 10 mV.

Catalyst thin films were obtained by drop cast of Mo_xS_y solution onto FTO substrate and heat treat at 110°C under air. EIS measurements were also carried out in a 3-electrode cell configuration. The potential range used of the as-prepared films was between -0.25 and +0.25V vs Ag/AgCl, in the same frequency range and AC amplitude as the TMDC films. The capacitance of the samples was obtained by fitting the simple RC series circuit to the measured impedance spectra. The Mott-Schottky plots were constructed by extracting a value of C from a defined frequency (1 Hz) for each applied potential.

II.3.6 Intensity Modulated Photocurrent Spectroscopy (IMPS)

This technique is utilized to understand the surface carrier dynamics at the semiconductor/electrolyte interface. IMPS is a form of impedance spectroscopy that measures the phase shift in photocurrent in relation to a sinusoidal modulation of the light source [18].

The light with a base intensity I_{DC} is focused on a surface. Upon the constant base intensity, a sinusoidal waveform with amplitude I_0 is superimposed. The frequency f of the sine wave is changed during the experiment (**Figure II - 13**). The potential is kept constant and the generated photocurrent is demodulated [19].

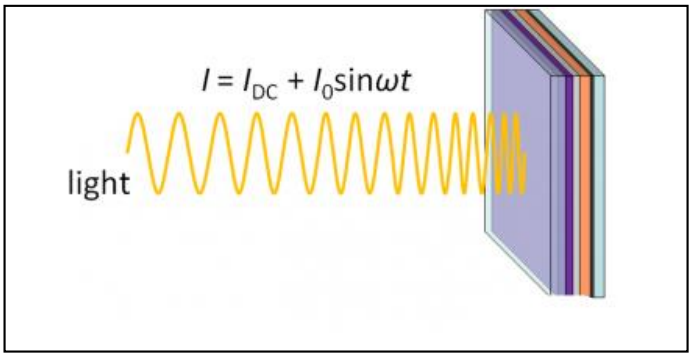

Figure II - 13: *Sketch of the light signal focused on a surface during IMPS [19].*

IMPS measurements were carried out in aqueous solution of 0.5M H_2SO_4. Bias range of 0 to -0.45 V vs Ag/AgCl was applied to electrodes of bares 2DWSe$_2$, 3D rGO-WSe$_2$ and to electrodes of 2D WSe$_2$, 3D rGO-WSe$_2$ with Mo_xS_y catalyst. The electrochemical cell configuration used was the same as in another electrochemical analysis. It was performed with modulated illumination provided by a light-emitting diode with wavelength of 760 nm (H2A1 Series LED), from Roithner Laser Technik. The base intensity of the light source was varied between 20 to 400 mW. The AC amplitude was set to 40 % of the applied base intensity. Frequency modulation was applied between 20 kHz to 100 mHz.

The system utilized had two potentiostats (Gamry Interface 1010E), where one drove the LED while the second potentiostat was used to characterize the cell. Data acquisition between the two potentiostats was synced so that phase information between the driving potentiostat and the acquiring potentiostat is obtained.

The total measure current corresponds to both minor and major charge carrier flow and the demodulated photocurrent response consists of the minority carrier current flow. An in-phase and out-of-phase components are obtained and result in a real and imaginary part of the

photocurrent, which can be plotted in a Nyquist plot. At low frequencies, this gives a semicircle that is located in the upper (for a photoanode) quadrant of the complex plane, see **Figure II - 14**.

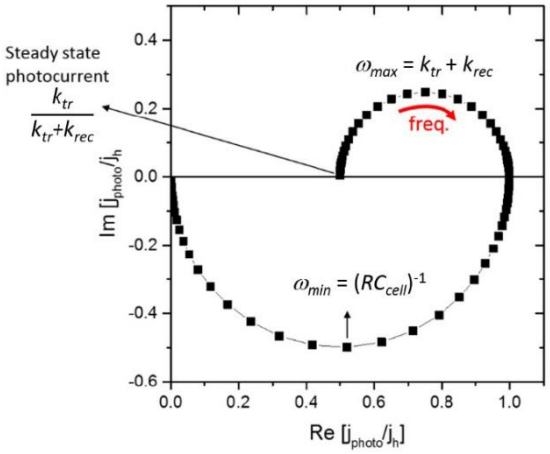

Figure II - 14: *A calculated example of complex photocurrent or IMPS spectrum for a photoanode, illustrating the recombination (upper quadrant) and attenuation (lower quadrant) semicircles [20].*

This part is called the "recombination semicircle" because the shape of the semicircle is largely dominated by surface recombination. The rate constants at the apex of the semicircle, where the maximum phase shift is measured, reports on the combination of charge transfer and recombination rate constants:

$$\omega_{max} = k_{tr} + k_{rec} \qquad (\text{II} - 17)$$

Where, k_{tr} and k_{rec} are first order the charge transfer and recombination rate constants (in s^{-1}), respectively. The high and low frequency intercepts of the x-axis (imaginary current = 0) are linked to the initial maximum (spike) and the steady state photocurrents obtained in a photocurrent transient plot, respectively [20].

At the low frequency intercept, it reports on the steady-state photocurrent, which measures the rate at which the charges are effectively transferred to the solution. The ratio of the photocurrents between the low-frequency intercept and the high-frequency one provides the charge transfer efficiency:

$$\eta_{CT} = \frac{k_{tr}}{(k_{tr} + k_{rec})} \qquad (\text{II} - 18)$$

Using Equations (II - 15) and (II – 16), the charge transfer rate constant, k_{tr}, and the surface recombination rate constant, k_{rec}, were calculated from the IMPS spectra.

II.3.7 Incident Photon-to-electron Conversion Efficiency (IPCE) – External Quantum Efficiency

The Incident Photon-to-Current Efficiency (IPCE) is one of the most important diagnostic figures of merit for PEC devices; it describes the photocurrent collected per incident photon flux as a function of illumination wavelength. In a PEC system, IPCE is usually obtained from a chronoamperometry measurement [21]. In this system, a constant potential is applied between the sample/working electrode versus a reference electrode (3-electrode experiment) while measuring the current that arises from subjecting the PEC electrode to monochromatic light at various wavelengths. The IPCE corresponds to the ratio of this photocurrent (converted to an electron rate) versus the rate of incident photons (converted from the calibrated power of a light source) – Equation $II-19$ [21]. Calibrated monochromatic light (alone, or superimposed over a background illumination level in the case of a white light bias experiment) should be used for this experiment to give IPCE as a function of wavelength k (nm).

$$IPCE(\lambda) = EQE\ (\lambda) = \frac{number\ of\ reacted\ electrons}{number\ of\ incident\ photons} = \frac{1240 \cdot j_{ph}}{P_{mono} \cdot \lambda} \qquad (II-19)$$

Where, 1240 is in $W.nm^{-1}.A^{-1}$ and comes from $\frac{(hc)}{e}$ where h is the Planck's constant; c, the light velocity and e the charge of an electron. P_{mono} is the calibrated and monochromatic illumination power intensity in $W\ m^{-2}$, and λ (nm) is the wavelength at which this illumination power is measured.

Incident-photon-to-current-efficiency (IPCE) was performed illuminating the photocathode using a set of high-power light emitting diodes (H2A1 Series LED) from Roithner Laser Technik. The spectrum emitted by the each of the LED is centered on a given wavelength with a half width at half maximum of 20 nm with optical power outputs ranging from 20 to 400 mW. The naturally diverging beam of the LED has been collimated to a ≈ 8 to 12 mm diameter beam, using special focusing optics designed for coupling the light of high-power LEDs into fiber bundles (Roithner part number 10034, (http://roithner-laser.com/datasheets/led_optics/10034.pdf). The distance between the LED considering the fiber bundles and the photocathode was ≈ 30 mm. **Figure II - 15** presents the set-up utilized to perform the IPCE measurements.

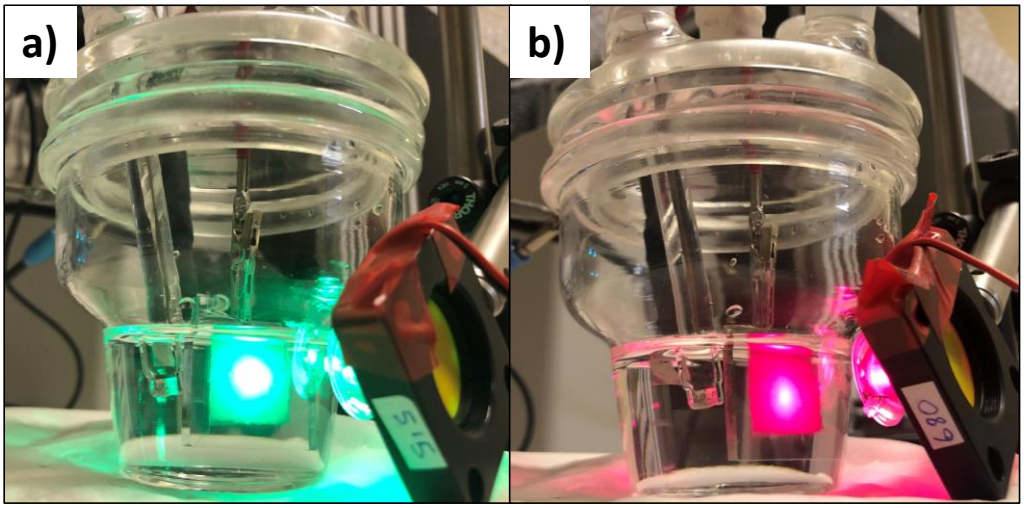

Figure II - 15: *Set-up of the IPCE measurements. LED is centered in front of the photocathode in the cell, where a diverging beam of ≈ 10mm is emitted towards the surface of the sample.*

The light intensity of each LED has been measured using a calibrated pyranometer Model PMA2144 Digital Class II Pyranometer from SOLAR LIGHT. The intensity sent onto each photocathode was adjusted for each LED in order to illuminate the photocathode with equivalent intensities of (0.1 (10mW/cm²), 0.5 (50 mw/cm²) and 1 sun (100mW/cm²) for each wavelength, taking into consideration the reflection on the cell facets. Typical LSV analysis were performed for the photocathode in the electrochemical cell of 3-electrode configuration, using Pt as counter-electrode and Ag/AgCl as reference electrode, in 0.5M H_2SO_4 aqueous electrolyte.

Considering the light intensity, the photocurrent obtained for each LED utilized and effects of reflectance of the material we calculated conversion-efficiencies for each wavelength using the Equation $II - 19$.

II.4 Hydrogen measurements

II.4.1 Gas Chromatography

This analysis allowed for real-time the composition of the gas produced inside the PEC cell. The working electrode was placed in a specifically designed PEC cell, acquired from Zähner – elektrik cell. The counter and reference electrodes, as well as the electrolyte, were the same as described in the PEC measurements section. A tube carrying Argon was connected into the cell, with its output positioned to purge the gas. A second pipe was used to connect the cell to a GC – 2014 Gas Chromatograph from Shimadzu (**Figure II - 16**).

Figure II - 16: *Photoelectrochemical cell – gas chromatograph set up for hydrogen measurements.*

The Chromatograph GC – 2014 has an injector type dual packed for the two flow paths handled (Argon and Hydrogen) with a Thermal Conductivity Detector (TCD). Presenting a capillary column of 500µl. First, the electrolyte and the space inside de cell were purged with Argon for 15 minutes, being this process monitored by GC analysis with a gas flow of 5 to 10 mg/min. Then cathodic currents of -0.25 to -2mA were set by chronopotentiometry under illumination, during 5 minutes. After, the composition of the output gas flow was analyzed by CG measurement.

II.5 Theoretical Methods

II.5.1 Density Functional Theory (DFT) Calculations

Density Functional Theory calculations was performed in collaboration with Dr. Iann Gerber and Dr. Romuald Poteau from the Laboratory of Physics and Chemistry of Nano-objects (LPCNO, Toulouse). In this work, DFT calculations were used to investigate the chemical interaction of the Mo thio, oxo-thio complexes films supported on the WSe_2 substrates obtaining adsorption energy values in case of interaction. DFT computational codes were performed to obtain values of Gibbs free energies of H adsorption on free-standing Mo-complexes. The results were published in our article.

BIBLIOGRAPHIC REFERENCES

[1] W. S. Hummers and R. E. Offeman, "Preparation of Graphitic Oxide," *J. Am. Chem. Soc.*, vol. 80, no. 6, p. 1339, 1958.

[2] X. Yu, N. Guijarro, M. Johnson, and K. Sivula, "Defect Mitigation of Solution-Processed 2D WSe2 Nanoflakes for Solar-to-Hydrogen Conversion," *Nano Lett.*, vol. 18, no. 1, pp. 215–222, 2018.

[3] J. R. McKone, A. P. Pieterick, H. B. Gray, and N. S. Lewis, "Hydrogen evolution from Pt/Ru-coated p-type WSe2 photocathodes," *J. Am. Chem. Soc.*, vol. 135, no. 1, pp. 223–231, 2013.

[4] A. Barnabé, "L ' enseignement de la cristallographie en sciences des matériaux," pp. 57–62, 2014.

[5] "The Absorption Coefficient: Definition & Calculation | Study.com." [Online]. Available: https://study.com/academy/lesson/the-absorption-coefficient-definition-calculation.html. [Accessed: 01-Mar-2020].

[6] A. Arora, M. Koperski, K. Nogajewski, J. Marcus, C. Faugeras, and M. Potemski, "Excitonic resonances in thin films of WSe2: from monolayer to bulk material," *Nanoscale*, vol. 7, no. 23, pp. 10421–10429, 2015.

[7] B. Zhu, X. Chen, and X. Cui, "Exciton binding energy of monolayer WS2," *Sci. Rep.*, vol. 5, p. 9218, 2015.

[8] W. Tang, S. S. Rassay, and N. M. Ravindra, "Electronic & optical properties of Transition-Metal Dichalcogenides," *Madridge J. Nanotechnol. Nanosci.*, vol. 2, no. 1, pp. 58–64, 2017.

[9] T. Academy, R. Academy, and S. S. Trakt, "Optical properties and electronic structure of amorphous Ge and Si," vol. I, pp. 1–21, 1968.

[10] E. Nurlaela, M. Harb, S. Del Gobbo, M. Vashishta, and K. Takanabe, "Combined experimental and theoretical assessments of the lattice dynamics and optoelectronics of TaON and Ta3N5," *J. Solid State Chem.*, vol. 229, pp. 219–227, 2015.

[11] H. Marom and M. Eizenberg, "The temperature dependence of resistivity in thin metal films," *J. Appl. Phys.*, vol. 96, no. 6, pp. 3319–3323, 2004.

[12] E. M. Girotto and I. A. Santos, "Medidas de resistividade elétrica DC em sólidos: Como efetuá-las corretamente," *Quim. Nova*, vol. 25, no. 4, pp. 639–647, 2002.

[13] S. B. Inthuga, "Etude de couches minces à base de delafossite CuCr 1-x Fe x O 2 (0 ≤ x ≤ 1) dopées au Mg déposées par pulvérisation cathodique radiofréquence en vue d ' optimiser leurs propriétés thermoélectriques," 2018.

[14] "CMi - Center of MicroNanoTechnology." [Online]. Available: https://cmi.epfl.ch/metrology/OmniMap_RS75.php. [Accessed: 07-Apr-2020].

[15] CS Ho et al., "Electrospray Ionisation Mass Spectrometry: Principles and Clinical Applications," Clin. Biochem. Rev., vol. 24, pp. 3–12, 2003.

[16] "Basics of EIS: Electrochemical Research-Impedance." [Online]. Available: https://www.gamry.com/application-notes/EIS/basics-of-electrochemical-impedance-spectroscopy/. [Accessed: 28-Oct-2019].

[17] A. Adán-Más, T. M. Silva, L. Guerlou-Demourgues, and M. F. Montemor, "Application of the Mott-Schottky model to select potentials for EIS studies on electrodes for electrochemical charge storage," *Electrochim. Acta*, vol. 289, pp. 47–55, 2018.

[18] J. E. Thorne, J. W. Jang, E. Y. Liu, and D. Wang, "Understanding the origin of photoelectrode performance enhancement by probing surface kinetics," *Chem. Sci.*, vol. 7, no. 5, pp. 3347–3354, 2016.

[19] "Dye Solar Cells - IMPS/IMVS Measurements." [Online]. Available: https://www.gamry.com/application-notes/physechem/dye-solar-cells-imps-imvs/. [Accessed: 10-Jan-2020].

[20] C. Zachäus, F. F. Abdi, L. M. Peter, and R. Van De Krol, "Photocurrent of $BiVO_4$ is limited by surface recombination, not surface catalysis," *Chem. Sci.*, vol. 8, no. 5, pp. 3712–3719, 2017.

[21] Z. Chen, H. N. Dinh, and E. Miller, *Photoelectrochemical water splitting: standards, experimental methods, and protocols*. 2013.

CHAPTER III

2D Tungsten Di-selenide (WSe_2) nanoflakes for Solar to Hydrogen Conversion

Introduction

Development of 2D materials for the solar water splitting has been gained attention due to its good optical and electronic properties and its potential to design high surface area microstructure. More specifically, 2D transition metal di-chalcogenides (TMDCs) can exhibit ultrathin thickness down to 0.7 nm, yielding high surface area. In addition to the band gap compatible for the visible-light absorption. Interested into the optoelectronic properties offered by these materials, we choose p-type WSe_2 to study as photocathode for the HER. In the first part of this chapter, we present the elaboration of exfoliated WSe_2 nanoflakes and important characterizations that contribute for the valorization of its properties as photocathode for the solar water reduction. Nevertheless, we also present how the PEC performances are limited by the high concentration of surface defects.

III.1 Elaboration of solvent-exfoliated p-WSe_2 nanosheets

Tungsten di-selenide (WSe_2) nanosheets were synthesized by exfoliation in Dichlorobenzene (DCB), as described in experimental section. Control of lateral size and thickness of the exfoliated nanosheets were achieved both by: adjusting time to approximately 8 hours of exfoliation in cold bath (4°C), the speed of centrifugation during the post selection stages (between 600 and 3000 rpm in 10 min) was adjusted. The as-exfoliated and selected nanosheets were collected by ultracentrifuge at 800 rpm during 10 minutes and transferred in DMF solvent. The WSe_2 nanosheets were transferred to DMF, because this solvent offers better stability and less toxicity than DCB. A final concentration of 8 g l^{-1} was obtained for the dispersion of WSe_2 nanosheets.

III.1.1 Fabrication of p-WSe_2 photoelectrodes

The as-exfoliated and selected WSe_2 nanosheets in DMF were deposited by multilayer drop casting onto FTO (F: SnO_2 coated glass) in 3-4 layers. Slow evaporation of the solvent was performed at room temperature to avoid the aggregation, improving the film homogeneity. The drop casted films were then calcined at 350°C during 2h in a N_2 furnace atmosphere. The average final weight of the WSe_2 electrodes is ≈ 1.5 mg for a surface of 1.0 cm^2.

III.2 Characterization of as-exfoliated WSe_2 films

III.2.1 Structure-properties of WSe_2 nanoflakes

The **Figure III - 1** shows a cross-section SEM image of exfoliated WSe_2 nanosheets selected at 800 rpm on FTO substrate. A homogeneous morphology of the film is observed in µm scale. The cross-sectional image indicates a film thickness of about 3 µm, with preferential orientation of the nanosheets parallel to the FTO substrate. From the SEM image, thickness of the individual nanoflakes can be estimated in the range of 50-200 nm and shows a film morphology corresponding to similar cross-section images presented in previous works in the literature [1].

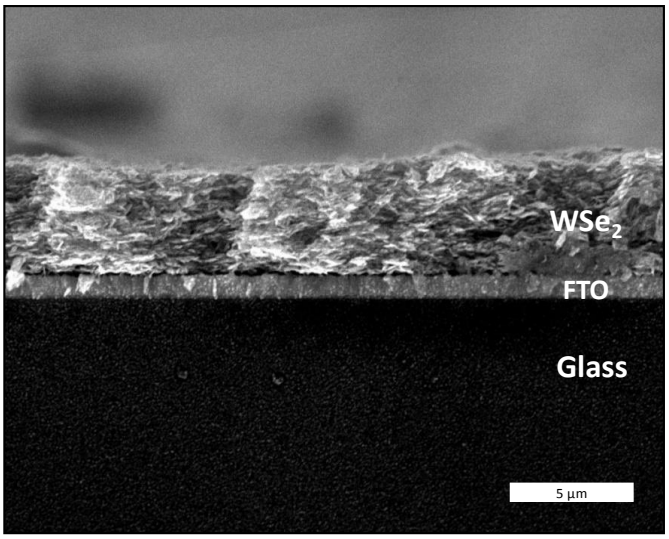

Figure III - 1: *SEM image of WSe_2 electrodes in cross-section morphology.*

X-Ray Diffractogram recorded from 2D WSe_2 samples is presented in **Figure III - 2.** All the diffraction peaks observed on the reference bulk material (see **Figure III - 2a**) can be assigned to hexagonal phase of WSe_2 structure with space group (P63mmc), JCPDS card No.38-1388 and unit cell parameters a = b = 0.3286 nm and c = 1.2983 nm. **Figure III - 2b** shows the exfoliated WSe_2 samples exhibiting intense (002) diffraction peak, while other peaks are absent or significantly weak**.** The high (002) diffraction peak, whose intensity is relatively weaker than from bulk, is observed for all exfoliated samples and is consistent with the well-ordered stacking structure of the nanoflakes showing high preferential orientation, as indicated on the cross-section SEM image (**Figure III - 1**). The absence of other peaks including peaks arising from the symmetry of the vertical crystal planes ((006) and (008)) confirms that the nanosheets have been exfoliated along the (002) axis. In addition, in the hexagonal system the (100) plane is vertical to

the (002) plane, which is the edge of the basal plane [2]. Thus, the decrease of the (100) plane diffraction intensity observed of the XRD pattern of the exfoliated samples indicates reduction of the stacked layers [3].

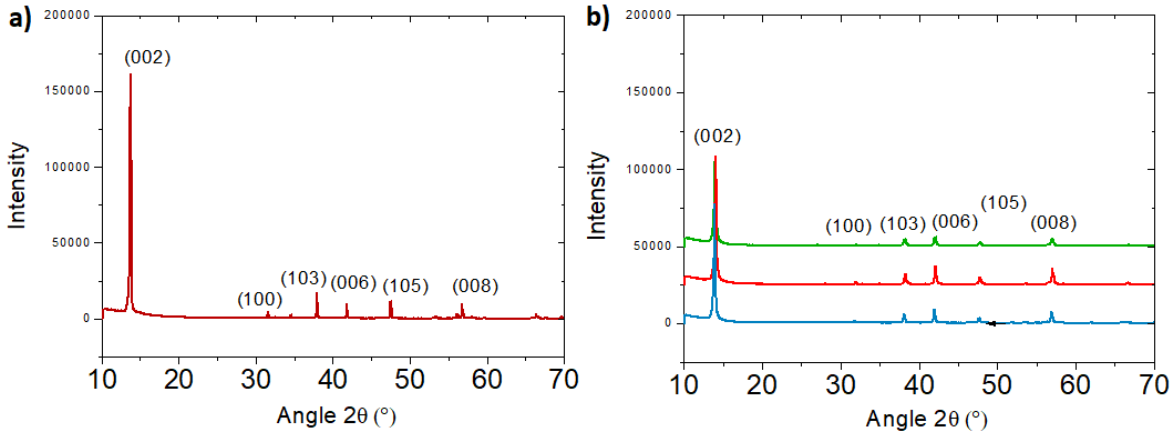

Figure III - 2: XRD patterns of WSe_2 (a) commercial powder and (b) nanosheets films on FTO substrate after heat treatment at 350°C in N_2.

For the commercial bulk powder, X-ray ordered domain sizes were calculated from full width at half maximum (FWHM) of the peaks (100) and (103) by the Debye and Scherrer relation. **Table III - 1** reports the XRD data used and the ordered size determined from the various diffraction peaks. The results revealed that the polycrystalline powder is composed of anisotropic crystallites displaying of large lateral size (> 150 nm).

Table III - 1: *XRD data of bulk WSe_2 used to calculate the size of ordered domains with the Debye and Scherrer relation.*

Sample	*h k l*	*2θ*	*θ* (rad)	(FWHM) obs	(FWHM) inst	(FWHM) sample (rad)	(FWHM) sample* *cos(θ)*	Size (nm)
Bulk	1 0 0	31.41	0.274	0.123	0.085	0.00066	0.000638	> 150
	1 0 3	37.805	0.33	0.13	0.085	0.00078	0.000743	> 150

Compared with the bulk commercial powder sample, fine inspection of the diffractograms recorded on the exfoliated samples reveals lower lower I_{103} / I_{006} and I_{105}/ I_{006} peak intensity ratio for these samples, I_{hkl} denotes for the peak intensity of the *hkl* diffraction peak. The lower thicknesses of the ordered domain observed for these diffraction peaks are consistent with the successful exfoliation of nanosheets perpendicular to the c-axis direction.

III.2.2 Optoelectronic Properties of the p-WSe_2 nanoflakes

III.2.2.1 Band gap determination from UV-Vis Absorbance

The optoelectronic properties of WSe_2 after exfoliation were assessed. UV-visible absorption spectra of the nanoflakes drop casted on a glass substrate and annealed at 350°C under N_2 atmosphere films by visible-light UV absorption is shown in **Figure III - 3**. The absorptance curve was determined from the transmittance and reflectance data, using the energy conservation law ($T + R + A = 1$). The total light absorptance, in absence of scattering, is about 60% of the accessible photons ($h\nu > 1.6$ eV).

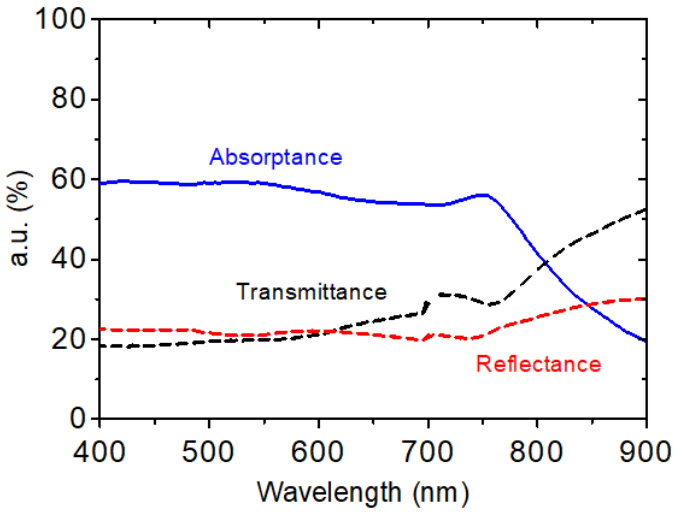

Figure III - 3: *Absorptance (black curve), transmittance (red curve) and reflectance (blue curve) of as-exfoliated WSe_2 nanoflakes drop casted on glass substrate and annealed at 350°C under N_2 atmosphere. The discontinuity observed on the experimental transmittance and absorbance curves probably arises from the switch from the Xe lamp used to ensure the whole range of wavelength investigated.*

The absorbance trace of the exfoliated WSe_2 film, obtained from the Beer-Lambert law [4], is presented in the **Figure III - 4**. As WSe_2 has an indirect band-gap for thickness larger than a single monolayer, the absorption becomes important only for photons with energies equal or larger than the direct band-gap transitions ($E \geq E_g$). The absorbance peak revealed at ca. 1.6 eV is, then, attributed to the excitonic transition in the direct band-gap of WSe_2 in correspondence with previously reported works [5]. IT stands for the transition associated with the indirect band-gap, which is located at ca. ≈ 1.4 eV. The larger peak centered around 2.2 eV is presumably due to transitions associated to the valence band. The band gap energy achieved for our WSe_2 films is consistent with previous studies performed with WSe_2 for solar hydrogen evolution [6]–[8].

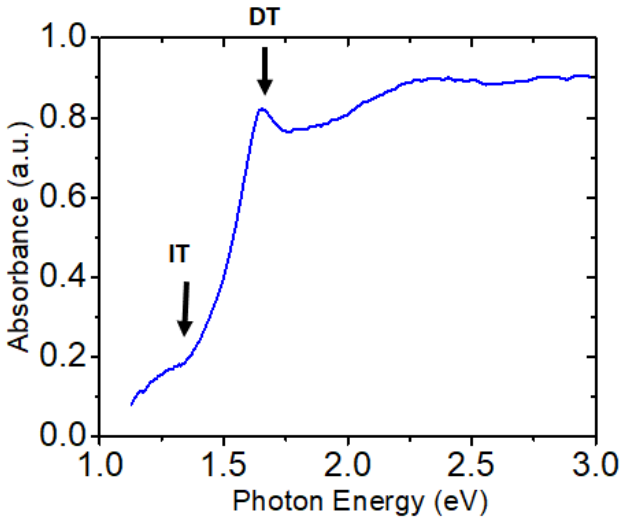

Figure III - 4: *Absorbance curve extrapolated for the 2D WSe_2 nanoflakes obtained using the Beer-Lambert law, which considers the attenuation of the transmitted fraction of the light.*

III.2.2.2 Flat band potential and p-type character of WSe_2 nanoflakes

Moreover, further investigations concerning the semiconducting properties of the WSe_2 was performed using the Mott-Schottky model for nanoflakes drop casted on FTO substrate in 0.5M H_2SO_4 (pH=0). Capacitances values extracted at 100 Hz from EIS data were used to obtain the Mott-Schottky Plot. From **Figure III - 5** – Mott-Schottky representation –, it can be seen a negative slope which confirms a p-type semi-conducting behavior of the exfoliated WSe_2.

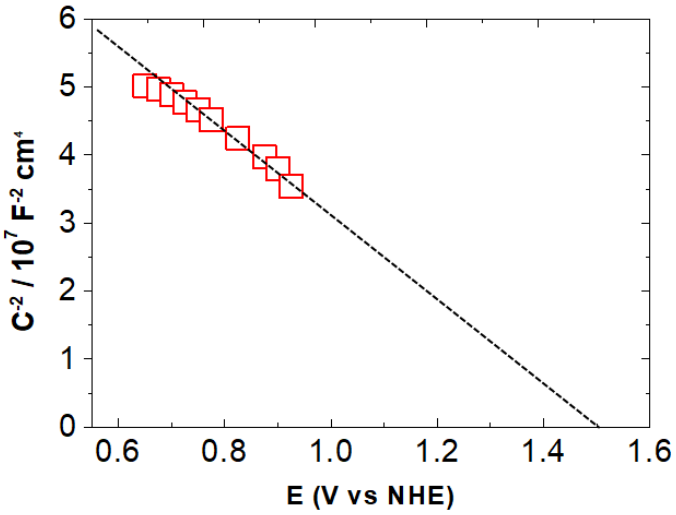

Figure III - 5: *Mott-Schottky plot of exfoliated WSe_2 showing a negative slope that corresponds with p-type semi-conduction. Obtained at 0.5M H_2SO_4.*

From the slope (7.25 x 10^7 $F^{-2}cm^4.V^{-1}$) of the Mott-Schottky plot, the charge carrier density of the exfoliated p-WSe_2 was calculated to be N_A = 4.35 x 10^{23} cm^{-3}. Here, the relative dielectric constant of the WSe_2 (ε_r) was taken as 4.5 [9][10] and with the device area (A) of 1 cm^2.

This charge carrier density value is found to be higher than what has been reported in the literature [7][9]. Some hypothesis about this high value can be: (i) the increase of edge sites after exfoliation process, approaching the particle size as the one of charge space layer; and/or (ii) because of the non-negligible Helmholtz capacitance. Besides that, from the intercept of the linear regression the flat band potential (E_{fb}) is measured to be about + 1.5 V vs NHE, pH=0. The E_{fb} of p-WSe_2 crystals has been previously reported at pH=7 in reference to saturated calomel electrode (SCE) [7],[9]. To verify the correspondence of our values with the ones found in the literature, we thus extrapolated the E_{fb} at pH=7 considering a Nernstian behavior (-0.06pH at 298K)[11][12]. Doing so, E_{fb} is about + 1.0 vs NHE, which is the same as reported by McKone *et.*al [9].

III.3 Photoelectrochemical evaluation of 2D p-WSe_2 films

Photoelectrochemical (PEC) solar hydrogen production performance has been evaluated by Linear Sweep Voltammetry (LSV) of exfoliated WSe_2 electrodes under intermittent (chopped) illumination (AM 1.5 G, 100 mW cm^{-2}) in 0.1M Na_2SO_4 electrolyte, pH 7, in the potential range $+0.4 \leq E \leq -0.4$ V vs NHE, as showed in **Figure III - 6**.

Here we note the onset of sustained p-type (cathodic) photocurrent at about + 0.4V vs NHE. The photocurrent density reaches approximately -80 µA cm^{-2} at 0V vs NHE for exfoliated WSe_2 (red curve). Bare FTO current is presented as reference (black curve). In the LSV curve referent to WSe_2, one can also observe high dark currents which likely is due to an electrocatalytic effect – and/or defects leading to a consequent current density due minority charge carriers; and because particle size is in the range of the space charge average thickness. Moreover, the presence of current spikes both under illumination (light on) and under dark (light off) is indicative of charge recombination and charge accumulation, respectively [13]. This recombination arises from accumulation of holes near the surface (cathodic transient), and/or trapping of electrons/holes at surface states. Previous works have questioned high recombination being reported to high density of edges sites (defects), which in turn leads to recombination sites of charge carriers, decreasing the hydrogen evolution reaction rate (HER) [14]–[16].

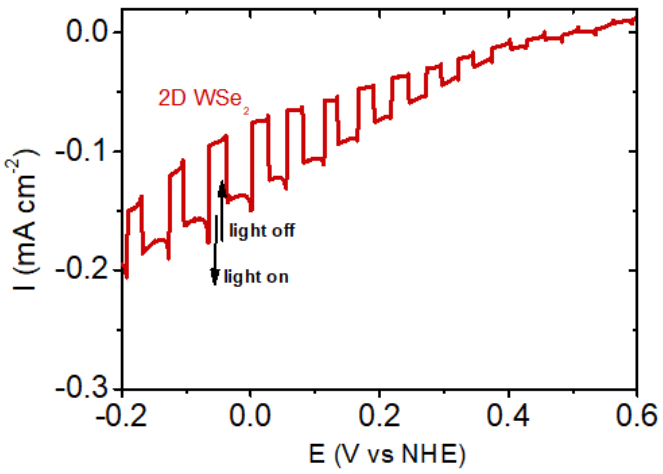

Figure III - 6: *Linear scanning voltammetry curve of p-WSe_2 electrode under constant chopped illumination. Scan Rate 10mV s^{-1} in 0.1M Na_2SO_4.*

III.3.1 Influence of the layer number on photoelectrochemical characteristics of 2D WSe_2 films

A study was performed involving the photocatalytic activity of exfoliated WSe_2 with different film thickness. **Figure III-7** presents LSV curves (log |i| vs. Potential) obtained upon irradiation (100 mW cm^{-2}) for the WSe_2 films with different mass loadings. Naturally, we can observe increase of photocurrent with increased mass loadings. Besides, for the thinner films, the photoactivity is practically negligible at high polarization, which may be due to higher presence of defect sites (green trace).

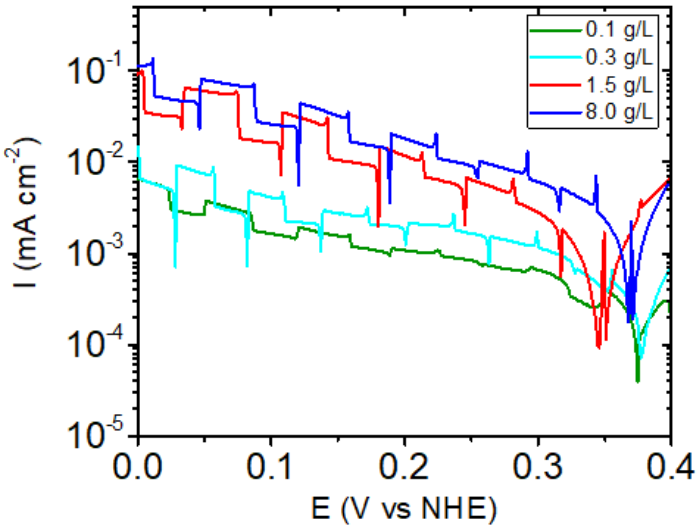

Figure III-7: *LSV curves (log |i| vs. Potential) under chopped light of WSe_2 films displaying of various thickness in 0.1M Na_2SO_4, annealed at 250°C under N_2.*

The presence of defects is also noticed for thicker flakes, which is responsible for the significant presence of current spikes [13][17] even though the steady state current is increasing with the electrode loading. Thicker films give increased presence of edge sites, where recombination of photogenerated charge carries has been showed to happen in 2D materials. What can be expected, since the WSe_2 nanoflakes have an overall thickness of 40 – 70 nm. Therefore, one can observe that an ideal photocatalytic activity can be attempted with elimination or even decrease of the defect sites present in the WSe_2 nanoflakes. Usually, the improvement of the photocathode performance is acquired through surface modifications [18].

III.3.2 Enhancement of photo-activity of p-WSe_2 based electrodes

As reported above from the photocatalytic evaluation of WSe_2 photoelectrodes, we could notice the significant presence of currents spikes, which indicates recombination of charge carriers, related to high concentration of surface defects [13]. In the literature is reported that thin films of TMDC materials of small flake size as WSe_2 has high concentration of surface defects acting as recombination sites for the photogenerated charges [19][20].

To passivate the defect sites present in the 2D materials, different approaches such as surface treatments and catalyst deposition are commonly applied to improve the photo-activity of the material. Therefore, we present next, surface modification *via* a surface passivation treatment and/or by the deposition of catalyst, as already reported in the literature for the WSe_2 [21]. As aforementioned (Chapter I), the photocurrent from an electrode under illumination results from an effective electron-hole separation and collection. The efficiency of the process is linked to a competition between the charge transfer at the electrode/electrolyte interface and the charge recombination rate. The former being enhanced thanks to the use of a co-catalyst; the latter being decreased thanks to a surface passivation. On top of that, an efficient charge percolation is required to ensure charge collection before recombination, which can be addressed by the addition of a conductive agent such as graphene oxide nanosheets [22][23].

III.3.2.1 HTS treatment on WSe_2 electrode surface for defect passivation

The surface defects of the WSe_2 nanoflakes with overall thickness of 40-70 nm were investigated by implementation of passivation approaches to repair the surface defects, considering its edge sites or chalcogenide vacancies, to improve the effectiveness of the photocathode. Hexyl-trichlorosilane (HTS) treatment on WSe_2 electrodes was proceeded similarly to the method used for the EPFL group on p-WSe_2 nanoflakes [21]. The electrodes were soaked in a HTS solution (1 to 5% wt.) in hexane, for 10 min and under stirring, followed by a drying in air at 70°C for 10 minutes.

Photoelectrochemical measurements obtained for an electrode of WSe_2 after HTS treatment is represented in **Figure III-8**. LSV curves show an increased photocurrent density of -200 µA cm^{-2} at -0.2V vs NHE for a WSe_2 film treated with 5% HTS. A slight decrease of the dark current compared with bare WSe_2 electrode can also be observed, but still a considerable photocurrent spike was assigned under illumination and it decreases thereafter; which is supposedly caused by charge recombination and slow interfacial electron transfer kinetics. So,

only a slight photocurrent increase is achieved through this passivation route, meaning there is still room for improvement.

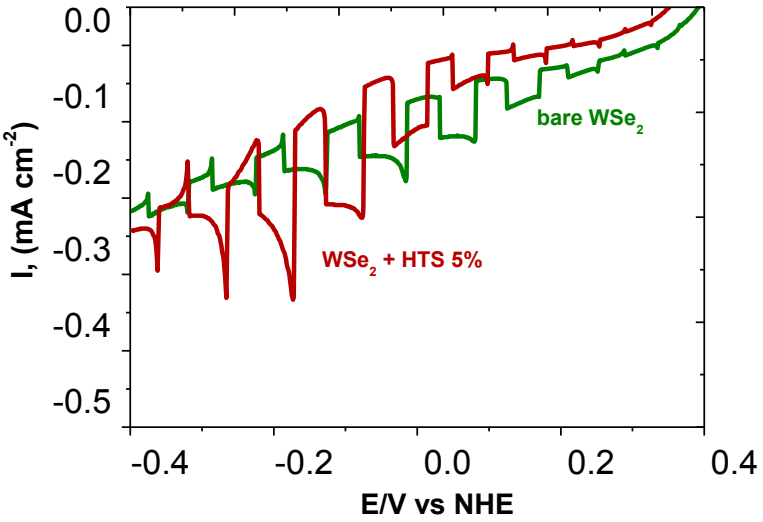

Figure III - 8: *j-E curve registered for 2D exfoliated WSe_2 film after HTS treatment (5%w.t.)in0.1M Na_2SO_4.*

The relatively low photocatalytic performance of these nanoflakes toward hydrogen evolution still does not preclude the possibility of obtaining reasonably efficient photocathodes from nanostructures that possesses high density of edge sites and exposed vacancies of chalcogen atoms [21]. Hence, to improve photo-electroactivity, as also worked by the EPFL group, we considered addition of catalyst Pt-Cu to enhance the charge transfer efficiency of the WSe_2 photoelectrodes.

III.3.2.2 Pt-Cu deposition as co-catalyst on WSe_2 photoelectrodes

Platinum is usually considered as the most suitable H_2 evolution co-catalyst and has been widely used as co-catalyst for HER on TMDC materials. The procedure for photoelectrochemical deposition of Pt-Cu was similar to an approach used previously for p-WSe_2 crystals [9]. To our WSe_2 electrodes, the procedure involved a potentiostatic deposition of a mixed solution containing 1 mM $H_2PtCl_4.6H_2O$ and 0.25 mM $Cu(NO_3)_2$ in 0.1 M HCl (aq), and at potential hold of −0.1 V vs NHE. The electrodes were then removed, thoroughly rinsed with water, dried, and tested for hydrogen evolution activity under illumination.

On **Figure III - 9a** is displayed the J–E curves obtained under illumination for p-type WSe_2 electrodes with and without Pt-Cu after HTS treatment at pH = 7.0. The same WSe_2 summited to HTS treatment revealed a decreased photocurrent of approximately -150 µA cm^{-2}

at -0.2V vs NHE. However, electrocatalytic current has increased to -900 µA cm^{-2} at -0.4V vs NHE against -300 µA cm^{-2} for the photoelectrode that only received HTS treatment. After Pt-Cu deposition, we observe elimination of the sharp photocurrent spike at high overpotentials, which is attributed to depressed charge recombination due to the facilitated electron transfer kinetics together with a more efficient band bending [21].

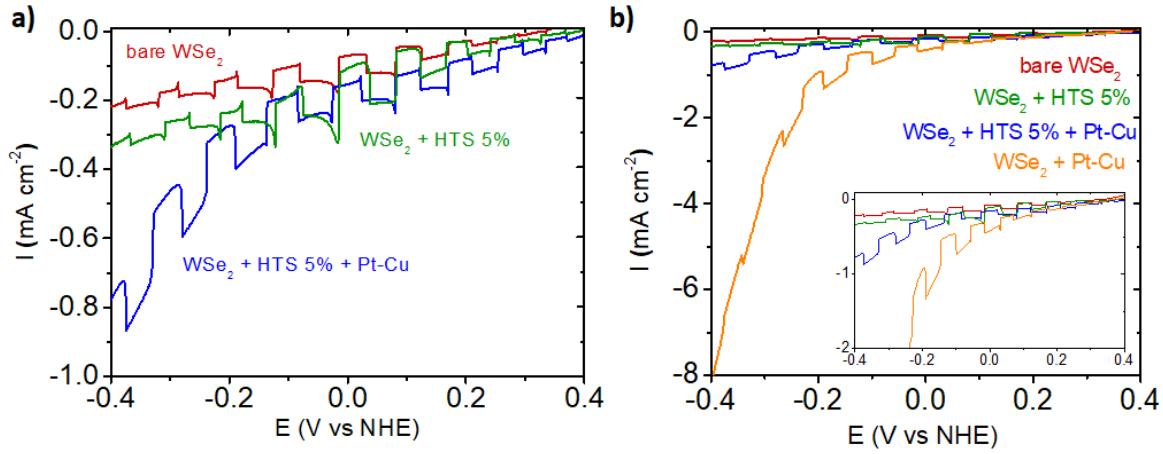

Figure III - 9: *LSV curves recorded on WSe_2 electrodes (a) after HTS treatment and Pt-Cu deposition, (b) after Pt-Cu deposition without HTS treatment in 0.1M Na_2SO_4.*

Willing to find effective results with introduction of Pt-Cu catalyst, a similar electro-deposition of Pt-Cu, previously reported in the literature [9]. No presence of photocurrent spike is observed and the current is likely to be due to a direct electrolysis via platinum site deposited onto the FTO since it is canceled out after HTS deposit, as observed on **Figure III - 9a**. As a result, only a photocurrent density of about 0.3 mA cm^{-2} at - 0.2V vs NHE is achieved. Analyzing the LSV curves for WSe_2 electrodes after Pt-Cu deposition with and without HTS treatment (**Figure III - 9b** – blue and orange traces), it is possible to say there is a synergic effect (increase of the charge transfer rate together with a decrease of the charge recombination rate). However, HTS treatment still falls short to rule out completely the recombination, as observed for instance for the electrode without Pt-Cu.

Despite these attempts searching to improve the performance of our photocathode to effective hydrogen evolution reaction, WSe_2 nanosheets still likely exhibits a large defect density that needs to be tackled. For that purpose, the following chapters will be devoting to the development of more specific surface treatment, ideally free of platinum.

Conclusion

Tungsten di-selenide (WSe_2) nanoflakes were obtained from solvent-exfoliation and WSe_2 photoelectrodes were fabricated by drop cast forming a thin film containing few-layers. XRD analysis confirmed well-ordered stacking structure and cross-section SEM image revealed single flake layer morphology. Mott Schottky model confirmed p-type semiconductor behavior for our WSe_2 electrode and charge carrier concentration value of about $4x\ 10^{23}\ cm^{-3}$ could be calculated. Photoelectrochemical characterization of WSe_2 films demonstrated its photoactivity to drive hydrogen evolution reaction with a photocurrent of $-100\ \mu A\ cm^{-2}$ at -0.2V vs NHE. Photoelectrochemical study on bare WSe_2 of various film thickness showed increased photocurrents as well as higher current spikes, due to more presence of nanosheet edge sites. Inspired by the literature, two approaches of photoactivity enhancement were tested by surface treatment with HTS and co-catalyst introduction with Pt-Cu deposition on WSe_2 electrodes. Slight improvements could be done in electrocatalytic activity; however, a more effective method for defects passivation and photocatalytic properties improvement must be implemented. In order to increase the offered options of co-catalysts well suited for the 2D TMDC materials, there is a large interest about finding an alternative involving an abundant and free of noble metal element.

BIBLIOGRAPHY REFERENCES

[1] X. Yu, M. S. Prévot, N. Guijarro, and K. Sivula, "Self-assembled 2D WSe2 thin films for photoelectrochemical hydrogen production.," *Nat. Commun.*, vol. 6, no. May, p. 7596, 2015.

[2] F. Paquin, J. Rivnay, A. Salleo, N. Stingelin, and C. Silva, "Multi-phase semicrystalline microstructures drive exciton dissociation in neat plastic semiconductors," *J. Mater. Chem. C*, vol. 3, no. 207890, pp. 10715–10722, 2015.

[3] R. K. Jha and P. K. Guha, "Liquid exfoliated pristine WS2 nanosheets for ultrasensitive and highly stable chemiresistive humidity sensors," *Nanotechnology*, vol. 27, no. 47, pp. 1–11, 2016.

[4] G. Wypych, "Photophysics," in *Handbook of Material Weathering*, 6th ed., ChemTec Publishing, 2018.

[5] A. Arora, M. Koperski, K. Nogajewski, J. Marcus, C. Faugeras, and M. Potemski, "Excitonic resonances in thin fi lms of WSe2: from monolayer to bulk material," *Nanoscale*, vol. 7, no. 23, pp. 10421–10429, 2015.

[6] F. Bozheyev, F. Xi, P. Plate, T. Dittrich, S. Fiechter, and K. Ellmer, "Efficient charge transfer at a homogeneously distributed $(NH_4)_2Mo_3S_{13}/WSe_2$ heterojunction for solar hydrogen evolution," *J. Mater. Chem. A*, vol. 7, no. 17, pp. 10769–10780, 2019.

[7] C. R. Cabrera and H. D. Abruna, "Synthesis and Photoelectrochemistry of Polycrystalline Thin Films of p-WSe2, p-WS2, and p-MoSe2," *J. Electrochem. Soc.*, vol. 135, no. 6, pp. 1436–1441, 1988.

[8] R. Roldán, J. A. Silva-Guillén, M. P. López-Sancho, F. Guinea, E. Cappelluti, and P. Ordejón, "Electronic properties of single-layer and multilayer transition metal dichalcogenides MX2 (M = Mo, W and X = S, Se)," *Ann. Phys.*, vol. 526, no. 9–10, pp. 347–357, 2014.

[9] J. R. McKone, A. P. Pieterick, H. B. Gray, and N. S. Lewis, "Hydrogen evolution from Pt/Ru-coated p-type WSe2 photocathodes," *J. Am. Chem. Soc.*, vol. 135, no. 1, pp. 223–231, 2013.

[10] S. Antoci, P. Camagni, A. Manara, and A. Stella, "Study of the optical response of WSe2 in the excitonic region," *J. Phys. Chem. Solids*, vol. 33, no. 6, pp. 1177–1185, 1972.

[11] S. R. Morrison, *Electrochemistry at semiconductor and oxidized metal electrodes*. Plenum Press, 1980.

[12] M. Ciobanu, J. P. Wilburn, M. L. Krim, and D. E. Cliffel, "Fundamentals," in *Handbook of Electrochemistry*, 2007, pp. 3–29.

[13] S. K. Choi, W. Choi, and H. Park, "Solar water oxidation using nickel-borate coupled $BiVO_4$ photoelectrodes," *Phys. Chem. Chem. Phys.*, vol. 15, no. 17, pp. 6499–6507, 2013.

[14] C. Backes *et al.*, "Guidelines for exfoliation, characterization and processing of layered materials produced by liquid exfoliation," *Chem. Mater.*, vol. 29, no. 1, pp. 243–255, 2016.

[15] B. A. Parkinson, T. E. Furtak, D. Canfield, K. K. Kam, and G. Kline, "Evaluation and reduction of efficiency losses at tungsten diselenide photoanodes," *Faraday Discuss. Chem. Soc.*, vol. 70, pp. 233–245, 1980.

[16] Z. Lin *et al.*, "Defect engineering of two-dimensional transition metal dichalcogenides," *2D Mater.*, vol. 3, no. 2, pp. 1-21, 2016.

[17] L. M. Peter, "Dynamic Aspects of Semiconductor Photoelectrochemistry," *Chem. Rev.*, vol. 90, no. 5, pp. 753–769, 1990.

[18] N. Guijarro, M. S. Prévot, and K. Sivula, "Surface modification of semiconductor photoelectrodes," *Phys. Chem. Chem. Phys.*, vol. 17, no. 24, pp. 15655–15674, 2015.

[19] B. Luo, G. Liu, and L. Wang, "Recent advances in 2D materials for photocatalysis," *Nanoscale*, vol. 8, no. 13, pp. 6904–6920, 2016.

[20] T. Su, Q. Shao, Z. Qin, Z. Guo, and Z. Wu, "Role of Interfaces in Two-Dimensional Photocatalyst for Water Splitting," *ACS Catal.*, vol. 8, no. 3, pp. 2253–2276, 2018.

[21] X. Yu, N. Guijarro, M. Johnson, and K. Sivula, "Defect Mitigation of Solution-Processed 2D WSe2 Nanoflakes for Solar-to-Hydrogen Conversion," *Nano Lett.*, vol. 18, no. 1, pp. 215–222, 2018.

[22] J. Guo, Y. Shi, X. Bai, X. Wang, and T. Ma, "Atomically thin MoSe2/graphene and WSe2/graphene nanosheets for the highly efficient oxygen reduction reaction," *J. Mater. Chem. A*, vol. 3, no. 48, pp. 24397–24404, 2015.

[23] X. Wang *et al.*, "Few-layered WSe2 nanoflowers anchored on graphene nanosheets: a highly efficient and stable electrocatalyst for hydrogen evolution," *Electrochim. Acta*, vol. 222, pp. 1293–1299, 2016.

CHAPTER IV

Mo Thio and Oxo-Thio Molecular Complexes Film as Healing Catalysts for HER on 2D TMDC Materials

Introduction

Despite of the unique properties of the 2D TMDC semiconductors for water splitting, optoelectronic defects limit considerably the photocatalytic performance of the TMDCs for the HER. These defects can be enclosed between layers and edges of the nanosheets having fundamental effects for the catalysis performance [1]. However, further insights about the defects on 2D layered TMDC remains unexplored. Therefore, passivation techniques have been applied in other to mitigate the effects of the defects to emphasize their catalytic properties.

In this chapter, we present the study of a potential catalyst well suited for p-WSe_2 photoelectrodes and its benefits for the photocatalytic performance of this TMDC material. The study intended for elaboration of a noble-metal free and environmentally friendly catalyst precursor based on thio, oxo-thio Mo complexes species (Mo_xS_y). The new water-stable Mo thio complexes for the hydrogen evolution reaction (HER) in water splitting under visible irradiation is proposed mainly resulting from: i) identification of the Mo complexes in solution by mass spectroscopy (ESI-MS), ii) collection of XPS data from the resulting catalyst film, iii) the study of its electronic properties, and iv) Density Functional Theory (DFT) calculations of the probable conformations of the Mo thio and oxo thio Mo complexes anchored on WSe_2 photo-electrodes and mechanisms catalysis for the HER. The photocatalytic activity and the charge transfer increase of the photoelectrodes and hydrogen measurement was performed with Gas Chromatograph. The obtained results propose unique properties of Mo thio complexes thin films as healing catalysts for the photocatalytic HER on 2D TMDC materials.

IV.1 Mo Thio and Oxo Thio Complexes Catalysts

IV.1.1 Elaboration of Water Soluble Mo Thio Oxo Thio Complexes

As presented in the Experimental Section (Chapter II), WSe_2 electrodes were fabricated by a simple method including deposition of solvent-exfoliated WSe_2 nanosheets by drop casting onto an FTO substrate. For the catalyst synthesis, $(MoS_4)^{2-}$ was used as Mo (VI) source salt and H_2O as solvent. We have, then, explored a large range of water-soluble, thio and oxo-thio complex distributions by variation of polycondensation degree (from pH 8.0 to pH 9.5) and of S^{2-} concentrations (S^{2-}/Mo mole or S/Mo mole = 5). As a result of various oxo reduction reactions involved in aqueous sulfide solutions - (Mo (VI) + $2e^- \longrightarrow$ Mo(IV), Mo(VI) + Mo(IV) $\longrightarrow$ 2 Mo(V)) - the synthesized Mo thio and oxo-thio complexes solutions displayed of Mo cations with various oxidation states, including Mo (VI), Mo (V) and Mo (IV).

The study of their catalytic properties was performed on FTO substrate and on exfoliated p-WSe_2/FTO electrodes. The Mo thio complexes were introduced onto the WSe_2 electrodes via two methods: drop casting of Mo thio complexes onto p-WSe_2 photoelectrode and by dip coating of p-WSe_2 photoelectrode into a Mo thio complex containing solution.

IV.1.2 Identification of Mo Thio and Oxo Thio Complexes formed in aqueous dispersions

Species formed in each solution were rationally identified using Electro-Spray Ionization Mass Spectroscopy (ESI-MS). The distribution diagram of typical species for solutions prepared for a total Mo concentration of 0.01 M, pH 9.0 and S/Mo= 5 is presented in **Figure IV-1**. Peaks attributions were performed as following: m/z= 210.8, MoS_3OH^-; 226.8, MoS_4H^-; 258.7, MoS_5H; 274.8, MoS_5OH^-; 290.7, MoS_6H^-; 416.6, $Mo_2S_6O_2H^-$; 432.6, $Mo_2S_7OH^-$; 448.6, $Mo_2S_8H^-$; 288.7, $Mo_2S_{12}^{2-}$; 576.5, $Mo_2S_{12}H^-$; 608.5, $Mo_2S_{13}H^-$; 280.7, $Mo_3S_8O^{2-}$; 562.7, $Mo_3S_8OH^-$.

The complexes distribution mainly includes Mo monomers, dimers and trimers under mono charged and di-charged forms. Using basic aqueous solutions, hydrolysis is favored and corresponding hydrolysis compounds of the thio complexes were clearly identified in significant proportions. Thus, previously largely described Mo sulfides compounds and their corresponding hydrolysis products such as $(MoS_4)^{2-}$, $(MoS_5)^{2-}$ [2], $(Mo_2S_7O)^{2-}$ [3] and $(Mo_3S_8O)^{2-}$ [4] were unambiguously identified in our solutions.

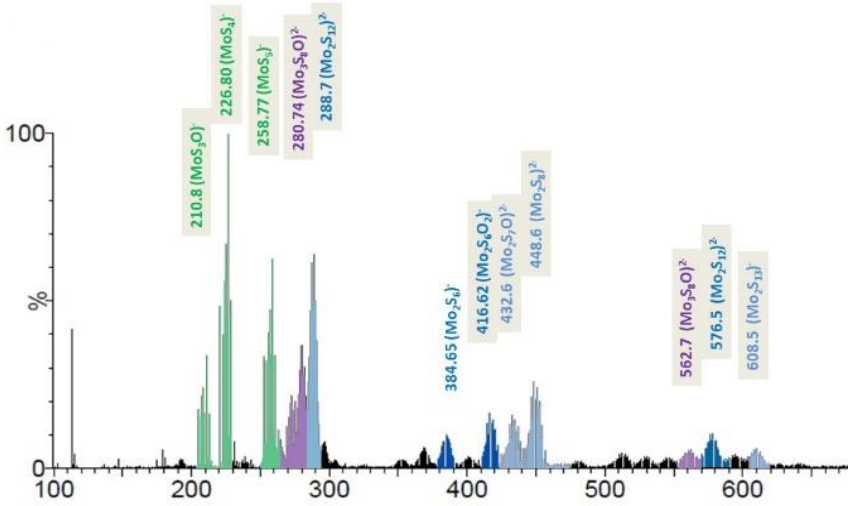

Figure IV - 1: *Typical ESI-MS spectra recorded on Mo thio complexes solution prepared at pH 9.00 and S/Mo=5.*

A semi-quantitative determination of the frequency of each species was achieved by comparison with the sum intensity of all the various peaks. For plotting this predominance diagram, note that i) we have grouped together for clarity the following intensities: in **Figure IV - 2** ($Mo_2S_6O_2H^-$, $Mo_2S_7OH^-$), **Figure IV - 3** ($Mo_2S_{12}^{2-}$, $Mo_2S_{12}H^-$) and **Figure IV - 4** ($Mo_3S_8O^{2-}$, $Mo_3S_8OH^-)^-$. The instable adducts, such as MoS_5OH^- or MoS_6^- was not considered.

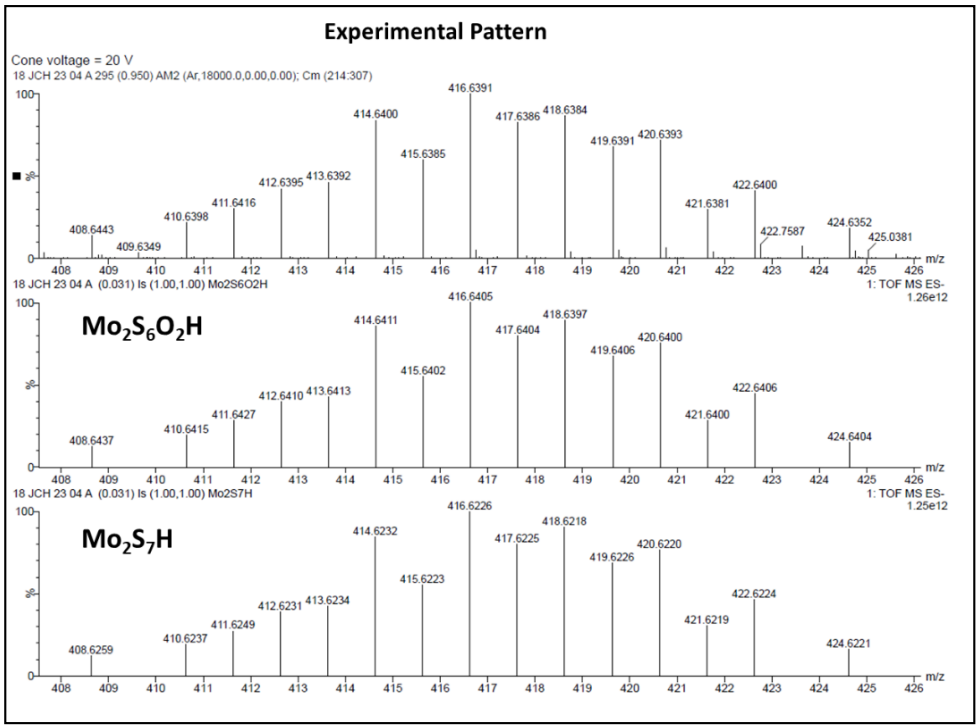

Figure IV - 2: *Peak identification of m/z=416.6, $(Mo_2S_6O_2H)^-$. Calculated isotope pattern of $(Mo_2S_7H)^-$ is given for comparison. The smaller mass difference value (1.93 mDa vs 16.46 mDa) is in agreement with attribution of this experimental peak to $(Mo_2S_6O_2H)$- vs (Mo_2S_7H).*

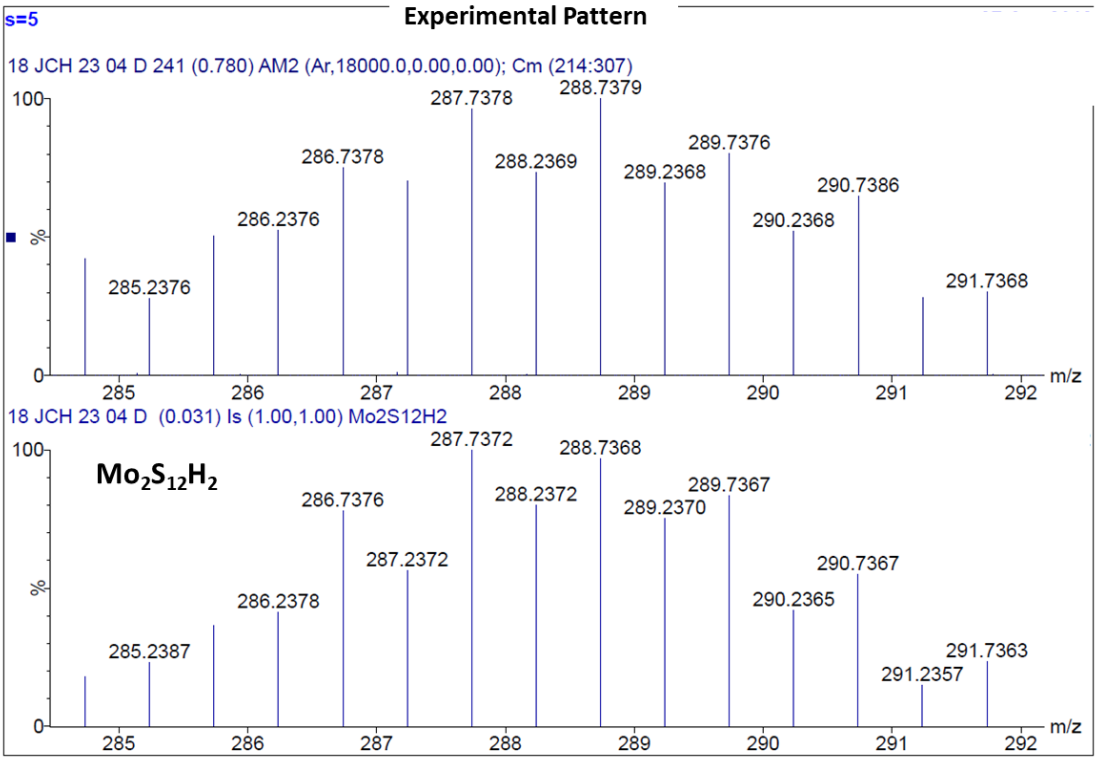

***Figure IV - 3**: Peak identification of m/z= 288.7, $(Mo_2S_{12})^{-2}$.*

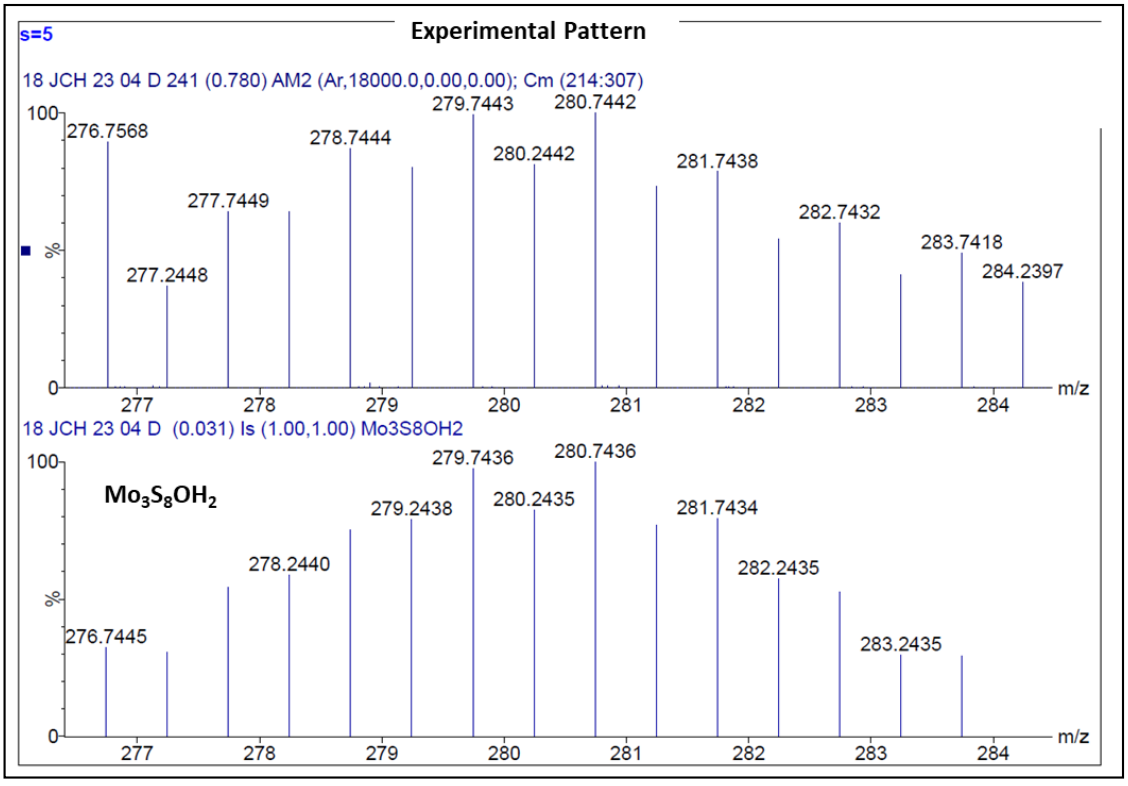

***Figure IV - 4:** Peak identification (c) m/z= 280.7, $(Mo_3S_8O)^{-2}$.*

Surprisingly, we can also note the detection of species at m/z= 274.8, m/z= 385 attributed to $(MoS_5OH)^-$ (**Figure IV - 5**) and $(MoS_6)^-$, respectively. Because these species were previously reported to date in the literature to the best of our knowledge exclusively as a radical $(MoS_5O)°$ [5]. We, then, hypothesized that these latter species can arise from some ionization or fragmentation in the ESI-MS chamber of less chemically-stable complexes such as $(Mo_2S_9O_2)^{2-}$[5], or $(Mo_2S_{10}O_2)^{2-}$ [6].

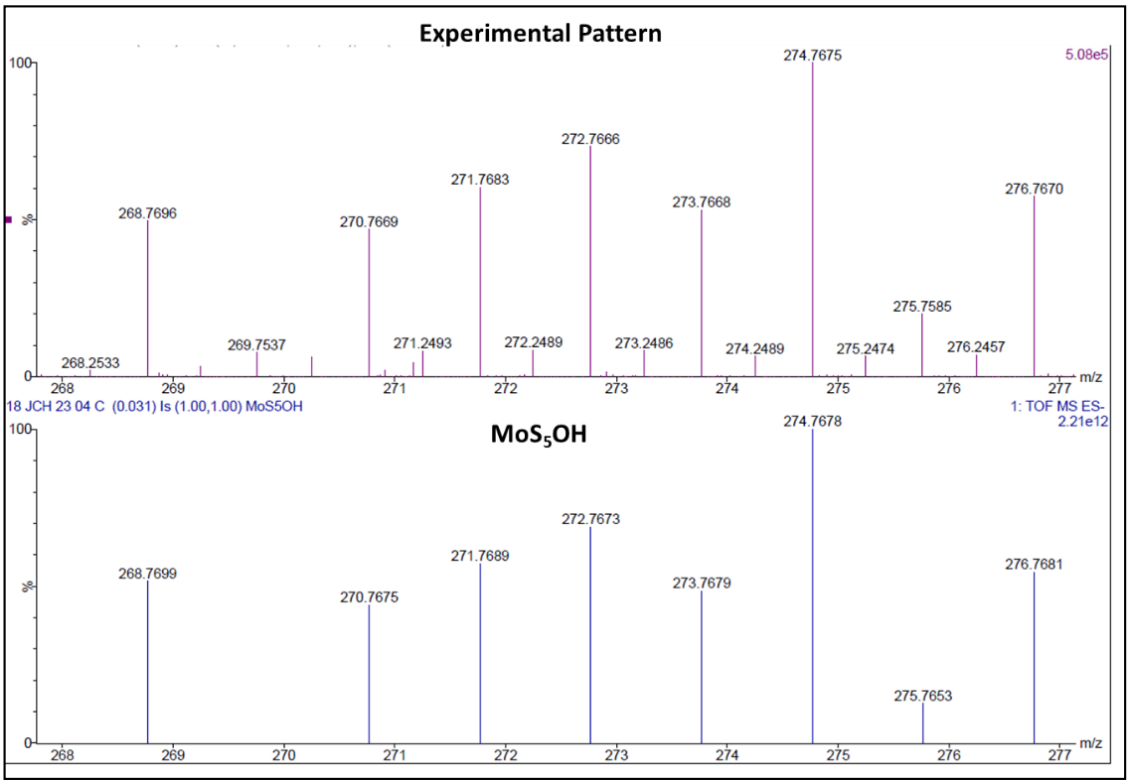

Figure IV - 5: *Peak identification of m/z= 274.8, $(MoS_5OH)^-$.*

As additional compounds, we can note $(Mo_2S_7)^{2-}$, which in turn can afford the formation of the tri-nuclear complexe $(Mo_3S_9)^{2-}$according to the reaction $(Mo_2S_7)^{2-}$ -> $(Mo_3S_9)^{2-}$+ $(MoS_5)^{2-}$, previously proposed [2]. Interestingly, we also demonstrate from our process route the formation of $(Mo_2S_6O_2)^{2-}$ [7],[8], $(Mo_2S_{12})^{2-}$ [9], $(Mo_3S_8)^{2-}$[10] complexes (respectively, **Figure IV - 2, Figure IV - 3, Figure IV - 4**). Although the preparation of these $(Mo_2S_6O_2)^{2-}$, $(Mo_2S_{12})^{2-}$, $(Mo_3S_8)^{2-}$ complexes were largely described in various solvents, such as acetonitrile (ACN) or di-methyl-formamide (DMF), our results show the formation of these complexes in H_2O solvent in significant proportions.

The peak intensities extracted from the ESI-MS data can be depended of the complex ionization properties. A comparison of the frequencies for a same species at different pH could

be achieved quantitatively, allowing determining its predominance domain and these values are presented in **Table IV - 1**.

Table IV - 1: *Species concentration present at 0.01M Mo and S/Mo = 5 from ESI-MS data for different pH.*

pH	$(MoS_3OH)^-$	$(MoS_4H)^-$	$(MoS_5H)^-$	$(MoS_5OH)^-$	$(MoS_6H)^-$	$(Mo_2S_6O_2H)^-$	$(Mo_2S_7OH)^-$	$(Mo_2S_8H)^-$	$(Mo_2S_{12})^{2-}$	$(Mo_2S_{13}H)^-$	$(Mo_3S_8O)^{2-}$
8.0	6.4	18.1	15	7.1	2.11	3.1	1.3	3.3	8.4	0.5	3.6
8.5	6.1	44.1	16.6	7.4	2.5	3.7	1.3	4.2	10.4	0.7	4.2
8.8	5.6	13.5	12.7	8	2.3	7.1	1.7	3.8	20	0.5	10.7
9.0	9.3	22.2	18.3	19.4	4.8	5.8	2.2	4.7	10.8	0.7	4.1
9.3	5	18	7.8	11.2	2.9	3	1	2.6	5.6	0.5	1.9

From these data, predominance diagram of the various species can be defined as a function of pH for each given value of S/Mo = 5. **Figure IV - 6** shows the predominance diagram for Mo sulfides and oxo sulfides species determined for S/Mo= 5 in the pH range 8.00 ≤ pH ≤ 9.5. Similarly to others metallic cations [11][12], speciation of the Mo cation clearly shows the coexistence of different species at a given pH. Consistently, decreasing pH favours polycondensation, as illustrated with the formation of $(Mo_2S_6O_2)^{2-}$, $(Mo_2S_{12})^{2-}$ dimers and $(Mo_3S_8O)^{2-}$ trimers displaying peak concentrations all occurring simultaneously in the pH window, 8.00 ≤ pH ≤ 9.3.

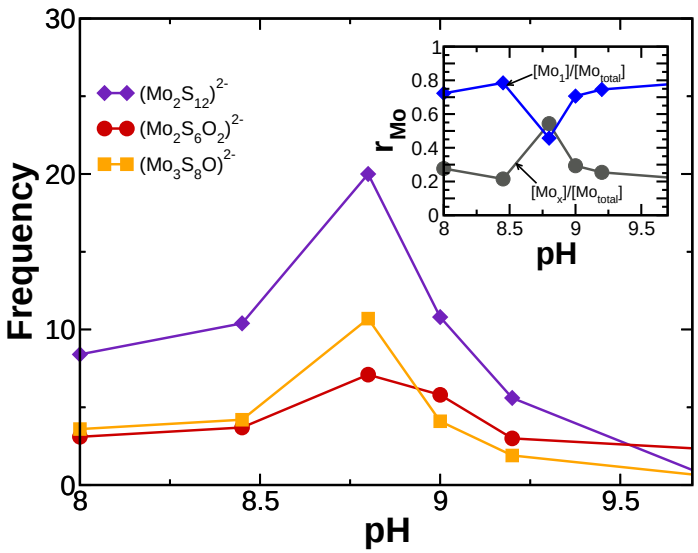

Figure IV - 6: *Species predominance diagram determined at 0.01 M Mo and S/Mo= 5 from ESI-MS data showing concentration peaks for $(Mo_2S_{12})^{2-}$, $(Mo_2S_6O_2)^{2-}$ and $(Mo_3S_8O)^{2-}$ complexes between pH 8.0 and pH 9.7.*

IV.2 Mo Thio and Oxo-thio complexes catalyst drop casted on FTO substrate and on 2D p-WSe_2 photocathodes

IV.2.1 Identification of Mo Thio and Oxo Thio Complexes on FTO substrate

The polycondensation degree evolution shown by ESI-MS of the Mo complexes with pH was confirmed by X-ray Photoelectron Spectroscopy (XPS) results. On films of low thickness (e ≤ 10 nm), XPS can offer precise information of each element present as the chemical composition of film surface and chemical state of the ejected atom. Various ratios such as the terminal sulfide ratio, rS_{ter}, (r$S_{ter} = S_{ter}/(S_{ter} + S_{br})$, where S_{ter} and S_{br} denote respectively terminal and bridging sulfides), or still the Mo oxysulfide ratio, $r_{MoOS,}$ ($r_{MoOS} = MoO_yS_z/(MoS_x + MoO_yS_z)_{molar}$)) were extracted from XPS data.

Figure IV - 7 reports the XPS spectra recorded on Mo thio complexes film fabricated by drop casting and subsequent solvent evaporation on FTO substrates at room temperature under air - from solutions prepared at S/Mo= 5, Mo= 0.01 M and at various pH. The Mo 3d spectrum (first line) is dominated by a doublet with a Mo $3d_{5/2}$ binding energy of 229.38 eV [13]. This doublet is attributed to the Mo (IV) ion in MoS_2. A small doublet with a Mo $3d_{3/2}$ peak at 232.20 eV is also visible. This binding energy corresponds to that of Mo (VI) ion, as in MoO_3. The doublet with a Mo $3d_{5/2}$ intermediate peak is visible at 230.10 and assignable to molybdenum oxysulfides $(MoO_xS_y)^{+6}$. The S 2s peak at 227.2 eV is also visible in the Mo region.

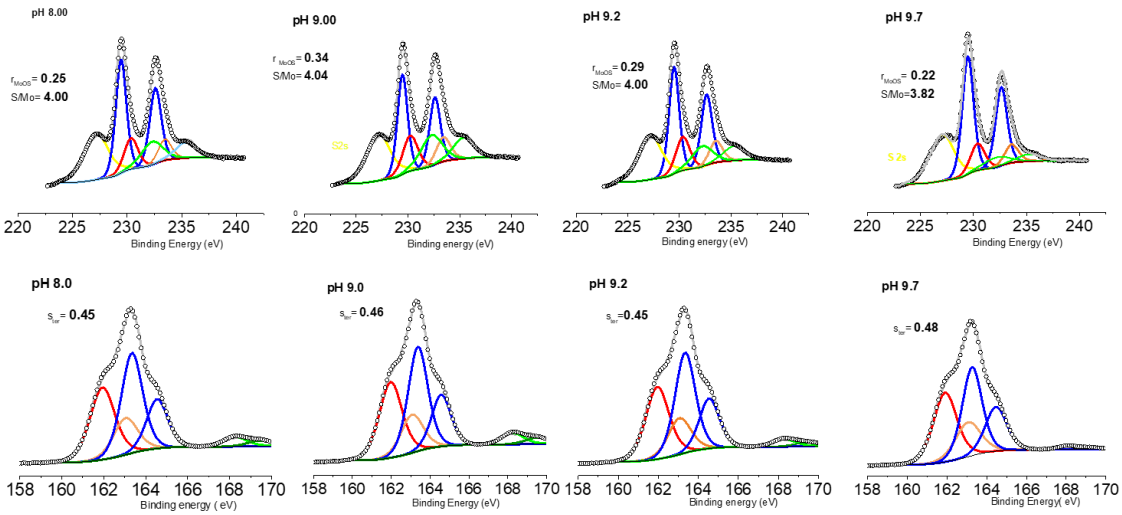

Figure IV - 7: XPS spectra of Mo thio complexes films prepared form solutions prepared at S/Mo= 5 and drop casted on FTO electrodes. Top: Mo 3d and S 2s region. MoS_2 (blue line), MoO_3 (green line), MoO_yS_z (red line) S^{2-} and $(S_2)^{2-}$ (Yellow line). Down: S 2p region: terminal $(S_2)^{2-}$ (red line), bridging $(S_2)^{2-}$ (blue line), $(SO_4)^{2-}$ (green line).

The assignment of this intermediate peak to the Mo oxysulfide complexes, previously identified in solution by ESI-MS, is in agreement with the r_{MoOS} ($r_{MoOS} = MoO_yS_z/(MoS_x + MoO_yS_z)_{molar}$) maximum value observed for the film prepared from the solution (S/Mo= 5, pH 8.7-9.0) possessing the highest oxysulfide concentration.

The S 2p spectra (**Figure IV - 7** - second line) were fitted with S $2p_{3/2}$ peaks having binding energies of 161.9, and 163.3 eV corresponding to terminal S_2^{2-} and bridging S_2^{2-}, respectively [13]. S_{ter} ratios, where ($rS_{ter} = S_{ter}/(S_{ter} + S_{br})$), turn out to vary in the range of $0.45 < S_{ter} < 0.48$ with a maximum value consistently for the solution prepared at pH 9.5 and containing the highest concentration of depolymerized or monomers Mo complexes. The higher ratio of terminal sulfide vs bridging sulfide, S_{ter} and S_{br} denoting respectively to terminal and bridging sulfides, was observed as expected on films prepared from the more depolymerized complex solution at pH 9.5.

All these results, i.e. presence of oxo-thio complexes, terminal S^{2-} ratios, show that the XPS data recorded on drop cast solid films are consistent with species previously identified by ESI/MS in solution. What indicates no significant transformation of the species during the film formation. Moreover, this validates XPS as a powerfull characterization tecnique for films of low thickness (< 10 nm).

IV.2.2 Characterization of thio, oxo-thio Mo complexes films drop casted on FTO and WSe_2 substrates

In the pH range of $8.0 \leq pH \leq 9.5$, Mo thio complexes dispersions (prepared at S/Mo= 5, Mo= 0.01 M) were drop casted on solvent-exfoliated p-type WSe_2 photo-electrode followed of evaporation at room temperature under Air. **Figure IV – 8** presents the XPS core-level spectra and deconvolution into S 2p and Mo 3d contributions for Mo thio complexes thin films deposited by drop-casting onto FTO substrate and onto WSe_2 electrodes.

XPS data recorded on the corresponding dried films indicate a significant decrease of ≈ 30 % of the terminal sulfide ratio, r_{ster}, compared with films drop casted on FTO (**Figure IV-8a and c**). This suggests that the observed decrease of r_{ster} probably arises from ligand interactions between terminal S anions of the thio or (oxo) thio complexes and W (IV) cations or surface defects of the 2D WSe_2 substrate. This ligand interaction involving terminal S^{2-} or S_2^{2-} thus drastically decreases the presence of available S^{2-} or S_2^{2-} catalytic sites of the films prepared from high pH dispersions. Nevertheless, the relatively higher concentration of $(Mo_2S_6O_2)^{2-}$, $(Mo_2S_{12})^{2-}$

and $(Mo_3S_8O)^{2-}$ complexes allow to preserve a reasonably high concentration of possible active catalytic sites in the optimal pH range. Similarly to the films prepared in the higher pH range, degradation of the electrocatalytic activity of films prepared in the lower pH range, pH < 8.5, probably results of the lower concentration of $(Mo_2S_6O_2)^{2-}$, $(Mo_2S_{12})^{2-}$ and $(Mo_3S_8O)^{2-}$ active catalytic complexes.

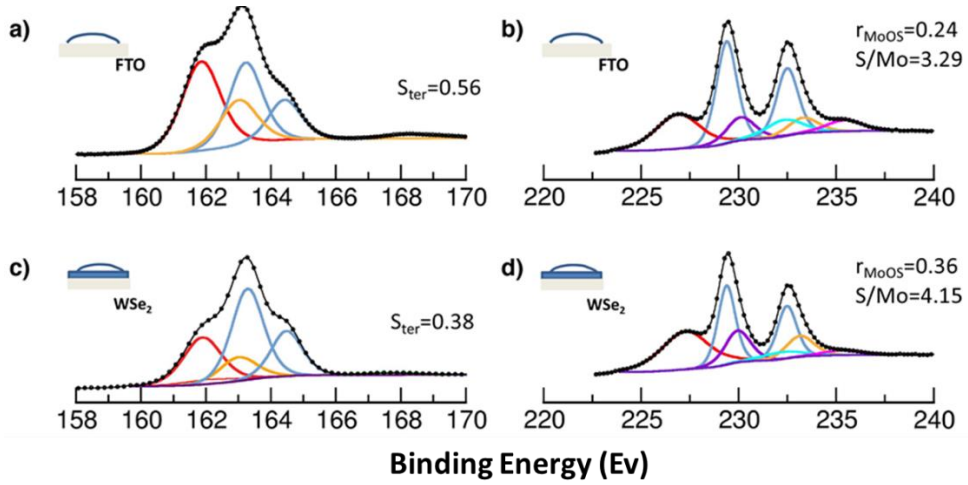

Figure IV - 8: *XPS core-level spectra and deconvolution into S 2p (left column) and Mo 3d (right column) contributions for Mo thio complexes thin films deposited by (a)-(b) drop-casting onto FTO electrodes (c)-(d) drop casting onto WSe_2 electrodes. XPS spectra were recorded after heat treatment110 °C, Air 10 min, immersion in H_2SO_4 0.5 M.*

Typical optical microscopy image of Mo thio oxo-thio complexes film (S/Mo = 5) deposited on FTO electrode by drop casting and air evaporated at room temperature represented in **Figure IV - 9** shows a continuous phase and acicular precipitates.

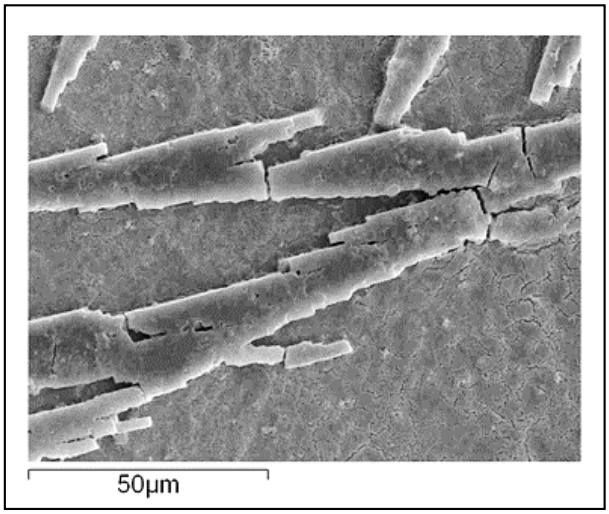

Figure IV - 9: *Optical Microscopy image of thio, oxo-thio Mo complexes film drop casted on FTO substrate showing a continuous phase and acicular precipitates.*

The micro-Raman spectra recorded on the continuous phase and on films prepared from solutions at S/Mo= 5 in the whole range of pH were investigated in the range 8.00 ≤ pH ≤ 9.5. Figure IV - 10 shows vibrations assigned to bridging/shared disulfide (ν (S-S)br/sh), terminal disulfide (ν (S-S)t) and molybdenum sulfide (ν (Mo-S)) observed respectively at 555 cm-1, 525 cm-1 and 382-284 cm-1 [14]. In spite of the large differences in the composition of these solutions, as revealed by ESI-MS, the corresponding spectra exhibit very slight differences mainly in the peak relative intensities indicating presence of all these bonds in the whole pH range. These spectra exhibit similar features to those previously reported for films composed of the tri-nuclear complex (Mo3S13)2- [13], although not identified in our solutions. Micro-Raman spectra recorded on the acicular particles (Figure IV - 10b) reveal a mean peak centered at 400 cm-1, which can be assigned to vibrations referred to MoS2 [13].

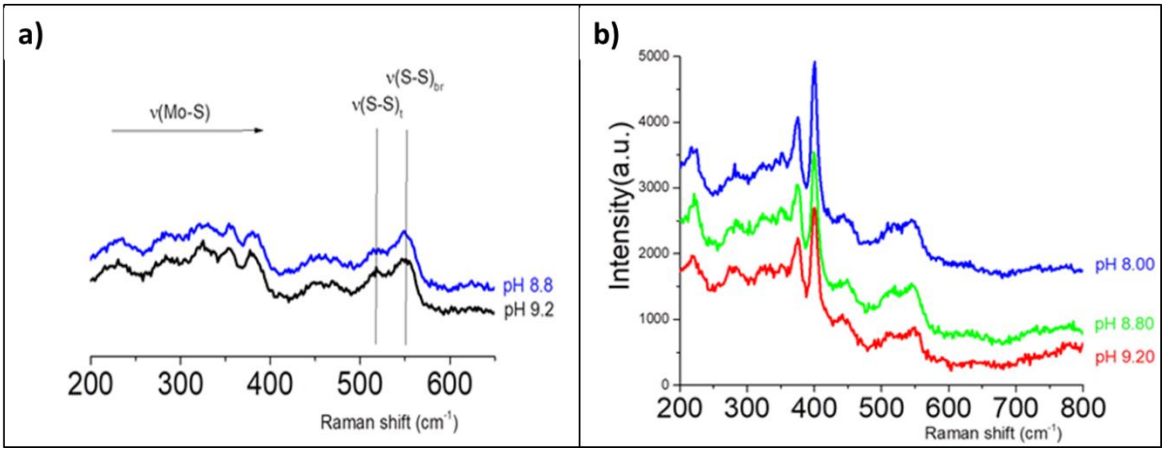

Figure IV - 10: *(a) Micro-Raman spectrum recorded on the continuous phase. (b) Micro-Raman spectrum recorded on the acicular particles.*

The spectroscopy analysis revealed decrease of S_{ter} bondings after drop casting of thio, oxo-thio Mo complexes onto the WSe_2 electrodes, indicating interactions between the ligands and W (IV) cations or existent surface defects and the relative high S/Mo ratio suggests presence of more polymerized complexes, as $(Mo_2S_6O_2)^{2-}$, $(Mo_2S_{12})^{2-}$ and $(Mo_3S_8O)^{2-}$. In addition, as no significant differences were observed in the assignement of peaks, it can be assumed the presence of all ligands (S_{ter}, S_{br} *and S-Mo*) for films prepared in different pHs.

IV.2.3 Contributions in the catalytic activity of drop casted Mo thio complexes on FTO substrate and WSe_2 photoelectrodes

To clarify the respective contributions on the catalytic performances of the thio and oxo-thio complexes, DMF dispersions of pure $(Mo_2S_{12})^{2-}$ complexes were prepared, following a procedure previously described [15]. The HER activity of pure $(Mo_2S_{12})^{2-}$ thio complex was

showed to be outperforming in electrocatalysis [15]. Therefore, properties of these pure $(Mo_2S_{12})^{2-}$ complexes were also investigated on films deposited on FTO substrate and on WSe_2 photo-electrodes and compared with the thio, oxo-thio Mo complexes.

Dispersions of Mo thio complexes aqueous solutions (S/Mo= 5, pH 8.8) and $((Mo_2S_{12})^{2-}, 2NH_4)^+$ DMF ink were deposited by drop casting onto FTO substrates and WSe_2 electrodes at room temperature and heat treated at 110 °C, 10 min under air before electrochemical tests. The films were drop casted from solutions displaying Mo concentration ranging from 0.63mM to 25 mM. Corresponding catalyst loadings are reported in the **Table IV - 2**:

***Table IV - 2**: Mo concentration of catalyst loadings.*

Concentration (mM)	**Catalyst loadings (nanomoles cm^{-2})**
1.3	62.5
2.5	125
5.0	250
10	500

Electrochemical characteristics of the films prepared from Mo thio oxo-thio complexes and of $(Mo_2S_{12})^{2-}$ catalysts are represented in **Figure IV - 11**. In our experimental conditions, similar current density values were recorded at E = -200 mV *vs* NHE, in large mass loadings for the pure $(Mo_2S_{12})^{2-}$ thio complex, as well as for our thio, oxo-thio Mo catalysts. What demonstrates that the thio, oxo-thio Mo complexes display of similar performances as $(Mo_2S_{12})^{2-}$ for the HER. In addition, electrocatalytic current increased with the concentration of thio, oxo-thio complexes on FTO electrode, while the current remained constant for $(Mo_2S_{12})^{2-}$ complexes (**Figure IV - 10c**, at E ≥ -200 mV). As the electrocatalytic activity is higher for mass loadings of 10 mM/cm^2, either for drop casted onto FTO or WSe_2 surfaces, all further analysis will take account concentration of thio, oxo-thio Mo complexes at 10 mM cm^{-2}.

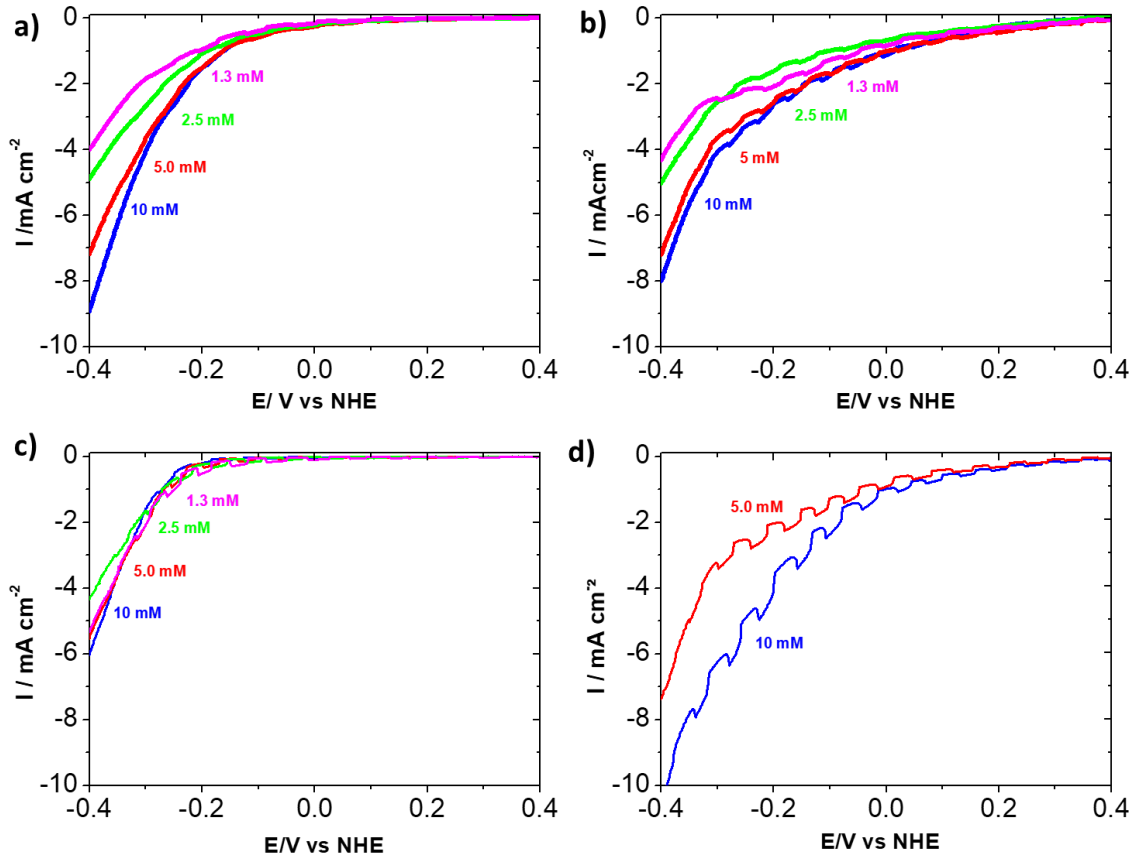

Figure IV - 11: *Electrochemical and photo-electrochemical characteristics of catalysts films. Mo_xS_y at S/Mo = 5, pH 8.8 on (a) FTO substrate and (b) drop casted on WSe_2 photo-electrode; (c) $(Mo_2S_{12})^{2-}$ on FTO substrate, (d) $(Mo_2S_{12})^{2-}$ drop casted on WSe_2 photo-electrode.*

In **Figure IV – 12** is presented the *J – V* curves recorded on WSe_2 electrodes after drop cast of Mo_xS_y complexes with different pH. The *J – V* curves obtained from Mo_xS_y complexes depositoed onto FTO substrate are also presented (first row of the panel), for a sake of comparison. Interestingly, the electroactivity turns out to be dependent on the pH synthesis of the oxo-thio complexes. It can be seen the electrocatalytic activity for films formed by drop casting onto WSe_2 substrates at pH between 8.5 and 9.0 is higher than for pH 9.5. Which is not the case on FTO electrodes (**Figure IV - 12**, first row), stressing out differents interactions with WSe_2 based electrode. As previously observed, this pH range ($8.5 \leq pH \leq 9.0$) corresponds to the predominance domain of Mo dimers or trimers.

Taking a closer look into the photoactivity of the WSe_2 electrodes, the photocurrent is negligible and does not show a clear trend, regarding the pH. Nevertheless, these diversified behaviors observed, depending on the nature of the electrode (and the pH), suggest specific interactions with the thio, oxo-thio Mo complexes. This observation can be emphasized by

boosting more spontaneaously these Mo complexes with a different deposition method, using a dip-coating technique.

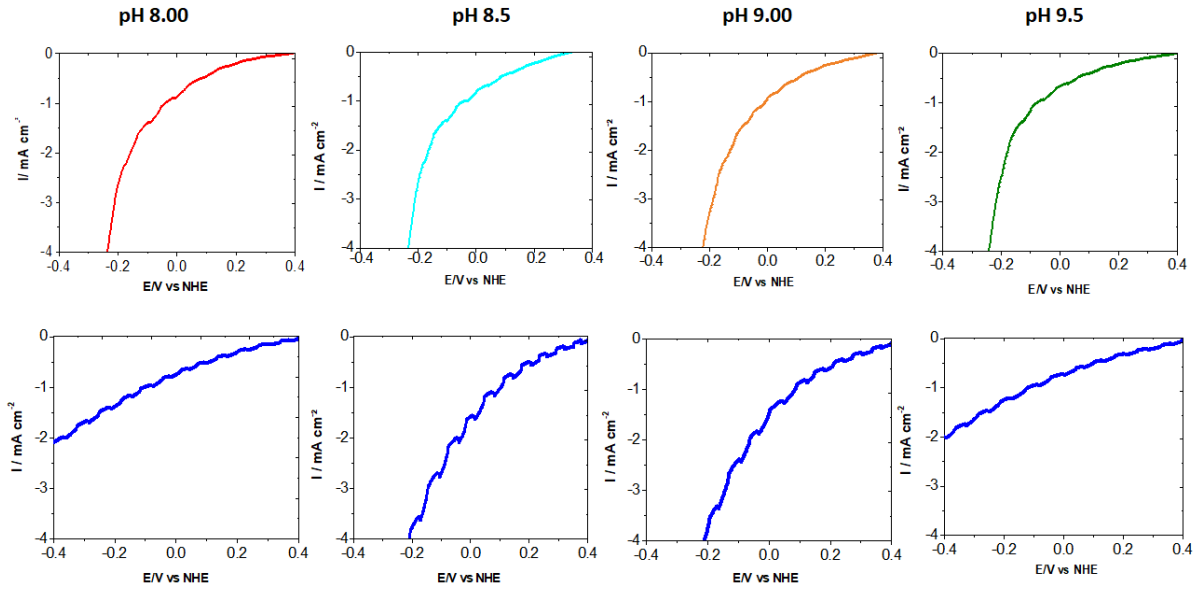

Figure IV - 12: *Electrochemical characterization of Mo_xS_y complexes films prepared at S/Mo= 5 and at various pH synthesis in H_2SO_4 0.5 M. (First row) J-E curves under intermittent illumination of corresponding films prepared on FTO are given as control. (Second row) The J-E curves are recorded under intermittent illumination on films prepared by drop casting onto WSe_2 electrodes.*

IV.3 Thio and oxo-thio Mo complexes (Mo_xS_y) catalyst dip coted on 2D p-WSe_2 photocathodes

IV.3.1 Selection of Mo thio oxo-thio complexes species by dip-coating and film formation

As aforementioned, taking advantage of the large variety of these Mo complexes distribution solutions, an interesting approach would be to select the most interactive species taking benefit of the "WSe_2-thio complexes" interactions that can be developed in contact with solution. So, we have focused on film forming process favoring the anchorage of thio - and oxo-thio-Mo complexes developing high complexing interactions with the WSe_2 surface and high catalytic performances. Similar to a strategy previously proposed to enhance the long term stability of the molybdenum sulfide clusters with defective graphene catalyst and involving S-C covalent bonding [16], chemical bond formation between thio or oxo-thio complexes and WSe_2 surface will improve anchoring of the thio-complexe catalysts onto the photo-electrode. More particularly, strong bonding formation between the thio complexe ligands and surface defects of WSe_2 2D material are expected to help to heal these defects, hence, improving the optoelectronic properties of the 2D materials.

A film forming process, denoted afterwards selective dip-coating, has been explored and involves successive dip coatings with long duration time (2 x 16h), followed by H_2O washing. For a well-defined range of S/Mo values and polycondensation ratios (or pH range), the performances of dip-coated photo-electrodes are observed to be significantly better than the drop casted ones in the large range of film thickness investigated, 50 nmoles $cm^{-2} \leq n \leq 750$ nmoles cm^{-2} of Mo thio, oxo-thio complexes.

IV.3.2 PEC performances of thio, oxo-thio Mo Complexes in 2D Materials

IV.3.2.1 Photocatalytic activity of 2D WSe_2 photoelectrodes dip coated in various pH range of Mo complexes

Figure IV - 13 reports selected J-V curves recorded on films prepared by selective dip coating in Mo complexes solutions fabricated at S/Mo= 5. On films displaying similar catalytic activity, different photocurrent densities ranging from -0.25 to -2.0 mA cm^{-2} have been observed on films prepared at various pH. The non-correlated evolutions of photocurrent activities on dip-coated and drop-coated samples suggest that our films are composed of different Mo

complexes, including complexes displaying high catalytic activity in association with Mo complexes capable to heal surface defects.

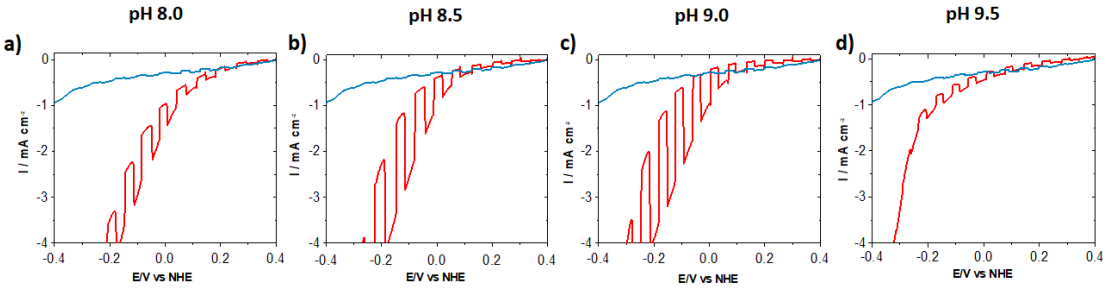

Figure IV - 13: *J-V curves recorded in 0.5 M H_2SO_4 on WSe_2 electrodes after selective dip coating into Mo complexes-solutions at various S/Mo = 5 and various pH range. The blue curves represent the photocurrent of bare 2D WSe_2 photo-electrode.*

Because Mo complexes are designed in basic pH, where monomers and oxo-thio-complexes are in significant proportions, it is thus crucial when designing Mo complexes in all-aqueous solvent to better evaluate the respective contributions of the thio Mo complexes ($(MoS_4)^{2-}$, $(Mo_2S_{12})^{2-}$) and of the oxo-thio Mo complexes on the catalytic activity and the healing effect.

Properties of pure $(Mo_2S_{12})^{2-}$ coated - WSe_2 electrodes were thus investigated in a large range of catalyst loadings (30 < n nanomoles < 500) cm^{-2}. Large current densities up to -10 mA cm^{-2} at -0.4 V vs NHE in the range of the best current densities recorded on films prepared from our thio Mo complexes were observed with pure $(Mo_2S_{12})^{2-}$ highlighting the high electro-catalytic activity displayed by this complex. Concerning its photo-catalytic properties, the $(Mo_2S_{12})^{2-}$ films display slightly larger photocurrent densities, as presented in **Figure IV - 14,** compared with drop casted films prepared from our thio Mo complexes solutions.

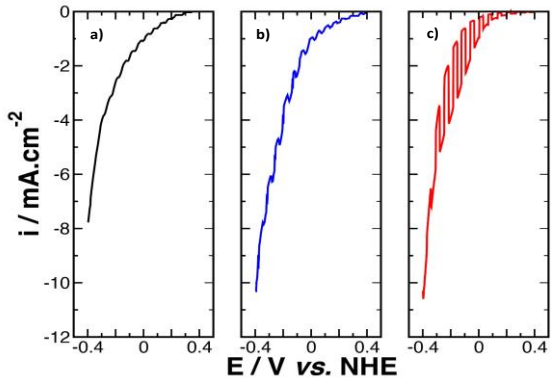

Figure IV - 14: *J-V curves recorded in 0.5 M H_2SO_4 on WSe_2 electrodes coated by (a) Mo thio complexes (S/Mo= 5, pH 8.8) film deposited by drop casting (b) pure $(Mo_2S_{12})^{2-}$ complex film deposited by drop casting (c) Mo thio complexes (S/Mo = 5, pH 9.0) film deposited by selective dip coating. Films were calcined 110 °C, 10 min under Air atmosphere before photo-electrochemical testing.*

Nevertheless, whatever the film forming process used (drop casting or selective dip coating), the photocurrents recorded on $(Mo_2S_{12})^{2-}$ films remain significantly lower than those observed on films fabricated from our oxo-thio Mo complexes solutions by dip coating process (**Figure IV - 12d and Figure IV - 14b**). As a consequence, the higher photocurrent densities up to -2 mA cm^{-2} at -0.2 V vs NHE recorded on our films highlight the beneficial effect of the Mo thio monomers or oxo-thio complexes compared with $(Mo_2S_{12})^{2-}$ to heal the 2D WSe_2 surface defects.

IV.3.2.2 Time influence of dip coating on the photocatalytic performance

The influence of the dip coating time has also been investigated for three different times. Mo thio complexes films characteristics prepared by selective dip coating on WSe_2 substrates (S/Mo= 5 and pH 9.0) were recorded by Linear Sweep Voltammetry (LSV) under intermittent light illumination. A slow and progressive increase of the photocatalytic activity is observed in **Figure IV - 15** with increased time duration clearly recorded throughout the 2 x 16h hours of dip coating.

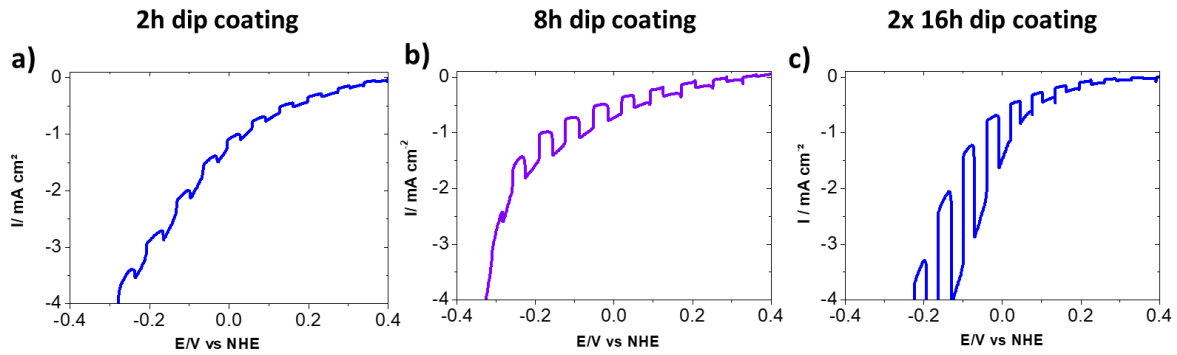

Figure IV - 15: *LSV curves recorded on films dip coated (a) 2h, (b) 8h and (c) 2x 16 h showing increase of photocurrent intensity with dip coating duration times. Electrolyte: H_2SO_4 0.5 M.*

XPS analysis was performed for the WSe_2 electrodes dip-coated in different times and the obtained data was compared with Mo thio oxo-thio films drop casted onto FTO substrate, as shown in **Figure IV - 16**. For the film withdrawn after the first hours of dip coating (t < 4h), XPS data recorded highlight a peak concentration of the oxo-thio-complexes, (**Figure IV-16b**) probably arising from preferred deposition of $(MoOySz)^{t-}$ monomers present in larger proportion in the solution. At longer dip coating duration times (**Figure IV - 16c**), changes in the film composition are clearly observed, illustrated by a decrease of the Mo-oxysulfide concentration and an increase of S/Mo ratio, indicating selection of complexes at high S/Mo

ratio. Various driving forces may cause the changes observed in the film composition. Selection of the thio, oxo-thio-Mo complexes may first be dictated by adsorption energy or complexation stability constants involving thio-Mo complexes and surface entities of the WSe_2 photo-electrodes. Then, this selection may be rather driven by interactions between thio Mo complexes and Mo sulphide film initially deposited on the photo-electrode surface. Both driven by evolution towards complexation equilibriums involving the various ligands and surface species of the WSe_2 electrodes. Consistently with this selection process, the best photocatalytic activities were achieved with dip coatings alternated with desorption stages favoring removal of less interactive species before subsequent impregnation.

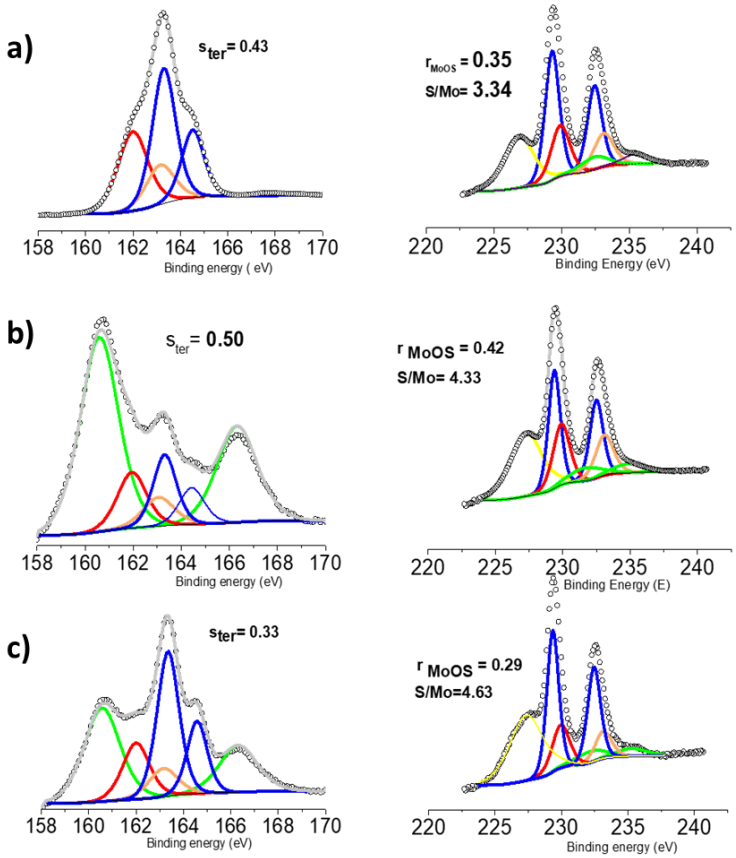

Figure IV - 16: *XPS spectra recorded on (a) Mo thio complexes films prepared by drop casting on FTO electrodes are given for comparison. Mo thio complexes films dip coated (b) 4h and (c) 2x 16h after photo-electrochemical testing in 0.5 M H_2SO_4. Mo 3d and S 2s region: MoS_2 (blue line), MoO_3 (green line), MoO_yS_z (red line), S^{2-} and S_2^{2-}, (Yellow line). S 2p and Se 3p region: terminal S_2^{2-} (red line), bridging S_2^{2-} (blue line), SO_4^{2-} (green line) Se 3p (green line).*

IV.3.3 Optimization of the photocatalytic activity of Mo thio oxo-thio complexes on WSe_2 electrodes

Best photocatalytic performances were observed for dip coated films fabricated from solutions at S/Mo = 5 and in the optimum pH range, 8.5 ≤ pH ≤ 9.0. More interesting, without the use of any passivating additive, much higher photocurrents were achieved after impregnation of the Mo thio complexes catalysts compared with noble metal catalyst such as Pt-Cu [17]. Although the two catalysts exhibit similar electroactivity, as revealed from the dark currents, a photocurrent of -2.5 mA cm^{-2} was recorded onto the WSe_2 photocathode after Mo thio complexes activation against -0.4 mA cm^{-2} when activated by Pt-Cu, as presented by the LSV curves in **Figure IV - 17**.

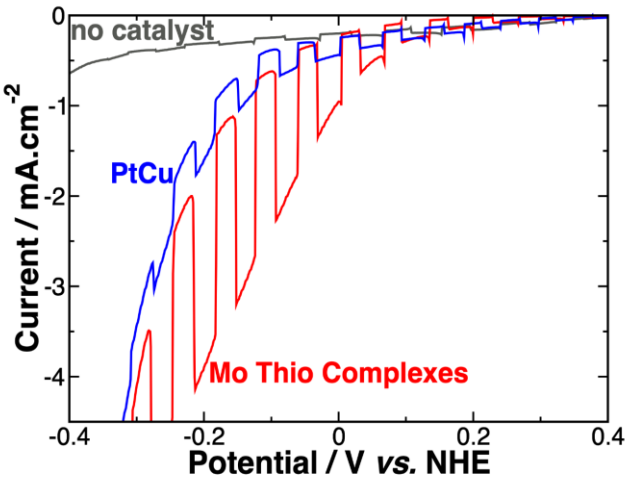

Figure IV - 17: *LSV curves under intermittent (1 sun) illumination showing higher photocurrent on WSe_2 photoelectrode after deposition of oxo-thio Mo complexes (S/Mo= 5. 2 x 16 h) compared with HTS free-WSe_2 photo-electrode activated by a Pt-Cu catalyst.*

The significant photocurrent improvement observed with Mo thio complexes could be attributed to a drastic decrease of recombination centers, making the Mo thio complexes acting both as active catalyst and as healing additive. Although this trend relates the importance of catalyst addition in the low overpotential domain, better catalytic performances also usually yield larger photocurrents at higher overpotentials [18]. Interestingly, close inspection of illuminated j-V curves recorded on the Mo complexes coated-2D WSe_2 reveals a more complex behavior.

A remarkable ability exhibited by the Mo sulfide complexes catalysts prepared in a well-defined pH window (8.5 < pH < 9.0) to produce the highest photocurrent at large overpotential was reproduced on two different sets of films prepared at S/Mo= 5 (**Figure IV - 18**). At low

overpotentials, 0.0 V < E < +0.4 V vs NHE, larger photocurrents were observed for WSe_2 electrodes displaying of better electro-activities (**Figure IV - 18**, inserts). In contrast, at high cathodic overpotentials, the larger photocurrents were not systematically recorded on the films displaying the best electro-catalytic performances at low potentials. Thus, the changing of catalytic behavior may result from the different specific interactions of the Mo complexes with the WSe_2 substrate.

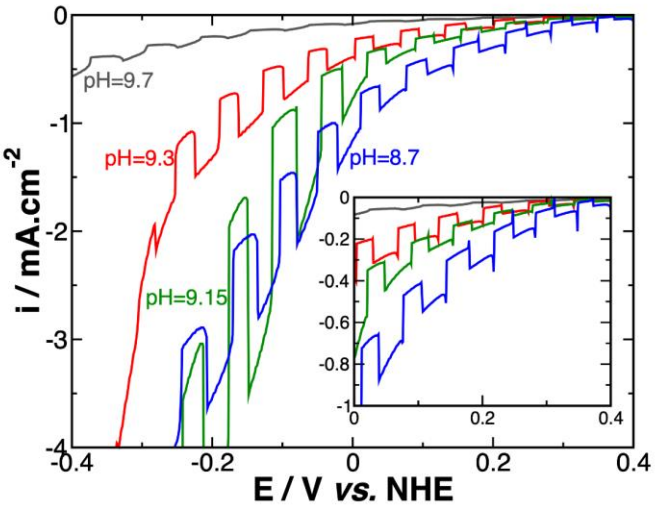

***Figure IV - 18**: LSV curves of WSe_2 dip coated 2x16h on Mo complexes catalysts at different pH and S/Mo ratio = 5. Electrolyte: 0.5 M H_2SO_4. Insert: Zoom of the low over-potential region highlighting electrocatalytic performances of the various Mo thio complexes catalysts.*

IV.3.4 Stability of Mo thio oxo-thio complexes-WSe_2 photo-electrodes

Still further, in **Figure IV - 19,** a chrono-amperiometric curve recorded under chopped light on a WSe_2 electrode - after dip coating in Mo_xS_y catalyst solution (2 x 16h) - demonstrated a good stability for 300s . Indeed, no significant photocurrent decrease over time is observed and XPS spectra recorded on films before and after the HER do not reveal significant change in the S/Mo or r_{Ster} ratios. According to previous works [13][15], our results demonstrated stability of the thio-Mo-complexes during the HER, in acidic electrolyte. We highlight that these first results were achieved on Mo complexes just deposited on the 2D materials by dip coating, and we anticipate that the electrode stability could be improved even furhter by subsequent encapsulation in Nafion [15].

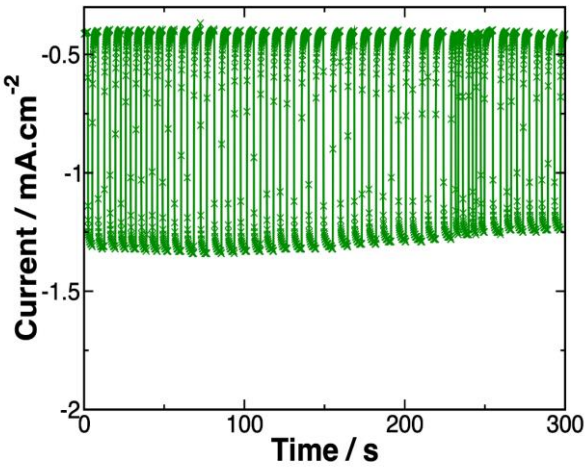

Figure IV - 19: *Chrono-amperiometric curve recorded on WSe_2 electrodes activated by Mo oxo-thio complexes (2x 16h) in 0.5 M H_2SO_4 under intermittent illumination (100 mW cm^{-2}).*

IV.3.5 H_2 production of Mo thio oxo-thio complexes-WSe_2 dip coated on 2D WSe_2 photoelectrodes

To demonstrate that the recorded photocurrent was ascribed to the hydrogen generation, we measured the real-time hydrogen evolution by gas chromatography using a closed photo-electrochemical cell. **Figure IV - 20** presents the hydrogen activity detected, giving the Faradic efficiency. Under constant illumination (1.5 AM 100 mW cm^{-2}, using a Pt calibration cell (Pt foils both as working and counter electrodes) and assuming a Faradic efficiency of 100 % for the Pt calibration device, we determined for j = -0.25 mA cm^{-2} (at E = -0.1 V vs NHE) a Faradic yield of about 97 %.

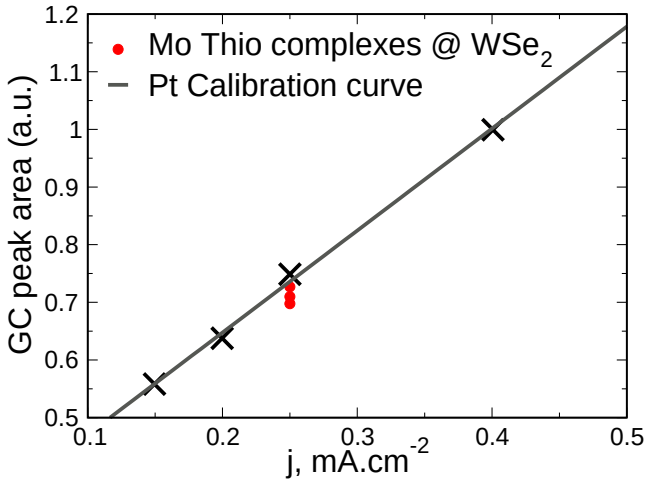

Figure IV - 20: *H_2 GC peak areas determined on a Pt electrode (calibration cell) and on WSe_2 photo-electrode activated by Mo_xS_y complexes catalyst at E = - 0.1 V vs NHE. Electrolyte: 0.5 M H_2SO_4. Counter electrode: Pt. 1 Sun illumination.*

IV.3.6 Material characterization of dip coated WSe_2 photoelectrodes with Mo thio oxo-thio catalyst film

IV.3.6.1Mo thio complex-coated WSe_2 film morphology

To get a better insight of the coated WSe_2 film morphology, HRTEM has been performed on the coated photo-electrodes samples before and after HER. Typical HRTEM image (see **Figure IV - 21**) reveals an ultrathin amorphous film of irregular thickness ranging from 2 to 10 nm coating well-crystallized 2D nanoflakes. The well-crystallized nanoflakes were unambiguously identified as WSe_2 from the lamellar structure displayed by the nanoflakes (≈ 12 nm thickness), in addition to the Se/W ratio value determined by EDS, $(Se/W)_{atom} = 2$. Although an accurate determination of the S/Mo ratio is relatively tricky due to the overlap of the 3d Mo and 4s S energy peaks, S and Mo were nevertheless detected as major elements into the amorphous ultrathin film, allowing the full identification of the amorphous coating related to the co-catalyst film.

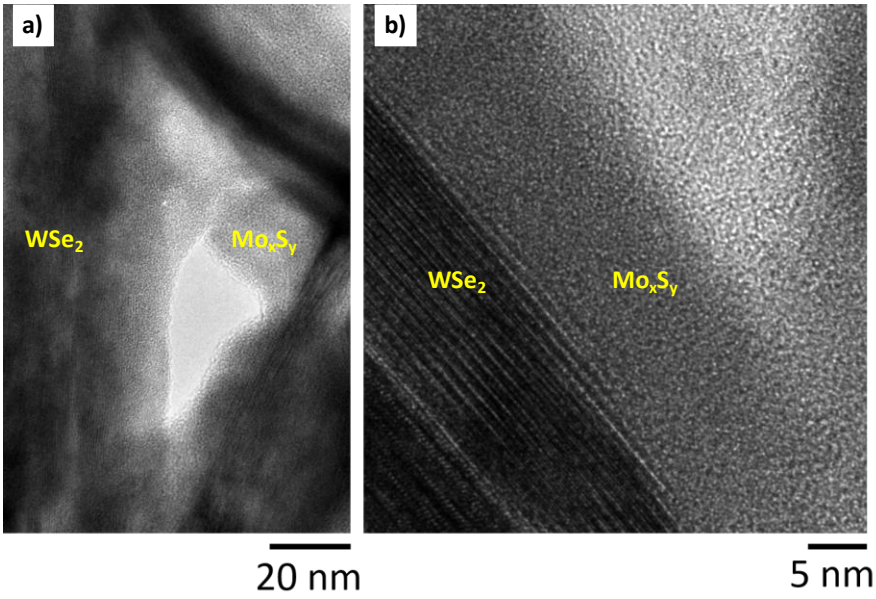

Figure IV - 21: *HRTEM images of the (a) ultrathin amorphous film of catalyst with thickness varying from 2 to 8 nm, (b) crystallized 2D WSe_2 nanoflakes of ≈ 12 nm thickness and the ultrathin catalyst film.*

The amount of the loaded Mo thio and oxo thio complexes on WSe_2 photoelectrode revealed by HRTEM investigation was quantitatively assessed (S/Mo = 5, pH 9.0, dip coated 2 x 16 h) by Inductive Coupled Plasma (ICP) measurements. After sonication and immersion of eight electrodes in 10 ml NaOH 0.1 M solution, the loaded amount was measured to be 100 -150 Mo nanomoles cm^{-2}. With the assumption of a full coverage of the surface area of the 2D

material including the basal plane and a head surface of 0.5 nm^2 for the Mo complexe, the film thickness is thus determined in the order of some few layers (two to ten monolayers).

As the catalyst film results from the conversion of the thio-, oxo-thio Mo oligomers into an amorphous polymeric phase, two different mechanisms could be proposed: i) Formation of an oligomer-based coordination polymer involving interactions between the sulfide-disulfide groups and the Mo centres [14]. Indeed, the coordination-reticulation of the polymer is promoted by the various oxidation states displayed by the Mo centres, as shown by XPS; ii) Oligomer-induced hetero-nucleation and growth, as previously observed in the preparation of metal organic framework [19]. The change of S/Mo ratio experimentally observed in our co-catalyst films, with dip coat time duration ($(S/Mo)_{atom}$ = 4.3 -> 4.6). Thus, we propose that the first layers of Mo thio, oxo-thio oligomers anchored on the WSe_2 substrate serve to direct the formation of the subsequent layers by hetero-nucleation. The observed increase of S/Mo ratio arises from addition of selected oligomers displaying of higher sulfide or disulfide groups density, or higher S/Mo ratio such as $(Mo_2S_{12})^{2-}$. Moreover, these various interactions and reticulation are probably enhanced during the final drying stage, which improves the film consolidation.

IV.3.6.2 Identification of thio, oxo thio Mo complexes thin films dip coated on p-WSe_2 electrodes by XPS

Best photocatalytic performances were thus observed on films prepared from solutions fabricated in the pH range 8.7 < pH < 9.3 exhibiting, in addition to Mo monomers, $(Mo_2S_6O_2)^{2-}$, $(Mo_2S_{12})^{2-}$ and $(Mo_3S_8O)^{2-}$ peaks concentrations. To demonstrate the presence of these latter complexes into the dip coated solid film, fine inspection was performed with XPS analysis. The XPS data recorded on these films clearly reveals an average r_{MoOS} ratio, r_{MoOS} = $(MoOS)/(MoOS+MS)_{molar}$, close to 0.23, as presented in **Figure IV-22**. This ratio was observed to be lower after complexes selection by dip coating on WSe_2 compared to values determined on drop casted FTO (r_{MoO} = 0.24-0.34) or on drop casted WSe_2 (r_{MoO} = 0.36) electrodes (**Figure IV-8)** . Although, this reasonable high ratio reveals that the complexes selection must include Mo oxo-thio-complexes such as $(MoOS_3)^{2-}$, $(Mo_2S_6O_2)^{2-}$ and $(Mo_3S_8O)^{2-}$ in association to the Mo thio complexes.

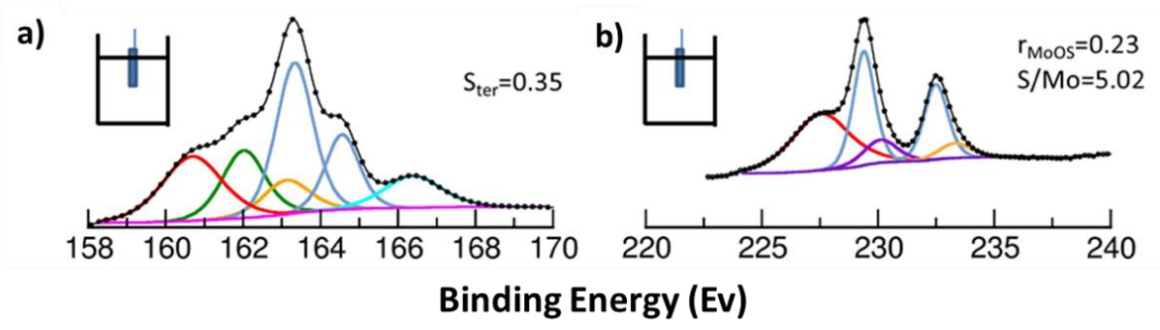

Figure IV - 22: *XPS core-level spectra and deconvolution into (a) S 2p and (b) Mo 3d contributions for Mo thio complexes thin films deposited by selective dip coating onto WSe_2 electrodes. Recorded after heat treatment 110 °C, Air 10 min, immersion in H_2SO_4 0.5 M, 15 min.*

Another interesting point is the high value of rs_{ter} (> 0.35) determined on photo-catalytically efficient dip-coated WSe_2 electrodes. Even some terminal sulfide-disulfide groups are partially removed as a consequence of their high interaction with the WSe_2 electrode substrate, this significant rs_{ter} value suggests presence of a high proportion of non-linked, accessible sulfide-disulfide groups arising probably from $(MoS_4)^{2-}$, $(Mo_2S_{12})^{2-}$ and $(Mo_2S_6O_2)^{2-}$ complexes for the HER, after anchoring on the WSe_2 photoelectrode. All these data show that our most efficient photocatalytic films are mainly composed of Mo monomers, $(Mo_2S_{12})^{2-}$, $(Mo_2S_6O_2)^{2-}$ and *to a lesser extend* $(Mo_3S_8O)^{2-}$ complexes in high interaction with the WSe_2 photo-electrode surface.

IV.3.6.3 Further insights about the thio, oxo-thio Mo complexes thin films on p-WSe_2 by Raman Spectroscopy

Complementary insights about the thio, oxo-thio Mo complexes dip coated onto WSe_2 photoelectrode were provided by Raman spectroscopy. The obtained Raman spectra for the WSe_2 electrode coated with Mo_xS_y catalyst is illustrated in **Figure IV - 23** (Raman spectra for Mo_xS_y drop casted onto FTO is given as reference). While vibration of bridging/shared disulfide (ν $(S\text{-}S)_{br/sh}$) and terminal disulfide (ν $(S\text{-}S)_t$) are clearly observed, respectively at 555 and 525 cm^{-1} - on the whole set of spectra (pH 8.0 < pH < PH 9.5) recorded on Mo thio complexes films drop casted on FTO (**Figure IV - 23a**). These vibrations were not observed onto the dip coated films on WSe_2 substrates (**Figure IV - 23b**).

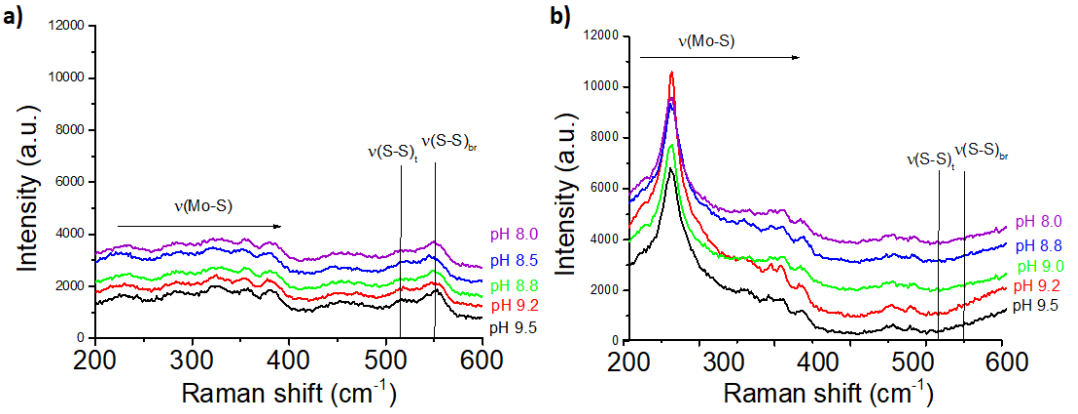

Figure IV - 23: *Raman spectra of Mo thio complexes films fabricated from solutions at S/Mo= 5 and at various pH and deposited by (a) drop casting onto FTO and (b) dip coating on WSe_2 electrodes. Raman spectra were recorded after heat treatment 110 °C, Air 10 min, immersion in 0.5 M H_2SO_4. For the selective dip coated film onto WSe_2 electrodes, spectra were recorded after electrochemical testing.*

The dendrite-like acicular particles have only been observed when the Mo complexes are deposited directly onto FTO substrate (**Figure IV - 9**), suggesting a phase separation during this film formation process by evaporation-drying – not observed by dip coating. In addition, the main Raman peak recorded on these acicular particles (at 400 cm^{-1}) is not observed on films spectra prepared on WSe_2 photo-electrodes, as showed in **Figure IV - 23b**. This probably results from the partial chemical transformation of the di-sulfide bonds in contact with the surface defects of the WSe_2 substrate, thus decreasing their concentration under the detection threshold. Note that the collapse of the di-sulfide bonds is associated to the emergence of two peaks at 455 and 500 cm^{-1} (**Figure IV - 23b**). Moreover, no significant evolution was observed on the Raman spectra recorded before and after acid soaking or HER cycling, revealing no changes of the structure or composition of the thio-, oxo-thio-Mo complexes. These results show to be consistent with previously reports in the literature [13][15].

To sum up, both XPS and Raman spectroscopy results have shown the existence of specific interactions of Mo thio complexes with WSe_2, confirming a selective deposition during the immersion step through the dip coating process.

IV.3.7 Physical properties of Mo thio oxo-thio complexes catalyst film

The opto-electronic properties of the catalyst thin film were performed to better understand its physical properties of the photocathode. First, optical properties were measured through UV-Vis absorption spectra recorded onto the catalyst film deposited on glass substrates and annealed at 110°C (**Figure IV - 24**).

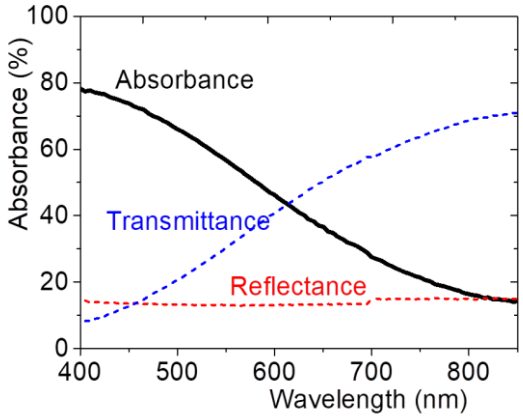

***Figure IV - 24**: transmission, reflectance and absorption curves of co catalyst films drop casted on FTO from thio-, oxo-thio-Mo complexes solutions (S/Mo= 5, pH 9.0). The co-catalyst films were Air evaporated at room temperature and heat treated at 110°C under air.*

The direct optical transition of the catalyst film was demonstrated from the straight line observed in the Tauc's Plot by plotting the square of the absorption coefficient $(\alpha h\nu)^2$ against the photon energy ($h\nu$), from which a band gap energy of 1.8 eV can be extrapolated, as presented in **Figure IV - 25a**. Moreover, further analysis concerning the catalyst film-electrolyte interface have been performed in 0.1M Na_2SO_4, pH 7, using a catalyst film deposited onto FTO substrate, using Electrochemical Impedance Spectroscopy (EIS). The Mott-Schottky plot showed in **Figure IV - 25b**, determined from capacitance values extracted at 100 Hz, revealed a n-type semi-conduction. In addition, a flat band potential (E_{fb}) of -0.2 V vs. NHE is determined from the intercept of the linear portion of the Mott–Schottky plot with the potential axis. From the slope of the Mott-Schottky plot (0.7 $10^9 cm^4 F^{-2} V^{-1}$ - for capacitance values extracted at f = 100 Hz), the charge carrier densinty was determined as being $N_D = 10^{21}$ cm^{-3}, considering a dieletric constant of $\varepsilon = 4.2$ [20].

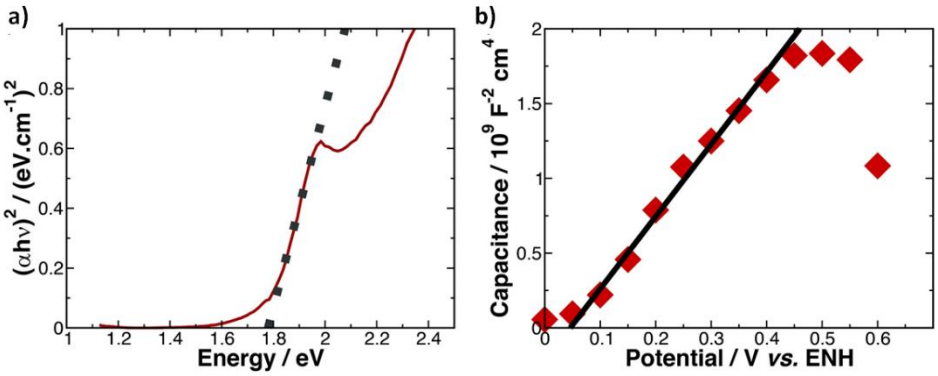

***Figure IV - 25:** (a) Tauc's Plot obtained from UV-vis absorption data recorded on Mo_xS_y complex co catalyst film drop casted on FTO substrate. (b) Mott-Schottky plot of Mo complexes co catalyst – FTO showing a positive slope and a flat band potential E_{Fb}= +0.47 V vs NHE.*

Thanks to these analyses (Tauc's plot and Mott-Schottky), we thus located its conduction band from the donor density (N_D) and the flat band potential (E_{fb}) values using the equation for the density states in conduction band, $N_D = N_v \, . e^{-(Efb-Ebc)/kT}$ [21], where N_v denotes for the density of states in the conduction band, which can be calculated from $N_V = 2. (2\, p\, m_e k\, T/h^2)^{3/2}$, where m_e is the effective mass of the electron in MoS_2 [22]. Thus, assuming $m_e = 0.4\, m_o$, N_D = 2.5 10^{19} cm^{-3}. The conduction band (E_{bc}) of Mo_xS_y complexes catalyst film was determined at -0.3V vs. NHE.

To construct the band energy diagram of the WSe_2 and the co-catalyst film, we have determined the band gap of our exfoliated nanoflakes, as being E_g = 1.45 eV. The optoelectronic properties determined for Mo complexes catalyst film and the conduction band energy level of -0.45 eV vs. NHE for the WSe_2 nanoflakes film [21] were used to obtain the band energy diagram of our photoelectrode, as presented in **Figure IV - 26**. The diagram shows that the n-Mo_xS_y catalyst film should favor charge separation and efficient migration of the photo-induced electrons from the p-WSe_2 to provide the hydrogen production.

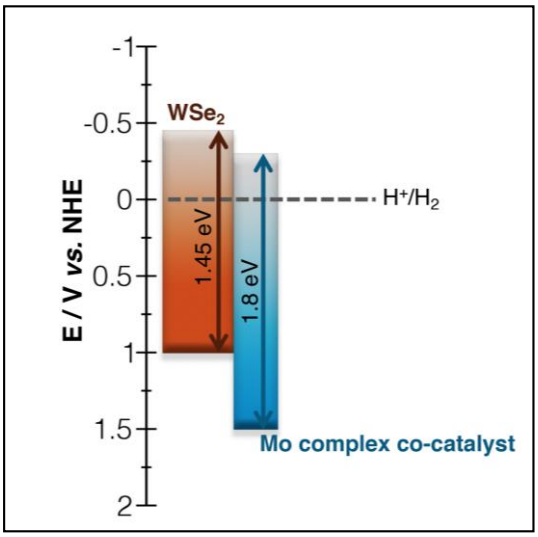

***Figure IV - 26**: Band energy diagram of WSe_2-Mo thio, oxo-thio catalyst photoelectrode.*

Hence, the catalyst film of n-type semi-conduction yield to a p/n junction with the p-WSe_2, which might result in a increase of the band bending in the p-type WSe_2 space charge region [23]. On the other hand, the catalyst has turned out to be able to improve the performance of 2D WSe_2 nanoflakes, which is assumed to exhibit high surface defect density. Further investigations of the respective role of the Mo complexes as healing additive and catalyst were carried out through different analysis and explored using DFT calculations. These investigations will be discussed in the following sections.

IV.3.8 Electrochemical evidences of Mo thio-, oxo-thio complexes film as Healing Catalysts for the 2D WSe_2

Figure IV - 27 shows the dimensionless current obtained from LSV measurements for a bare WSe_2 (grey curve) and a Mo thio-, oxo-thio complex coated WSe_2 (blue curve). An interesting change of behavior is observed. The current obtained from bare WSe_2 electrode exhibits currents spikes typical for the presence of charge recombination and/or accumulation (positive spikes); such behavior is completely eliminated for the coated WSe_2. We can also notice that the current slope is the same for the dark current and the current under light for the bare WSe_2 electrode. In contrast, for thio-, oxo-thio Mo complex-WSe_2 a clear change of slope is observed from dark current to current under illumination: a lower overall polarisation resistance is obtained. It is likely related to a decrease of the recombination rate together with an activation of the charge transfer over polarization.

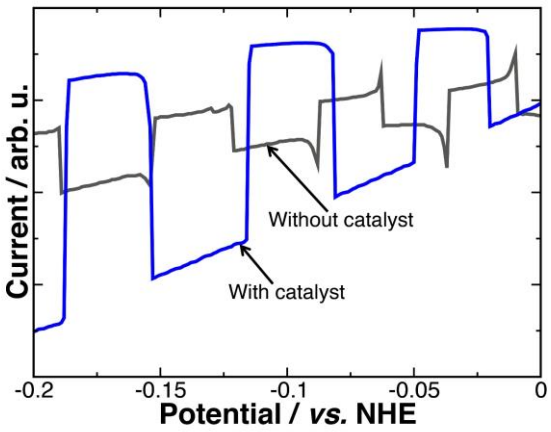

Figure IV - 27: *LSV curves under intermittent illumination (1.5 AM 100 mW cm^{-2}) showing a significant decrease of transient photocurrent on thio, oxo-thio Mo complexes coated WSe_2 photo-electrode compared with a bare photo-electrode.*

To gain more insights into the enhancement of the photocatalytic performance after the thio-, oxo-thio Mo complexes catalyst deposition, electrochemical impedance spectroscopy (EIS) was performed on bare and coated WSe_2 using Mo_xS_y catalyst film photoelectrodes. The analysis aimed to provide an experimental evidence of the decrease of the charge transfer resistance after catalyst deposition under illumination, using a LED (λ = 450 nm).

Bode plots obtained from impedance data are presented in **Figure IV - 28.** The bode plot corresponding to a bare WSe_2 shows no significant variation on the modulus plot compared with the catalyst-coated WSe_2 under illumination. The phase angle variation plots show changes in the time constants. At high frequency a time constant is present for both samples, attributed

to the bulk resistance of the electrode. Two time constants are clearly visible for the bare WSe_2, at about 10^2 rad s^{-1} and 10^0 rad s^{-1}, whereas the last one tends to vanish under electrode polarization. Differently, only one time constant is detected for the coated sample, which decreases upon polarization.

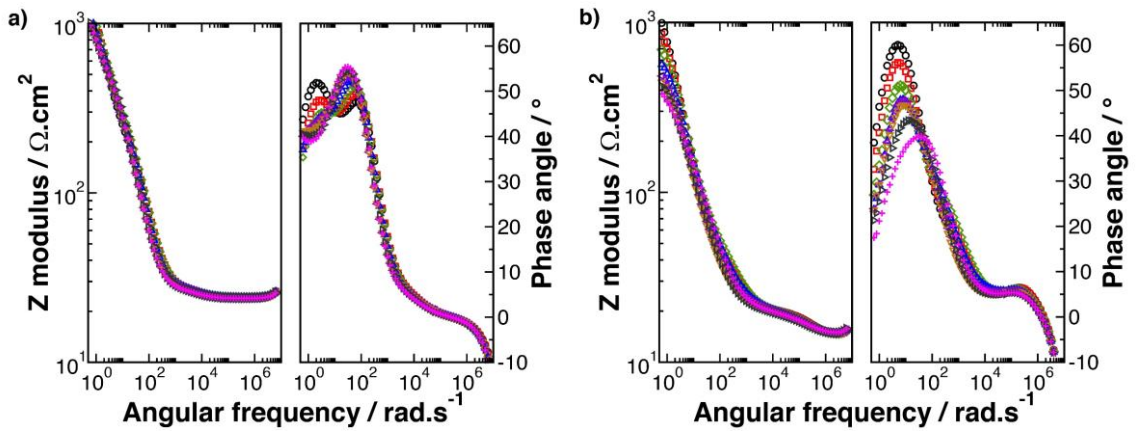

Figure IV - 28: *Bode plots representation from EIS measurements of (a) bare and (b) Mo complexes co catalyst coated WSe_2 photo electrodes under illumination (λ = 450 nm) at various applied potentials from 0.2 V to -0.15V vs NHE. Electrolyte 0.5 M H_2SO_4, pH1.*

To get a better insight regarding the charge process within the different electrodes, an equivalent circuit has been proposed, **see Figure IV - 29**. To take into account the different time constants, we propose to use a string of three Z_{arc} in series with a series resistance (R_S), the latter standing for the electrolyte resistance. Each Z_{arc} has been ascribed to different processes: $Z_{arc}(1)$ for the so called bulk impedance [24]– the electric impedance of the electrode –; $Z_{arc}(2)$ for the recombination process and $Z_{arc}(3)$ for the interface impedance (charge transfer resistance together with the interface capacitance). Where Z_{arc} element is equivalent to a constant phase element ($Z_{arc} = \frac{R}{1+(j\omega\tau)^{\alpha}}$). With R: the resistance (width of the semicircle), $\boldsymbol{\tau}$: the time constant of the (R)(P) process and $\boldsymbol{\alpha}$: the CPE alpha parameter.

This element has been used here because it makes the analysis of the different parameters easier since there is no need for instance to use the Brug-Formula to extract the capacitance.

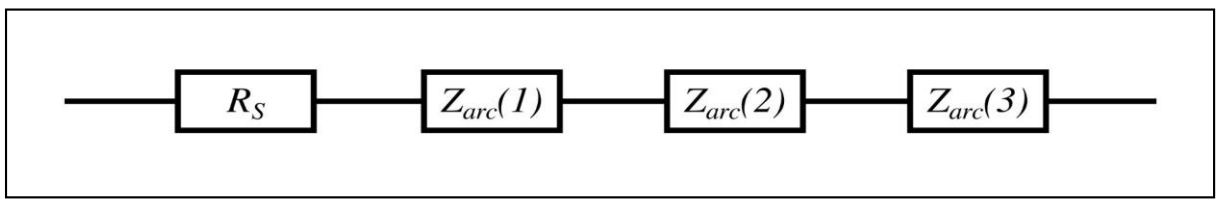

Figure IV - 29*: Association Z_{arc} elements in series to account for the different time constants. Z_{arc} is equal to CPE but make extraction of capacitance straightforward.*

The different time processes for the bare and for the coated WSe_2 electrodes could be easily revealed using admittance plots, presented in Figure IV - 30. The black markers represent the experimental data. As observed, three different semi-circles can be split apart for the two different admittance plots: in the right side of the plot, a first semi-circle appears at high frequency and its diameter is stable over electrode polarisaion. The two other semicircles, more visible for the coated WSe2 electrode (Figure IV - 30b), changed over polarization (from right to the left), but not for the bare one. Looking into the admittance plot of the coated WSe2, at low polarization, two loops are visible which tend to merge beyond 0V vs NHE until only one prevails. We highlight that in the admittance representation, the higher the loop diameterthe lower the resistance.

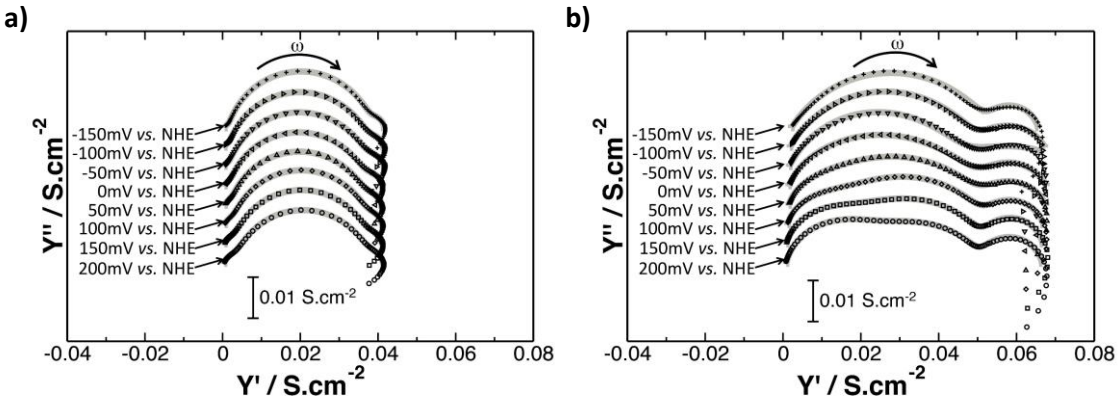

Figure IV - 30: *Admittance representation from EIS measurements of (a) bare and (b) Mo complexes co catalyst coated WSe_2 photo electrodes under illumination (λ = 450 nm) at various applied potentials from 0.2 V to -0.15V vs NHE. Electrolyte 0.5 M H_2SO_4, pH1.*

The fitted curves are represented by the solid grey lines in **Figure IV - 30**. For the WSe_2 photoelectrode after catalyst coating, beyond 0 V vs NHE only one time constant was necessary to fit the curves. This fact corresponds with what was observed in the respective bode plots over polarization.

From these results, it has been extracted two kind of resistances, where one is ascribed to recombination processes and the other to charge transfer, as presented in **Figure IV-31**. The series equivalent circuit that have been chosen (**Figure IV - 29**) means that the higher the respective resistance, the slower the overall electrode kinetic. In this model, the more there is recombination of the charge carriers, the higher will be the resistance denoted R_{rec}. The same applies for the charge transfer resistance (R_{CT}). The changes of the interface capacitance represented in **Figure IV - 31a** gives a good estimation of the electrochemical surface area (ESA). No relevant variation of the interface capacitance was revealed for the bare and coated WSe_2

photoelectrodes. Thus, the ESA is observed for both electrodes that the impedance of the interface is mainly driven by charge transfer resistance.

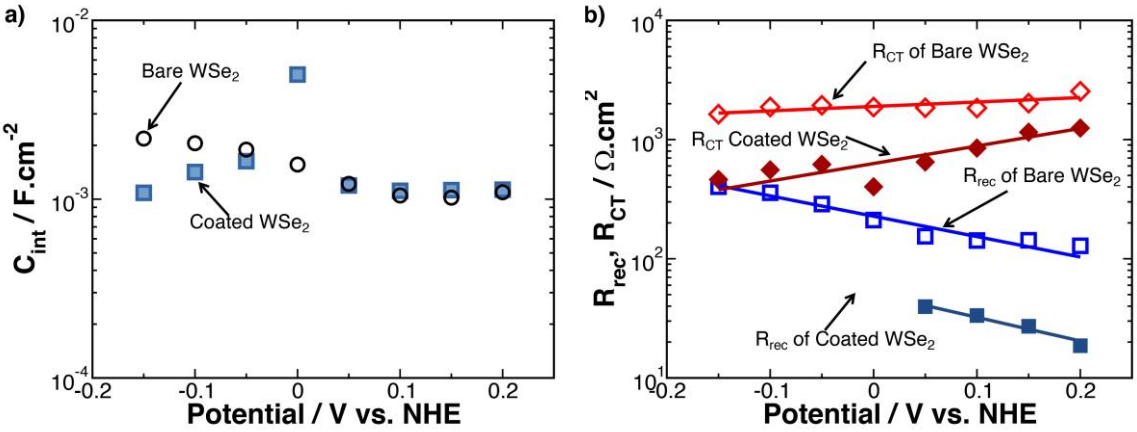

Figure IV - 31: *(a) variation of the interfacial capacitance, (b) variation of the different resistances extracted from fit parameters for bare WSe_2 and coated WSe_2 at different polarization potentials.*

As it can be noticed in **Figure IV - 31b**, the overall resistance – the sum of the two resistances – of the coated WSe_2 electrode is always below the one of the bare WSe_2 electrode. Indeed, the R_{rec} of the coated WSe_2 is always one order of magnitude below the charge transfer resistance one which makes the latter drive the electrode kinetic; for bare WSe_2, the two resistance (R_{rec} and R_{CT}) are closer and could explain why the impedance of this electrode is less sensitive to the electrode polarization, since the recombination is a non-negligible part of the whole electrode process.

The bottom line is that the coated WSe_2-based electrode is driven by the charge transfer resistance with negligible contribution of the recombination resistance, what results in the higher photocurrent observed in the LSV curve (**Figure IV - 29**). Whereas for bare WSe_2-based electrode a less effective charge transfer process is observed, because of the recombination process occurring. Overall, these impedance data are in line with healing of material defects thanks to thio, oxo-thio Mo complex treatment.

IV.3.9 Photoluminescence spectroscopy of 2D WSe_2 photoelectrodes with deposited catalyst film

An additional evidence for defects passivation was obtained by evaluating the photo-response of the material. Room temperature photoluminescence (PL) characterization was performed on two WSe2 photo-electrodes, with and without Mo thio-complexes catalyst impregnation, as indicated in Figure IV - 32. While no photoluminescence was recorded on the

catalyst-free sample, we clearly observed a peak of PL at 1.43 eV on the sample coated by the Mo-thio-complex. Because a low photoluminescence intensity, in these materials, is usually attributed to defect-mediated non-radiative recombination, the observed increase photoluminescence intensity of the MoxSy coated WSe2 photo-electrode can be linked to a decrease of the recombination probability of photo-induced electrons and holes. This likely occurs from surface defects passivation by the thio-, oxo-thio-Mo-complexes coating film.

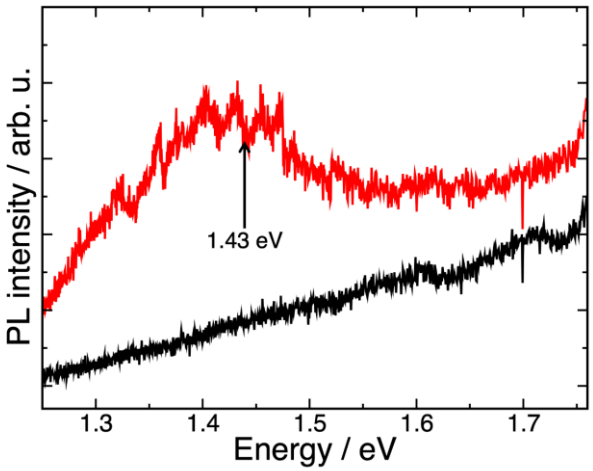

Figure IV - 32: *Photoluminescence spectra of bare WSe_2 (red curve) and WSe_2 with Mo thio complexes (black curve) catalyst film photo-electrodes.*

Further insights about the Mo thio, oxo-thio complexes film as healing catalysts

To support these findings, DFT calculations of adsorption energies for the various Mo complexes onto the WSe_2 photo-electrodes were performed to analyze the respective contributions of the thio and oxo-thio complexes catalyst on the healing process.

Adsorption energies of Mo thio, oxo-thio complexes on point defects of 2D WSe_2 materials

Defects in 2D TMDC nanosheets occur on the edges or are located in the basal plane due to non-stoichiometry. From HRTEM observations, our WSe_2 nanoflakes possess average lateral dimensions of 1 µm x 1 µm and a thickness composed of about 5 monolayers. When assuming a defect concentration of 0.5 % for the peripheral in-plane sites, a simple calculation reveals an equivalent number of peripheral edge or in-plane defect sites. From these results, we thus have paid particular attention in our DFT calculations to point defects.

Regarding point defects, best performances for the HER were achieved on films prepared from solutions containing MoS_4^{2-}, MoS_3O^{2-} monomers, $(Mo_2S_{12})^{2-}$ and $(Mo_2S_6O_2)^{2-}$ dimers in high proportions. During the catalyst film formation, these negatively charged thio-complexes preferably interact electrostatically in basic aqueous solution with locally charged defects of the 2D substrate. Reported defects on the 2D substrate include edges [17], large scale defects such as tears [25][26] or point defects such as Se vacancies, W vacancies [27][28]. Typical point defects of the WSe_2 substrate, namely Se-vacancy and W-vacancy are known to be electron acceptors [28]-[30]. With formation energy, we have determined respectively 2.6 and 5.3eV for Se- and W-vacancy, as illustrated in **Figure IV - 33**. Note that these vacancies always yield very small atomic reorganization with stretching of the W-Se bonds less than 0.1 Å. In addition, to have a considerable effect on carrier recombination, scaling of these point defects with the molecular size of the Mo complexes makes meaningful a DFT investigation focussed on point defects vs. large scale defects.

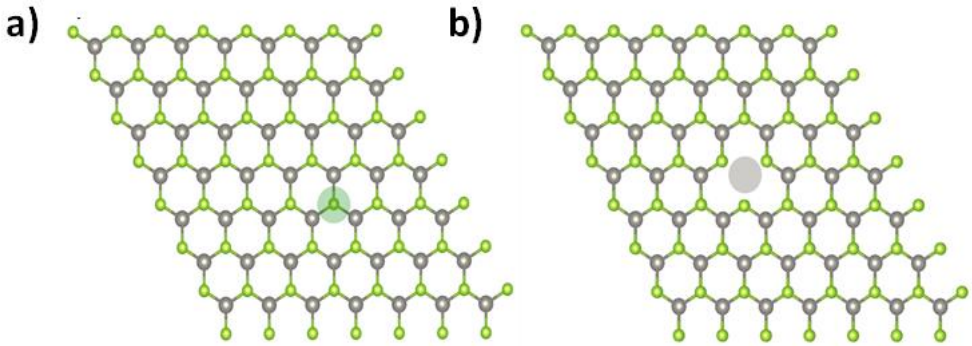

Figure IV - 33: *Atomic structure and densities of state for a) Se-vacancy and b) W-vacancy in a (7x7) supercell.*

Concerning the Mo complexes, we have investigated the roles of free-standing and anchored thio-, oxo-thio- Mo complexes respectively as healing additives and catalysts. $(MoS_4)^{2-}$, $(MoOS_3)^{2-}$ monomers, and $(Mo_2S_{12})^{2-}$, $(Mo_2S_6O_2)^{2-}$ dimers were chosen as model of Mo species. These thio and oxo-thio complexes were put in interaction in their radical form with (i) a pristine, (ii) a single Se-vacancy and (iii) a W-vacancy on WSe_2 monolayer. **Table IV - 3** summarizes the adsorption energy of Mo-complexes, defined as $E_{ads} = E_{Mo\text{-}comp@subst} - E_{subst} - E_{Mo\text{-}comp}$ on a model substrate presenting (or not) Se or W vacancy, where $E_{Mo\text{-}comp@subst}$, E_{subst}, and $E_{Mo\text{-}comp}$ stand for the total energy of the adsorbed species on the model WSe_2 substrate, for the total energy of the substrate alone and of the Mo-complex alone, respectively.

Table IV - 3 : *Adsorption energies (in eV) of various Mo-complexes in their radical forms, for three distinct substrate configurations of the WSe_2 monolayer.*

Adsorption energies onto WSe_2 (in eV)	***Free –defect Pristine substrate***	***Se-Vacancy containing WSe_2 substrate***	***W-vacancy containing WSe_2 substrate***
$(MoS_4)^{2-}$	*+0.09*	*-0.15*	*-1.75*
$(MoS_3O)^{2-}$	*-0.59*	*-0.97*	*-2.64*
$(Mo_2S_{12})^{2-}$	*-0.09*	*-0.11*	*-0.29*
$(Mo_2S_6O_2)^{2-}$	*-0.13*	*-0.19*	*-0.99*

From those values, it appears that the Mo-complexes weakly bind with defect-free pristine WSe_2 substrate and always prefer to stack on W-vacancy. **Figure IV - 34** presents the adsorption modes on the W-vacancy site on side and top views. Interestingly, $(MoS_4)^{2-}$, $(MoS_3O)^{2-}$ monomers or polycondensed species displaying small size such as $(Mo_2S_6O_2)^{2-}$ were shown to bind more strongly than the $(Mo_2S_{12})^{2-}$ complex with point defects of the WSe_2 substrate.

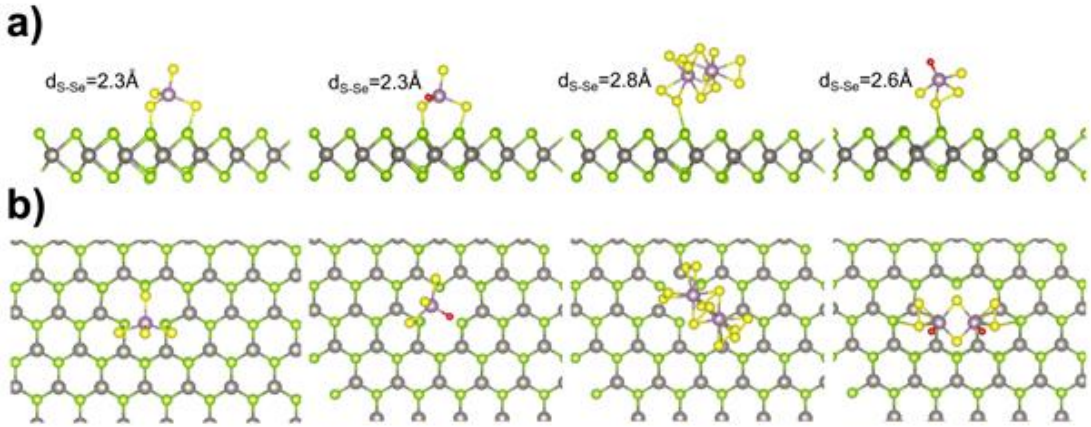

Figure IV - 34: *(a) Side views and (b) top views of the atomic structures for the Mo oxo-thio complexes on WSe_2 monolayer possessing a W-vacancy, showing S-Se interactions and accessible disulfide groups for the dimer Mo complexes. From left to right: adsorption of MoS_4, MoS_3O, Mo_2S_{12} and $Mo_2S_6O_2$ radicals. Yellow: Sulfur, Red: Oxygen, Violet: Mo, Green: Se and Grey: W.*

DFT calculations show that oxo-thio complexes are better adsorbed compared with their thio analogues on the Se or W vacancy containing WSe_2 substrate. In contrast to the disruption of S_2^{2-} bonds into active S^{2-} anions, it was previously reported in the presence of nucleophiles, favoured subsequent reactions with metal ions to produce metal sulphides [31][32]. Thus, the interaction between a W-vacancy and the various complexes investigated ($(MoOS_3)^{2-}$,

$(Mo_2S_6O_2)^{2-}$, $(Mo_2S_{12})^{2-}$) results in the formation of new Se-S bonds (d_{Se-S} = 2.3 Å), as illustrated in **Figure IV - 35** a and b reporting the resulting atomic structure.

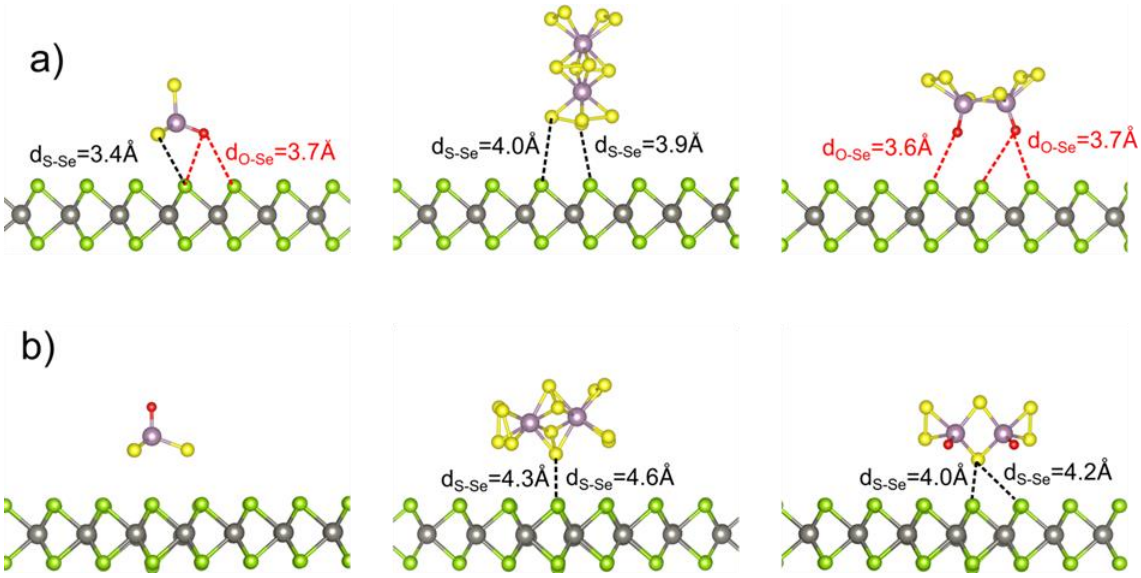

Figure IV - 35: *Atomic structures of the thio and oxo-thio complexes from left to right: MoS_3O, Mo_2S_{12} and $Mo_2S_6O_2$ on a) free-defect pristine and b) Se-vacancy WSe_2 monolayer. The smallest distances between the Mo-cluster and the substrate are also given.*

Therefore, we propose that the passivation of the WSe_2 nanosheets surface defects arises from the strong adsorption of these Mo complexes onto the WSe_2 nanosheets, by interactions with the Se and W vacancies. Note that the stronger adsorption energies toward point defects displayed by Mo monomers or small size dimers, such as $(Mo_2S_6O_2)^{2-}$, is consistent with our experimental results. This highlights the crucial role of these latter Mo complexes compared with pure $(Mo_2S_{12})^{2-}$ to passivate the 2D WSe_2 surface defects.

Potentialities of the Mo thio oxo-thio Complexes for HER catalyst given by Gibbs Energy of H-adsorption

More insights into the intrinsic catalytic activities of the various thio and oxo thio complexes including $(MoS_4)^{2-}$, $(MoS_3O)^{2-}$ monomers and $(Mo_2S_{12})^{2-}$, $(Mo_2S_6O_2)^{2-}$ dimers were gained in a first stage by gas-phase DFT calculations, carried out using molecular approachon H absorption energies on free-standing $(MoS_4)^{2-}$, $(MoS_3O)^{2-}$ monomers and free-standing $(Mo_2S_{12})^{2-}$, $(Mo_2S_6O_2)^{2-}$ dimers in their radical forms. The free Gibbs energy of H-adsorptionisa good descriptor of the ability of a given compound to be active for HER, when ΔG_H remains close to ± 0.1 eV [33].

DFT calculations of free energy changes during the HER were performed both on free-standing complexes, as well as on complexes anchored Mo complexes onto the 2D substrates. The obtained free energy diagram for the hydrogen evolution is shown in **Figure IV - 36**. Although in our DFT calculations we exclusively consider point defects and deal with adsorption of radical vs charged Mo complexes, our calculations highlight that good catalytic performances will mainly arise from dimers such as $((Mo_2S_6O_2)^{2-}$ or $(Mo_2S_{12})^{2-}$ preferably in a free standing regime or anchored in a low adsorption regime, i.e. on point defect-free WSe_2 substrates. While confirming the low hydrogen adsorption energy of the $(Mo_2S_{12})^{2-}$ thio complexes reported in the literature [15], these calculations highlight the ability of oxo-thio Mo complexes such as $(Mo_2S_6O_2)^{2-}$ to catalyse the HER.

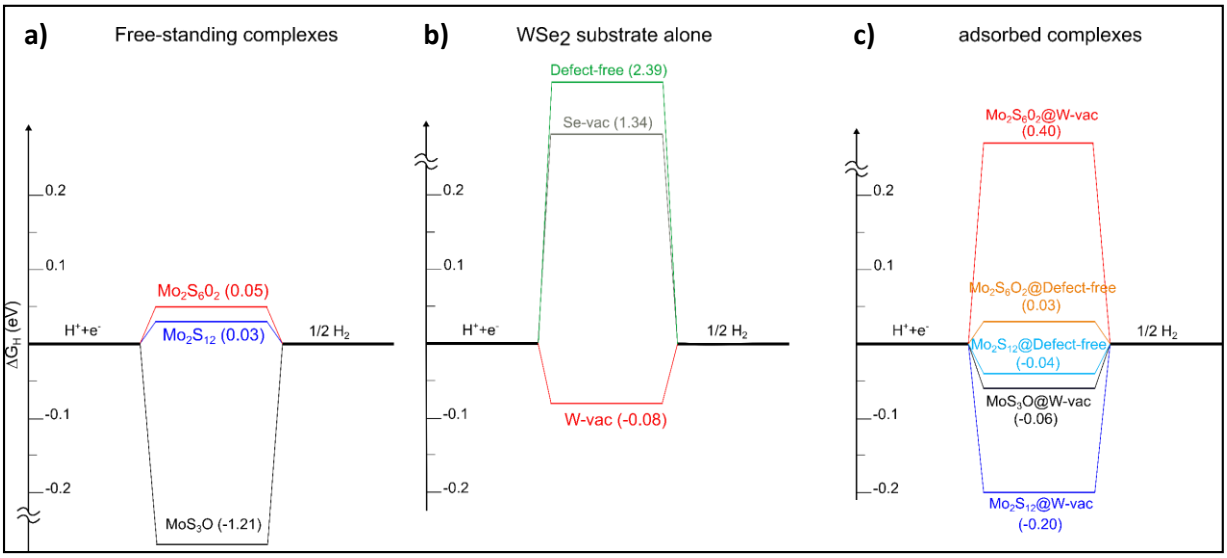

Figure IV - 36: *Free energy diagram for Hydrogen evolution at equilibrium. (a) $\Delta G_{ads}H$ showing values close to the optimum of the volcano curve for free standing $(Mo_2S_{12})^{2-}$ and $(Mo_2S_6O_2)^{2-}$ complexes (b) $\Delta G_{ads}H$ values for WSe_2 monolayers alone, namely point defect –free or W or Se vacancies-containing WSe_2 monolayers (c) $\Delta G_{ads}H$ values for various adsorbed Mo complexes on point defect –free or W or Se vacancies-containing WSe_2 monolayers.*

In contrast, $(MoS_4)^{2-}$, $(Mo_2S_6O_2)^{2-}$, $(Mo_2S_{12})^{2-}$ complexes strongly adsorbed on W-vacancy containing WSe_2 monolayers show $AG_{ads}H$ values far from the optimum value of the volcano curve [33], displaying thus a low activity for the HER. Thus, DFT calculations showed that our water-soluble Mo-oxo-thio complexes distributions are composed of three various classes of molecular species: i) Mo monomers possessing a low catalytic activity in its free-standing configuration but displaying high adsorption energy onto 2D WSe_2. ii) $(Mo_2S_{12})^{2-}$ dimer displaying high catalytic activity for the HER but with relatively low affinity for the 2D WSe_2 substrate. iii) $(MoS_3O)^{2-}$ oxo thio monomer displaying strong adsorption towards the WSe_2 substrates and reasonable catalytic activity in its anchored configuration. These Mo oxo-thio

complexes distributions capable of both passivating surface defects and displaying catalytic activity can, thus, be described as healing catalysts.

Consistent with our experimental results, we propose that the observed high HER performances arise from oxo-thio Mo complexes films probably composed of Mo monomers, dimers and trimers which are present both in free-standing and anchored configurations. Low and high adsorption modes of the Mo complexes should coexist for the anchored configurations depending of the point defects local concentration. We have demonstrated that the optimum structure of the catalyst film including free-standing and strongly adsorbed complexes providing respectively catalytic and healing properties can be successfully achieved from well-defined aquo-oxo-thio Mo complexes distributions by selective dip coating. Nevertheless, deep insights into the film structure describing respective proportions of healing and catalytic additives, as well as the detailed conformation of the complexes inside the film remain to be elucidated.

Catalytic Mechanism of the Mo thio oxo-thio complexes to drive HER

Different scenarios are proposed to date for the Hydrogen Evolution Reaction catalytic cycles on Mo thio complexes especially in the presence of M=O moiety [14][34][35]. More particularly, the HER catalytic cycle reported in the case of high performance amorphous MoS_x films prepared by electrodeposition involves unsaturated Mo(IV) and Mo(V) sites [14] with transient formation of the M=O moiety during the catalytic cycle. In another work concerning the same material, the catalytic cycle is shown to rather involve the S_2^{2-} -> S^{2-} redox reaction [34]. In recent works [34][36] dealing on $MoO(S_2)_2$(2,2′-bipyridine) as oxo thio Mo model molecule, a H_2 evolution catalytic cycle involving a hardly attached M=O moiety which functions as a proton relay is proposed for the HER reaction. In this catalytic mechanism, the S_2^{2-} anion represents the redox centre associated with a Mo(V) site. We highlight that these various catalytic cycles were proposed for the electrocatalytic hydrogen evolution reaction. A crucial difference between the photocatalytic *versus* electrocatalytic electrochemical water decomposition is the shift of potential arising from the solar energy harvesting. This shift towards lesser cathodic potentials does not favour the Mo(V)⟶ Mo(IV) reduction which is reported to occur at -0.3 V /NHE in slightly acid medium [14]. Because hydrogen evolution in our photocatalytic experiments does not require any cathodic pre-activation or neither the high cathodic potentials for the Mo(V) ⟶ Mo(IV) reduction, we believe that our photocatalytic cycle for the HER rather implies terminal $(S_2)^{-2}$ [37].

While this work was focused on 2D WSe_2 materials, which possess a considerable surface defect density, use of these highly interactive, oxo-thio, molecular complexes could be extended to passivate surface defects of a larger range of high surface area photo-electrodes including p-WS_2, p-MoS_2 for the HER. Further developments could also be anticipated with the design of M doped- Mo-oxo-thio-complexes [35], where M is a metallic cation [38], rare earth element [39], especially to achieve lower cathodic HER onset potentials or higher catalytic activity in neutral aqueous electrolytes . Therefore, the use of 2D TMDC materials displaying of various onset potentials for HER [21] represents an ideal photocathode device for the engineering of PEC tandem cells [40].

Conclusion

Mo thio- and oxo-thio- complexes distributions were spontaneously formed in H_2O in well-defined S/Mo ratio and pH conditions. ESI-MS and XPS characterizations gave more insights into the formation of these complexes in solution and after film formation. These complexes were proposed as HER catalysts for the photocatalytic water splitting. Photocatalytic decomposition of water was successfully achieved on films prepared from exfoliated 2D-WSe_2 and activated by highly interacting complexes selected from Mo oxo-thio complexes distributions via a selective dip coating film forming process. Best photocatalytic results were thus observed onto 2D p-WSe_2 photo-electrodes after deposition of Mo monomers, $(Mo_2S_{12})^{2-}$, $(Mo_2S_6O_2)^{2-}$ and $(Mo_3S_8O_2)^{2-}$ with photocurrents up to -2.0 mA cm^{-2} at - 0.2 V vs. NHE. Compared with Pt-Cu catalysts, the higher photocurrents observed after deposition of the thio- and oxo-thio- Mo complexes without the use of any passivating additive onto the 2D photo-electrodes reveal a healing effect from the water-soluble oxo-thio Mo complexes distributions. Insights into electrochemical properties demonstrated charge transfer increase after catalyst deposition onto WSe_2 photo-electrodes. DFT calculations gave adsorption energies of the thio and oxo-thio complexes onto the 2D photo-electrodes. DFT results demonstrated the role of oxo-thio Mo monomers and to a lesser extent, of oxo- thio- Mo dimers of small size in the healing effect, probably arising from the strong adsorption of these Mo complexes on point defects of the 2D substrate. In this chapter, we could present the design of a larger range of environmentally-friendly, aqueous-stable, catalytically active passivation layers made of oxo-thio Mo complexes as healing photo-catalysts. The formed multicomponent film with n-type semi-conduction has suitable optoelectronic properties and showed improvement of charge separation and migration for the HER onto the WSe_2 electrode. These results have provided an example of band engineering envolving a multicomponent and passivating layer displaying of multiple properties. We, next, present a second strategy involving optimization of the 2D WSe_2 microstructure resulting in increased surface area together with deposition of thio, oxo-thio Mo complexes catalyst thin layer to elaborate a new WSe_2 electrode of higher photocatalytic activity.

BIBLIOGRAPHY REFERENCES

[1] Z. Lin *et al.*, "Defect engineering of two-dimensional transition metal dichalcogenides," *2D Mater.*, vol. 3, no. 2, pp. 1-2, 2016.

[2] M. Draganjac, E. Simhon, L. T. Chan, M. Kanatzidis, N. C. Baenziger, and D. Coucouvanis, "Synthesis, interconversions, and structural characterization of the [(S4)2MoS]2–, [(S4)2MoO]2–, (Mo2S10)2–, and (Mo2S12)2– Anions," *Inorg. Chem.*, vol. 21, no. 9, pp. 3321–3332, 1982.

[3] X. Xin, N. L. Morris, G. B. Jameson, and M. T. Pope, "Characterization of an usymmetrical oxo-sulfido complex, [(n-Bu)4N]2[syn-(S2)OMo(μ-S)2MoS(S2)]," *Inorg. Chem.*, vol. 24, no. 21, pp. 3482–3485, 1985.

[4] Y. Do, E. D. Simhon, and R. H. Holm, "Trinuclear oxothiomolybdates from the reductive cleavage of [Mo8O26]4- with hexamethyldisilthiane," *Inorg. Chem.*, vol. 24, no. 18, pp. 2827–2832, 1985.

[5] A. I. Hadjikyriacou and D. Coucouvanis, "Synthesis, structural characterization, and properties of the [MO2O2S9]2 thio anion and the [MO4O4S18]2-, [MO2O2S8(SCH3)]_, and [MO 2O2S8C1]-derivatives," *Inorg. Chem.*, vol. 28, no. 11, pp. 2169–2177, 1989.

[6] A. Müller, M. Römer, C. Römer, U. Reinsch-Vogell, H. Bögge, and U. Schimanski, "Zweikern-komplexe des wolframs und molybdiins," *Monatscefte für Chemie*, vol. 717, pp. 711–717, 1985.

[7] W. Rittner, A. Muller, A. Neumann, and R. C. Bather, Wolfgang, Sharma, "Generation of the triangulo-Group Mo(V)-S_2 in the 'condensation' of $[Mo(V)_2O_2S_2(S_2)_2]_2$," *Angew. Chem. Int. Engl*, vol. 18, no. 7, pp. 530–531, 1979.

[8] Y. H. Xing *et al.*, "A new dinuclear molybdenum(V)-sulfur complex containing citrate ligand: Synthesis and characterization of K2.5Na2NH4[Mo2O2S 2(cit)2].5H2O," *Eur. J. Solid State Inorg. Chem.*, vol. 35, no. 10–11, pp. 745–756, 1998.

[9] Achim Müller, W.-O. Nolte, and B. Krebs, "[(S2)2Mo(S2)2Mo(S2)2]2-, a novel complex containing only S: - ligands and a Mo-Mo bond," *Angew. Chem. Int. Ed. Engl.*, vol. 17, p. 279, 1978.

[10] W. H. Pan, M. A. Harmer, T. R. Halbert, and E. I. Stiefel, "Induced internal redox processes in Molybdenum-Sulfur chemistry: conversion of MoS42– to MO2S82– by organic disulfides," *J. Am. Chem. Soc.*, vol. 106, no. 2, pp. 459–460, 1984.

[11] D. Rickard and G. W. Luther, "Chemistry of iron sulfides", *Chem. Rev.*, vol. 107, no. 2, pp. 514-562, 2007.

[12] R. T. Wilkin, D. Wallschläger, and R. G. Ford, "Speciation of arsenic in sulfidic waters," *Geochem. Trans.*, vol. 4, no. 1, pp. 1–7, 2003.

[13] J. Kibsgaard, T. F. Jaramillo, and F. Besenbacher, "Building an appropriate active-

site motif into a hydrogen-evolution catalyst with thiomolybdate [Mo3S13]2– clusters," *Nat. Chem.*, vol. 6, p. 248, Jan. 2014.

[14] P. D. Tran *et al.*, "Coordination polymer structure and revisited hydrogen evolution catalytic mechanism for amorphous molybdenum sulfide," *Nat. Mater.*, vol. 15, no. 6, pp. 640–646, 2016.

[15] Z. Huang *et al.*, "Dimeric [Mo2S12]2– cluster: a molecular analogue of MoS_2 edges for superior hydrogen-evolution electrocatalysis," *Angew. Chemie*, vol. 127, no. 50, pp. 15396–15400, 2015.

[16] Y. Ouyang, Q. Li, L. Shi, C. Ling, J. Wang, "Molybdenum sulfide clusters immobilized on defective graphene: a stable catalyst for the hydrogen evolution reaction," *J. Mater. Chem. A,* vol 6, no. 5, pp. 2289-2294, 2018.

[17] X. Yu, N. Guijarro, M. Johnson, K. Sivula, "Defect mitigation of solution-processed 2D WSe2 nanoflakes for solar-to-hydrogen conversion," *Nano Lett.,* vol. 18, no. 1, pp. 215-222, 2018.

[18] F. Meng, J. Li, S. K. Cushing, M. Zhi, and N. Wu, "Solar hydrogen generation by nanoscale p–n Junction of p -type Molybdenum Disulfide/n-type Nitrogen-doped reduced graphene oxide," *J. Am. Chem. Soc.*, vol. 135, pp. 10286–10289, 2013.

[19] A. L. Grzesiak, F. J. Uribe, N. W. Ockwig, O. M. Yaghi, and A. J. Matzger, "Polymer-induced heteronucleation for the discovery of new extended solids," *Angew. Chemie-Int. Ed.*, vol. 45, no. 16, pp. 2553–2556, 2006.

[20] W. Kautek and H. Gerischer, "Photoelectrochemical reactions and formation of inversion layers at n-type MoS2-, MoSe2-, and WSe2-electrodes in aprotic solvents," *Berichteder Bunsengesellschaft für Phys. Chemie*, vol. 84, no. 7, pp. 645–653, 1980.

[21] C. R. Cabrera and H. D. Abruna, "Synthesis and photoelectrochemistry of polycrystalline thin films of p-WSe2, p-WS2, and p-MoSe2," *J. Electrochem. Soc.*, vol. 135, no. 6, p. 1436, 1988.

[22] H. Peelaers and C. G. Van De Walle, "Effects of strain on band structure and effective masses in MoS2," *Phys. Rev. B - Condens. Matter Mater. Phys.*, vol. 86, no. 24, pp. 1–5, 2012.

[23] M. Zhong *et al.*, "Surface modification of CoOx loaded $BiVO_4$ photoanodes with ultrathin p-type NiO layers for improved solar water oxidation," *J. Am. Chem. Soc.*, vol. 137, no. 15, pp. 5053–5060, 2015.

[24] B. Klahr, S. Gimenez, F. Fabregat-Santiago, J. Bisquert, and T. W. Hamann, "Photoelectrochemical and impedance spectroscopic investigation of water oxidation with 'co-Pi'-coated hematite electrodes," *J. Am. Chem. Soc.*, vol. 134, no. 40, pp. 16693–16700, 2012.

[25] S. S. Chou *et al.*, "Ligand conjugation of chemically exfoliated MoS2," *J. Am. Chem. Soc.*, vol. 135, no. 12, pp. 4584–4587, 2013.

[26] Z. Liu, H. Zhao, N. Li, Y. Zhang, X. Zhang, and Y. Du, "Assembled 3D electrocatalysts for efficient hydrogen evolution: WSe_2 layers anchored on graphene sheets," *Inorg. Chem. Front.*, vol. 3, no. 2, pp. 313–319, 2016.

[27] S. Zhang *et al.*, "Defect structure of localized excitons in a WSe2 monolayer," *Phys. Rev. Lett.*, vol. 119, no. 4, pp. 1–6, 2017.

[28] S. Haldar, H. Vovusha, M. K. Yadav, O. Eriksson, and B. Sanyal, "Systematic study of structural, electronic, and optical properties of atomic-scale defects in the two-dimensional transition metal dichalcogenides MX2 (M = Mo, W; X = S, Se, Te)," *Phys. Rev. B - Condens. Matter Mater. Phys.*, vol. 92, no. 23, pp. 1–12, 2015.

[29] J.Y. Noh, H. Kim, Y.S. Kim, "Stability and electronic structures of native defects in single-layer MoS_2," *Phys. Rev. B*, vol. 89, no. 20, pp. 205417, 2014.

[30] H. P. Komsa and A. V. Krasheninnikov, "Native defects in bulk and monolayer MoS_2 from first principles," *Phys. Rev. B - Condens. Matter Mater. Phys.*, vol. 91, no. 12, pp. 1–17, 2015.

[31] J. Sheng, L. Wang, Y. Han, W. Chen, H. Liu, M. Zhang, L. Deng, Y.-N. Liu, "Dual roles of protein as a template and a sulfur provider: a general approach to metal sulfides for efficient photothermal therapy of cancer," *Small*, vol. 14, pp. 1702529, 2018.

[32] A. J. Parker and N. Kharasch, "The scission of the sulfur-sulfur bond," *Chem. Rev.*, vol. 59, no. 4, pp. 583–628, 1959.

[33] J. K. Nørskov *et al.*, "Trends in the exchange current for hydrogen evolution," *J. Electrochem. Soc.*, vol. 152, no. 3, pp. 26–29, 2005.

[34] B. R. Garrett, S. M. Polen, M. Pimplikar, C. M. Hadad, and Y. Wu, "Anion-Redox Mechanism of $MoO(S_2)_2$(2,2′-bipyridine) for Electrocatalytic Hydrogen Production," *J. Am. Chem. Soc.*, vol. 139, no. 12, pp. 4342–4345, 2017.

[35] J. Y. Chane-Ching *et al.*, "Water-soluble, heterometallic chalcogenide oligomers as building blocks for functional films," *Inorg. Chem. Front.*, vol. 3, no. 5, pp. 689–701, 2016.

[36] B. R. Garrett, K. A. Click, C. B. Durr, C. M. Hadad, and Y. Wu, "$[MoO(S_2)_2L]_1$-(L = picolinate or pyrimidine-2-carboxylate) Complexes as MoSx-inspired electrocatalysts for hydrogen production in aqueous solution," *J. Am. Chem. Soc.*, vol. 138, no. 41, pp. 13726–13731, 2016.

[37] M. Chhowalla, H. S. Shin, G. Eda, L.-J. Li, K. P. Loh, and H. Zhang, "The chemistry of two-dimensional layered transition metal dichalcogenide nanosheets," *Nat. Chem.*, vol. 5, p. 263, Mar. 2013.

[38] M. L. Grutza, A. Rajagopal, C. Streb, and P. Kurz, "Hydrogen evolution catalysis by molybdenum sulfides (MoSx): Are thiomolybdate clusters like $[Mo_3S_{13}]^{2-}$ suitable active site models?," *Sustain. Energy Fuels*, vol. 2, no. 9, pp. 1893–1904, 2018.

[39] W. Gao, D. Wen, J. C. Ho, and Y. Qu, "Incorporation of rare earth elements with transition metal–based materials for electrocatalysis: a review for recent progress," *Mater. Today Chem.*, vol. 12, pp. 266–281, 2019.

[40] M. S. Prévot and K. Sivula, "Photoelectrochemical tandem cells for solar water splitting," *J. Phys. Chem. C*, vol. 117, no. 35, pp. 17879–17893, 2013.

CHAPTER V

Design of layered hetero-structures of rGO-WSe_2/Mo_xS_y for H_2 Generation through Water Splitting

Introduction

To design an efficient solar splitting cell and achieve the conversion of solar energy into hydrogen, the semiconductor system must present high surface area for catalytic kinetics to decrease the overpotential [1]. Nanostructured semiconductors with large surface area offer an enhanced exchange surface with the electrolyte, promoting a faster charge transfer [2]. Moreover, surface functionalization/modification, for instance *via* surface heterojunctions and/or co-catalyst surface deposition, lead to improve charge separation within the semiconductor/electrolyte interface: more efficient electron-hole pairs separation, faster charge transfer. All in all, photocatalytic efficiency is ramped up. In this study, we present optimized nanostructure of exfoliated 2D WSe_2 with high surface area, pore walls composed of few layers, and in-plane WSe_2/GO layered junctions. The new layered nanojunctions exhibits increased photocatalytic activity for the HER, after anchoring Mo thio and oxo-thio co-catalyst film well suited for the 2D WSe_2 nanoflakes, as previously proposed. The new morphology provides more accessible surface area, and self-assembly of WSe_2 nanoflakes with GO nanosheets enhances the conductivity, improving the charge collection after separation. SEM – FIB images indicated a microstructure 3D interconnected edge-to-edge of WSe_2 building blocks constituted of few nanoflakes. Chemical analysis demonstrated the simultaneous presence of rGO and WSe_2 through the film network. The photocatalytic performance of 3D rGO-WSe_2 photoelectrodes is compared with 2D WSe_2 photoelectrodes after addition of Mo thio complexes co-catalyst film by electrochemical measurements. A photocurrent of -5.0 mA cm^{-2} at -0.2 V vs NHE was obtained for the new hetero-structure and incident photon-to-current conversion revealed efficiency of about 10% (for $\lambda > 500$ nm). The surface defects passivation promoted by Mo_xS_y co-catalyst coating, demonstrated using PL spectroscopy and IMPS analysis, collaborated to design a photocathode for the HER with improved photocatalytic properties.

V.1 Preparation of rGO-WSe_2/Mo_xS_y hetero-structures

V.1.1 Use of Sb_2S_3 –SnS_2 amorphous colloids as etching template

In an attempt to prepare high surface area films made of exfoliated p-WSe_2 of molecular range thickness, we used Sb_2S_3 – SnS_2 colloidal solution. This template was specifically designed to develop short range complexing interactions with the WSe_2 nanosheets favoring their self-assembly. Sb_2S_3 –SnS_2 amorphous colloids were developed and selected to be a good candidate as hard transient template. Indeed, Sb_2S_3 and SnS_2 can form highly soluble complexes with sulfide anions [3], [4] allowing their post-solubilisation, the Sn (IV) addition to Sb_2S_3 compound improves significantly its colloidal stabilization. More importantly, the Sn (IV) addition favors the formation of Sn (IV) chalcogenide surface ligands on its outer surface. Besides, the use of a metallic chalcogenide template minimizes the chemical degradation of the molecularly thin TMDC nanosheets, particularly at the intermediate temperatures required by the thermal consolidation of the nanosheets network in close contact with the template. **Figure V - 1** illustrates the self-assembly process between the TMDC nanosheets and the colloid template.

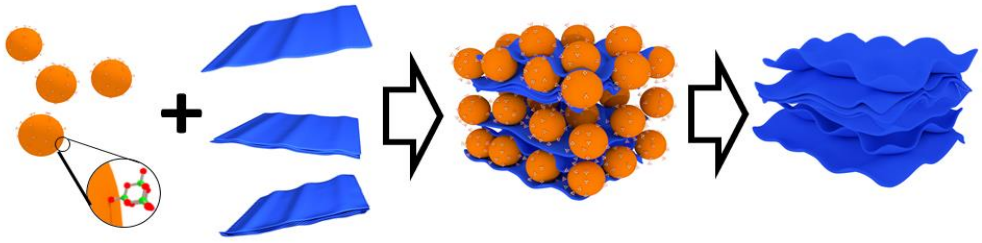

***Figure V - 1**: Process route for the self-assembling of TMDC nanosheets. The self-assembly is driven by complexing interactions involving a chalcogenide oligomer ligand localized on the outer surface of the colloid template.*

V.1.2 $Sn_xSb_yS_z$ colloid surfaces characterization

In-depth characterization of the $Sn_xSb_yS_z$ colloid surfaces has been obtained by performing ^{119}Sn liquid NMR. In **Figure V - 2** is presented the liquid NMR spectra of the colloidal template dispersion of high concentrated dispersions (> 200 g l^{-1}), synthetized with two different molar ratio (r_{Sn}) and long acquisition time. A large peak (FMWH = 12 ppm) was recorded at δ = - 28 ppm, for Sb_2S_3- SnS_2 concentrated colloid dispersions synthetized with a molar ratio (r_{Sn})= 0.25 (green trace) and (r_{Sn})= 0.5 (red trace). To ascribe this peak, an ultrafiltration – using a 3 kDa membrane – has been performed on the dispersion. After ultrafiltration, on the ^{119}Sn liquid NMR spectrum of the ultrafiltrate (**Figure V - 2**- blue trace) the peak at δ = - 28 ppm is no longer

present. So, this peak has been assigned to Sn (IV) chalcogenide soluble condensed mobile species [3] attached to the surface of the Sb_2S_3- SnS_2 colloids. The *in-situ* generation of these surface oligomer species is probably favored, from surface solubility, because of the alkaline pH condition (pH = 8.75). The Sn (IV) containing chalcogenide surface oligomers is assumed to coordinate metal cations of the TMDC nanosheets, as previously reported [5][6].

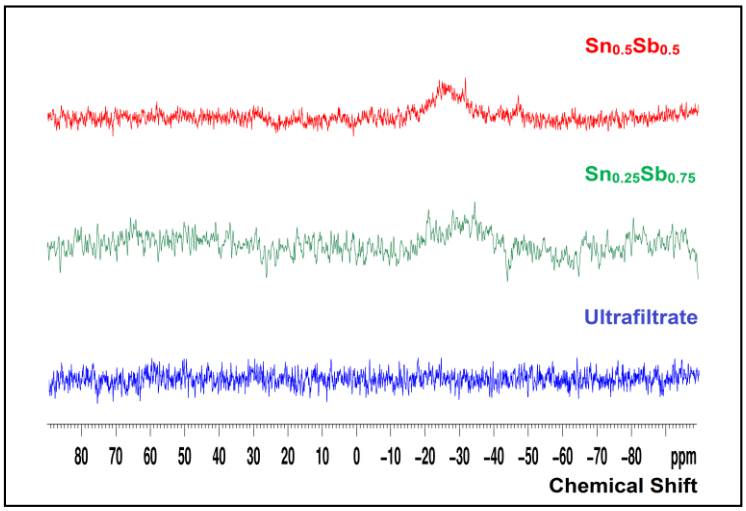

Figure V - 2: *^{119}Sn liquid NMR spectra recorded on Sn (IV)-Sb_2S_3 concentrated colloidal dispersions (200 g.l^{-1}, $Sn(IV)_{molar}$ = 0.25 and 0.5 - green and red traces, respectively). ^{119}Sn liquid NMR spectrum (blue trace) recorded in similar conditions on the ultrafiltrate collected by ultrafiltration on a 3KD membrane is given for control.*

V.1.3 Self-assembly of WSe_2 nanoflakes, Sb_2S_3 – SnS_2 template and GO nanosheets

Our synthetic process (more details in Chapter II) involved colloidal self-assembly of GO nanosheets and WSe_2 nanoflakes with optimal thickness and a post leachable template of controllable size. **Figure V - 3** shows the scheme of the self-assembly process to elaborate rGO-WSe_2 nanojunctions.

In a first step, the mixing of spherical Sb_2S_3 – SnS_2 template and WSe_2 nanoflakes colloidal dispersions were self-assembled with the GO nanosheets dispersion. To prevent any phase separation, the self-assembly was conducted in a highly repulsive regime, with polar solvent media (di-methyl-formamide), achieved with $Sn_{0.5}Sb_{0.5}S_y$ colloids, WSe_2 nanoflakes building blocks and GO nanosheets exhibiting similar negative surface charge.

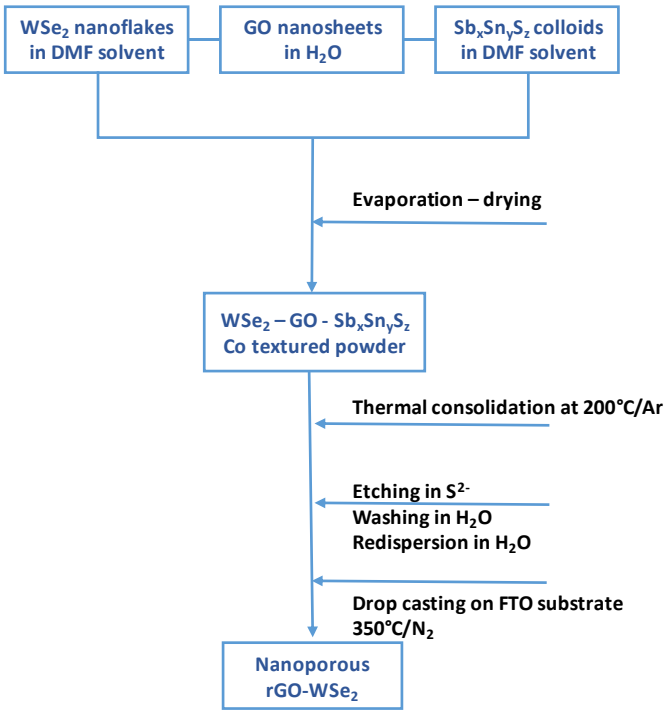

Figure V - 3: *Scheme of the self-assembly process to elaborate nanojunctions of rGO-WSe_2 with juxtaposed nanoflakes with high surface area.*

Short-range complexing interactions operate between metallic cations of the nanoflakes and the chalcogenide ligand localized on the outer surface of the sacrificial template. In addition, to fully exploit the layered character of the photoactive film, ultrathin GO nanosheets with similar lateral size as the WSe_2, were selected as the building blocks to construct the conducting percolating network. Preliminary experiments defined GO nanosheets of lateral size (L = 150 nm), selected consistently both with the WSe_2 nanoflake lateral size (200 ≤ L ≤ 1000 nm) and template average size (D = 60 nm). **Figure V - 4** shows TEM images of GO nanosheets, exfoliated WSe_2 nanoflakes and $Sn_xSb_yS_z$ colloids showing a monodisperse repartition of individualized spheres.

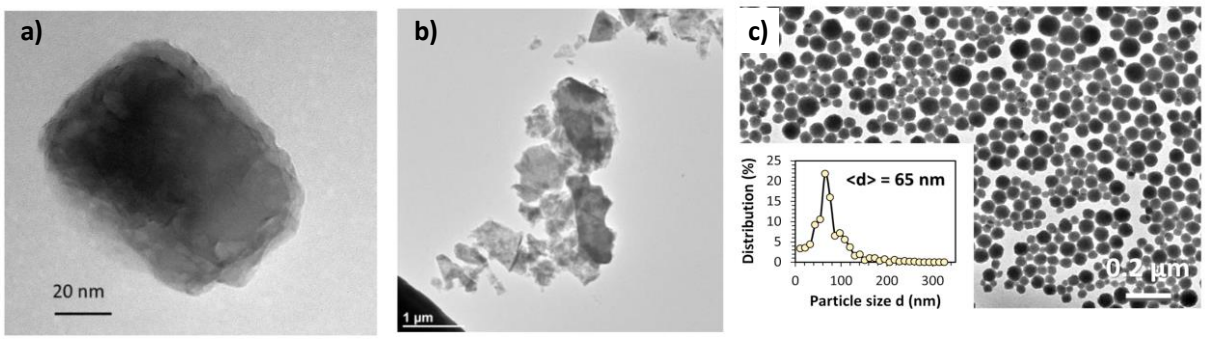

Figure V - 4: *TEM images of (a) GO nanosheets selected at 15 300 rp; (b) exfoliated WSe_2 nanoflakes after selection at 800 rpm and (c) $Sn_xSb_yS_z$ colloids showing a monodisperse repartition of individualized spheres.*

Then, thermal consolidation of the dried GO-WSe_2- ($Sn_{0.5}Sb_{0.5}S_y$) was realized under Argon at 200°C. The as-calcined solid was etched in a $(NH_4)_2S$ 1.5M solution to remove the $Sn_{0.5}Sb_{0.5}S_y$ template and finally washed with H_2O.

BET measurements were performed after evaporation-drying of 3D GO-WSe_2 assemblies after etching Sb_2S_3-SnS_2 colloidal spherical templates. **Figure V-5** presents the cumulative pore volume and pore area of WSe_2 with and without GO addition after self-assembly procedure. WSe_2 nanoflakes volume fraction ($\phi_{V_{WSe_2}}$) corresponding to an optimal surface coverage of the Sb_2S_3-SnS_2 colloidal template promoted a surface area estimated to be 7 m^2 g^{-1}, using WSe_2 nanoflakes selected at 800 rpm. We observe significant pore volume, after the co-texturation of WSe_2 nanoflakes (**Figure V-5b**). Low pore volumes and larger pore width up to 100 nm can be assigned to larger thickness of solvent-exfoliated WSe_2 nanoflakes increasing their stiffness [7] and yielding lesser strain when submitted to short-range complexing interactions. The specific surface area presented by the self-assembled 3D rGO-WSe_2 powder after self-assembly and template etching did not show significant differences without GO.

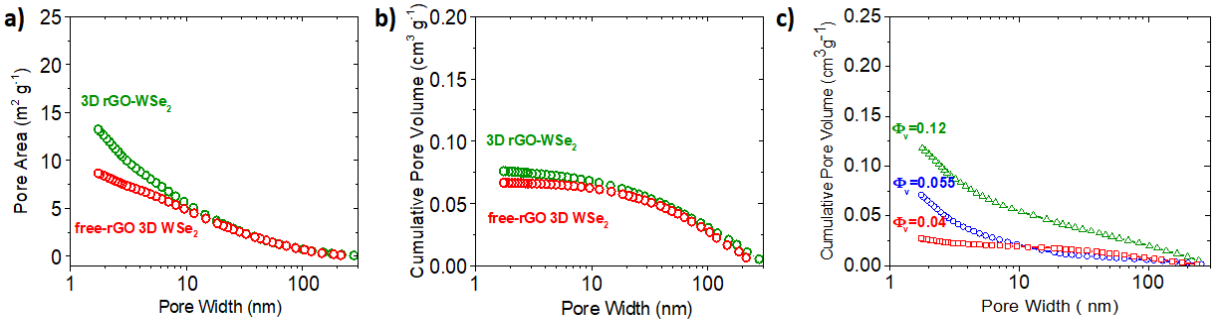

Figure V-5: *Pore distribution of 3D assemblies prepared from various 2D nanosheets and using Sb_2S_3-SnS_2 colloidal spherical templates and GO nanosheets. (a) Pore area characteristics of nanostructured WSe_2 flakes selected at 800 rpm; (b) Pore volume determined from N_2 adsorption-desorption data; (c) smaller pore volumes and more polydispersity pore distributions were observed for assemblies prepared from GO nanosheets.*

In order to gain better insights into the self-assembly process, control experiments were performed with colloidal template and graphene oxide nanosheets at various graphene oxide volume fractions, $\Phi_{V\,GO} = V_{GO} / (V_{GO} + V_{Sb_2S_3-Sn(IV)})$. No monodisperse distribution of pores along with lower porous volumes was observed on the graphene oxide samples after texturation (**Figure V-5c**). These results demonstrate that the specific interactions are developed between the chalcogenide oligomers localized on the template surface and the WSe_2 surface. Therefore, it is proposed that short-range complexing interactions are involved similar to those previously described [5] between chalcogenide oligomers and nanocrystals, such as CdSe, Bi_2S_3, Au, Pd.

The rGO-WSe_2 co-textured powder was, then, dispersed in **H_2O** and drop casted on FTO substrate, yielding a porous self-assembled film, denoted 3D rGO-WSe_2. Some infiltrations of colloidal GO nanosheets were eventually introduced, between two successive depositions of 3D rGO-WSe_2. The conversion of GO in conductive rGO (reduced Graphene Oxide) was performed during the heat treatment of the as-made electrodes, under slow heating rate at 350°C during 2 hours and in N_2 atmosphere. Finally, the formation of rGO-WSe_2/Mo_xS_y hetero-structures involved the deposition of an ultrathin film of Mo_xS_y catalyst onto the 3D rGO-WSe_2 film.

V.1.4 Catalyst deposition on the assembled 3D rGO-WSe_2 films

The 3D self-assembled rGO-WSe_2 films were dip coated in the catalyst solution of Mo thio, oxo-thio complexes containing various Mo-S species, such as monomers $(MoS_4)^{2-}$, $(MoS_3O)^{2-}$, dimers $(Mo_2S_{12})^{2-}$, $(Mo_2S_6O_2)^{2-}$ and trimers $(Mo_3S_8O)^{2-}$, as presented in the previous chapter. Best results were achieved in a growth regime from a diluted Mo thio oxo-thio complexes solution (0.01M Mo, pH 8.75 < pH < 9.0, S/Mo = 5), dip coated during 2 x 16h. Then, the photoelectrodes were heat treated at 110°C under Air, for 10 minutes and submitted to photo-electrochemical characterizations.

V.2 Characterization of nanostructured 3D rGO-WSe_2

V.2.1 Morphology of nanostructured 3D rGO-WSe_2

The cross-sectional images of Focused Ion Beam Scanning Electron Microscopy (FIB-SEM) of 2D as-exfoliated WSe_2 and 3D rGO-WSe_2 are presented in **Figure V - 6.** Differently of the 2D WSe_2 film, where the preferential orientation parallel to FTO substrate is remarkable (**Figure V - 6a**), the 3D self-assembled rGO-WSe_2 shows a porous nanosheets film with lower densification, displaying of interconnected building blocks and anisotropic morphology (**Figure V - 6b**). The pores dimensions of the film are ranging from 0.1 to 5.0 µm. The film is composed of nanoflakes with thickness ranging from ≈ 120 to 150m and lateral sizes between 200-500nm. The orientation of the WSe_2 nanoflakes varies randomly from parallel to perpendicular in the cross-sectional view of the FTO surface, suggesting a 3D self-assembly arrangement. In addition, the FIB-SEM image also points out continuity of coating film, as we observe junctions between the nanoflakes of WSe_2 over the FTO substrate (**Figure V - 6b insert**).

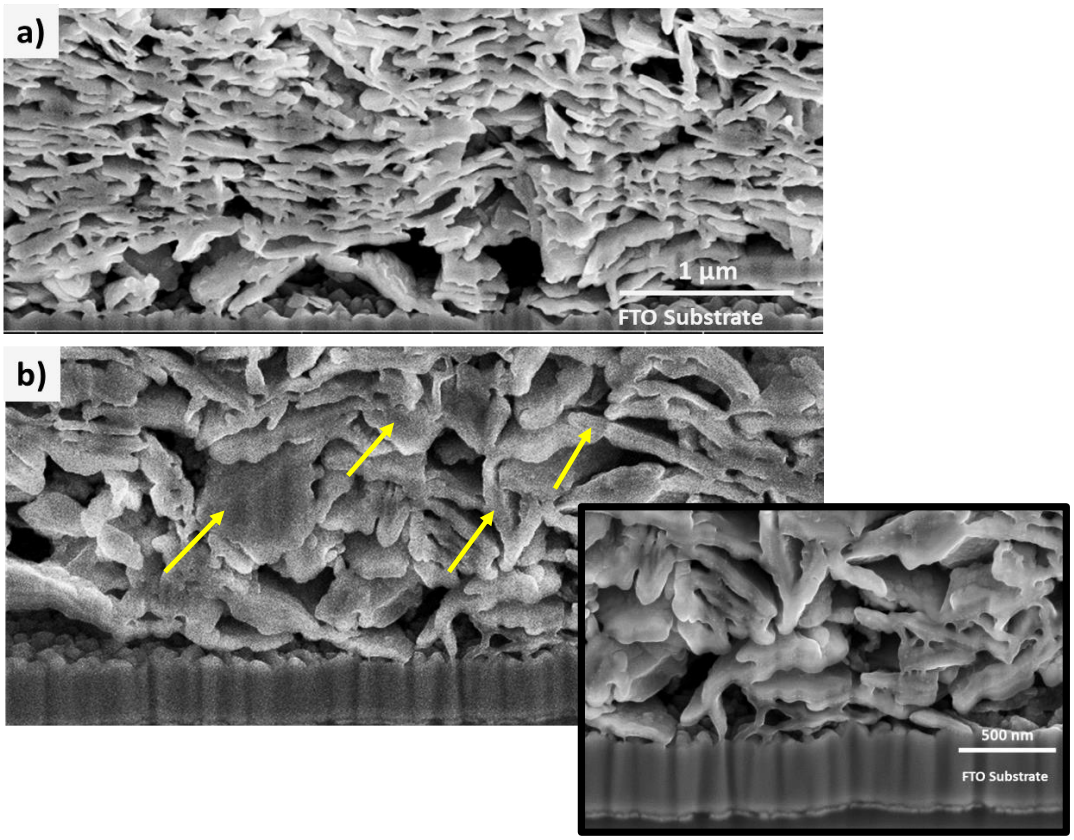

Figure V - 6: *Focused ion beam-scanning electron microscopy images in cross-section of WSe_2 films on FTO substrate: (a) 2D exfoliated photoelectrode of WSe_2, (b) 3D rGO-WSe_2 photoelectrode after self-assembly process. Insert: higher magnification of 3D rGO-WSe_2 self-assemblies showing interconnected nanoflakes with anisotropic orientation.*

Fine inspection of the interconnected network reveals presence of irregular contour on the periphery of the nanoflakes and curved domains at inter-nanoflakes junctions, as shown in **Figure V - 7**. This indicates formation of a continuous film coating the WSe_2 nanoplates. It can also be noticed in the TEM cross-sectional image of 3D rGO-WSe_2 film, internal linear domains exhibiting higher contrast in some nanoflakes, suggesting that these anisotropic building blocks may be built up from juxtaposition of several primary nanoflakes. It can be observed the edge-to-edge inter-connections between the nanoflakes, as well as the contact of the nanoflakes with the FTO substrate. The precise determination of the average thickness of the WSe_2 nanoflakes is difficult, but we estimated WSe_2 nanoflake-based wall thickness of about 120 nm.

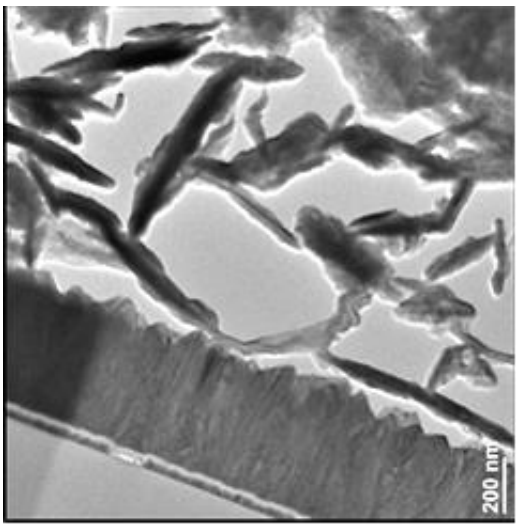

***Figure V - 7**: TEM image detailing the arrangement of self-assembled 3D rGO-WSe_2 nanoflakes uniformly distributed in the nanostructure network.*

V.2.2 X-ray Diffraction investigation of nanocrystal domains on 3D rGO-WSe_2

X-ray diffraction (XRD) patterns recorded on 3D self-assembled rGO-WSe_2 films displayed all the attributed peaks to the hexagonal 2H type of WSe_2 structure, as presented in **Figure V - 8**. X-ray diffraction patterns of bulk and 2D exfoliated WSe_2 are presented as reference.

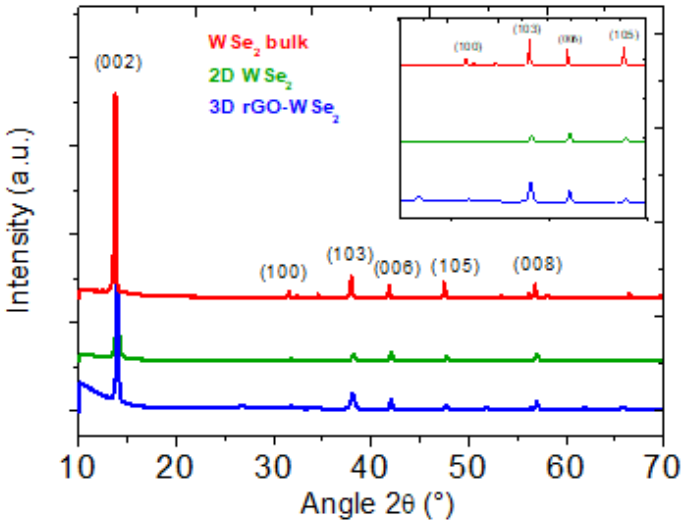

Figure V - 8: *XRD patterns of WSe_2 bulk (red line), exfoliated WSe_2 (green line) and 3D self-assembled WSe_2 (blue line) photoelectrodes after calcination at 350°C/2h at N_2 atmosphere.*

Further investigation of XRD results determined size of nanocrystal domains for 3D rGO-WSe_2 nanoflakes selected at 800 rpm. By using the Debye-Scherer relation [8], values of ordered domain sizes were determined for important plans of the WSe_2 structure. **Table V - 1** presents the data used to calculate the size of nanocrystal domains of the three samples. The size of ordered domains in the (100) and (103) directions are in the order of 30 to 70 nm. As revealed by the SEM image from **Figure V - 6,** the WSe_2 nanoflakes exhibited an average thickness of around 120 nm. Thus, the size of ordered domains found through XRD data indicates that the nanostructure of the WSe_2 film is composed of building blocks composed of 2-5 primary nanoflakes.

Table V - 1*: X-ray diffraction data, scattering angles and full width at half maximum intensities (FWHM) from Debye-Scherrer relation.*

Sample	h k l	2θ	θ (rad)	$(FWHM)_{sample}$ (rad)	$(FWHM)_{sample}$ *Cos θ	Size (nm)
Bulk WSe_2	1 0 0	31.41	0.274	0.00066	0.00064	215
	1 0 3	37.805	0.33	0.00078	0.00074	185
2D WSe_2	1 0 0	31.41	0.274	0.00232	0.00223	65
	1 0 3	37.805	0.33	0.00420	0.00398	40
WSe_2	1 0 0	31.41	0.274	0.00357	0.00344	40
	1 0 3	37.805	0.33	0.00565	0.00535	30

V.2.1 Electrical conductivity of nanostructured 3D rGO-WSe_2 films

A four-electrode set up of in plane electrical conductivity was performed on 2D, free rGO-WSe_2 3D and rGO-WSe_2 3D films deposited on glass substrate, at room temperature. The electrical conductivities of the thin films studied were calculated from the measurements of the electric current for different potentials applied. **Figure V - 9** shows the J-V data obtained from the conductivity measurements on films of 2D WSe_2, 3D free-rGO/WSe_2 and 3D rGO-WSe_2 films drop casted on glass substrate. From ohm law ($i = \sigma|V|$), the film resistance of each sample was calculated. As presented in Chapter II, the resistivity of each sample was calculated considering a thickness layer of e ≈ 2 µm. Thus, a resistivity value is found to be in the order of 10^2 Ω.cm for the 2D WSe_2 film and is in the range of values previous reported [9]. For the 3D free rGO-WSe_2 film a resistivity in the order of 10^4 Ω.cm was calculated and for the 3D rGO-WSe_2 film a corresponding resistivity was obtained in the order of 10^1 Ω.cm.

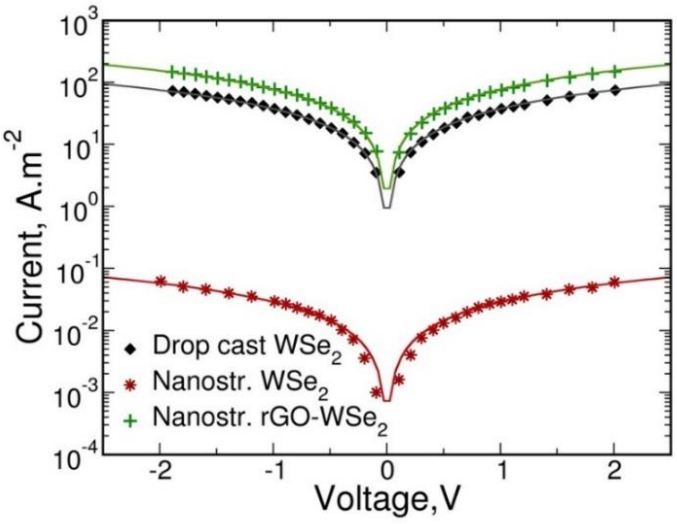

Figure V - 9: *J-V data for the conductivity measurements on films of 2D WSe_2, 3D free-rGO/WSe_2 and 3D rGO-WSe_2 films drop casted on glass substrate, at 25°C.*

In case of free rGO 3D WSe_2 film, despite the presence of large number of inter-nanoflake contacts arising from the self-assembly, the high resistivity highlights the poor electrical connectivity of edge-to-edge or edge-to-plane configuration, as shown in the FIB-SEM and TEM images (**Figure V - 6 and Figure V - 7**). A significant decrease of the lateral resistivity over large distance was observed between drop–casted films prepared from exfoliated nanosheets (2D WSe_2 film), if compared with rGO-free 3D WSe_2 films (**Figure V - 9**, red trace). The lower resistivity achieved by 2D WSe_2 films is resulting from the continuous plan-to-plan contacts with

the in-plane conductivity of primary WSe_2 nanoflakes. As showed in the FIB-SEM image (in **Figure V - 6**), the 2D configuration, having more regularity in the horizontal cross section, favors the decrease of the sheet resistance.

Interestingly, the resistivity is still decreased for the films prepared from co-textured rGO nanosheets with WSe_2 nanoflakes (**Figure V - 9,** green trace). The post-addition of rGO nanosheets results in restored long range electrical conductivity. Considering that the mean free path of electrons is ≈ 100 nm in semiconductors [10][11], the transport of electrons can be interrupted by the connectivity of the nanoflakes in the out-of-plane direction [12][13]. Therefore, the introduction and homogenous distribution of rGO nanosheets during self-assembly with WSe_2 nanoflakes improves the electrical conductivity of the film because this nanojunction favors electrical interactions, ensuring the charge percolation through the whole film, and thus, effective charge transport over large distances.

In this first part of the chapter, a self-assembled process involving a colloidal template without degradation of WSe_2 nanoflakes promoted formation of a nanoporous film composed of anisotropic building blocks constituted of primary nanoflakes. With careful observation, the SEM images revealed WSe_2 nanoflakes building blocks of ≈ 150 nm. The XRD data analysis showed these building blocks with thickness range varying from 30 to 70 nm, corresponding to 2 to 5 primary nanoflakes of WSe_2. The electrical conductivity measurements demonstrated that the self-assembly process built a percolating network formed of rGO nanosheets, which restored the long range electrical conductivity of edge-to-plane or edge-to-edge contacts. To illustrate these findings, **Figure V - 10** presents a scheme of the morphology obtained for our 3D self-assembled rGO-WSe_2 electrode.

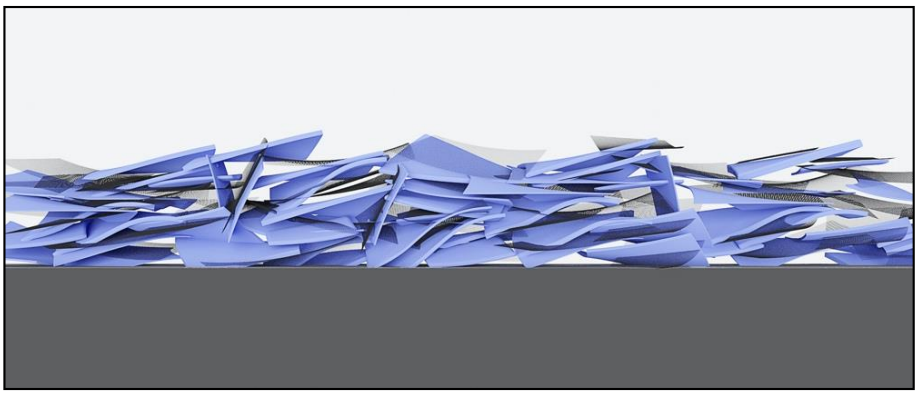

Figure V - 10: *Scheme representing the morphology of the 3D rGO-WSe_2 self-assemblies, showing anisotropic morphology of WSe_2 building blocks (blue objects) and rGO nanosheets (grey objects) and continuity of the coating film on the FTO substrate.*

V.3 Characterization of hetero-structures composed of self-assembled rGO-WSe_2 3D films and Mo_xS_y catalyst

V.3.1 High Resolution TEM investigation of 3D rGO-WSe_2/Mo_xS_y films

We have presented the use of thio, oxo-thio Mo complexes working as healing catalysts for 2D exfoliated WSe_2 electrodes. The elaboration and deposition of Mo_xS_y complexes catalyst film was obtained as previously described for the 2D exfoliated WSe_2 electrodes and significant improvement of its photocatalytic activity have been discussed, demonstrating the potentialities of this noble metal-free catalysts on TMDC materials.

Figure V - 11 shows a typical HRTEM image obtained after photoelectrochemical measurements of a 3D rGO –WSe_2/Mo_xS_y electrode. In this more detailed view, it is possible to observe the presence of isolated WSe_2 nanoflakes of lower thickness embedded in an amorphous film, having ≈ 12 nm thickness size.

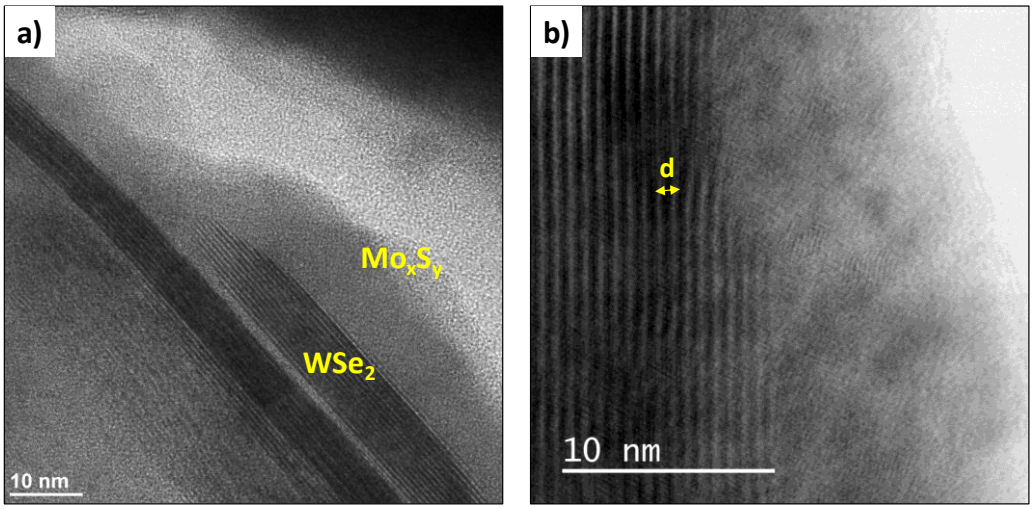

Figure V - 11: *HRTEM top view images of 3D rGO-WSe_2 nanoflakes and Mo_xS_y complexes catalyst in formation of a hetero-structure, showing (a) the arrangement of the TMDC nanosheets and the film constructed in the nanosheets periphery; (b) higher magnification of the WSe_2 nanoflake showing no degradation after co-catalyst deposition.*

HRTEM investigation also could demonstrate the formation of hetero-structures resulted from the deposition of Mo thio oxo-thio catalyst onto 3D rGO-WSe_2 films. The typical HRTEM image reveals an ultrathin amorphous film at the nanosheets periphery, displaying of irregular thickness ranging from 2 to 10 nm. Furthermore, we can assume that the thin catalyst film is chemically bonded to the WSe_2 nanoflakes due to its homogeneity and compactness in

the nanoflakes periphery. In **Figure V - 11b,** the HRTEM image taken at nanometer scale shows the Van der Waals layered structures with an interlayer spacing (*d*) of ≈ 0.66 nm. Besides, it is possible to observe the preserved structure of the WSe_2 nanoflake after catalyst deposition, showing no degradation at the edges of the WSe_2 nanoflake.

V.3.2 High-angle Annular Dark-field STEM on 3D rGO-WSe_2/Mo_xS_y hetero-structures

To further investigate the as formatted hetero-structures, HAADF-STEM analysis was performed on the 3D rGO-WSe_2/Mo_xS_y film. The ADF image, in cross sectioned view, presented in **Figure V - 12a** reveals an isolated WSe_2 nanoflake with 12 nm of thickness composed of ~ 15 elementary nanosheets observed by contrast. The EELS mapping of the ADF image, showed in **Figure V - 12b**, enabled us to see, in nanometric scale, the distribution of the atomic species of our photoelectrode film with Mo thio oxo-thio complexes catalyst. The presence of carbon was detected only along the 12 nm cross section of the WSe_2 nanoflake. Mo and S analysis identified their homogeneous presence on the periphery of the nanoflake in a 1 to 2 nm thick ultrathin film of Mo_xS_y coated on the WSe_2 nanoflake.

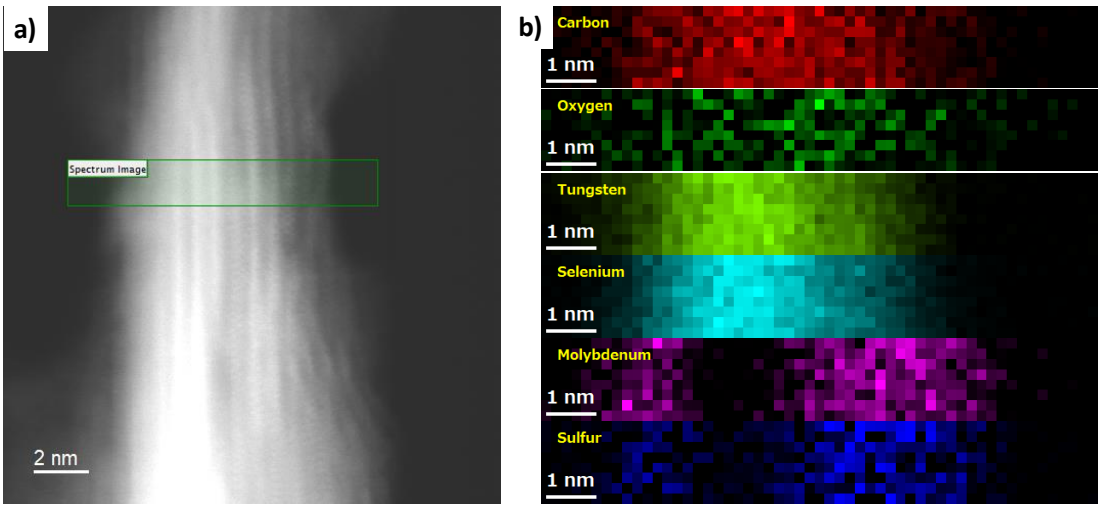

Figure V - 12: *(a) ADF image of textured WSe_2/RGO photoelectrode film in presence of Mothiooxo-thio complexes catalyst; (b) 3D elemental mapping reconstructed from the sample shown in (a). Colors indicate atomic species: red (C), dark green (O), green (W), blue (Se), purple (Mo), dark blue (S).*

Another HAADF-STEM image presented in **Figure V - 13** indicates a WSe_2 nanoflake 40 nm thick. The identification of WSe_2 nanosheets is provided by EELS mapping of W and Se (**Figure V - 13**b). However, differently from the previous ADF image, we can observe the presence of carbon nanosheets apart from the WSe_2 nanoflake spreading out on about 60 nm, probably in a non-extended conformation. Although presence of rGO nanosheets was detected attached

to the WSe_2 nanoflakes, free rGO nanosheets were also detected probably due to their low stiffness.

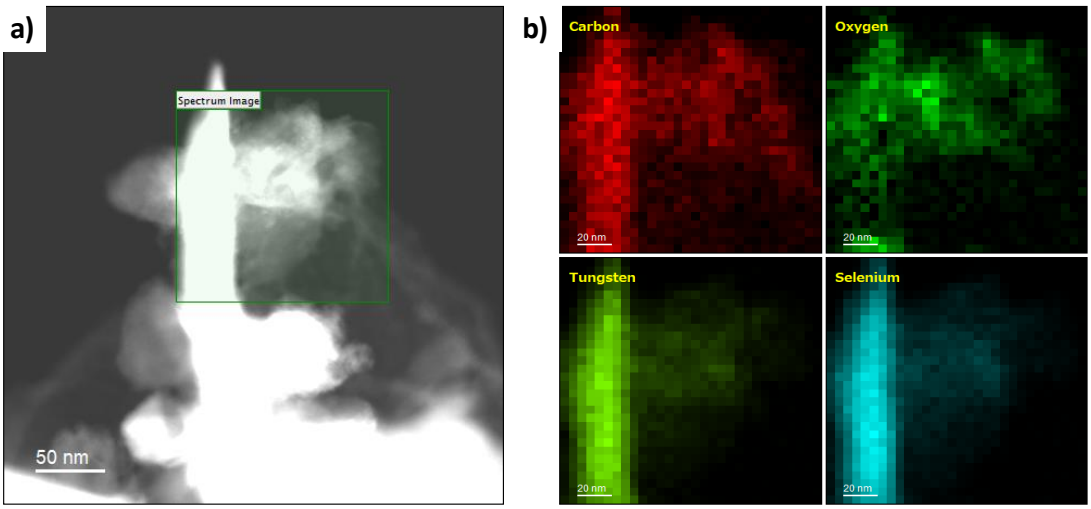

Figure V - 13: *(a) ADF image of 3D rGO-WSe_2/Mo_xS_y hetero-structure. (b) 3D elemental mapping reconstructed from the sample shown in (a). Colors indicate atomic species: red (C), dark green (O), green (W) and blue (Se).*

The XPS analysis together with DFT calculations, presented in Chapter IV, suggested the presence of $(MoS_4)^{2-}$, $(MoOS_3)^{2-}$ species developing high adsorption energy with WSe_2 surface defects and acting as passivation additives. These species should be located near the edges sites (defects) of the WSe_2 nanoflakes, and the presence of $(Mo_2S_{12})^{2-}$, $(Mo_2S_6O_2)^{2-}$ complexes provide high catalytic activity. These observations make relevance to the catalytic performances of the film; taking into account, the properties promoted by the standing Mo complexes anchored on the WSe_2 nanosheets.

V.3.3 Surface investigation of 3D rGO-WSe_2/Mo_xS_y hetero-structures probed by XPS

V.3.3.1 Chemical composition and oxidation state of 3D rGO-WSe_2 films surface

Chemical state of 3D self-assembled rGO-WSe_2 films surface were investigated using X-ray photoelectron spectroscopy (XPS). In the spectrum of W 4f presented in **Figure V - 14a**, the binding energies of $W4f_{7/2}$ and $W4f_{5/2}$ indicate that the elemental chemical state of W remains similar as for a 2D exfoliated WSe_2 film, given as reference in **Figure V - 14b**. Meanwhile, the doublet peaks located at 35.5 and 37.5 eV is ascribed to an amount of WO_3 in exfoliated sample due to the partial oxidation of the WSe_2 nanosheets [14]. The best photoelectrodes are composed

of nanoflakes selected at 800 rpm and after graphene oxide co-texturation to form our 3D rGO-WSe_2. XPS quantifications determined Se/W ratio of 1.95 for the 3D self-assembled rGO-WSe_2 film and the Se/W ratio of 1.94 for the 2D WSe_2 film. This demonstrates that no significant chemical degradation of the WSe_2 nanoflakes existed during the self-assembly process, using primary nanoflakes with 30 to 70 nm thickness.

Analysis of quantitative data of XPS revealed that the partial oxidation of the nanosheets was relatively low, atomic ratio (r_{WO}), ($r_{WO} = WO/(WO + WSe_2)$), between 10-20%. Small value of r_{WO} molar was also observed on 2D exfoliated WSe_2 nanoflakes before self-assembly. This second data set indicates that partial nanoflakes oxidation in both structures comes from the exfoliation process performed in Air atmosphere. Furthermore, comparing r_{WO} of 3D rGO-WSe_2 and 2D WSe_2, we notice higher r_{WO} for the 2D as-exfoliated sample. Ultrathin nanosheets favor high temperature degradation associated with Se elementary formation. Hence, the smaller value of r_{WO} for the 3D rGO-WSe_2 is probably associated with the use of $Sn_xSb_yS_z$ template to form the 3D nanostructure, which delays WSe_2 decomposition.

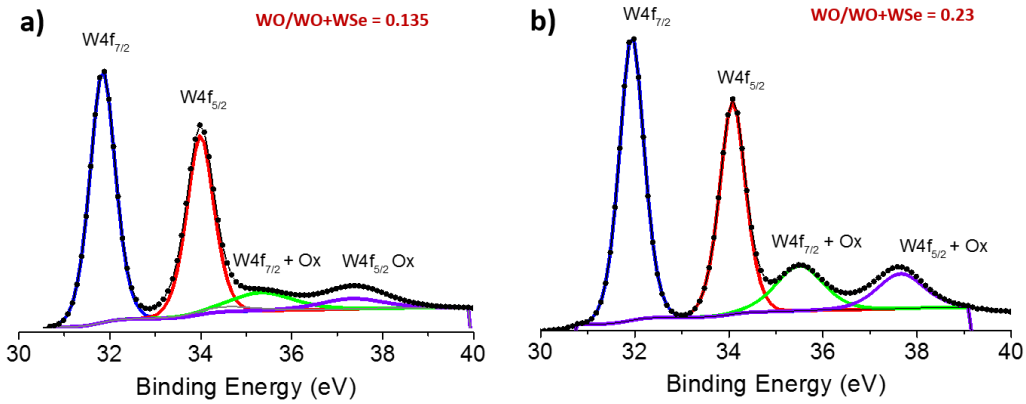

Figure V - 14: *XPS core-level spectra and deconvolution into W 4f contributions for (a) 3D rGO-WSe_2/Mo_xS_y hetero-structure and (b) 2D WSe_2/Mo_xS_y film.*

In addition, the XPS spectrum in **Figure V - 15** shows the C 1s core level deconvoluted into four peaks. The main peak at 284.3 eV is assigned to C-C bond. The weakened peaks at 282.6 eV, 285.6 eV and 288.08 eV is corresponding, respectively, to metal carbides, C-O and C=O bonds. This shows effective reduction of GO and it is in accordance with previous reports [15]. From XPS data, we determined an amount of oxygen (r_{CO}) content for the 3D films prepared from WSe_2 of lower thickness ($r_{CO} = CO/(CO + CC)$) of 0.14. This fraction of CO bonds is relatively important and suggests a relative high content of non-reduced graphene oxide.

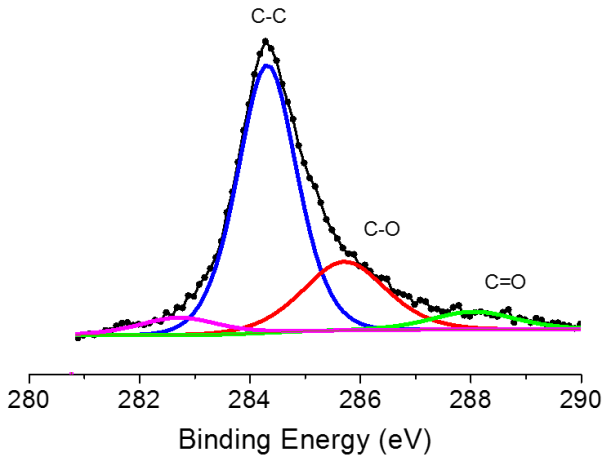

Figure V - 15: *XPS core-level spectra and deconvolution into C 1s contributions of exfoliated 3D rGO-WSe_2/Mo_xS_y.*

V.3.3.2 Chemical composition of rGO-WSe_2/Mo_xS_y complexes films

Knowing that the average thickness of the catalyst film is lower than 10 nm, the chemical composition of the whole catalyst film and the WSe_2 nanoflake surface could be further investigated by XPS. **Figure V - 16** shows the XPS spectra obtained for the Mo_xS_y complexes catalyst coating onto the WSe_2 surface.

The Mo 3d spectrum, shown in **Figure V - 16**a, is dominated by a doublet of Mo $3d_{5/2}$ peak with binding energy (BE) of 229.08 eV. This doublet is attributed to the Mo (IV) ion in MoS_2[16]. A smaller doublet Mo $3d_{3/2}$ peak at 232.3 eV is also visible. The Mo 3d spectrum shows a mixture of Mo oxidation states Mo (IV), whereas the intermediate peak observed at BE $3d_{5/2}$+ O_x = 232.82 eV and BE $3d_{3/2}$ + O_x = 234.82 eV is assigned to MoO_yS_z, as previously identified in the Mo thio, oxo-thio complexes precursor solution, by ESI-MS analysis (Chapter IV). The assignment of this intermediate peak to the oxysulfides complexes corresponds to (r_{MoOS}) atomic ratio of 0.16 ($r_{MoOS} = MoOS/(MoOS + MoS)$), the maximum value of r_{MoOS} observed for the film. The Mo oxidation states should be originated from the oxo-thio Mo complexes present in the precursor solution as evidenced by ESI-MS (in Chapter IV).

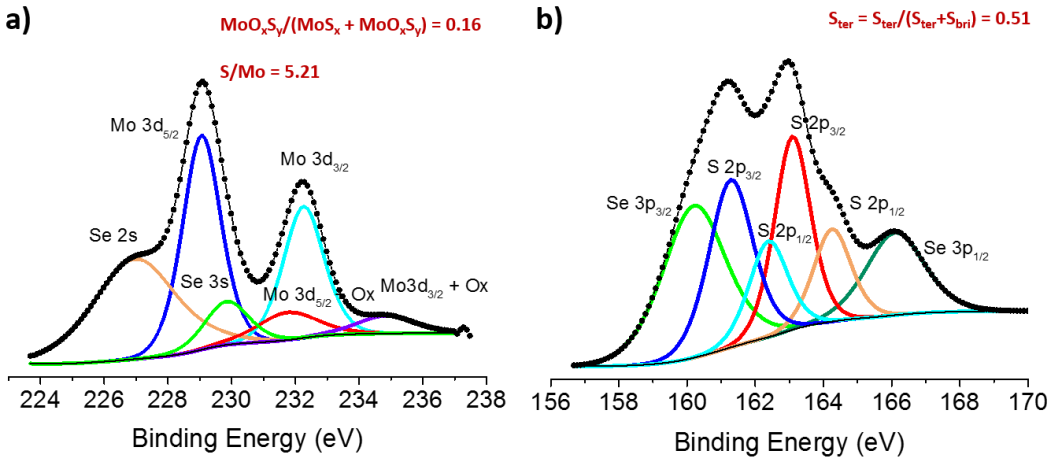

***Figure V - 16**: XPS core-level spectra and deconvolution into (a) Mo 3d contributions for a dip coated 3D WSe_2/RGO thin film. (b) S 2p spectra consist of two different doublets (S $2p_{1/2}$ and S 2 $p_{3/2}$).*

Figure V - 16b shows a doublet corresponding to $S2p_{1/2}$ and $S2p_{3/2}$ peaks with binding energy of 162.4 and 161.3 eV, respectively in the S 2p spectrum, and probably assigned to terminal sulfide (S^{2-}) and disulfide groups (S_2^{2-}). A second doublet was noticed after deconvolution corresponding to $S2p_{1/2}$ and $S2p_{3/2}$ peaks with binding energy of 164.24 and 163.1 eV, respectively. This second doublet can be assigned to multilayer deposits that gave surfaces with higher BE corresponding to disulfide bridging groups (S_2^{2-}) [17].

Further data quantification analysis extracted from both Mo 3d and S 2p spectra could gave an average value of (S/Mo) = 5.21, in the optimum pH range 8.7 < pH < 9.3. This S/Mo atomic ratio gives a value between the atomic ratio of Mo clusters known in the literature $(MoOS_3)^{2-}$ [18], $(MoS_4)^{2-}$ [19] and $(Mo_2S_{12})^{-2}$ [20] and suggests the presence of both small healing complexes such as $(MoS_4)^{2-}$ and $(MoOS_3)^{2-}$ associated with more catalytically active Mo dimers or trimers complexes such as $(Mo_2S_{12})^{2-}$ or $(Mo_3S_6O)^{2-}$.

In the Chapter IV, 2D WSe_2 electrodes showed high value of sulfide terminal ratio ($rS_{ter} \geq 0.4$) - where $rS_{ter} = S_{ter}/(S_{ter} + S_{br})$ - through dip coating of thio, oxo-thio Mo complexes film. XPS data recorded on the 3D self-assembled rGO-WSe_2/Mo_xS_y hetero-structures reveals $S_{ter} = 0.51 > 0.4$ for the most efficient dip coated photoelectrodes. The significant rS_{ter} value suggests high proportion of non-linked, accessible disulfide groups (S_2^{2-}), arising probably from $(MoS_4)^{2-}$, $(Mo_2S_{12})^{2-}$ and $(Mo_2S_6O_2)^{2-}$ complexes actives for the HER, after anchoring on the WSe_2 surface.

In summary, HRTEM images could reveal the presence of isolated WSe_2 nanoflakes of lower thickness, varying from 10 to 15 nm, with an average thickness around 40 nm. HRTEM and HAADF-STEM images set evidence of formation of an ultrathin thio, oxo thio Mo complexes homogeneous film (2 - 10 nm thickness) coating WSe_2 nanoflakes. Identification of rGO-WSe_2 and Mo_xS_y was provided by HAADF-STEM with EELS mapping, setting an experimental evidence of the formation of the layered hetero-structure of rGO-WSe_2/Mo_xS_y in a well-defined sequence. XPS analysis showed no chemical degradation of WSe_2 nanoflakes after self-assembly process, with a partial oxidation of 10-20%, lower than partial oxidation of 2D WSe_2 films. This decrease of the r_{WO} presented by the nanostructured rGO-WSe_2 film is assigned to delayed degradation of the nanoflakes, thanks to the use of the $Sn_xSb_yS_z$ colloidal template. Besides that, C 1s spectrum confirmed reduction of the graphene oxide. Concerning the deposition of Mo_xS_y catalyst film, the XPS spectra revealed presence of oxy-sulfides complexes, involving the selection of complexes such as $(MoOS_3)^{2-}$, $(Mo_2S_6O_2)^{2-}$ and $(Mo_3S_8O)^{2}$. Similarly, as the anchoring of these complexes for the 2D WSe_2 films, the important value of S_{ter} suggests, besides the high interactions with the WSe_2 surface, the presence of accessible sulfide-disulfide groups attributed to $(MoS_4)^{2-}$ and $(Mo_2S_{12})^{2-}$ complexes.

V.4 Photoelectrochemical characterizations of 3D rGO-WSe_2/Mo_xS_y hetero-structures

V.4.1 Photocatalytic activity on bare 3D self-assembled rGO-WSe_2 films

Before Mo_xS_y catalyst deposition to form hetero-structures, photo-electrochemical production of hydrogen was investigated on 3D-free rGO-WSe_2 and 3D rGO-WSe_2 electrodes in 0.1 M Na_2SO_4. **Figure V - 17** presents LSV curves obtained for the self-assembled electrodes and as reference, polarization curve of as-exfoliated 2D WSe_2 electrode. A photocurrent density up to -50 µA cm^{-2} at +0.0 V vs NHE was recorded under chopped light (100 mW cm^{-2}) for the rGO-free 3D WSe_2 (red curve). Significant improvement of the photocatalytic activity was observed for 3D rGO-WSe_2 film, producing a photocurrent of -150 µA cm^{-2} at 0 V vs NHE without any Pt catalyst addition (blue curve). Although photocurrent of -70 µA cm^{-2} was observed at 0 V vs NHE on control films prepared by drop casting of exfoliated 2D WSe_2 nanosheets dispersion (green curve).

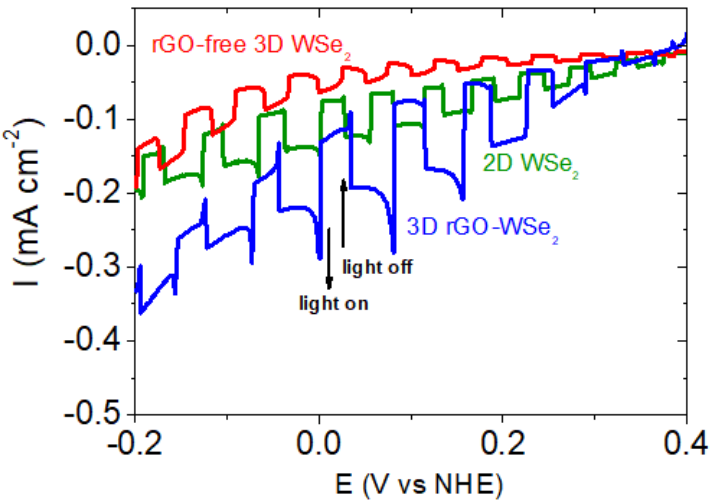

Figure V - 17: *J-V photocurrent density-voltage curves recorded on exfoliated WSe_2 2D (red curve), 3D free rGO-WSe_2 (red curve) and 3D rGO-WSe_2 (blue curve) films.*

For a potential E = 0 V vs NHE, the different photocurrents revealed by the polarization curves of the three different WSe_2 electrodes can be directly associated with the different resistivities promoted by each sample (**Figure V - 9**). Thanks to the introduction of rGO nanosheets, charge percolation and collect showed to be more efficient. Therefore, the higher photocurrent obtained for the 3D rGO-WSe_2 electrode is highly likely due to an improvement of

the material conductivity. Nevertheless, by optimizing the rGO/WSe_2 ratio, the photoelectrochemical response can be improved even further.

V.4.2 Optimization of the rGO nanosheets ratio for improved charge carrier collect

A study involving rGO nanosheets self-assembled with WSe_2 nanoflakes is intended to highlight the correlation between the charge transfer resistance and the different rGO/WSe_2 ratios. To find the optimum ratio, it was investigated different quantities of GO dispersion (% wt.) self-assembled with the WSe_2 nanoflakes. Three different 3D rGO-WSe_2 electrodes with different r_{rGO}, where $r_{rGO} = rGO/(rGO + WSe_2)_{\text{molar}}$, are presented in **Table V - 2** with their respective mass ratios.

***Table V - 2**: rGO molar and mass ratios obtained from different volume of GO dispersions used for co-texturation with WSe_2 nanoflakes.*

	$\boldsymbol{r_{rGO} = n_{rGO} / (n_{rGO} + n_{WSe_2})}$	$\boldsymbol{\% wt = (m_{rGO} / (m_{rGO} + m_{WSe_2})) x 100}$
Sample 1	0.03	0.1
Sample 2	0.08	0.3
Sample 3	0.2	0.7

The 3D rGO-WSe_2 electrodes have been evaluated via Linear Sweep Voltammetry under chopped light. In **Figure V - 18** is reported the LSV plots for 3D rGO-WSe_2 samples obtained in 0.5 M H_2SO_4, for the different ratios. For a low rGO ratio (around 0.03 i.e. 0.1 % wt.) a very low photocurrent, in order of -10 µA cm^{-2}, is achieved (green trace); for a medium rGO ratio (around 0.08, i.e. 0.3 % wt.), a photocurrent of -100 µA cm^{-2} (red trace) is obtained. As expected, for the higher rGO ratio (0.22, i.e. 1 % wt.), significant photocurrent was registered, being around -400 µA cm^{-2} at -0.1V vs NHE.

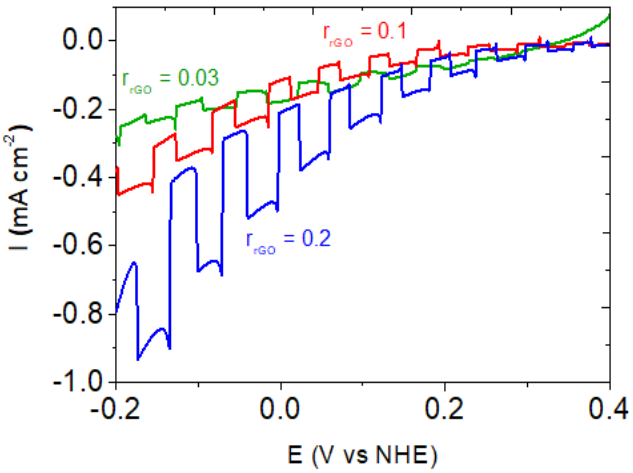

Figure V - 18: *(a) LSV curves of 3D rGO-WSe_2 photoelectrodes with different r_{rGO} ratios under internment light (100 mW cm^{-2}). Electrolyte: 0.5M H_2SO_4.*

To further understand the differences in the photoactivity promoted by the 3D rGO-WSe_2electrodes, Electrochemical Impedance Spectroscopy (EIS) was performed to investigate the electrode charge transfer resistance (R_{ct}). **Figure V - 19** presents the Nyquist plots obtained with EIS data and fitted with a simplified Randle-equivalent circuit. Charge transfer resistances (R_{ct}) of ≈ 2500, 1500 and 1000 Ω cm^{-2} are measured for the 3D rGO-WSe_2 electrodes with rGO ratios of respectively 0.03, 0.08 and 0.2. This result is in agreement with the increase of the photocurrent with the rGO ratio (**Figure V - 18**), and is consistent with the formation of a percolating network constituted of rGO nanosheets and WSe_2 nanoflakes. It also evidences how a minimum film resistivity is associated with a lower charge transfer resistance.

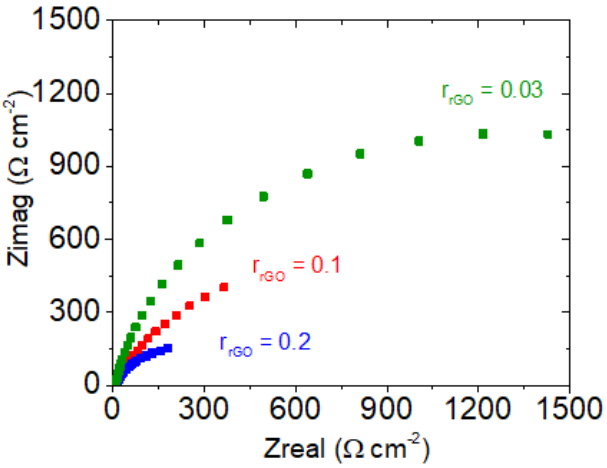

Figure V - 19: *Nyquist plots of 3D rGO-WSe_2 photoelectrodes with different r_{rGO} ratios. Electrolyte: 0.5M H_2SO_4. AC impedance measurements at -0.2 V vs NHE.*

Considering the surface coverage ratio (σ) of the WSe_2 nanoflakes by the rGO nanosheets,

$$\sigma = \frac{S_{GO}}{2\ S_{WSe2}} \qquad (V-1)$$

Where, S_{GO} and S_{WSe2} stand for respectively the surface area of one rGO nanosheet and the surface of one WSe_2 nanoflake.

Taking into account the total surface of the film:

$$N = \frac{Total\ surface}{S_{nanosheet/nanoflake}} \qquad (V-2)$$

Where, N is the number of rGO nanosheets or WSe_2 nanoflakes present in the total surface. So the coverage ratio (σ) stands for,

$$\sigma = \frac{N_{rGO} * S_{GO}}{2\ N_{WSe2} * S_{WSe2}} \qquad (V-3)$$

With, $n = \frac{m}{M_w} = \frac{\rho * V}{M_w} = \frac{\rho * S * e}{M_w}$, we obtain:

$$S = \frac{n * M_w}{\rho * e} \qquad (V-4)$$

Where, M_w is the molar mass, ρ is the material density and e is the nanosheet/nanoflakes thickness. Thus, we have:

$$\sigma = \frac{[r_{rGO}] * Mw_{GO} *}{\rho_{GO} * e_{GO}} * \frac{\rho_{WSe2} * e_{WSe2}}{2 * Mw_{WSe2} * S_{WSe2}} \qquad (V-5)$$

Thus, we have the coverage ratio as being:

$$\sigma = \frac{[r_{rGO}] * Mw_{GO} * \rho_{WSe2} * e_{WSe2}}{2 * \rho_{GO} * e_{GO} * Mw_{WSe2}} \qquad (V-6)$$

Thus, considering WSe_2 an overall nanoflakes thickness of 45 nm and a single GO nanosheet thickness of approximately 1 nm [21], for r_{rGO} being 0.7 % wt., a coverage ratio (σ) of 0.75 was obtained.

Despite the improvement of the photocurrent on 3D rGO-WSe_2 electrodes with an optimum rGO ratio, current density still remained far from the photocatalytic performance

offered for the best photocathodes in solar water splitting [22][23]. As reported for the 2D as-exfoliated WSe_2 film in the previous chapter, the photocurrent curve referred to the 3D rGO-WSe_2 presents high transient photocurrent response – current spikes while the light is turned on. Although photocatalytic activity is better in presence of rGO, these current spikes result from charge recombination because of the existence of high defect concentration [9]. The charge collection has been improved, but photogenerated electrons still experience a high recombination rate. In other words, charge transfer across the electrode/electrolyte is poorly efficient because of the short lifetime of electron before its recombination [24]. Therefore, the same surface modification approach presented in the Chapter IV was performed for the 3D self-assembled rGO-WSe_2 film. After the deposition of thio, oxo-thio Mo complexes catalyst, electrochemical analysis was realized to investigate the photocatalytic properties of the new 3D rGO-WSe_2/Mo_xS_y hetero-structure.

V.4.3 Photocatalytic activity of 3D rGO-WSe_2/Mo_xS_y hetero-structures

Figure V - 20 reports a typical Linear Scanning Voltammetry curve recorded on a film of 3D rGO-WSe_2/Mo_xS_y hetero-structure in 0.5M H_2SO_4 electrolyte. A high photocurrent up to -5.0 mA cm^{-2} at -0.2 V vs. NHE under intermittent 1 sun illumination was registered for the 3D rGO-WSe_2/Mo_xS_y film. A significant improvement of the photocurrent is clearly seen, compared with the exfoliated 2D WSe_2 film, also after thio, oxo-thio Mo complexes catalyst deposition, with photocurrent of -2.0mA cm^{-2} at -0.2 V vs NHE. The lower charge carrier recombination is attributed probably to the self-assembly of rGO nanosheets into the WSe_2-based hetero-structures in the interconnected network. Then, it can be assumed the achievement of an improved charge percolation network, thanks to the rGO, which ensures a more efficient charge collection, because of a shorter charge-to-current collector distance [25][26]. It has been already reported that higher photocurrent can be obtained while the charge transfer distance to the current collector is shortened [27][28].

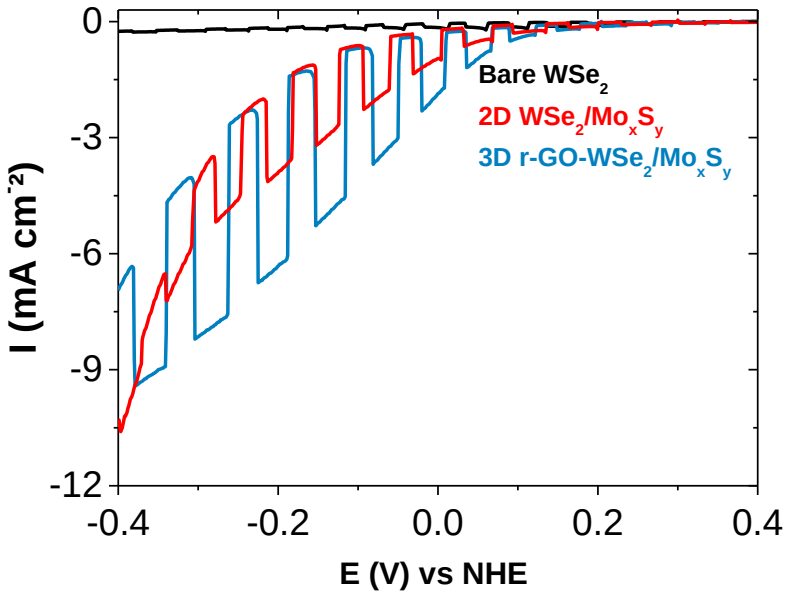

Figure V - 20: *Linear Scanning Voltammetry (LSV) curves recorded on 3D self-assembly of rGO-WSe_2 nanoflakes (blue trace). Electrolyte: 0.5 M H_2SO_4. LSV curves recorded on bare WSe_2 (black trace) and 2D WSe_2/Mo_xS_y film (red trace) are given for comparison.*

Photoelectrochemical responses under intermittent light of the different nanostructured 3D WSe_2 electrodes have been gathered in **Figure V - 21**. The photo-electrode film without rGO incorporation (free-rGO 3D WSe_2 film – green trace) yield very low photocurrent (-10 µA cm^{-2} at – 0.2V vs NHE). After rGO incorporation (3D rGO WSe_2 – orange trace), we can notice an improvement of the photocurrent (up to -400 µA cm^{-2} at -0.2 V vs NHE). Despite increased photocurrent, recombination of charge carriers still remained predominant, as showed by the current spikes and the slight photocurrent. Co-catalyst of Mo-thio complexes were deposited onto free-rGO 3D WSe_2 (**Figure V - 21**, cyan trace) and besides an increase of the electrocatalytic activity, photocurrent still remained low. What can be associated with the high layer resistivity, due to the edge-to-edge or edge-to-plan nanoflakes configuration. Finally, the contribution of the Mo_xS_y catalyst film is highlighted when associated to the efficient charge percolation into the WSe_2 nanoflakes thanks to rGO nanosheets (**Figure V - 21**, blue trace). One no longer observes the presence of transient currents after co-catalyst deposition and the photocurrent ramps up under polarization.

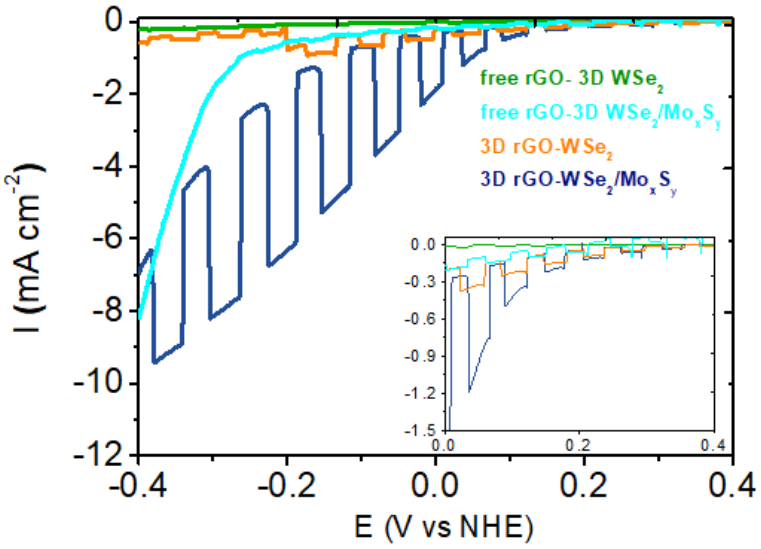

Figure V - 21: *LSV curves recorded on 3D self-assembly of WSe_2 nanoflakes (green trace), 3DrGO-WSe_2 (orange trace), free-rGO 3D WSe_2/Mo_xS_y (cyan trace) and 3D rGO-WSe_2/Mo_xS_y (blue trace). Electrolyte: 0.5 M H_2SO_4. Mo thio complexes aqueous solution (S/Mo= 5; pH 9.0) impregnation by selective dip coating film (2 x 16 h).*

The addition of rGO nanosheets within the WSe_2 nanoflakes together with the efficiency of depositing the ultrathin multicomponent catalyst film has improved the photoelectrode performance, reaching photocurrent up to -5.0 mA cm^{-2} at -0.2 V vs NHE. This value is in the range of the best values reported in the literature on 2D photocathodes to the best of our knowledge. The rGO-based nanojunctions has been reported as leading to a faster charge transport through the interfacial layers, hindering the recombination of the photogenerated electron–hole pairs and ensuring the availability of free charge carriers to assist the catalytic activity [29]. Therefore, to get a better insight regarding the improvement of the photocurrent obtained by the hetero-structure, electrochemical impedance spectroscopy has been performed.

V.4.4 Charge-transfer resistance of 3D rGO-WSe_2/Mo_xS_y hetero-structures

Electrochemical Impedance Spectroscopy (EIS) of the 3D rGO-WSe_2 photoelectrodes was performed, before and after co-catalyst deposition, to investigate the charge transfer resistance of the new hetero-structure for the HER. Similarly as for the 2D as-exfoliated WSe_2, the samples showed decreased charge transfer resistance over polarization after catalyst coating. **Figure V - 22** presents Nyquist Plots of 2D WSe_2 (given as reference) and 3D rGO-WSe_2 without Mo_xS_y catalyst, in the potential range of 0.2 V to -0.2V vs NHE, obtained in 0.5M H_2SO_4, under illumination (λ = 450 nm). A decrease of the charge transfer resistance for the self-assembled 3D

rGO-WSe_2 sample is clearly noticeable. Besides, a more regular decrease of the semi-circles is observed for the 3D rGO-WSe_2 electrode over polarization.

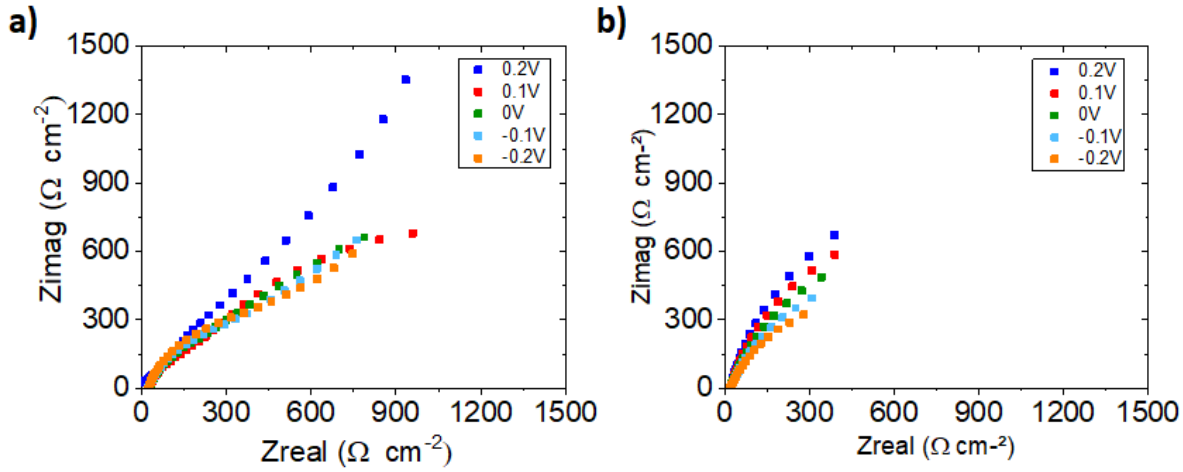

Figure V - 22: *Nyquist plots obtained from EIS data of (a) 2D WSe_2 and (b) 3D rGO-WSe_2 before Mo thio, oxo-thio catalyst deposition. Electrolyte: 0.5M H_2SO_4. Potential range: from 0.2 to -0.2V vs NHE; under illumination (λ = 450 nm).*

Figure V - 23 is presenting the Nyquist plots of 2D WSe_2 and 3D rGO-WSe_2 after catalyst deposition under illumination (λ = 450 nm). Similarly as for the 2D WSe_2 film, after Mo_xS_y catalyst deposition, we notice yet decrease in the charge transfer resistance for the self-assembled 3D rGO-WSe_2 sample (**Figure V - 23b**). Indeed, the 3D rGO-WSe_2/Mo_xS_y film achieved lower charge transfer resistance over the whole potential range compared with the 2D WSe_2/Mo_xS_y, in agreement with the highest photocurrent obtained from the j – V curve (**Figure V - 20**).

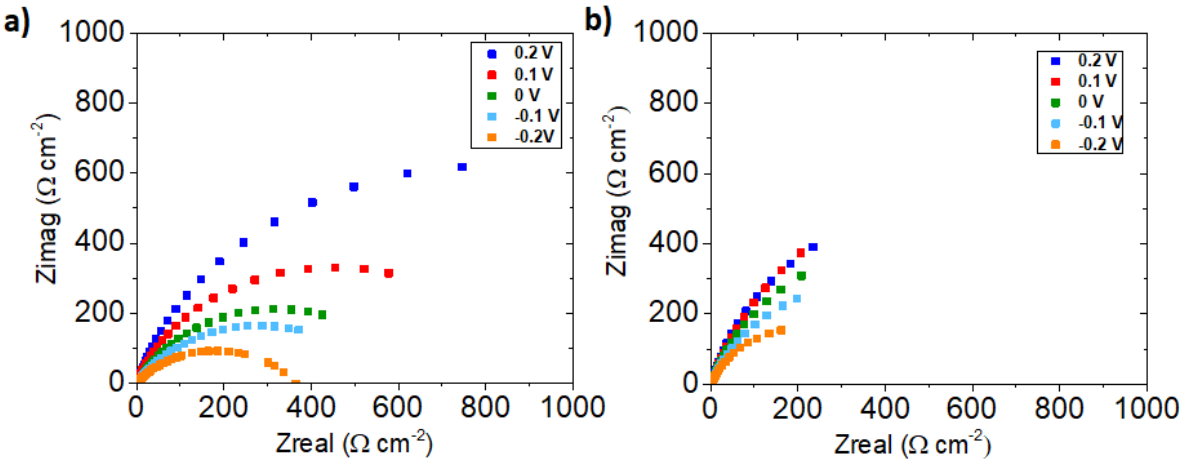

Figure V - 23: *Nyquist Plots obtained for (a) 2D WSe_2-Mo_xS_y and (b) 3D rGO-WSe_2-Mo_xS_y films in 0.5M H_2SO_4. AC impedance measurements were carried out between 0.2 and -0.2 V vs NHE, under illumination (λ = 450 nm). Electrolyte: 0.5M H_2SO_4.*

Phase angle variation plots of 3D rGO-WSe_2 electrodes exhibit different profiles of that one from the 2D WSe_2 electrodes with and without Mo_xS_y catalyst deposition, as shown in **Figure V - 24**.

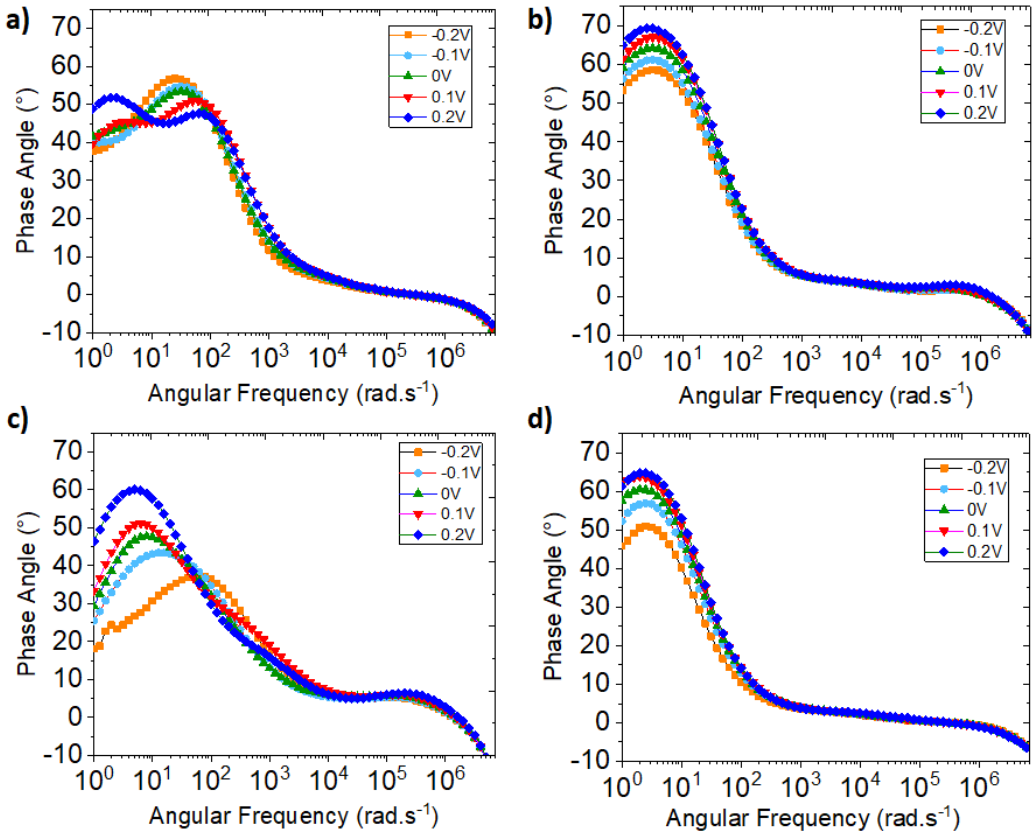

Figure V - 24: *Bode plots representation of phase angle variation from EIS data of (a) bare 2D WSe_2, (b) bare 3D rGO-WSe_2, coated (c) 2D WSe_2 and (d) 3D rGO-WSe_2 with Mo_xS_y co-catalyst photoelectrodes under illumination (λ = 450 nm) at various applied potentials from 0.2 V to -0.2V vs NHE. Electrolyte 0.5M H_2SO_4.*

As discussed in Chapter IV, for bare 2D WSe_2 electrodes three different time constants are observed, where each of them corresponded to bulk resistance at high frequency range (10^6 rad.s^{-1}), recombination process and the interface impedance, at low frequency ranges (10^2 and 10^0 rad.s^{-1}, respectively). After Mo_xS_y catalyst deposition, the coated 2D WSe_2 electrode revealed only two time constants assigned respectively to the bulk recombination and to the impedance at the interface.

Both 3D self-assembled rGO-WSe_2 electrodes (with and without co-catalyst), interestingly, revealed only two phase angle variations – two time constants –, that is similarly associated to bulk resistance, at 10^6 rad.s^{-1} and to the impedance at the interface, at low frequency

range. Differently from the bare 2D WSe_2 electrode, no presence of phase angle variation at 10^2 rad.s^{-1} was detected and besides that, the Mo_xS_y coated 3D rGO WSe_2 electrode showed phase angle variation decreasing upon polarisation between 10^1 and 10^0 rad.s^{-1}, as for the 2D WSe_2 Mo_xS_y catalyst coated.

The different time processes for the bare and Mo_xS_y coated 3D rGO electrodes could be easily deconvoluted using admittance plots, represented in **Figure V - 25**. Different semi-circles could be emphasized in the admittance representation: in the right hand side of the plots (high frequencies), a first semi-circle appears, which diameter is stable over polarization. Two other semicircles, only visible for the bare 3D rGO-WSe_2 electrode, do not change over polarization (from right to the left). Looking into the admittance plot of the sample coated with Mo_xS_y catalyst, only one low frequency semi-circle is observed (from right to the left).

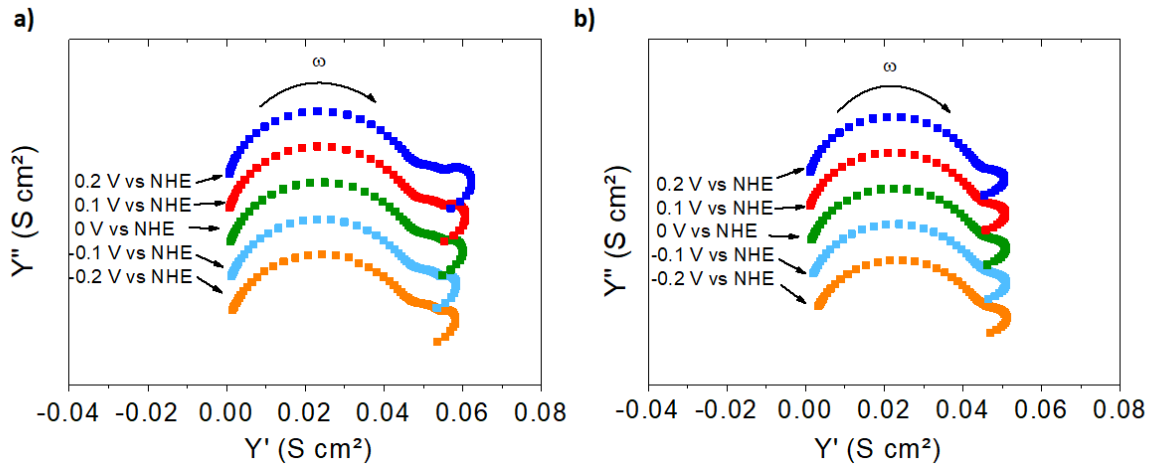

Figure V - 25: *Admittance representation from EIS data of (a) bare and (b) Mo complexes co catalyst coated 3D rGO-WSe_2 photo electrodes under illumination (λ = 450 nm) at various applied potentials from 0.2 V to -0.2V vs NHE. Electrolyte 0.5 M H_2SO_4.*

Finally, we have plotted the evolution of the charge transfer resistances extracted from the two different electrodes in function of the applied potential, as presented in **Figure V-26a**. A lower charge transfer resistance is achieved by the coated 3D rGO-WSe_2 than for the bare electrode. For regular electrochemical processes under charge transfer control, the current is expected to vary exponentially over polarization - such situation should occurs under dark condition or for poor photocurrent. Then, charge transfer resistance can be well described by the expression ($R_{CT} = R_0 * \exp[-\frac{\beta F(E-E_{i=0})}{RT}]$) [30]. This situation is observed for the bare sample, by assuming that recombination occurs via electron transfer from an exponential distribution of

surface trap states. Which is not the case of the 3D rGO-WSe_2/Mo_xS_y electrode, where a better charge separation and collection is assumed.

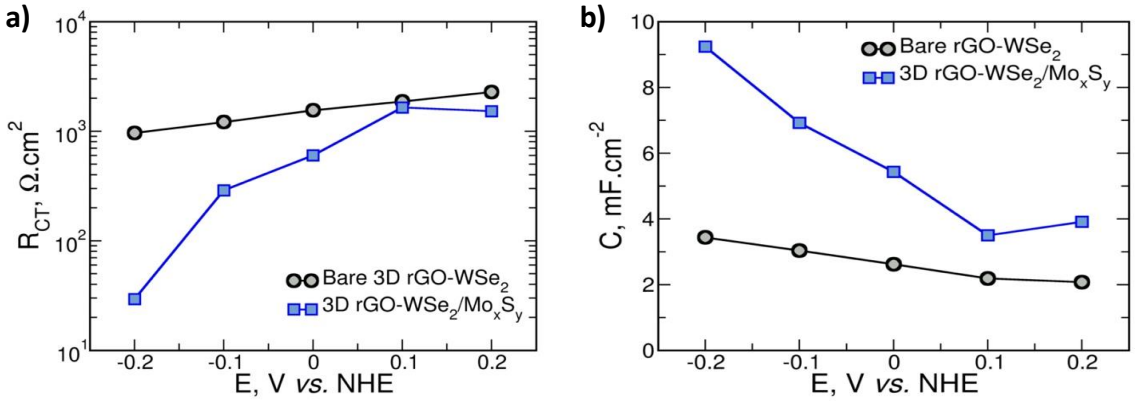

Figure V-26: *(a) variation of the charge transfer resistances and (b) variation of the interfacial capacitance extracted from fit parameters for bare 3D rGO-WSe_2 and coated 3D rGO-WSe_2 at different polarization potentials and under illumination (λ = 450 nm).*

As a matter of fact, for a poor minority charge carrier lifetime – which is expected without the co-catalyst – the overall current is mainly resulting from the major charge carriers, which leads to a regular exponential charge transfer dependence. In contrast, for a more efficient charge separation and a longer minority charge carrier lifetime, the concentration of charge carriers at the interface must be large. Thus, it is expected a more defined charge space region with complex dependence of the charge transfer resistance over the polarization. Actually, upon polarization the interface can experience different regimes under current flow: depletion, inversion and strong inversion, progressively with the increase of the electrode polarization.

The capacitance of the 3D rGO-WSe_2 samples was determined experimentally from the frequency dependence of the impedance. The experimental results have been fitted to the sample equivalent circuit and the capacitance obtained with different applied potentials are presented in **Figure V-26b**. Indeed, higher capacitance is expected for 3D rGO-WSe_2/MoxSy sample, because there is higher minority charge carrier concentration at the interface. Indeed, the increase of the effective charge transfer surface site number is in accordance with what is observed in **Figure V-26b**, presenting the real capacitance – per footprint area. Also, one can notice that the capacitance varies more importantly with the polarization for the coated sample than the bare one. This is assumed to be in line with a more effective formation of the space charge region for 3D rGO-WSe_2/Mo_xS_y, that is, over polarization the space charge region width

decrease and so the capacitance increase. While the bare nanostructured rGO-WSe_2 film shows capacitance linearly dependent on the applied potential, due to a limited charge space region.

In summary, as well as for 2D WSe_2/Mo_xS_y electrodes, 3D rGO-WSe_2 electrode charge transfer resistance is greatly enhanced by the deposition of Mo_xS_y catalyst. Faster charge transfer, lower recombination rate and faster charge collection are likely responsible for a better built-up space region, leading to better charge transfer efficiency and so a lower effective charge transfer resistance.

V.4.5 Incident Photon-to-Current Efficiency

The incident photon-to-electron conversion efficiency (IPCE) is an important indicator of solar cells and it has been used to better understand the current generation, recombination and diffusion mechanism in the PEC cell. In this method, we compared the photon absorption spectroscopy with the IPCE spectra in function of the illumination wavelength (λ) and calculated the efficiency of the light absorbed and the observed cathodic photocurrent generated by the WSe_2 films as indicated in **Figure V - 27**. The IPCE spectra was obtained by measurements of photocurrent at – 0.2V vs NHE with monochromatic lights at various wavelengths, using 3D rGO-WSe_2/Mo_xS_y photoelectrode in 0.5M H_2SO_4. We compared the photon absorption with the incident-photon-to-current (IPCE) spectra as a function of the wavelength, λ, to demonstrate that the observed cathodic photocurrent results from light absorption by the WSe_2 photoelectrode. The UV-vis spectrum of ≈ 2 µm thickness WSe_2 film shows several transition modes and a peak corresponding to an overall onset of *ca.* 750 nm.

From the absorbance spectra (red curve), the absorption coefficient increases with photon energy, so decreases with the monochromatic light wavelength. The absorption depth can vary also upon photon energy and it has been demonstrated that for a 2D TMDC few layer the absorbance depth as being maximum of 100 nm for high photon energies (400 nm) [31].

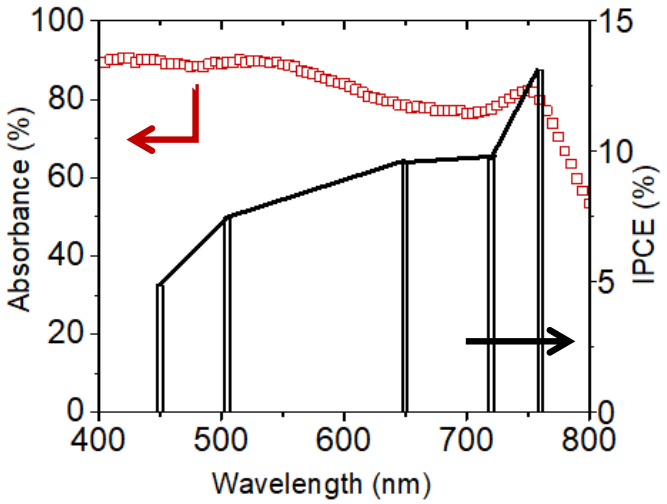

***Figure V - 27**: UV-vis absorption (red marks) and IPCE (black curve) spectra for the Mo_xS_y coated photoelectrode of 3D rGO-WSe_2 are shown together.*

The IPCE spectra obtained for our photoelectrode gave low efficiency in the blue region. We assume that the thickness range of our WSe_2 film is a limiting factor. There is probably a decreased collect and diffusion of charge carriers generated in the blue region and thus electrons generated cannot be collected in large distances of percolation. What indicates non-optimal charge carrier collection to the back of the electrode. Differently, in the region of higher wavelength ($\lambda > 650$ nm), the light can be absorbed in bigger thickness range (1 µm), whereas the collect and diffusion of the photogenerated carriers are more favorable. This explains the higher efficiency ($\eta = 12$ %) achieved in this region of the visible light spectrum.

The IPCE envelope corresponds with the absorption spectrum from the onset at $\lambda = 750$ nm to about 500nm, where it then remains roughly constant. The leveling off of the IPCE over decreased wavelengths ($\lambda < 500$ nm) confirms that factors other than light absorption limit the photocurrent of the film, such as an imperfect percolation along the whole film thickness. Assuming charge recombination is higher at the near surface, it is consistent with a drop of the IPCE with the light wavelength.

V.5 Healing Properties of the Mo_xS_y complexes catalyst onto 3D rGO-WSe_2 films

V.5.1 Additional evidence of surface defect passivation

The nanostructures obtained from direct bandgap semiconductors usually strongly emit upon photoexcitation and no PL peak intensity for these materials is usually attributed to defect-mediated non radiative recombination [32]. Photoluminescence (PL) was performed on 3D rGO-WSe_2 with and without Mo thio-complexes catalyst deposition. The PL spectra for the free-catalyst 3D rGO-WSe_2 film at room temperature, represented in **Figure V - 28**, revealed no PL peak, as consequence of the high concentration of electronically active surface defects, suspected here for this 3G rGO-WSe_2 materials.

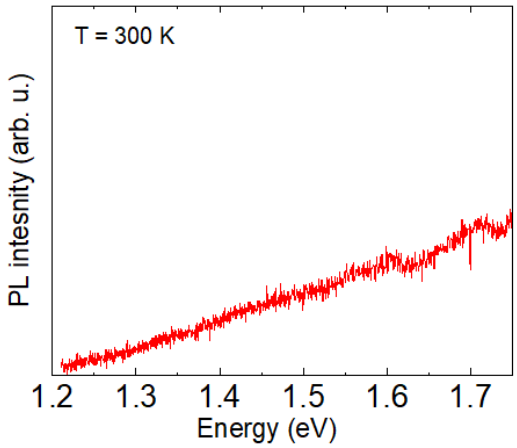

Figure V - 28: *Photoluminescence performed on bare 3D rGO-WSe_2 at 300 K.*

Despite WSe_2 bulk is known to display poor luminescence due to its nature of band gap [33], luminescence signals were recorded for measurements performed on the 3D rGO-WSe_2/Mo_xS_y hereto-structures, at two different temperatures and various lasers powers. **Figure V - 29** a and b shows respectively the wavelength shift of the PL emission peak-position observed with a laser power of 500 µW from 909 nm (1.36 eV) at 300K to 780 nm (1.59 eV) at 4K, in the measurements performed.

In the PL spectra we can notice the attenuation of PL peak with increased laser power. The PL peak position blue-shifting with temperature decreased is generally observed in traditional semiconductor, as well as we observed in our 3D rGO-WSe_2/Mo_xS_y sample (1.36 to 1.79 eV). PL signals measured at 300K exhibits an obvious enhancement with the excitation

power compared with the PL measured at 4K. This difference between 300 and 4K could possibly be due to a strong contribution of the surface defects at 4K./. From the peak energy at room temperature photoluminescence, the average thickness of the WSe_2 nanoflakes could be assessed around 40-70 nm [34] and we notice that this value correspond to the range of the building blocks thickness derived from XRD data.

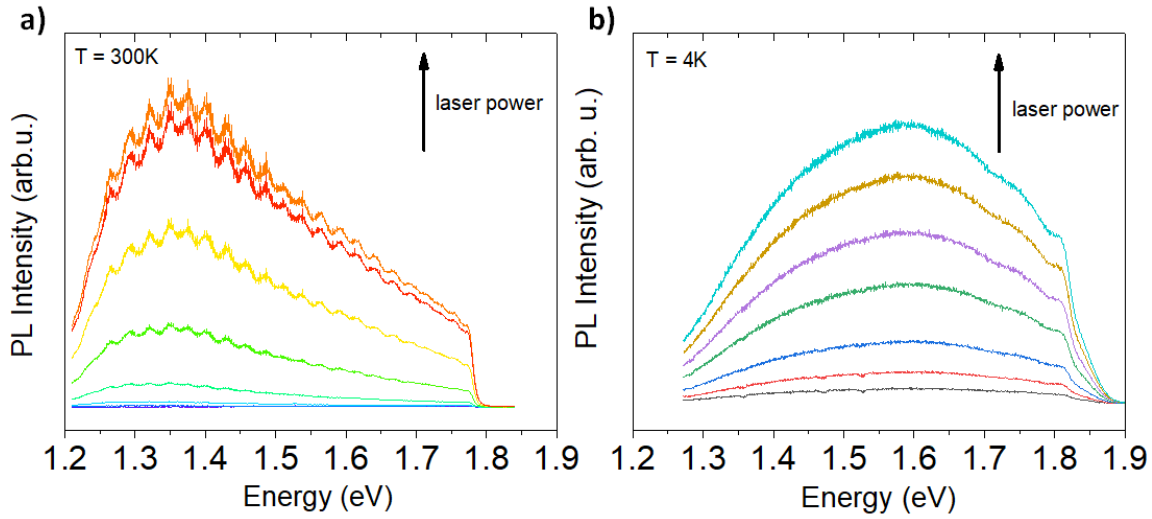

Figure V - 29: *Photoluminescence performed on 3D rGO-WSe_2/Mo_xS_y films (a) at 300K and (b)at 4K temperature. Peak attenuation is observed with the increase in laser power.*

According to PL spectra of both 3D rGO-WSe_2 with and without catalyst acquired in the same temperature, the last one exhibited a PL peak at 909 nm (1.36 eV). Thus, after co-catalyst deposition, the ultrathin film of catalyst onto WSe_2 nanoflakes periphery possibly restructure its surface from deep-level traps to reduce defected-mediated non-radiative recombination processes.

The results here reported of PL spectroscopy for the 3D rGO-WSe_2 photoelectrodes remains in agreement with the PL results discussed in the previous chapter for the as-exfoliated 2D WSe_2 after catalyst film coating. This fact put in evidence the healing property provided by the catalyst film onto the WSe_2 electrodes and also shows no interference on its properties in presence of graphene oxide. Even though, further investigations are still remaining about the surface states of the WSe_2 after both rGO self-assembly and Mo_xS_y catalyst deposition.

V.5.2 Investigation of charge transfer and recombination kinetics by IMPS

To gain further insights about the enhancement of the charge transfer offered after catalyst deposition, Intensity Modulated Photocurrent Spectroscopy was performed on 3D rGO-WSe_2 photoelectrodes with and without catalyst film coating. This analysis allows deconvolution of the contributions promoted a more effective charge transfer and could put in evidence if the better performance came from an increase of the intrinsic electron charge transfer rate or from the decrease of the recombination rate.

The IMPS responses were measured in aqueous 0.5M H_2SO_4 using monochromic illumination (λ = 680 nm) and potentials ranging from -0.05 to 0.2 V vs NHE. A set of representative Nyquist plots for 3D rGO-WSe_2 with and without presence of catalyst are shown in **Figure V - 30**, from which the surface charge transfer efficiencies ($\eta_{ct} = k_{tr}/(k_{tr} + k_{rec})$) were extracted [35].

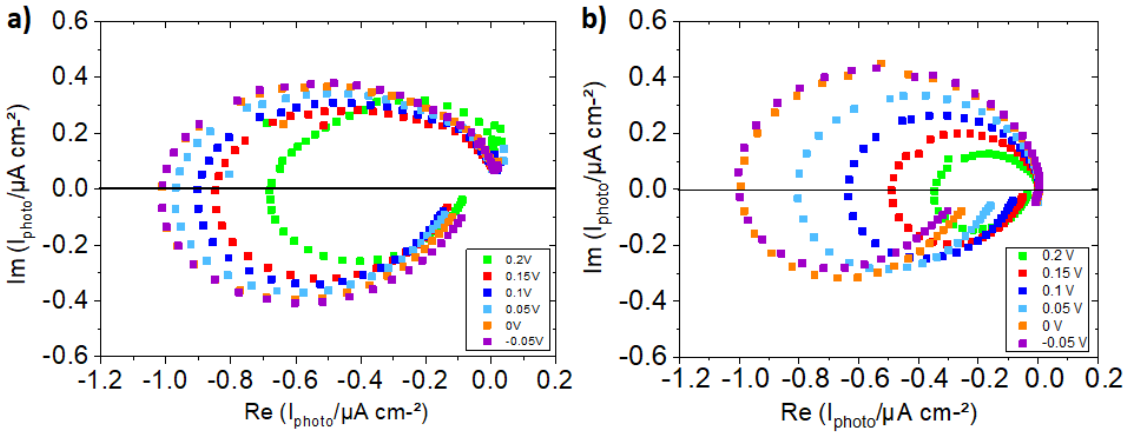

***Figure V - 30**: Representative IMPS data for (a) bare 3D rGO-WSe_2 and (b) 3D rGO-Mo_xS_y coated with Mo_xS_y catalyst under monochromic illumination (λ = 680 nm). Electrolyte: 0.5M H_2SO_4; Potential range: from 0.2 to -0.1V vs NHE; Frequency range: 20k-0.1 Hz and AC amplitude: 0.1V.*

Looking at the Nyquist Plot of the bare sample (**Figure V - 30a**), we can notice that for the entire potential range (between 0.2 and – 0.05 V vs NHE) the intercept at ω → 0 goes towards the origin, which illustrates that surface recombination wins over electron transfer to the solution. Interestingly, the catalyst coated sample exhibits much different behavior. We observe that the photocurrent is more dependent of the potential than for the bare sample – in line with charge transfer resistance variation measured from EIS. As a consequence, the deposition of the catalyst has a significant effect on the charge transfer and recombination ratios, observed through an increase of the semicircle towards for more negative polarizations (**Figure V - 30b**).

This notable difference is in agreement with the J –V curve (**Figure V - 20**) of the 3D rGO-WSe_2 after catalyst deposition.

In the ideal case, without Fermi level pinning, the energy position of the valence and conduction band edges at the interface are independent of the applied potential and the potential dependence of the charge carrier density at the surface determines the corresponding reaction rates [36]. **Figure V - 31** shows the rate constants versus applied potential obtained for the two samples, by calculating the constants rates from the Nyquist plots in **Figure V - 30** and the charge transfer efficiency (η_{ct}) extracted from the low frequency intercept, at each applied potential.

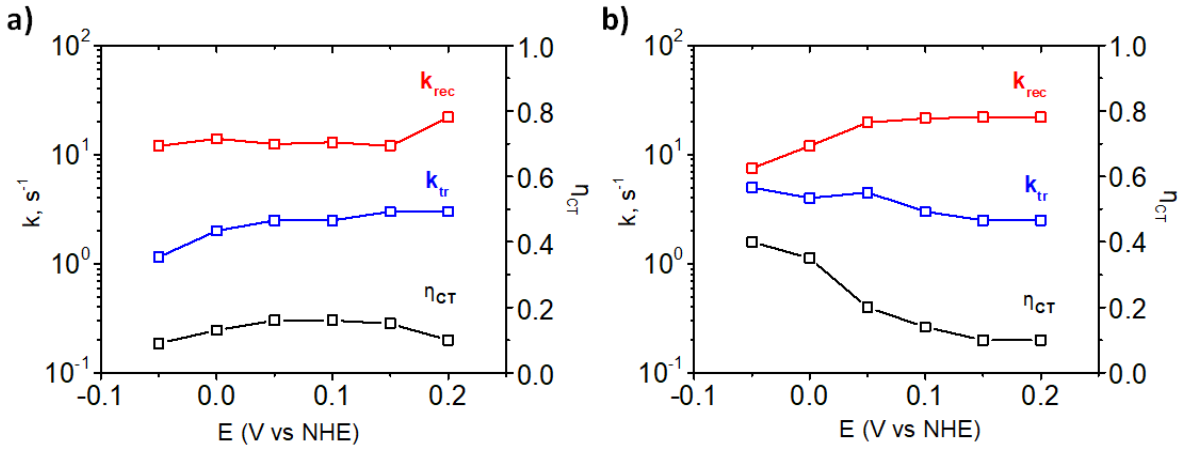

Figure V - 31: *Rate constants extracted from IMPS data for (a) bare 3D rGO-WSe_2 and (b) 3D rGO-WSe_2 coated with Mo_xS_y catalyst, at different applied potentials. Rate constants of recombination are shown as black symbols; rate constants for surface charge transfer are shown as red symbols.*

For the free-coating catalyst sample, we observe that the recombination rate constant (k_{rec}) is independent of the applied potential – as observed in the Nyquist plot, and it does not change significantly over polarization. On the other hand, the charge transfer rate constant (k_{tr}) continuously decreases over the whole potential range. Another important observation is that the recombination rate constant is larger than the charge transfer rate constant, which is responsible for a poor charge transfer efficiency in the entire potential range.

Concerning the sample of 3D rGO-WSe_2 coated with Mo_xS_y catalyst, we can notice a monotonous decrease of k_{rec} and an increase of k_{tr}, resulting, accordingly, in an improvement of the charge transfer efficiency with the polarization. It demonstrates the Mo_xS_y co-catalyst plays a double role: surface passivation (lower recombination) and charge transfer rate increase.

Interestingly, the variation of these kinetic constants is consistent with that of charge transfer resistance observed in EIS, which was decreasing with the polarization.

Besides, for the catalyst coated sample, the increase of charge transfer efficiency at more cathodic potentials is consistent with the overall increase of the photocurrent and decrease of transient current spikes. So, the IMPS data have shown that, for 3D WSe_2 electrode, the Mo_xS_y co-catalyst induces an increase of the charge transfer efficiency. Interestingly, it is highly dependent on the polarization in line with our previous findings. This co-catalyst allows for a better space charge build-up thanks to larger minor charge carrier concentration at the interface. As a result, a decrease of the recombination rate and an increase of the intrinsic charge transfer are observed with the polarization.

Conclusion

In this chapter, we proposed an optimized microstructure of WSe_2 with anisotropic morphology, provided by the self-assembly using a colloidal template that interacts with the WSe_2 nanoflakes and do not degrades its properties. SEM-FIB images showed that this process contributed to the obtention of juxtaposed and interconnected WSe_2 building blocks with thickness ranging from ≈ 120 to 150nm composed of 2 to 5 primary nanoflakes. Moreover, after introduction of rGO, the juxtaposed nanoflakes provided improvement of the charge collect creating a percolating network, as demonstrated by the conductivity measurements. We then demonstrated the existence of an optimal ratio of rGO onto WSe_2 nanoflakes to obtain an efficient charge carrier collect and percolation. Slight increase of the photocurrent was achieved for the self-assembled 3D rGO-WSe_2 photoelectrode, however presence of significant charge transfer recombination still remained. Then, catalyst thin film of Mo thio, oxo-thio complexes was deposited onto the 3D rGO-WSe_2 electrode surface by dip coating and promoted significant enhancement of the photoactivity, with an increased photocurrent up to -5.0 mA cm^{-2}, 2.5 x higher than for the 2D WSe_2/Mo_xS_y coated and the best PEC performance achieved for the WSe_2 based photoelectrode. HRTEM images showed nanoflakes of WSe_2 coated homogeneously by an amorphous thin film of Mo_xS_y catalyst forming a hetero-structure. Further electrochemical analysis revealed lower charge transfer resistances and increase of the effective charge transfer surface site number upon polarization, thanks to a better space region build-up from faster charge carrier collection and transfer, leading to higher concentration at the interface. As discussed in the chapter IV, a PL peak observed in different temperatures could be attributed to the passivation of surface defects after Mo thio, oxo-thio complexes deposition and the average thickness of the WSe_2 building blocks could be assessed from the energy peak corresponding to values obtained by XRD data. Investigations about the surface passivation by IMPS demonstrated decreased constant rate of charge recombination and increase of the effective charger transfer upon polarization after the deposition of Mo_xS_y catalyst. Indeed, we have showed that the hetero-structure formed of 3D self-assembled rGO-WSe_2 and Mo thio, oxo-thio catalyst film has improved photocatalytic properties, efficient charge collect and transfer, achieving IPCE conversion of approximately 10%. The elaboration of 3D rGO-WSe_2/Mo_xS_y hetero-structure is a strategy developed to assembly two important requirements in photocatalysis: nanostructure optimization of nanoflakes with and surface defect passivation promoting increased percolation of photogenerated charge carriers and more effective charge space region, leading to the elaboration of a high performance photocathode for the HER.

BIBLIOGRAPHY REFERENCES

[1] Y. Hou *et al.*, "Layered nanojunctions for hydrogen-evolution catalysis," *Angew. Chemie - Int. Ed.*, vol. 52, no. 13, pp. 3621–3625, 2013.

[2] K. Sivula, F. Le Formal, and M. Grätzel, "Solar water splitting: Progress using hematite (α-Fe 2O3) photoelectrodes," *ChemSusChem*, vol. 4, no. 4, pp. 432–449, 2011.

[3] M. V. Kovalenko, M. I. Bodnarchuk, J. Zaumseil, J. S. Lee, and D. V. Talapin, "Expanding the chemical versatility of colloidal nanocrystals capped with molecular metal chalcogenide ligands," *J. Am. Chem. Soc.*, vol. 132, no. 29, pp. 10085–10092, 2010.

[4] J. Y. Chane-Ching *et al.*, "Water-soluble, heterometallic chalcogenide oligomers as building blocks for functional films," *Inorg. Chem. Front.*, vol. 3, no. 5, pp. 689–701, 2016.

[5] M. V. Kovalenko, M. Scheele, and D. V. Talapinl, "Colloidal nanocrystals with molecular metal chalcogenide surface ligands," *Science*, vol. 324, no. 5933, pp. 1417–1420, 2009.

[6] S. S. Chou *et al.*, "Ligand conjugation of chemically exfoliated MoS2," *J. Am. Chem. Soc.*, vol. 135, no. 12, pp. 4584–4587, 2013.

[7] A. Castellanos-Gomez, M. Poot, G. A. Steele, H. S. J. Van Der Zant, N. Agraït, and G. Rubio-Bollinger, "Elastic properties of freely suspended MoS2 nanosheets," *Adv. Mater.*, vol. 24, no. 6, pp. 772–775, 2012.

[8] B. Ingham and M. F. Toney, *X-ray diffraction for characterizing metallic films*. 2013.

[9] X. Yu, M. S. Prévot, N. Guijarro, and K. Sivula, "Self-assembled 2D WSe2 thin films for photoelectrochemical hydrogen production," *Nat. Commun.*, vol. 6, no. May, 2015.

[10] J. S. Blakemore, "Lattice Dynamics," in *Solid State Physics*, 2nd ed., Cambridge University Press, pp. 87–148. 1985

[11] C. Kim, D. H. Kim, H. Kim, and J. S. Chung, "Significant enhancement in the thermoelectric performance of a bismuth telluride nanocompound through brief fabrication procedures," *ACS Appl. Mater. Interfaces*, vol. 4, no. 6, pp. 2949–2954, 2012.

[12] C. Kim *et al.*, "Decoupling of thermal and electrical conductivities by adjusting the anisotropic nature in tungsten diselenide causing significant enhancement in thermoelectric performance," *J. Ind. Eng. Chem.*, vol. 60, pp. 458–464, 2018.

[13] Y. Jung, J. Shen, Y. Liu, J. M. Woods, Y. Sun, and J. J. Cha, "Metal seed layer thickness-induced transition from vertical to horizontal growth of MoS2 and WS2," *Nano Lett.*, vol. 14, no. 12, pp. 6842–6849, 2014.

[14] P. Biloen and G. T. Pott, "X-ray photoelectron spectroscopy study of supported tungsten oxide," *J. Catal.*, vol. 30, no. 2, pp. 169–174, 1973.

[15] S. Stankovich *et al.*, "Synthesis of graphene-based nanosheets via chemical reduction of exfoliated graphite oxide," *Carbon N. Y.*, vol. 45, no. 7, pp. 1558–1565, 2007.

[16] J. Kibsgaard, T. F. Jaramillo, and F. Besenbacher, "Building an appropriate active-site motif into a hydrogen-evolution catalyst with thiomolybdate [Mo3S13]2– clusters," *Nat. Chem.*, vol. 6, p. 248, Jan. 2014.

[17] R. S. C. Smart, W. M. Skinner, and A. R. Gerson, "XPS of sulphide mineral surfaces: metal-deficient, polysulphides, defects and elemental sulphur," *Surf. Interface Anal.*, vol. 28, no. 1, pp. 101–105, 1999.

[18] B. R. Garrett, S. M. Polen, M. Pimplikar, C. M. Hadad, and Y. Wu, "Anion-redox mechanism of MoO(S2)2(2,2′-bipyridine) for electrocatalytic hydrogen production," *J. Am. Chem. Soc.*, vol. 139, no. 12, pp. 4342–4345, 2017.

[19] W. H. Pan, M. A. Harmer, T. R. Halbert, and E. I. Stiefel, "Induced internal redox processes in molybdenum-sulfur chemistry: conversion of MoS42– to MO2S82– by organic disulfides," *J. Am. Chem. Soc.*, vol. 106, no. 2, pp. 459–460, 1984.

[20] Z. Huang *et al.*, "Dimeric [Mo2S12]2- cluster: a molecular analogue of MoS2 edges for superior hydrogen-evolution electrocatalysis," *Angew. Chemie - Int. Ed.*, vol. 54, no. 50, pp. 15181–15185, 2015.

[21] C. J. Shearer, A. D. Slattery, A. J. Stapleton, J. G. Shapter, and C. T. Gibson, "Accurate thickness measurement of graphene," *Nanotechnology*, vol. 27, no. 12, p. 0, 2016.

[22] A. Paracchino, V. Laporte, K. Sivula, M. Grätzel, and E. Thimsen, "Highly active oxide photocathode for photoelectrochemical water reduction," *Nat. Mater.*, vol. 10, no. 6, pp. 456–461, 2011.

[23] Y. Lin *et al.*, "Amorphous Si thin film based photocathodes with high photovoltage for efficient hydrogen production," *Nano Lett.*, vol. 13, no. 11, pp. 5615–5618, 2013.

[24] D. Colombara, P. J. Dale, G. P. Kissling, L. M. Peter, and S. Tombolato, "Photoelectrochemical screening of solar cell absorber layers: electron transfer kinetics and surface stabilization," *J. Phys. Chem. C*, vol. 120, no. 29, pp. 15956–15965, 2016.

[25] N. N. Rosman *et al.*, "Photocatalytic properties of two-dimensional graphene and layered transition-metal dichalcogenides based photocatalyst for photoelectrochemical hydrogen generation: An overview," *Int. J. Hydrogen Energy*, vol. 43, no. 41, pp. 18925–18945, 2018.

[26] Y. Yuan *et al.*, "Excellent photocatalytic performance of few-layer MoS2/graphene hybrids," *J. Alloys Compd.*, vol. 700, pp. 12–17, 2017.

[27] M. V. A. Martins, A. R. Pereira, R. A. S. Luz, R. M. Iost, and F. N. Crespilho, "Evidence of short-range electron transfer of a redox enzyme on graphene oxide electrodes," *Phys. Chem. Chem. Phys.*, vol. 16, no. 33, pp. 17426–17436, 2014.

[28] M. Wu, Y. Li, B. Yao, J. Chen, C. Li, and G. Shi, "A high-performance current

collector-free flexible in-plane micro-supercapacitor based on a highly conductive reduced graphene oxide film," *J. Mater. Chem. A*, vol. 4, no. 41, pp. 16213–16218, 2016.

[29] A. Mukherjee, S. Chakrabarty, N. Kumari, W. N. Su, and S. Basu, "Visible-light-mediated electrocatalytic activity in reduced graphene oxide-supported bismuth ferrite," *ACS Omega*, vol. 3, no. 6, pp. 5946–5957, 2018.

[30] C. He, Z. Zheng, H. Tang, L. Zhao, and F. Lu, "Electrochemical impedance spectroscopy characterization of electron transport and recombination in ZnO nanorod dye-sensitized solar cells," *J. Phys. Chem. C*, vol. 113, no. 24, pp. 10322–10325, 2009.

[31] Z. Cao, M. Harb, S. Lardhi, and L. Cavallo, "Impact of Interfacial Defects on the Properties of Monolayer Transition Metal Dichalcogenide Lateral Heterojunctions," *J. Phys. Chem. Lett.*, vol. 8, no. 7, pp. 1664–1669, 2017.

[32] M. Amani *et al.*, "Near-unity photoluminescence quantum yield in MoS2," *Science*, vol. 350, no. 6264, pp. 1065–1068, 2015.

[33] S. B. Desai *et al.*, "Strain-induced indirect to direct bandgap transition in multilayer WSe 2," *Nano Lett.*, vol. 14, no. 8, pp. 4592–4597, 2014.

[34] Y. Li *et al.*, "The Auger process in multilayer WSe2 crystals," *Nanoscale*, vol. 10, no. 37, pp. 17585–17592, 2018.

[35] C. Zachäus, F. F. Abdi, L. M. Peter, and R. Van De Krol, "Photocurrent of $BiVO_4$ is limited by surface recombination, not surface catalysis," *Chem. Sci.*, vol. 8, no. 5, pp. 3712–3719, 2017.

[36] I. Rodríguez-Gutiérrez *et al.*, "Charge transfer and recombination dynamics at inkjet-printed $CuBi_2O_4$ electrodes for photoelectrochemical water splitting," *J. Phys. Chem. C*, vol. 122, no. 48, pp. 27169–27179, 2018.

Outlook

Development of 2D TMDC properties for Solar Water Splitting

Introduction

To complete the electrochemical reactions involved in water splitting while harvesting sufficient portion of the solar spectrum and providing sufficient photo-potential, the PEC tandem cell is seem as a more viable device [1]. The search of semiconductors working as photocathode has showed to be in a stage less advanced than that from the photoanode side [2]. As discussed in the previous chapters, p-WSe_2 photocathodes demonstrated to achieve significant enhancement of their photocatalytic activity under implementation of healing-catalyst deposition and of a self-assembly procedure allowing the obtention of juxtaposed and interconnected building blocks with improved charge carrier collection. The positive responses obtained among the strategies developed for the p-WSe_2 promoted motivations to apply them using another TMDC material.

Despite of being not much yet investigated in photoelectrochemical applications, p-WS_2 is also HER active. Very few works have been addressed to WS_2 because it generally displays a n-type semi-conduction. Preparation of p-WS_2 requiring specific doping is still available only in laboratory scale. With an analogous structure to MoS_2, primary studies revealed WS_2 individualized sheets with excellent HER activity [3]. This TMDC material has a direct band-gap energy of 2.05 eV [4]. Besides, the band edge positions on its exfoliated form can be highly differentiated from the bulk. In addition, easier access to the monolayer thickness than for WSe_2 was previously reported [5]. These particular reasons, led us to investigate the photoelectrochemical performance of exfoliated tungsten disulfide as photocathode for HER. We thus have tried to replicate the same strategies to achieve optimized p-WS_2 photoelectrodes by: i) exfoliation and selection of p-WS_2 nanosheets, ii) self-assembly procedure with rGO nanojunctions and iii) surface functionalization by depositing Mo_xS_y co-catalyst. First results on the 2D p-WS_2/Mo_xS_y hetero-structures exhibited enhanced photoelectrochemical activity. Overall, it also validates the concept and open the way for spreading this strategy to other TMDC compounds or other 2D materials and their application as photocathodes in PEC tandem cells.

1 Self-assembly of exfoliated p-WS_2 films

1.1 2D p-WS_2 nanoflakes fabrication by solvent exfoliation

The p-WS_2 powder was obtained in collaboration with Prof. Dr. Sefaattin Tongay (Arizona State University, USA). The exfoliation of p-WS_2 was performed in dimethyl sulfoxide (DMSO, 99.7% - Fisher Bioreagents) using an ultra-sonicator 750W (Biobloc Scientific). 3g of WS_2 was exfoliated at 40% amplitude (6 sec on/4 sec off) for 18h in a 4°C bath in 30 ml of DMSO. After exfoliation, the WS_2 nanosheets were collected in the supernatant phase. Removal of soluble impurities of the WS_2 nanosheets were performed by a series of ultracentrifugation/re-dispersion at 15.300 rpm/10 min. Lastly, the WS_2 nanosheets selected between 1.500 and 6.000 rpm were re-dispersed in DMF in a final DMF solvent volume adjusted to a concentration of 8.0 g l^{-1}.

1.2 Self-assembly of WS_2 nanoflakes, Sb_2S_3 – SnS_2 template and GO nanosheets

The self-assembly process was, then, applied to p-WS_2, as presented in the previous chapter for the p-WSe_2. Co-texturation of graphene oxide (GO) and WS_2 nanosheets, both in presence of the colloidal template $Sn_xSb_yS_z$, was performed for the achievement of textured WS_2. The colloidal dispersion of WS_2 nanosheets selected at 6000 rpm in DMSO was mixed with the structuring agent consisting of spherical colloids - $Sn_xSb_yS_z$ in DMSO, similarly prepared for the WSe_2 in the previous chapter. The composition of the mixture was determined to ensure a volume fraction (Φ_{VWS2}) between the structuring agents and the WS_2 nanosheets of $\Phi_{VWS2} \approx 0.1$, similar performed as for the self-assembly with WSe_2 nanoflakes.

1.3 Fabrication of p-WS_2 electrodes and Mo_xS_y catalyst deposition

We will report here first results concerning exclusively p-WS_2 electrodes fabricated from as-exfoliated 2D p-WS_2 nanosheets without co-texturation. After drop-cast of nanosheets dispersion onto the FTO substrate and an annealing step at 350°C during 2h, under N_2 atmosphere, Mo_xS_y thin film catalyst was deposited dip coating onto WS_2 electrodes during 2 x 16h, similarly as for the WSe_2 electrodes (see chapters II and IV). The electrodes were then washed in H_2O and heat treated at 110 °C during 10 minutes. Lastly, the electrodes were submitted to photo-electrochemical characterizations. The results will allow us to evaluate the quality of the nanosheets obtained in the conditions of exfoliation and selection and to validate the use of the Mo_xS_y co catalyst as a healing catalyst on p-WS_2.

2 Characterization of high specific surface microstructure made of 2D TMDCs

2.1 Surface area and pore volume of TMDC materials

BET surface analysis was performed on textured WSe_2 and WS_2 prepared from self-assembly of nanosheets (or nanoflakes) respectively selected at 800 and 6000 rpm. Cumulative pore volumes determined from N_2 adsorption-desorption data obtained for the TDMC textured materials are presented in **Figure 1.** As observed, higher pore volume is achieved with WS_2, displaying a surface area estimated to be 30 $m^2 g^{-1}$, in line with the nanoflakes thickness defined by the selection step of the respective compounds: (800 rpm for WSe_2 and 6000 rpm for WS_2).

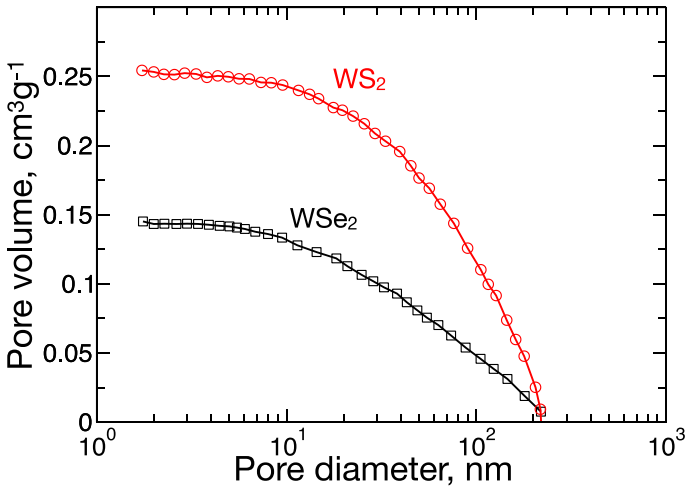

Figure 1: *Cumulative pore volume of different TMDC materials presented different nanoflakes thickness, determined from N_2 adsorption-desorption data. WS_2 - red curve (6000 rpm), WSe_2 – black curve (800 rpm).*

3 Properties of exfoliated p-WS_2 nanosheets: Preliminary results

3.1 Optical properties of exfoliated p-WS_2 thin films

UV-vis spectroscopy has been performed for thin films of WS_2 composed of exfoliated nanoflakes selected at 6000 rpm and deposited onto a glass substrate. The absorptance curve presented in **Figure 2a** was determined from the transmittance and reflectance data, using the energy conservation law ($T + R + A = 1$). The total light absorptance, in absence of scattering, is about 80% of the accessible photons ($h\nu > 1.9$ eV). The characteristic excitonic A band shows a prominent peak at 626 nm while a small peak at 526 nm is assigned to indirect B excitonic transition, also previously reported [6], [7]. According to a reported work, it is ascribed to the optical transitions between the DOS peaks from the valence and conduction bands, is characteristic of the semiconducting character with a direct band-gap [6].

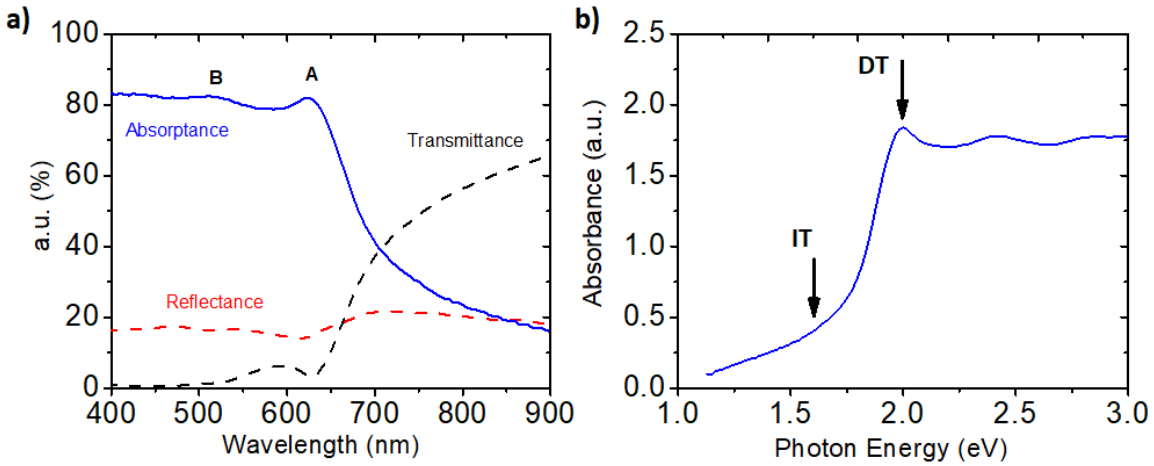

Figure 2: *(a) Absorptance (blue curve), transmittance (black curve) and reflectance (redcurve)of as-exfoliated WS_2 nanoflakes drop casted on glass substrate and annealed at 350°C under N_2 atmosphere. (b) Absorbance spectra of WS_2 thin film obtained using the Beer-Lambert law.*

The absorbance plot of the exfoliated WS_2 film, obtained from the Beer-Lambert law [8] is shown in **Figure 2b**. As similarly discussed for the exfoliated film of WSe_2 in Chapter III, this TDMC material has an indirect band-gap, as its thickness is larger than a single monolayer. Thus, the absorption becomes important only when the photons have energies equal or larger than the direct-band gap transition, indicated by DT at ≈ 1.9 eV. IT stands for the transition associated

with the indirect band-gap, which is located at ca. ≈ 1.6 eV. The larger peak centered around 2.4 eV might be associated to transitions in the valence band.

Because bulk WS_2 has an indirect band-gap energy of 1.3 eV and WS_2 monolayers has a band-gap of 2.05 eV [4], we can conclude that our WS_2 thin film is constituted of nanoflakes of few layers thickness. This result highlights the efficiency of nanosheets exfoliation, which could be a way to tune the band-gap energy of WS_2 by adjusting the thickness or the number of monolayers of the nanoflakes.

3.2 Photocatalytic performance of p-WS_2 nanoflakes for the HER

Photocatalytic performances of films composed of WS_2 nanoflakes selected at 1500 rpm are investigated.

3.2.1 PEC Performance of bare p-WS_2 photocathode

PEC evaluation of bare p-WS_2 electrodes revealed good photoactivity for films selected at 1500 rpm for the water reduction reaction in acidic media. **Figure 3** shows the LSV curve of WS_2 obtained showing a photocurrent up to -100 µA cm^{-2}) upon intermittent light (100 mW cm^{-2}). At potentials lower than -0.1 V *vs.* NHE a drastic decrease of photocurrent is observed, probably because the electrode is under inversion regime: the current is driven by the majority charge carriers.

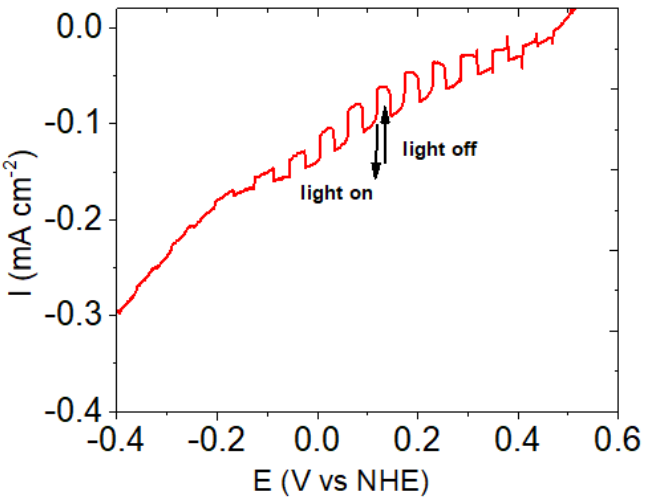

Figure 3: *LSV curve obtained for exfoliated p-WS_2 electrode deposited onto FTO substrate and after annealing at 350°C, under N_2 atmosphere.*

However, the small photocurrent and the transient current spikes observed for the WS_2 electrode are assumed to be largely driven by charge carrier recombination, due to the presence of surface defects. As we have discussed in the previous chapters, these defects are very typical on 2D materials because of volatility of the chalcogens promoting trapping states or undesirable doping [9]. Following the same approach as to WSe_2 films, we applied a surface treatment to passivate the surface defects by deposition of thio, oxo-thio Mo complexes catalyst ultrathin film.

3.2.2 PEC Performance of 2D p-WS_2 with Mo_xS_y co-catalyst

The photoelectrochemical activity of the WS_2 electrode has been evaluated after deposition of thio, oxo-thio Mo complexes catalyst, added as an ultrathin film onto the 2D-TMDC film surface. The LSV curve illustrated in **Figure 4**, obtained under intermittent illumination (100 mW cm^{-2}), shows a photocurrent up to -1.5 mA cm^{-2} at -0.2 V vs NHE for the 2D WS_2/Mo_xS_y electrode. The significant improvement of the photocatalytic activity revealed by the WS_2 electrode highlights once more that the thio, oxo-thio Mo complexes are an efficient class of catalyst well suited for the TMDC materials for the HER.

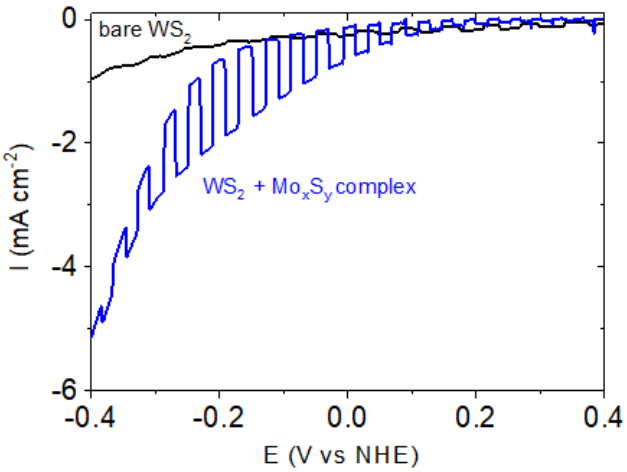

Figure 4: *LSV curve obtained in 0.5M H_2SO_4 for p-WS_2 electrode after thio, oxo-thio catalyst deposition by dip coating (2 x 16h).*

Despite large improvement of WS_2 photocatalytic activity, still further investigations need to be performed. It has been demonstrated that PEC performance of p-doped WS_2 constituted of few layers can be improved using Mo complexes catalyst, as presented in these first results. The self-assembly process performed on WSe_2 was shown to be versatile and successfully extrapolated to WS2. Besides, since the WS_2 can be exfoliated into thinner nanoflakes, we expect higher surface area and improved photochemical performances on WS_2.

4 Perspectives

To lead to a further development of 2D materials based on solar energy conversion, it is necessary to produce high quality films of 2D materials at a high rate and low cost [10]. It is also necessary to retain the desired optoelectronic properties offered by the 2D TMDC materials. For this reason, self-passivation and morphology optimization using abundant materials and techniques that are more accessible will enable the construction of promising photocathodes, with different bandgaps values, which is able to make full use of the solar spectrum and lead to higher conversion efficiency.

The challenge is to develop - without compromising, the TMDC optoelectronic properties while enhancing considerably PEC efficiency. The approaches implemented in this work have shown promising results about the performance of the 2D TMDC materials applied for hydrogen evolution. Nevertheless, further investigations involving the microstructure optimization and the passivation of surface defects remains necessaire to improve the photocatalytic activity of the TMDCs using the strategies adopted during the experiments.

Firstly, to understand the differences in the PEC performances of the p-WSe_2 in comparison with the p-WS_2 electrode, further investigations must be considered such as (i) the optimization of electric percolation promoted by the rGO nanosheets. As WS_2 has presented thinner film thickness than WSe_2 due to ultra-selection of thinner nanoflakes, the co-assembly rGO-WS_2 can form nanoflakes with more curvature and increase the sites electrochemical accessible for water reduction reaction; (ii) the precise identification of the rGO nanosheets and the co-catalyst thin film location over the WS_2 network; (iii) the optoelectronic properties of the WSe_2 and WS_2 could be further characterized, more particularly it is wanted to understand how the variation of their nanosheet thickness affects their band-gap energies and onset potentials. Besides, it would be necessary to determine conduction band levels and construct corresponding energetic diagrams for HER. Lastly, optimization of the thio, oxo-thio Mo complexes catalyst layer deposition to investigate differences in the photoelectrochemical performance of the photocathode.

All these complementary investigations might contribute for the design of tandem cells using TMDC materials as photocathodes. Nevertheless, the use of thio, oxo-thio Mo complexes as another class of catalyst material composed of various molecular species and with passivation properties for different TMDC materials can favor the band bending engineering corresponding to energetic diagrams for HER and for the future application of these tandem cells.

Conclusion

Herein, another TMDC material, p-WS_2, has started to be investigated as photocathode for the HER. We have demonstrated that our self-assembly process could be extended to another TMDC material. What highlights the beneficial use of a sulfide template easily etchable, facilitating the fabrication of high surface films composed of more thinner and more chemically stable nanosheets. Moreover, preliminary results of exfoliated p-WS_2 have demonstrated efficient exfoliation of WS_2 film composed of few-layers with 15 nm thickness. Optical measurements showed indirect and direct band-gap transitions, at respectively 1.6 and 1.9 eV, for the 2D WS_2 film, being consistent with the transitions present in TMDC thicker than a monolayer. Photoelectrochemical characterization showed p-WS_2 film photoactive for the HER, reaching a photocurrent up to -100 µA cm^{-2}. Surface modification via deposition of Mo-S based complexes catalyst showed to be similarly effective as demonstrated for p-WSe_2, and revealed a significant improvement in the photocatalytic activity of the 2D WS_2 electrodes, with a photocurrent up to -1.5 mA cm^{-2} at -0.2 V vs NHE.

These preliminary results obtained for the WS_2 could give interesting insights about its performance for the application in solar water splitting. By implementation of a self-assembly process that showed to be efficient for other TMDC material, the PEC performance of this material can be significantly improved. In addition, further investigation of this material as photocathode, such as increase of the surface area of the self-assemblies with variation of nanosheets thickness, as well as bandgap values; also other important analysis including photoluminescence and other electrochemical investigations (EIS, IMPS) will contribute to the elaboration of another TMDC-based photocathode with high performance and suitable properties for application in PEC tandem cells.

BIBLIOGRAPHIC REFERENCES

[1] K. Sivula and R. van de Krol, "Semiconducting materials for photoelectrochemical energy conversion," *Nat. Rev. Mater.*, vol. 1, p. 15010, 2016.

[2] K. Sivula, "Advancing materials and methods for photoelectrochemical energy conversion," *Chimia (Aarau).*, vol. 71, no. 7–8, pp. 471–474, 2017.

[3] D. Voiry *et al.*, "Enhanced catalytic activity in strained chemically exfoliated WS 2 nanosheets for hydrogen evolution," *Nat. Mater.*, vol. 12, no. 9, pp. 850–855, 2013.

[4] G. L. Frey and R. Tenne, "Optical properties of MS2 (M 5 Mo, W) inorganic fullerene- like and nanotube material optical absorption and resonance Raman measurements," *J. Mater. Res.*, vol. 13, no. 9, pp. 2412–17, 1998.

[5] J. Kang, S. Tongay, J. Zhou, J. Li, and J. Wu, "Band offsets and heterostructures of two-dimensional semiconductors," *Appl. Phys. Lett.*, vol. 102, no. 1, p. 012111, 2013.

[6] G. Pagona, C. Bittencourt, R. Arenal, and N. Tagmatarchis, "Exfoliated semiconducting pure 2H-MoS2 and 2H-WS2 assisted by chlorosulfonic acid," *Chem. Commun.*, vol. 51, no. 65, pp. 12950–12953, 2015.

[7] R. K. Jha and P. K. Guha, "Liquid exfoliated pristine WS2 nanosheets for ultrasensitive and highly stable chemiresistive humidity sensors," *Nanotechnology*, vol. 27, no. 47, pp. 1–11, 2016.

[8] G. Wypych, "Photophysics," in *Handbook of Material Weathering*, 6th ed., ChemTec Publishing, 2018.

[9] J. H. Park *et al.*, "Defect passivation of transition metal dichalcogenides via a charge transfer van der Waals interface," *Sci. Adv.*, vol. 3, no. 10, pp. 1–7, 2017.

[10] S. Das, D. Pandey, J. Thomas, and T. Roy, "The Role of Graphene and Other 2D Materials in Solar Photovoltaics," *Adv. Mater.*, vol. 31, no. 1, pp. 1–35, 2019.

Conclusion

The present work aimed at the study and application of 2D TMDC materials as photocathodes for hydrogen evolution from the visible light. Since the solar-to-hydrogen efficiency is highly dampened by the presence of surface states, the main strategy was devoted to the photocurrent enhancement. A surface treatment turned out to be a good strategy to reduce recombination kinetic while boosting the charge transfer kinetic. Tungsten di-selenide (WSe_2) was evaluated as a photocathode after solvent-exfoliation into 2D nanoflakes, fabricated by simple drop-cast deposition onto FTO substrate. First characterizations demonstrated that the exfoliated films of 2-3 µm thickness were constituted of well-ordered stacking nanoflakes selected at 800 rpm. Indirect and direct band-gap transitions could be observed for the exfoliated WSe_2 films, respectively, at 1.4 and 1.6 eV. First photoelectrochemical characterizations revealed a photocurrent lower than –100 µA cm^{-2} at 0V vs NHE under intermittent illumination (100 mW cm^{-2}). As noted, without any further surface modifications, the current density value is pretty low, which is in line with the presence of current spikes; high recombination rate – due to a high surface defect concentration – of photogenerated charge carriers is known to be responsible for a poor steady-state photocurrent.

To lessen or eliminate the high concentration of surface defects present in this material and take benefit of its good optoelectronic properties, different surface treatments were applied onto the exfoliated WSe_2 based photo-electrode: a Pt catalyst electrodeposition, with and without a passivation treatment, and a Mo-complex surface modification. The first approach was inspired by previous reports found in the literature, and despite a slight enhancement of the photoactivity, the photoelectrochemical response was yet beneath the values reported in the literature. Combining the necessity of finding a more effective method to improve the photocatalytic activity of the WSe_2 electrodes and the interest in alternative catalyst materials involving abundant and free of noble metal element, a study was performed involving thio, oxo-thio Mo-complexes as catalyst precursor.

In a well-defined S/Mo ratio and pH conditions (0.01 M, pH 9.0 and S/Mo = 5), distributions of Mo-S complexes species precursor catalyst were spontaneously formed in aqueous media. ESI-MS analysis could reveal the presence of monomers, dimers and trimers species of Molybdenum, such as $(MoS_4)^{2-}$, $(Mo_2S_6O_2)^{2-}$, $(Mo_2S_{12})^{2-}$, $(Mo_3S_8O)^{2-}$. XPS analysis indicated the presence of terminal and bridging sulfides (S_{ter} and S_{br}), and Mo oxysulfides (MoO_yS_z) ligands in the films formed from the aforementioned solution. The thio, oxo-thio Mo

complexes were successfully deposited onto the 2D WSe_2 surface via dip-coating, and XPS analyses showed the decrease of -S_{ter} and MoO_yS_z in contact with the WSe_2 surface after the catalyst deposition. Besides, Raman analyses revealed a partial chemical transformation of the di-sulfide bonds in contact with the WSe_2 surface. These changes are consistent with the existence of specific interactions between the WSe_2 surface and the Mo oxo-thio complexes via a selective dip-coating process.

The photoelectrochemical measurements recorded on the surface-modified WSe_2 electrodes revealed an increase of current density up to -2.0 mA cm^{-2} at -0.2V vs NHE after Mo_xS_y catalyst deposition *via* dip-coating. When compared with Pt-Cu-modified WSe_2 photoelectrodes, a higher photocurrent value is observed - after deposition of the thio- and oxo-thio- Mo-complexes, without the use of any passivating additive – was ascribed to a healing effect of surface defects. In other words, this photocatalytic improvement was successfully achieved on films activated by highly interacting complexes selected from Mo oxo-thio complexes aqueous-based solution via a simple selective dip coating film forming process. More insights about this healing effect were obtained through further electrochemical investigations, which revealed a decrease of charge transfer resistance – with a negligible contribution of the recombination resistance over photoelectrode polarization. Additional evidence of defect passivation of WSe_2/Mo_xS_y photoelectrode after Mo_xS_y deposition layer was obtained with photoluminescence spectroscopy, pointing out an indirect band-gap transition at 1.43 eV.

Further characterizations of the thio, oxo-thio Mo-complexes catalyst revealed the formation of an ultrathin amorphous film of irregular thickness ranging from 2 to 8 nm coating the 2D WSe_2 nanoflakes. Different mechanisms involving the formation of the ultrathin catalyst film were considered, such as the formation of oligomer-based of coordinated-reticulated polymer through interactions between sulfide – disulfide groups and the Mo centers with different oxidation states, followed of hetero-nucleation and growth of selected oligomers displaying of high sulfide or disulfide groups density. The optoelectronic properties of the catalyst thin film showed a direct band-gap transition of 1.8 eV and a n-type semi-conduction. These results contributed to the construction of a band energy diagram of the WSe_2 and the Mo_xS_y catalyst thin film, assuming a p/n-junction with a band engineering that favors the charge separation and the efficient migration of the photo-induced electrons.

More insights about the Mo thio, oxo-thio complexes film, as healing catalysts, were supported by DFT calculations of Mo_xS_y adsorption energies onto the 2D WSe_2 surface. It was

demonstrated the role of the oxo-thio Mo monomers and dimers of small sizes, such as $(MoOS_3)^{2-}$, $(Mo_2S_6O_2)^{2-}$, $(Mo_2S_{12})^{2-}$ to the healing process, having strong adsorption on point defects (W and Se vacancies) of the 2D WSe_2, with the formation of new Se-S bonds. Moreover, DFT calculations of H-adsorption free energies were performed on free-standing complexes, as well as on complexes anchored Mo complexes onto the 2D substrates. The resulting free energy diagram highlighted that good catalytic performances mainly arise from dimers such as $((Mo_2S_6O_2)^{2-}$or $(Mo_2S_{12})^{2-}$, preferably in a free standing regime or anchored in a low adsorption regime.

To optimize the nanostructure of the WSe_2 photoelectrode, a self-assembly process involving a colloidal template and reduced graphene oxide (rGO) nanosheets was developed to enlarge WSe_2 surface area while improving the charge carrier percolation through the nanoflakes network. SEM and TEM observations carried out on the self-assembly morphology unveiled a porous film nanostructure composed of rGO nanosheets and WSe_2 nanoflake building blocks. These building blocks were randomly oriented, with an edge-to-edge and an edge-to-plan contacts, and were composed of 2 to 5 primary stacked nanoflakes of about 150 nm thick. The anisotropic morphology presented by the self-assembly showed a significant impact in the electrical resistivity of the nanostructured WSe_2 network, which was recovered and even decreased in presence of rGO nanosheets. Images obtained in high-resolution TEM exhibited a single nanoflake of 12 nm thickness was composed of around 15 elementary nanosheets. Formation of a hetero-structure involving the self-assembled rGO-WSe_2 and the deposited Mo_xS_y catalyst could be fully identified at the nanometric scale. A 2 nm-thick amorphous film of catalyst could also be observed attached to the WSe_2 nanoflake and coating homogenously the nanoflake periphery and extension of rGO nanosheets.

Linear scan rate voltammetry under intermittent light was performed on the architectured photoelectrodes and a photocurrent as high as -5.0 mA cm^{-2} at -0.2V vs NHE was achieved, reaching the best photocatalytic performance among the reported so far the WSe_2-based photoelectrodes works. The EIS measurements demonstrated an increase of the effective charge transfer over polarization, likely because of an enhanced space charge region achieved through a better charge carrier percolation and a decrease of recombination processes. Moreover, additional analyses could highlight, once again, the passivation of surface defects after deposition of the thio, -oxo-thio Mo-complexes catalyst onto the rGO-WSe_2 surface. As exhibited in the 2D WSe_2/Mo_xS_y photoelectrodes, the PL peak attributed in the 3D rGO-WSe_2/Mo_xS_y hetero-structure indicated an enhancement of energetic transitions due to effective

separation of charge carriers. Besides, IMPS analyses demonstrated a decrease of the charge recombination constant rate with an increase of the charge transfer rate constant upon polarization; in line with the decrease of the effective charge transfer resistance observed in the EIS results. All in all, the improved photocatalytic properties achieved by the 3D rGO-WSe_2/Mo_xS_y photoelectrode allowed reaching a conversion efficiency of about 10%.

Since our strategy turned out to be promising, we have started to transpose our synthesis route and surface modification to another 2D TMDC compound: the WS_2. Our preliminary results have shown we can achieve a WS_2 porous nanostructure exhibiting indirect and direct band-gap transitions, at respectively 1.6 and 1.9 eV, and showing a photocurrent as high as -1.5 mA cm^{-2} at – 0.2V vs NHE– whereas a few tens of µA.cm^{-2} are achieved without any optimization. Even though further investigations remain necessary to improve their photocatalyst properties, the first results are encouraging and confirm WS_2 can be made suitable as a photocathode. Asides, the Mo_xS_y complexes catalyst surface modification has shown to relevant for another TMDC material.

In conclusion, the present work was addressed to the study and the development of 2D TMDC materials as photocathodes used in photoelectrochemical cells. A photocathode of exfoliated Tungsten di-Selenide (WSe_2) was elaborated by a simple process route, in the context of low-cost fabrication. The surface functionalization/modification of the WSe_2 photoelectrodes, for instance *via* surface heterojunctions and/or co-catalyst surface deposition, led to improve charge separation within the semiconductor/electrolyte interface due to more efficient electron-hole separation and faster charge transfer. The elaboration of 3D rGO-WSe_2/Mo_xS_y hetero-structure is a strategy developed to assembly two important requirements in photocatalysis: nanostructure optimization of nanoflakes and surface defect passivation. Once combined, these requirements promoted an increase in the percolation of photogenerated charge carriers and a more effective charge transfer, leading to the elaboration of a high-performance photocathode for the HER. Moreover, the design of an environmentally-friendly, aqueous-stable, catalytically active passivation layer made of oxo-thio Mo complexes as healing photo-catalysts, exhibited suitable optoelectronic properties and showed improvement of charge separation and migration for the HER onto the TMDC (p-WSe_2 and p-WS_2) photoelectrodes. These complexes have proven to be considered as ideal candidates to be coated onto 2D photoactive materials such as 2D TMDC, providing an example of band engineering involving a multicomponent and passivating layer displaying of multiple properties.

RÉSUMÉ DE THÈSE

Introduction Générale

Le réchauffement climatique accéléré et la forte demande énergétique mondiale ont conduit la communauté scientifique à se concentrer sur le développement de sources d'énergie propres et renouvelables. Parmi les nouvelles alternatives, l'hydrogène est l'un des vecteurs d'énergie les plus prometteurs. Son utilisation comme carburant est exempte de formation de gaz toxiques et d'émissions de CO_2, où le seul produit est la vapeur d'eau. Cependant, l'hydrogène n'existe pas librement dans la nature et sa production est encore d'origine fossile. Avec l'intérêt mondial pour la recherche sur l'énergie solaire, la production d'hydrogène propre peut être réalisée en utilisant des ressources durables telles que le soleil et l'eau. À cette fin, des matériaux semi-conducteurs ont été envisagés pour la collecte d'énergie solaire, permettant la conversion des photons en composés chimiques - hydrogène et/ou oxygène - par séparation de charges, souvent désignée comme conversion solaire en combustible.

Entre autres possibilités, la conversion solaire en combustible peut être réalisée en utilisant un dispositif photo-électrochimique (PEC) constitué d'une électrode semi-conductrice en contact direct avec un électrolyte liquide. En effet, pour la réalisation de cette économie de l'hydrogène, la communauté scientifique a activement recherché des cellules PEC efficaces composées de photo-catalyseurs semi-conducteurs abondants et peu coûteux.

La plupart des études portent sur des semi-conducteurs de type n, mais le développement de matériaux semi-conducteurs de type p, présentant des performances photo-catalytiques décentes, a été signalé en utilisant des photocathodes, y compris du phosphure de gallium-indium de type p (p-$GaInP_2$), silicium de type p (p-Si), type p (p-Cu_2O), tels que CZTS (cuivre zinc étain sulfure, p-Cu_2ZnSnS_4) et CIGS (cuivre indium gallium séléniure, p-$CuInGaSe_2$). Cependant, leur faible stabilité et leur coût de fabrication élevé à grande échelle limitent encore l'utilisation de ces matériaux comme photocathodes. Pour relever ce défi, le développement de nouveaux matériaux photo-catalyseurs a été ciblé pour permettre une conversion directe de l'énergie solaire en hydrogène, et donc la réalisation des cellules PEC avec des matériaux semi-conducteurs peu coûteux, robustes et hautes performances.

De nouvelles opportunités ont été présentées avec l'émergence de matériaux 2D, affichant des propriétés optoélectroniques uniques et des surfaces spécifiques élevées qui sont importantes pour les applications de catalyse et de stockage d'énergie. La structure lamellaire des matériaux 2D favorise une collecte de photons solaire avantageuse et diminue les voies des porteurs de charge. Bien que le graphène est le matériau 2D le plus connu, les di-chalcogénures

de métaux de transition (TMDC) représentent également une classe intéressante de matériaux photo-actifs avec la capacité d'être exfoliés jusqu'au stade de monofeuillet. Leur structure et leurs propriétés d'absorption uniques fournissent des caractéristiques de bande interdite accordables, correspondant au nombre feuillets, et possèdent une forte interaction lumière-matière, leur conférant des performances exceptionnelles dans le domaine de la conversion de l'énergie solaire. Des voies viables pour une production économique appropriée de dispositifs photo-catalyseurs de grande surface ont été explorées pour poursuivre le développement de procédures de conversion de l'énergie solaire utilisant ces matériaux.

Les matériaux TMDC 2D ont cependant une concentration élevée de défauts de surface pouvant agir comme des pièges à porteurs de charge efficaces (sites de recombinaison) et sont l'un des centres de diffusion les plus courants limitant la mobilité électronique. Les surfaces des TMDC présentent de nombreux défauts électroniques sous forme d'atomes de di-chalcogénures insaturés sur les bords.

Les réactions électrochimiques se déroulant à l'interface semi-conducteur/électrolyte et font appel à des mécanismes complexes impliquant plusieurs étapes : des étapes de transfert de charges et des étapes de transport de charges. Ces réactions électrochimiques sont favorisées par la présence de sites de surface catalytiques; et sont donc sensibles aux propriétés de surface du semi-conducteur. Par conséquent, les défauts de surface, contrairement aux sites catalytiques, sont le siège de réactions compétitives (corrosion, recombinaison de charges) finissant par ralentir la cinétique des réactions électrochimiques d'interface. C'est l'un des enjeux les plus importants de la photo-catalyse et différentes stratégies ont été proposées pour éliminer ou neutraliser ces défauts de surface et ainsi améliorer les performances des semi-conducteurs en photo-catalyse : la modification et/ou la structuration de l'interface semi-conducteur/électrolyte constitue un moyen efficace de contrôler la cinétique des réactions électrochimique. Pour ce faire, les principales stratégies impliquent des traitements de surface qui comprennent la passivation des états de surface, l'ajout de couches de protection et de co-catalyseurs - généralement des métaux nobles; des hétérojonctions p/n et de dopage .

Le choix du co-catalyseur est primordial et doit être adapté à la morphologie du semi-conducteur. Dans le cas des matériaux 2D exfoliés, les co-catalyseurs moléculaires peuvent s'avérer intéressants car ils peuvent facilement être infiltrés entre les feuillets du semi-conducteur. Les nanomatériaux à base de MoS_2, tels que les complexes moléculaires de Mo, y compris Mo_3S_4, $(Mo_2S_{12})^{2-}$, $(Mo_3S_{13})^{2-}$, ont été proposés comme matériaux photo-catalytiques.

Leur efficacité catalytique prometteuse, comparable à celle de Pt, en font des candidats idéaux pour une utilisation sur des matériaux photo-actifs 2D, tels que les TMDC 2D.

Un autre aspect important est la morphologie du semi-conducteur et sa nanostructuration. En dehors de son influence sur la cinétique de transfert de charge, la morphologie du semi-conducteur, et donc sa structuration, joue un rôle important sur l'absorption optique. Des morphologies favorisant l'augmentation de la surface spécifique sont donc à privilégier, mais peuvent conduire à limiter la mobilité des charges. La mise au point de nanojunctions à base de carbone peut s'avérer être une stratégie payante : le graphène ayant une conductivité élevée, et sa morphologie 2D s'avère un très bon candidat. Ce type de nanojunction doit faciliter le transport de charges et ainsi conduire à une plus grande efficacité photocatalytique.

Afin d'optimiser le rendement du semi-conducteur, il est important Parmi les défis pour tirer pleinement parti de la morphologie en couches des matériaux 2D, l'optimisation de la microstructure du film et de la collecte des charges vers les électrodes est hautement souhaitable pour augmenter considérablement l'accès aux sites catalytiques, car le remplissage des couches TMDC peut se produire avec des repeuplements. Une stratégie pertinente peut impliquer la conception et la fabrication d'hétéro-structures en couches composées de TMDC nanoporeux interconnectés par des nanojunctions à base de carbone. Dans ce contexte, les di-chalcogénures de métaux de transition (TMDCs) sont des candidats intéressants en raison de leurs bonnes propriétés d'absorption de la lumière et aussi leurs propriétés peuvent être modulées en fonction du nombre de feuillets.

Dans cette optique, le présent travail a été consacré à l'utilisation d'un matériau 2D TMDC comme photocatalyseur pour la génération d'hydrogène à partir de la photo-électrolyse de l'eau. L'objectif de la thèse a donc été concentré sur la mise au point de stratégies visant à améliorer le rendement phot-catalytiques.

Nanoflakes de di-séléniure de tungstène (WSe_2) 2D pour la conversion solaire en hydrogène.

Tout d'abord, nous avons travaillé sur l'élaboration de nanoplaques de p-WSe_2 exfoliés et sur l'obtention des films photo-actifs pour la production d'hydrogène, par une voie de synthèse simple. Les films de WSe_2 exfoliés par voie solvant ont été sélectés a 800 rpm et formés par le dépôt de la dispersion de WSe_2 par drop-casting sous le substrat de FTO, en plusieurs couches et étapes d'évaporation de solvant.

Des importantes caractérisations ont contribué à la valorisation des propriétés de la photocathode pour la photo-réduction de l'eau. Une morphologie homogène du film a été observée en Microscopie Electronique à Balayage, d'une épaisseur d'environ 3 µm, avec une orientation préférentielle des nanofeuillets parallèles au substrat FTO. L'analyse par Diffraction des Rayons X (DRX) réalisée pour des films de WSe_2 a démontré la diminution ou l'absence des pics en comparaison du le cristal de WSe_2 (plans cristallins verticaux : (002), (006) et (008)), confirmant que les nano-feuillets ont été exfoliées selon l'axe (001). De plus, la diminution de l'intensité de diffraction du plan (100) observée sur le diffractogramme des échantillons exfoliés a indiqué une réduction de l'empilement des couches.

Les propriétés optoélectroniques du film de WSe_2 ont été examinées. Des mesures d'absorbance UV-visible ont été réalisés, qui en utilisant la loi de Beer-Lambert, a donné le spectre d'absorbance pour le film exfolié de WSe_2. La **Fig. 1a** montre un pic d'absorbance révélé à env. 1.6 eV, alors attribué à la transition excitonique dans la bande interdite directe (DT) de WSe_2 en correspondance avec des travaux précédemment rapportés. IT représente la transition associée à la bande interdite indirecte, qui se situe à env. ≈ 1,4 eV.

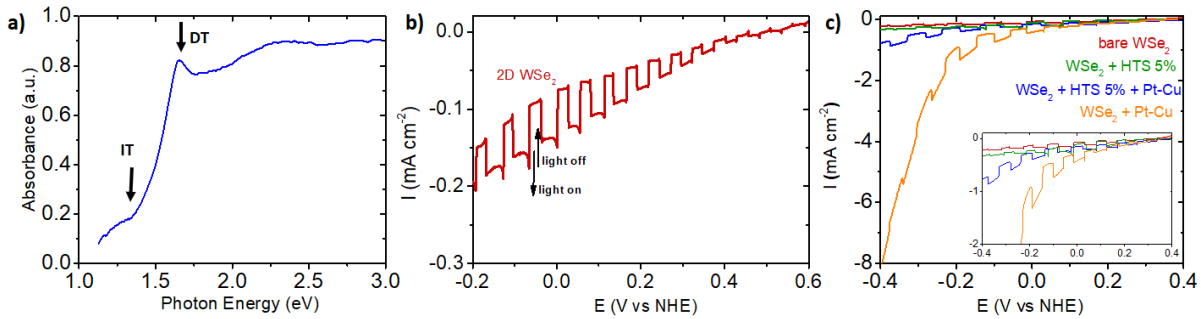

Fig. 1: *(a) Courbe d'absorbance extrapolée pour les nanoplaques 2D WSe_2, Courbes de LSV de l'électrode (b) p-WSe_2 pure sous éclairage intermittente, et (c) après dépôt de Pt-Cu avec et sanstraitement HTS.*

D'autres investigations concernant les propriétés semi-conductrices du WSe_2 ont été effectuées en utilisant le modèle Mott-Schottky pour les nanoplaquettes déposés sur le substrat FTO dans 0.5 M H_2SO_4 (pH 0). Les valeurs de capacités extraites à 100 Hz des données EIS ont été utilisées pour obtenir le tracé de Mott-Schottky. D'après cette analyse, le comportement semi-conducteur de type p du WSe_2 exfolié est confirmé. À partir de la pente du tracé de Mott-Schottky, la densité de porteur de charge du p-WSe_2 exfolié a été calculée comme étant $N_A = 4.35 \times 10^{23}$ cm^{-3}.

La photo-activité des films exfoliés de WSe_2 a été évaluée par Linear Sweep Voltammetry sous éclairage intermittent (haché) dans un électrolyte Na_2SO_4 0.1M, pH 7, dans l'intervalle de potentiel +0.4 ≤E ≤ -0.4 V par rapport à NHE, comme le montre la **Fig. 1b**. La densité de photocourant est d'environ -80 µA cm^{-2} à 0 V vs NHE pour le WSe_2 exfolié. Des courants d'obscurité élevés sont probablement dû à un effet électro-catalytique - et/ou des défauts, conduisant à une densité de courant conséquente sans éclairement des porteurs de charge minoritaires. De plus, la présence de pics de courant transitoire lors de la commutation de la lumière indique l'existence de recombinaisons de charges – se produisant lorsque l'électrode passe d'une phase d'obscurité à une phase d'éclairement – et d'accumulation de charges – se produisant lorsque l'électrode passe d'une phase d'éclairement à une phase d'obscurité.

Dans la littérature, des films minces de matériaux TMDC de quelques nanomètres, comme le WSe_2, ont une concentration élevée de défauts de surface agissant comme sites de recombinaison pour les charges photo-générées. Pour passiver ces défauts de surface, différentes approches telles que les traitements de surface et le dépôt de catalyseur sont couramment appliquées pour améliorer la photo-activité du matériau.

Dans un premier essai, la passivation des défauts de surface du film de WSe_2 a été réalisé par un traitement de surface un utilisant de l'hexyl-trichlorosilane (HTS - 1 à 5% wt.), suivi de l'électrodépôt du co-catalyseur Pt, en appliquant un protocole déjà rapporté dans la littérature. Les courbes obtenues par LSV, comme indiqué dans la **Fig. 1c**, après le traitement de surface ont montré une augmentation du photo-courant de -80 à -300 µA cm^{-2} à -0.2V vs NHE et une suppression des pics de courant transitoire. Le courant d'obscurité est de –900 µA cm^{-2} est probablement dû à une électrolyse directe via le site de platine déposé sur le FTO.

Malgré ces tentatives visant à améliorer les performances de notre photocathode, les nanofeuillets WSe_2 présentent probablement une grande densité de défauts qui ne sont pas efficacement passivés par la stratégie précédente. C'est pourquoi, au cours de ce travail de thèse il a été recherché une méthode plus efficace de modification de la surface, en travaillant sur deux axes : la passivation des défauts de surface et l'amélioration de la cinétique de transfert de charge, de préférence par l'utilisation d'un co-catalyseur exempt de métal noble tel que le platine.

Film de complexes moléculaires de Thio et Oxo-Thio de Mo en tant que catalyseurs cicatrisants pour la réaction de dégagement d'H_2 sur des matériaux 2D TMDC.

Cette partie a concerné l'étude d'un catalyseur potentiel bien adapté aux photoélectrodes p-WSe_2 et ses avantages pour les performances photo-catalytiques de ce matériau TMDC.

L'étude vise à l'élaboration d'un précurseur de catalyseur sans la présence de métaux nobles à base d'espèces complexes thio, oxo-thio Mo (Mo_xS_y).

Les solutions aqueuses à base de cation Mo et d'anions sulfures offrent une large gamme de distribution de complexes aqueux poly-condensés (complexes de thio-, oxo-thio – Molybdène). Nous avons exploré le potentiel de ces distributions de complexes comme co-catalyseur pour la photo-décomposition de l'eau. En mettant à profit des interactions de type chimique entre le substrat photo-actifs WSe_2 et les complexes thio-, oxo-thio- de Mo, nous avons pu sélectionner et isoler une gamme d'oligomères permettant l'obtention de co-catalyseur développant des propriétés photo-catalytiques intéressantes.

Différents thio et oxo-thio complexes de molybdène identifiées par spectrométrie de masse comme le $(MoOS_3)^{2-}$, $(Mo_2S_{12})^{2-}$, $(Mo_2S_6O_2)^{2-}$, $(Mo_3S_8O)^{2-}$ au sein des solutions lui confèrent ainsi un caractère multi-composant. Une comparaison des fréquences pour une même espèce à différents pH a pu être réalisée quantitativement, permettant de déterminer son domaine de prédominance. La **Fig. 2a** montre le diagramme de prédominance des espèces de Mo sulfures et oxo-sulfures déterminé pour un rapport S/Mo = 5 dans la gamme de pH 8.0 ≤ pH ≤ 9.5. Ainsi, la spéciation du cation Mo montre clairement la coexistence de différentes espèces à un pH donné.

En profitant de la grande variété de ces solutions de distribution de complexes de Mo, une approche intéressante serait de sélectionner les espèces les plus interactives en profitant des interactions « WSe_2- complexes de Mo-thio » qui peuvent être développées au contact de la solution. Ainsi, nous nous sommes concentrés sur le processus de formation de film favorisant l'ancrage des complexes thio- et oxo-thio de Mo développant des interactions complexantes avec la surface du WSe_2. Pour cela, un procédé de formation de film, désigné par enduction sélective par immersion, a été exploré et implique des enductions successives par immersion avec un temps de longue durée (2 x 16 h), dans des solutions de complexes avec une gamme bien définie du rapport S/Mo et du pH.

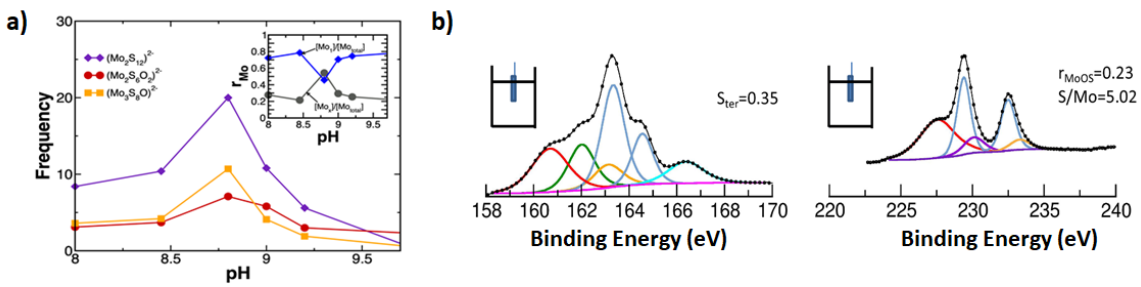

Fig. 2 : *(a) Diagramme de prédominance des espèces déterminé par ESI-MS à 0.01 M de Mo et S/Mo = 5, (b) Spectres de XPS déconvolués avec contributions S 2p et Mo 3d pour les couches minces de complexes thio, oxo-thio de Mo sur des électrodes WSe_2.*

Diverses observations ont confirmé un processus de sélection mis en œuvre lors de la confection de ces photo-électrodes d'haute performance. La composition chimique globale des films de photocathode a pu être déterminée par XPS. La présence de liaisons oxo-thio ainsi que des rapports élevés en S/Mo mis en évidence, suggèrent la présence de composés oxo-thio de type $(MoOS_3)^{2-}$ et de complexes à haut rapport S/Mo comme le $(Mo_2S_{12})^{2-}$ au sein du co-catalyseur solide, dénommé par la suite Mo_xS_y. La **Fig. 2b** présente les spectres de XPS enregistrés sur des électrodes recouvertes de films de co-catalyseurs complexes thio-, oxo-thio de Mo par trempé sélective sur le WSe_2.

La morphologie du dépôt de co-catalyseur a été précisée par microscopie électronique à transmission. Une image HRTEM couplées EDS montre que le co-catalyseur est déposé sous forme d'un film continu, amorphe de très faible épaisseur d'environ 2 à 8 nm. Le processus de formation de ce film amorphe de co-catalyseur met en œuvre la formation d'un polymère de coordination dont la réticulation est favorisée par la présence de centres Mo à différents degrés d'oxydation - présent au sein de différents oligomères.

Les performances photo-catalytiques de nos photo-électrodes de WSe_2 activées par le co-catalyseur à base de complexes thio, oxo-thio de Mo ont été comparées à celles avec un catalyseur à base de métal précieux, de type Pt-Cu. Concernant les photo-électrodes de WSe_2, nous avons enregistré des faibles photo-courants de l'ordre -0.3 mA cm^{-2} à -0.2V vs NHE en présence du catalyseur Pt-Cu. Des photo-courants importants jusqu'à -2.0 mA cm^{-2} (**Fig. 3a** – courbe rouge) a été obtenus sur nos photoelectrodes activées par distributions de complexes thio-oxo thio de Mo. Ce résultat a suggéré la présence d'agents passivants au sein de ces distributions de complexes en association à des molécules délivrant l'activité catalytique. L'effet cicatrisant de nos distributions de complexes thio oxo thio de Mo a été mis en évidence par les courbes de voltammetrie linéaire.

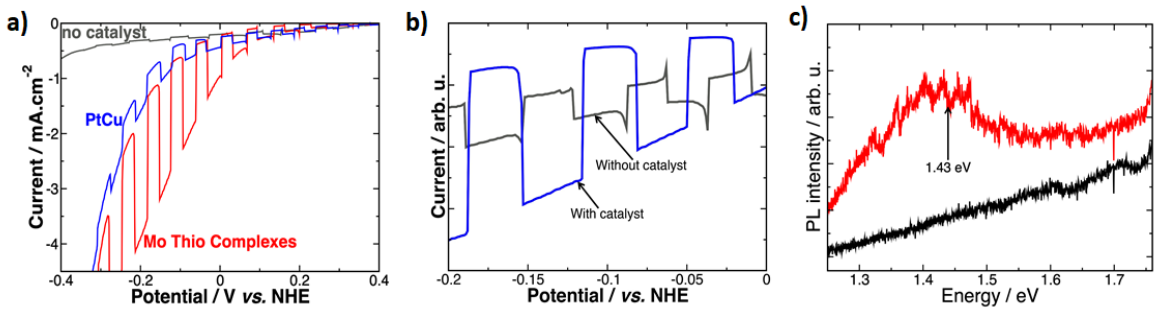

Fig. 3: *Courbes LSV (a) de la photo-électrode de WSe_2 après dépôt de Mo_xS_y par rapport à la photo-électrode WSe_2 activée par un catalyseur Pt-Cu, (b) montrant une diminution significative du photo-courant transitoire sur la photo-électrode de WSe_2/Mo_xS_y par rapport à une photo-électrode nue, (c) Spectres de PL de WSe_2 nue (courbe noire) et WSe_2 avec des photo-électrodes de film catalyseur à complexes de Mo_xS_y (courbe rouge).*

En effet, les courbes enregistrées sous illumination intermittente sur électrodes de WSe_2 sans co-catalyseur montrent des pics de courant transitoire importants (« spikes »), comme indiqué dans la **Fig. 3b**. Ces pics attribués à des phénomènes de forte recombinaison sont éliminés pour les photoélectrodes après activation par le film de co-catalyseur à base de thio complexes de Mo. Une autre preuve expérimentale de l'effet cicatrisant de notre film de co-catalyseur a été démontrée par photoluminescence statique, **Fig. 3c**. Contrairement à la photoelectrode de WSe_2 nue, un pic de photoluminescence est nettement observé pour la photoelectrode de WSe_2 activée par le film de co-catalyseur.

Une étude approfondie des mécanismes présents lors de la réaction de dégagement d'hydrogène et découlant de la formation d'un film de co-catalyseur a été réalisée par des caractérisations photo électrochimiques. Par spectroscopie d'impédance électrochimique (EIS) sous illumination, les diagrammes de Bode ont mis en évidence la présence de trois constantes de temps. La résistance correspondante à la constante de temps relative aux mesures très haute fréquence étant de quelques ohms en comparaison de l'impédance globale de l'ordre de quelques k-ohms. Les phénomènes à moyenne et à basse fréquences sont représentatifs respectivement des phénomènes relatifs aux défauts de surface (recombinaison de surface) ou d'interface photoelectrode-électrolyte liquide.

De manière intéressante, trois constantes de temps sont détectées pour la photoelectrode WSe_2 nue alors que la photoelectrode recouverte du film de co catalyseur ne possède que deux constantes de temps. La **Fig. 4a** indique les résistances correspondantes extraites dans des courbes indiquant la variation du module en fonction de l'angle de phase. Ces courbes montrent clairement une diminution de la résistance de transfert de charge liée à l'interface photoelectrode–électrolyte après dépôt du film de co-catalyseur.

De plus, la mise en évidence uniquement dans le cas de la photoelectrode WSe_2 nue de la résistance liée aux phénomènes de recombinaison est en cohérence avec l'absence de constante de temps constatée pour la photoelectrode recouverte de co-catalyseur. Ces résultats confirment une passivation des défauts de surface résultant du dépôt du film de co-catalyseur.

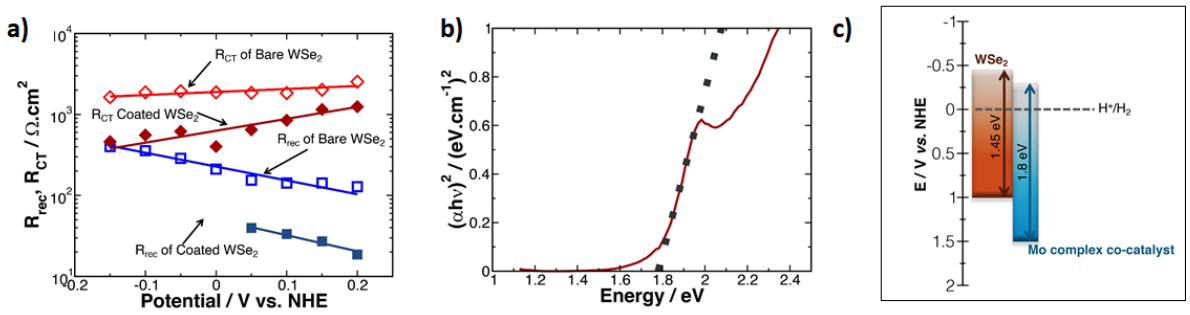

Fig. 4: *(a) Variation des différentes résistances extraites pour le film de WSe_2 nu et WSe_2 revêtu avec Mo_xS_y à différents potentiels de polarisation, (b) Tracé de Tauc obtenu à partir des données d'absorption UV-vis enregistrées sur un film de catalyseur complexe Mo_xS_y, (c) Diagramme d'énergie de bande de WSe_2/Mo_xS_y photo-électrode.*

Les propriétés optoélectroniques du film de co-catalyseur ont été également précisées. Une largeur de bande interdite d'environ 1.8 eV a été déterminée à partir de la courbe d'absorption UV-visible, montré dans la **Fig. 4b**. La représentation donnant le carré du photo-courant en fonction de l'énergie du photon indique une transition optique de nature directe. Le caractère n du film semi-conducteur du co-catalyseur est démontré par la pente positive de la courbe de Mott-Schottky. Cette semi-conduction de type n du film Mo_xS_y est cohérente avec celle de type n largement décrite pour les matériaux MoS_2.

A partir de la courbe de Mott-Schottky, un potentiel de bande plate a été déterminé à environ de +0.05 V pour le film amorphe Mo_xS_y par rapport à la référence NHE à pH 7 - permettant le calcul de la position de la bande de conduction du co-catalyseur. Concernant le matériau WSe_2, la courbe d'absorbance obtenue auparavant, nous a permis de déterminer la transition de bande interdite directe (1.4 eV) de la photoelectrode constituée des lamelles de WSe_2 exfoliées et sélectées suivant notre procédé. Toutes ces données nous ont permis de construire un diagramme d'énergie de bande concernant l'hétérojonction WSe_2 et co-catalyseur Mo_xS_y (**Fig. 4c**). Ce diagramme de bande d'énergie montre un positionnement approprié de la bande de conduction du film de co-catalyseur par rapport au potentiel de dégagement d'hydrogène. Et en plus, illustre ainsi une propriété supplémentaire du film de co-catalyseur formant une hétérojonction p/n appropriée à la séparation de charge et à leur migration vers l'électrolyte en vue de la réaction de dégagement d'hydrogène.

Ensuite, pour préciser les contributions respectives des différents oligomères du film multi-composant, nous nous sommes intéressés d'une part, aux performances d'oligomères modèles comme le $(Mo_2S_{12})^{2-}$ et d'autre part, nous avons déterminé - à l'aide de calculs DFT - les

énergies d'adsorption des oligomères sur le film de WSe_2, ainsi que les enthalpies libres d'adsorption de H, $\Delta G_{ads}H^+$, sur divers oligomères isolés ou en interaction sur le substrat WSe_2.

Les performances de la molécule modèle $(Mo_2S_{12})^{2-}$ ont été examinées à partir d'oligomères synthétisés dans le DMF, comme précédemment reporté dans la littérature. Malgré des performances électrocatalytiques conformes à celles attendues, les photo-courants de photoelectrodes WSe_2 activés par le composé $(Mo_2S_{12})^{2-}$ pure, déposé par évaporation séchage ou par trempé sélectif sont nettement inférieurs à ceux obtenus en présence du film de co-catalyseur à base de complexes de sulfure de molybdène. De plus, la dé-corrélation possible des propriétés electrocatalytiques et photocatalytiques des films en fonction de leur condition de préparation montrent la présence d'oligomères à propriété cicatrisante en association à des oligomères apportant l'activité catalytique, confirmant le caractère multicomposant du film.

Ces diverses observations indiquent la présence au sein du film de co-catalyseur en association au $(Mo_2S_{12})^{2-}$ d'autres molécules de type monomères $(MoS_4)^{2-}$, $(MoS_3O)^{2-}$ ou d'oxo thio oligomères de type $(Mo_2S_6O_2)^{2-}$ responsables des propriétés cicatrisantes du WSe_2.

Concernant les défauts de surface, très communs dans les matériaux 2D, les défauts ponctuels typiques du substrat WSe_2, la vacance de Se et la vacance de W, sont connus pour être des accepteurs d'électrons. Par nos résultats de calculs DFT, nous avons déterminé de hautes énergies de formation pour les vacances de Se et W. Pour avoir un effet considérable sur la recombinaison des porteurs de charge, la mise à l'échelle de ces défauts ponctuels avec la taille moléculaire des complexes Mo rend significative l'étude par DFT.

En conclusion, les divers avantages de ce film de co-catalyseur multi-composant ultramince mis en œuvre par une méthode de trempé sélectif ont ainsi été mis en évidence. Parallèlement à l'obtention de densité photo-courant important (gain x 40 par rapport à la photoelectrode WSe_2 nue), le caractère passivant de ce film a été démontré par diverses techniques (photoluminescence et spectroscopie d'impédance). Dans ce film multi-composant, nous avons pu préciser les contributions des motifs monomères comme additifs de passivation et des dimères en particulier $(Mo_2S_{12})^{2-}$ à haut rapport S/Mo comme catalyseurs. Le film de co-catalyseur proposé à base de complexes sulfures de Molybdène représente ainsi une nouvelle classe de films passivants, particulièrement adaptée à des surfaces photoactives à forte densité de défauts, développant une bonne activité catalytique et favorisant la séparation et la migration des porteurs de charge grâce à sa semi-conduction de type n.

Design d'hétérostructures en couches de rGO-WSe2/Mo_xS_y pour la génération de H_2 par photo-décomposition de l'eau

L'optimisation de la microstructure de film constitue une étape primordiale dans l'obtention de photoélectrodes de haute performance. De récents travaux ont également montré que les semi-conducteurs nanostructurés à grande surface offrent une surface d'échange améliorée avec l'électrolyte, favorisant un transfert de charge plus rapide. De plus, la fonctionnalisation/modification de surface, par exemple via des hétérojonctions de surface et/ou un dépôt de surface de co-catalyseur, conduit à améliorer la séparation des charges au sein de l'interface semi-conducteur/électrolyte : une séparation plus efficace des paires électron-trou, et transfert de charge plus rapide. Donc, cette étude concerne l'optimisation de microstructure formée de nanofeuillets, de briques élémentaires à morphologie fortement anisotrope. Nous présentons une nanostructure optimisée de WSe_2 2D exfolié avec une surface spécifique élevée, des parois de pores composées de quelques couches et des jonctions WSe_2/GO dans le plan.

Le film à base de WSe_2-rGO à haute surface spécifique, formé de nanofeuillets à briques élémentaires, a été préparé par auto assemblage colloïdal de nanofeuillets de WSe_2, de GO (Graphene Oxide) et d'un template sacrificiel. Ce template sacrificiel est composé de sulfure métallique et présente une morphologie sphérique. Il a été développé à façon afin de ne pas dégrader chimiquement les nanofeuillets de WSe_2. Afin d'assurer une collecte optimale de porteurs de charge, nous avons aussi exploré la formation d'un réseau percolant électriquement également à base de nanofeuillets juxtaposant idéalement le réseau de nanofeuillets de WSe_2.

L'auto assemblage est réalisé en milieu solvant polaire DMF avec utilisation de briques élémentaires GO et $Sn_xSb_yS_z$ préparées en milieu alcalin de manière à développer des charges de surface identiques au WSe_2. La préparation des poudres texturées WSe2-rGO met en œuvre une consolidation par traitement thermique à basse température (200 °C) et une post re-dissolution du template en milieu alcalin. La conversion du GO en rGO (reduced Graphene Oxide) conducteur est obtenue par traitement thermique à vitesse de montée très lente.

La caractérisation approfondie par BET réalisée sur des poudres texturées ont montré des surfaces spécifiques de l'ordre de 7.0 $m^2 g^{-1}$ et des volumes poreux jusqu'à 0.07 $cm^3 g^{-1}$ sur les différentes poudres texturées en présence ou non de rGO, indiquent un recouvrement partiel des nanofeuillets de WSe_2 par le rGO.

Des photoélectrodes WSe_2-rGO, dénommées par la suite films texturés 3D, sont préparées par dépôt de ces poudres texturées sur l'électrode transparente conductrice de type

FTO. Afin d'améliorer la percolation électrique au sein de ces photoélectrodes, des infiltrations de nanofeuillets GO colloïdal sont éventuellement réalisées entre deux dépôts successifs de poudre texturée WSe_2-rGO.

Une image MEB enregistrée sur une coupe transversale de la photo-électrode 3D réalisée au FIB montre les contacts les plus robustes au sein du film texturé présenté dans la **Fig. 5a**. L'orientation des nano-plaquettes de WSe_2 varie de façon aléatoire de parallèle à perpendiculaire dans la vue en coupe de la surface FTO, suggérant un agencement d'auto-assemblage 3D. En plus, l'image montre que le film est composé de nano-plaquettes d'une épaisseur allant de 120 à 150 nm et des tailles latérales entre 200 et 500 nm. Les données des diffractogrammes des rayons-X enregistrés sur des films 3D rGO-WSe_2 ont démontré que la taille des domaines ordonnés est de l'ordre de 30 à 70 nm. Ce qu'indique que la nanostructure du film WSe_2 est composée de blocs de construction composés de 2-5 nanoplaques primaires.

Les conductivités électriques des différents films de WSe_2 (sans et avec rGO) ont été réalisés à partir des mesures du courant électrique pour différents potentiels appliqués. Concernant nos films 3D, les contacts, en faible nombre, entre les lamelles de WSe_2, sont majoritairement des contacts plan/bord ou bord/bord. Ces contacts impliquant les bords des nanofeuillets sont peu efficaces pour un bon écoulement des porteurs de charges car ces bords ont été largement décrits comme des défauts siège de recombinaison e^-/h^+. La **Fig. 5b** illustre la difficulté de la bonne collecte des porteurs de charge à l'électrode arrière. Les meilleures valeurs de conductivité électrique sur des films rGO-WSe_2/ verre en comparaison des films WSe_2/verre démontrent clairement l'intérêt de l'insertion du rGO au sein des films 3D, et montre une amélioration de la percolation électrique.

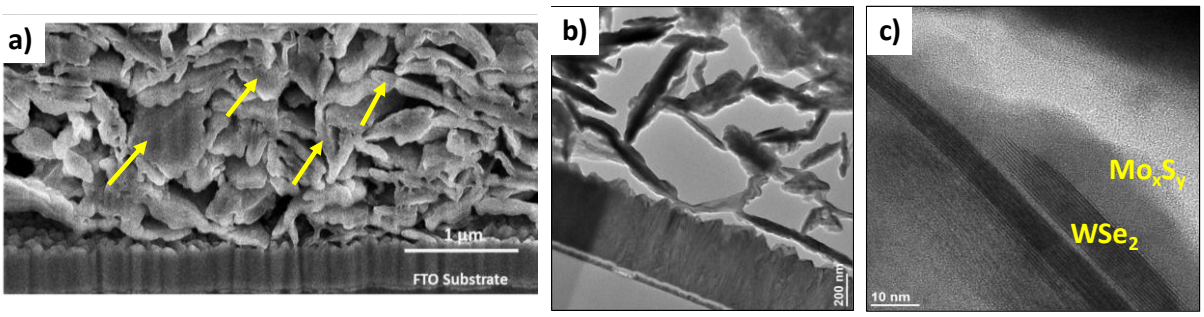

Fig. 5: *(a) Image MEB enregistrée sur une coupe transversale de la photo-électrode 3D réaliséeau FIB, (b) Image TEM détaillant l'arrangement du rGO-WSe2 3D auto-assemblé, (c) Image deMETmontrant des nanofeuillets de WSe2 3D et catalyseur de complexes Mo_xS_y en formation d'une hétéro-structure.*

Afin de préserver le caractère lamellaire et la haute surface spécifique de cette microstructure à base de WSe_2, nous avons exploré l'activation de cette microstructure par un co-catalyseur déposé sous forme d'un film ultramince multi-composant. Comme réalisé pour le film de WSe_2 2D, la mise en œuvre d'un film multi-composant ultrafin à base de complexes sulfures métalliques développé a permis l'activation catalytique et la cicatrisation des défauts en préservant la haute surface spécifique de la microstructure du WSe_2-rGO 3D. Le caractère d'hétéro-structure de ces films a été mis en évidence par HRTEM (**Fig. 5c**). La présence du co-catalyseur amorphe est observée sur une épaisseur d'environ 5 nm en périphérie de la lamelle anisotrope de WSe_2 avec une interface de WSe_2-co-catalyseur non dégradée.

Dans nos conditions opératoires (mise en œuvre d'un template non totalement exempt d'eau, exfoliation du WSe_2 réalisée sous air, processus d'auto-assemblage en présence de GO), une dégradation des feuillets de WSe_2 a été observée par XPS, notamment avec suivi du rapport atomique (r_{WO}), $(r_{WO} = WO/(WO + WSe_2))$. Le suivi de ce rapport (r_{WO}) a montré une oxydation du rGO-WSe_2 3D relative petites, comparés avec celui du WSe_2 2D. Probablement associé à l'utilisation du template $Sn_xSb_yS_z$ pour former la nanostructure 3D, ce qui retarde la décomposition de WSe_2.

De plus, le spectre XPS du C 1s a confirmé la réduction de l'oxyde de graphène. Concernant le dépôt de film catalyseur Mo_xS_y, les spectres XPS ont révélé la présence de complexes oxysulfures, impliquant la sélection de complexes tels que $(MoOS_3)^{2-}$, $(Mo_2S_6O_2)^{2-}$ et $(Mo_3S_8O)^{2-}$. De même, comme l'ancrage de ces complexes pour les films 2D WSe_2, la valeur importante de S_{ter} laisse suggérer la présence de groupes sulfure-disulfure accessibles, attribués à $(MoS_4)^{2-}$ et $(Mo_2S_{12})^{2-}$ complexes.

La formation du réseau percolant, à un taux important de juxtaposition des nanofeuillets de graphène sur les nanofeuillets de WSe_2 a aussi été démontré par des caractérisations électrochimiques. Des mesures d'impédance électrochimique sur une électrode WSe_2-rGO immergée au sein d'un électrolyte liquide a présenté une diminution de la résistance de transfert de charge en comparaison avec des électrodes de WSe_2 texturés sans rGO, et le film de WSe_2 2D. En complément, des courbes i(v) et des diagrammes de Nyquist ont démontré l'existence d'un taux de r_{rGO} optimal, $(r_{rGO} = rGO/(rGO + rWSe_2)_{molaire})$ avec rGO et $rWSe_2$ représentant le nombre de nanofeuillets ou de lamelles respectivement de rGO et de WSe_2. Ce taux a été déterminé d'être proche de 0.7.

L'efficacité du dépôt du film ultramince multi-composant du film de co-catalyseur en présence de ces nanofeuillets de rGO sur les performances de la photoelectrode a été examinée. Un photo-courant important de l'ordre de -5.0 mA cm^{-2} a été déterminé à -0.2 V vs NHE sur nos photoelectrodes activées par le film de Mo_xS_y (**Fig. 6a**). Ainsi un gain d'environ x 2.5 sur le photo-courant par optimisation de la microstructure est observé par rapport à des électrodes WSe_2 2D.

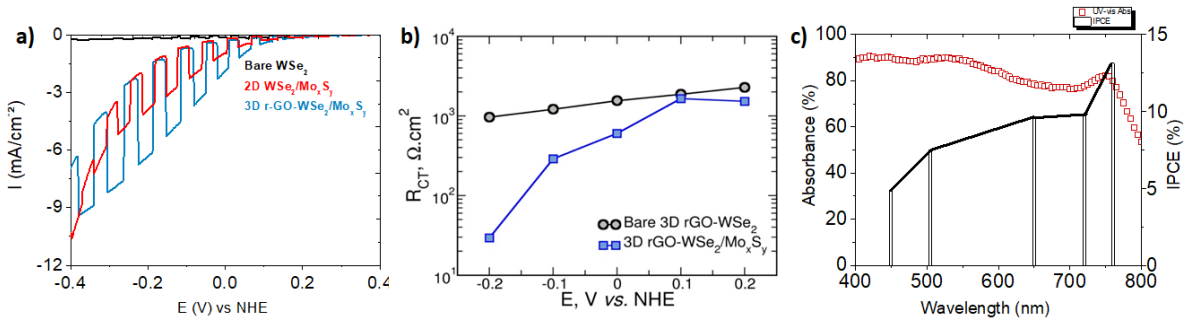

Fig. 6: *(a) courbes LSV enregistrées l'électrode 3D rGO-WSe_2 (tracé bleue) après déposition de Mo_xS_y, (b) variation des résistances de transfert de charge pour rGO-WSe_2 3D nu et rGO-WSe2 3D/Mo_xS_y, (c) Spectres d'absorption UV-vis (marques rouges) et IPCE (courbe noire) pour la photo-électrode de 3D rGO-WSe_2 avec Mo_xS_y.*

Des spectroscopies d'impédance électrochimique (SIE) des photo-électrodes 3D rGO-WSe_2 ont été réalisées avant et après dépôt de co-catalyseur, pour étudier la résistance de transfert de charge de la nouvelle hétéro-structure. Les diagrammes de Nyquist obtenus ont montré que le film 3D rGO-WSe_2/Mo_xS_y a une résistance de transfert de charge inférieure sur toute la gamme de potentiel par rapport au 2D WSe_2/Mo_xS_y, en accord avec le photo-courant le plus élevé obtenu par le film rGO-WSe_2 texturé. Le transfert de charge plus rapide est une conséquence d'un taux de recombinaison plus faible et d'une collecte de charge plus rapide. Cela amène probablement à la formation d'une région de charge d'espace bien définie, conduisant à une meilleure séparation de charges et ainsi à une amélioration de l'efficacité de transfert de charge : une diminution de la résistance de transfert de charge en découle (**Fig. 6b**).

Des mesures d'efficacité quantique ont été réalisées à l'aide de LED à lumière monochromatique à diverses longueurs d'ondes, présenté dans la **Fig. 6c**. Un rendement quantique de l'ordre de 10% a été observé pour des longueurs d'onde $\lambda > 650$ nm.

La passivation des défauts ponctuels suite au dépôt du co-catalyseur a été également mise en évidence par photoluminescence statique. Contrairement à l'électrode rGO-WSe_2 3D nue, un pic de photoluminescence est clairement observé sur l'électrode après déposition du

film de co-catalyseur, centré sur E = 1.36 eV (λ = 909 nm), et indique une épaisseur des lamelles d'environ une dizaine de monocouches, cohérente avec les données extraites des spectres de diffraction de rayons-X (environ 70 nm).

La diminution de la résistance de transfert de charge a été mise en évidence par une analyse plus précise, obtenue par spectroscopie de photo-courant à intensité modulée (IMPS). Cette étude réalisée de manière comparative sur des électrodes texturées 3D revêtues ou non de co-catalyseur met en évidence une forte augmentation de la constante de vitesse de transfert de charge et la diminution de la constante de vitesse de recombinaison à des potentiels cathodiques élevés, pour le film de rGO-WSe_2 3D/Mo_xS_y. Ceci découle vraisemblablement du rôle prépondérant du caractère semi-conducteur n de la couche de co-catalyseur, augmentant la courbure de bande et améliorant ainsi considérablement l'extraction des porteurs de charge, parallèlement à la diminution des phénomènes de recombinaison.

Dans cette partie du travail de thèse, nous avons proposé un procédé d'optimisation de la microstructure de films composés de briques élémentaires à morphologie très anisotrope mettant en œuvre un template élaboré à façon. Plus particulièrement, nous proposons une voie mettant en œuvre un co-auto assemblage permettant la construction d'un réseau juxtaposé interconnecté conducteur également à base de nanofeuillets avec un bon écoulement des charges, et adapté à ces microstructures à faible densité de points de contacts. Nous avons aussi montré que l'hétéro-structure formée de rGO-WSe_2 et de Mo thio, oxo-thio complexes a des propriétés photo-catalytiques améliorées, avec la collecte et le transfert de charge efficaces, atteignant une conversion IPCE d'environ 10%.

L'élaboration de l'hétérostructure rGO-WSe_2 3D/Mo_xS_y a été une stratégie développée pour associer deux exigences importantes en photo-catalyse : l'optimisation de la nanostructure des nano-plaques ; la passivation des défauts de surface, favorisant la percolation des porteurs de charge photo-générés ; et une région de charge d'espace plus efficace, conduisant à l'élaboration d'une photocathode haute performance pour la génération de l'Hydrogène.

Perspectives : Développement des propretés de différents matériaux TMDC 2D pour la photo-décomposition de l'eau

Les réponses positives obtenues parmi les stratégies développées pour le p-WSe_2 nous ont incités à démarrer une nouvelle étude sur d'autres types de TMDC, comme le p-WS_2. Plusieurs raisons nous ont amenés à étudier le disulfure de tungstène (p-WS_2) : des études préliminaires ont révélé que les feuilles individualisées de WS_2 ont une excellente activité

catalytique, et le WS_2 présente une énergie de bande interdite directe qui permet l'absorption d'une plus grande partie du spectre solaire. Nous avons donc essayé de reproduire les mêmes stratégies pour obtenir des photo-électrodes p-WS_2 optimisées par l'exfoliation et la sélection de nanofeuillets de p-WS_2, par la procédure d'auto-assemblage avec des nanojunctions rGO, suivi de la fonctionnalisation de surface en déposant le co-catalyseur Mo_xS_y.

Les nanofeuillets de WS_2 ont été exfoliés via solvant DMSO et sélectés à des vitesses d'ultracentrifugation entre 1500 et 6000 rpm. Le procédé d'auto-assemblage a été appliqué au p-WS_2, comme présenté pour le p-WSe_2 avec co-texturation d'oxyde de graphène (GO) et de nanofeuillets WS_2, toutes les deux en présence du template colloïdal $Sn_xSb_yS_z$.

L'analyse de surface BET a été réalisée sur la poudre de WS_2 texturés préparés à partir de l'auto-assemblage de nanofeuillets (ou nanoplaques) sélectionnée à 6000 rpm, et ensuite comparée avec la poudre texturée de WSe_2 obtenue à partir des nanofeuillets sélectés à 800 rpm. Un volume de pores plus élevé est obtenu pour le WS_2, et une surface estimée à 30 m^2g^{-1}. Comme attendu, cette surface spécifique étant principalement réglée par l'épaisseur des nanofeuillets de TMDC.

Les propriétés optoélectroniques du film exfolié de WS_2 ont été analysées par spectroscopie d'absorbance UV-visible. En utilisant la loi de Beer-Lambert, le spectre d'absorbance pour le film exfolié de WS_2 a été obtenu, comme montre la **Fig. 7a**. Un pic d'absorbance est observé à env. 1.9 eV, alors attribué à la transition excitonique dans la bande interdite directe (ID) de WS2. IT représente la transition associée à la bande interdite indirecte, qui se situe à env. ≈ 1.6 eV.

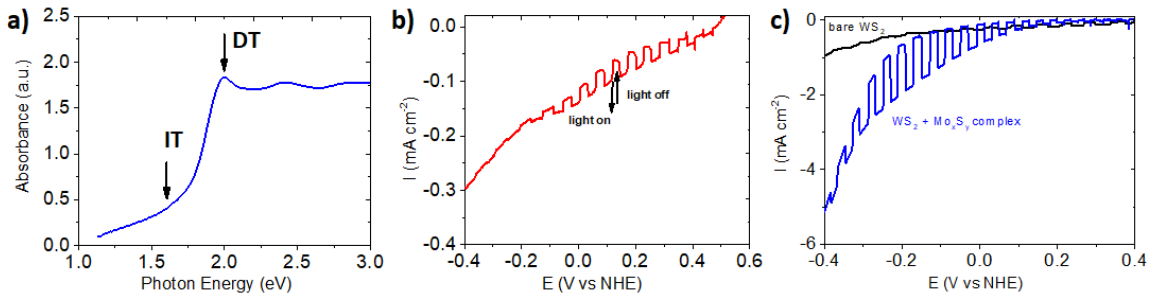

Fig. 7: *(a) Spectre d'absorbance du film mince de WS_2 exfolié, Courbes LSV obtenue pour (b) l'électrode de p-WS_2 nu déposée sur le substrat FTO, et (c) pour l'électrode p-WS2 après dépôt decatalyseur Mo_xS_y par trempage (2 x 16h).*

L'activité photoélectrochimique des électrodes nues de p-WS_2 a révélé une bonne photo-activité pour les films sélectionnés à 1500 rpm/min pour la réaction de réduction de l'eau dans

les milieux acides. La **Fig. 7b** montre la courbe LSV de WS_2 obtenue montrant un photo-courant jusqu'à -100 µA cm^{-2} sous lumière intermittente (100 mW cm^{-2}).

Le faible photo-courant et les pics de courant transitoires observés pour l'électrode WS_2 sont supposés être largement provoqués par la recombinaison des porteurs de charges, en raison de la présence de défauts de surface. En suivant la même approche que pour les films WSe_2, nous avons appliqué un traitement de surface pour passiver les défauts de surface par dépôt de films ultraminces de catalyseur de complexes thio, oxo-thio Mo.

La courbe LSV illustrée sur la **Fig. 7c**, obtenue sous éclairage intermittent, montre un photo-courant jusqu'à -1.5 mA cm^{-2} à -0.2 V vs NHE pour l'électrode 2D WS_2/Mo_xS_y. L'amélioration significative de l'activité photocatalytique révélée par l'électrode WS_2 souligne une fois de plus que les complexes thio, oxo-thio Mo sont une classe efficace de catalyseur bien adaptée aux matériaux TMDC pour le HER.

Malgré l'amélioration de l'activité photocatalytique de WS_2, des investigations supplémentaires doivent être effectuées. Il a été démontré que les performances PEC du WS_2 dopé p constitué de quelques couches peuvent être améliorées en utilisant le catalyseur de complexe Mo, comme présenté dans les premiers résultats de cette étude. Le processus d'auto-assemblage effectué sur WSe_2 s'est révélé polyvalent et a donc été extrapolé avec succès. En outre, puisque le WS_2 peut être exfolié en nanoflakes plus minces, nous nous attendons à une surface plus élevée et à des performances photochimiques améliorées sur WS_2.

Pour conduire au développement de matériaux 2D basés sur la conversion de l'énergie solaire, il est nécessaire de mettre au point un procédé de synthèse à faible impact environnemental et offrant des matériaux ayant une faible densité de défauts de surface ; ceux-ci permettant de conserver les propriétés optoélectroniques du TMDC et donc d'obtenir un rendement quantique optimisé. Pour ce faire, il est donc utile de développer des traitements de surface (passivation, co-catalyseur) ainsi que des procédés de synthèse facilement transférable à une plus grande échelle : le choix du type de composés chimiques, l'utilisation de l'eau comme solvant de synthèse ainsi qu'une recherche d'économie d'atome permettent d'aller dans la bonne direction. Le développement d'un catalyseur moléculaire, sans platine, en milieu aqueux est donc tout à fait en accord avec cette stratégie.

Même si nos résultats sont encourageants, des recherches supplémentaires impliquant l'optimisation de la microstructure et la passivation des défauts de surface restent nécessaires pour améliorer l'activité photo-catalytique des TMDC.

En particulier, pour comprendre les différences des performances entre le p-WSe_2 et le p-WS_2, d'autres investigations doivent être envisagées telles que : (i) l'optimisation de la percolation électrique, favorisée par les nanofeuillets rGO – les morphologies du WS_2 et du WSe2 exfolié sont différentes ce qui implique différentes conditions lors du restacking en présence du rGO ; (ii) un meilleur contrôle du procédé d'exfoliation du rGO permettant un réassemblage plus homogène avec les feuillets WS_2 ; (iii) une étude approfondie des propriétés optoélectroniques du WSe_2 et WS_2 en fonction du nombre de feuillets reste à mettre en place – en particulier la possibilité de moduler la largeur de bande interdite ; (iv) l'optimisation du dépôt de la couche de catalyseur des complexes thio, oxo-thio Mo afin d'augmenter autant que possible la cinétique de transfert de charge. Toutes ces études complémentaires pourraient contribuer à la conception de cellules tandem – Z-scheme – utilisant des matériaux TMDC comme photocathodes.

Conclusions Générales

Le présent travail visait l'étude et l'application de matériaux TMDC 2D comme photocathodes pour la production d'hydrogène à partir de la photo-électrolyse de l'eau via la lumière visible. Le di-séléniure de tungstène (WSe_2) a été évalué comme photocathode après exfoliation en nanofeuillets 2D, fabriqué par simple par drop-casting sur le substrat FTO. Les premières caractérisations ont démontré que les films exfoliés et sélectionnés à 800 rpm permettaient d'obtenir des nanoplaquettes de 2-3 µm d'épaisseur composées de nanofeuillets de 150 nm. Des transitions indirecte et directe de bande interdite ont pu être observées pour les films WSe_2 exfoliés à respectivement 1.4 eV et 1.6 eV. Les premières caractérisations photo-électrochimiques ont révélé des photo-courants allant jusqu'à –80 µA cm^{-2} à 0 V vs NHE sous un éclairage intermittent de 100 mW cm^{-2}. La faible valeur de la densité de courant et la présence de pics de courant transitoire indiquent une recombinaison importante des porteurs de charge photo-générés, en raison d'une forte concentration de défauts de surface.

Afin de réduire la concentration en défauts de surface, deux méthodes d'amélioration de la photo-activité ont été réalisées : un traitement de surface avec HTS et un électrodépôt de Pt, comme décrit dans la littérature ; un traitement de surface impliquant la mise au point d'un co-catalyseur moléculaire à base de complexes thio, oxo-thio Molybdène. Le premier type de traitement a amené à une amélioration du comportement photo-électrochimique marginale ; le second type de traitement de surface, développé au cours de cette thèse, a donné des résultats encourageants.

Il a été montré que dans des conditions bien définis (0.01 M, pH 9.0 et S/Mo = 5), des distributions de complexes Mo-S sont spontanément formées en le milieu aqueux. Des analyses ESI-MS ont révélé la présence d'espèces de monomères, dimères et trimères de molybdène, tels que $(MoS_4)^{2-}$, $(Mo_2S_6O_2)^{2-}$, $(Mo_2S_{12})^{2-}$, $(Mo_3S_8O)^{2-}$. Des analyses XPS ont indiqué la présence de ligands sulfures terminaux et pontants (S_{ter} et S_{br}), et oxysulfures de Mo (MoO_yS_z) dans les films formés par ces distributions de complexes. Les complexes thio, oxo-thio Mo ont été déposés avec succès sur la surface 2D WSe_2 par trempage. Plus précisément, les données XPS ont montré qu'en contact du WSe_2 les taux de S_{ter} et de MoO_yS_z diminuent, démontrant une interaction spécifique entre ces complexes le TMDC.

Les mesures photo-électrochimiques enregistrées sur les électrodes de WSe_2 ont révélé une augmentation de la densité de courant jusqu'à -2.0 mA cm^{-2} à -0.2 V vs NHE après le dépôt de catalyseur Mo_xS_y. En comparaison avec les photo-électrodes WSe_2 après dépôt d'un catalyseur Pt-Cu, les valeurs de photo-courant sont plus élevées. L'amélioration du photo-courant a été obtenue grâce à un dépôt sélectif obtenu par immersion de l'électrode dans la solution de de complexes Mo oxo-thio : un effet « cicatrisant » de ces complexes est observé puisqu'ils interagissent préférentiellement avec les défauts du WSe_2. Une diminution de la résistance de transfert de charge ainsi qu'une augmentation de la résistance à la recombinaison ont été observées par spectroscopie d'impédance électrochimique. Des preuves supplémentaires de la passivation des défauts de la photo-électrode WSe_2 après interaction avec les complexes Mo_xS_y ont été obtenues par spectroscopie de photoluminescence : une transition énergétique à 1.43 eV, correspondant à sa transition indirecte de bande interdite est observée alors qu'elle est absente lorsque le WSe_2 n'est pas traité.

Des observations en microscopie électronique ont montré que le catalyseur des complexes thio, oxo-thio Mo sont présent sous forme d'un film amorphe ultramince d'épaisseur irrégulière allant de 2 à 8 nm recouvrant les nanoplaquettes de 2D WSe_2. Différents mécanismes impliquant la formation du film de catalyseur ultrafin ont été envisagés : la formation à base d'oligomères de polymère réticulé coordonné par le biais d'interactions entre les groupes sulfure - disulfure et les centres Mo de différents nombres d'oxydation ; suivis d'une hétéro-nucléation et d'une croissance d'oligomères présentant une densité élevée de groupes sulfure ou disulfure. Les propriétés optoélectroniques du film mince de catalyseur ont montré une transition de bande interdite directe de 1.8 eV et une semi-conduction de type n. Ces résultats laissent penser qu'en contact du p-WSe_2 une jonction se forme en partie, favorisant la séparation de charge et donc la migration des charges mobiles.

Afin d'aller plus loin dans la compréhension des interactions entre les complexes de Mo thio, oxo-thio et le WSe_2, une étude par DFT a été menée. Il a été démontré le rôle des monomères et dimères oxo-thio Mo de petites tailles, tels que $(MoOS_3)^{2-}$, $(Mo_2S_6O_2)^{2-}$, $(Mo_2S_{12})^{2-}$ dans le processus de « cicatrisation »/passivation des défauts : une forte énergie d'adsorption des complexes de Mo sur les défauts ponctuels (vacances de W et Se), avec formation de nouvelles liaisons Se-S, a été démontrée. De plus, les calculs DFT des énergies libres d'adsorption H ont été effectués sur des complexes libres – n'ayant pas interagi avec la surface du WSe_2 –, ainsi que sur des complexes de Mo ayant interagi avec le WSe_2 : le diagramme d'énergie libre résultant a mis en évidence que les bonnes performances catalytiques proviennent principalement de dimères tels que $(Mo_2S_6O_2)^{2-}$ ou $(Mo_2S_{12})^{2-}$ ayant peu interagi avec la surface du TMDC.

Afin d'optimiser la nanostructure de la photo-électrode WSe_2, un processus d'auto-assemblage impliquant une solution colloïdale et des nanofeuillets d'oxyde de graphène réduit (rGO) a été développé pour donner des surfaces WSe_2 plus exposées avec une meilleure percolation des porteurs de charge à travers le réseau de nano-plaquettes. Le film composite obtenu est poreux et est composé de nanofeuillets de rGO et de plaquettes de nanofeuillets de WSe_2. Ces plaquettes ont une orientation aléatoire avec des contacts bord à bord et bord à plan, et sont composés de 2 à 5 nanoplaquettes empilées primaires d'une épaisseur de 150 nm. La morphologie anisotrope présentée par l'auto-assemblage a un impact négatif sur la résistivité électrique du réseau WSe_2 nanostructuré ; celle-ci est diminuée en présence de nanofeuillets rGO. Les images obtenues microscopie électronique à haute résolution présentent une nanoplaquette unique de 12 nm d'épaisseur, composé de ≈ 15 nanofeuillets élémentaires. La formation d'une hétéro-structure impliquant le rGO-WSe_2 auto-assemblé et le catalyseur film de Mo_xS_y déposé a pu être entièrement identifiée à l'échelle nanométrique, celui-ci étant amorphe.

L'évaluation photo-électrochimique de la nouvelle photo-électrode a permis de montrer qu'il était possible d'obtenir des photo-courants jusqu'à -5.0 mA cm^{-2} à -0.2 V vs NHE, atteignant les meilleures performances photo-catalytiques parmi les photo-électrodes à base de WSe_2. Les mesures en SEI ont démontré une diminution de la résistance de transfert de charge attribuable à une meilleure percolation des porteurs de charge et à une diminution des processus de recombinaison : la région de charge d'espace est donc mieux définie. Les mesures réalisées par photoluminescence (PL) ont montré une passivation des défauts de surface effective après dépôt

du catalyseur complexe Mo thio, oxo-thio sur la surface rGO-WSe_2 : une amélioration des transitions énergétiques, en raison de la séparation efficace des porteurs de charges, est à l'origine de ce pic. De plus, une analyse par IMPS a démontré une diminution de la constante cinétique de recombinaison de charge et une augmentation de la constante cinétique de transfert de charge : ces deux évolutions expliquent la diminution de la résistance de transfert de charge apparente observée en SEI. Grâce à cela, les propriétés photo-catalytiques améliorées obtenues par la photo-électrode 3D rGO-WSe_2/Mo_xS_y ont atteint une efficacité de conversion d'environ 10% pour $\lambda > 650$ nm.

Nous avons également montré en perspective que la stratégie développée lors de ce travail sur le WSe_2 était transposable à d'autres TMDC tels que le WS_2.-Les résultats préliminaires obtenus ont montré une exfoliation de WS_2 en films 2D présentant des transitions indirectes et directes de bande interdite, respectivement à 1.6 et 1.9 eV, et montrant un photo-courant de -0.1 mA cm^{-2}, atteignant des valeurs plus élevées de -1.5 mA cm^{-2} à – 0.2V vs NHE après passivation de surface avec dépôt de catalyseur complexe thio, oxo-thio de Mo. Même s'il reste encore à optimiser le procédé d'exfoliation, de modification de surface et de restacking du WS_2, ces premiers résultats sont très encourageants.

Abstract

Collecting and storing solar energy in chemical energy is a highly desirable approach to solve energy challenge. The great potential of a photoelectrochemical cell technology combines the harvesting of solar energy with the water splitting into a single device. 2D semiconducting nanosheets of Transition Metal Di-Chalcogenides (TMDC) are seen as an attractive material to design an efficient photocatalyst for the conversion of solar energy into hydrogen. Despite the unique optoelectronic properties of the TMDCs, the passivation of surface defects in high concentration is a remaining challenge for the development of this class of materials. In this context, the present work has aimed the elaboration of thin 2D TMDC photocatalyst for solar water splitting. The development of high performance photocatalysts was evaluated following two main axis.

A first strategy consists in the surface defects passivation of 2D p-WSe_2 nanosheets using Mo-S complexes to decrease the photogenerated charge carrier recombination and improve photocatalytic activity. We demonstrated these Mo thio and oxo-thio-molecular complexes films as an ideal class of catalysts, well-suited to functionalize 2D materials since they are stable in aqueous environments, cheap and environmentally benign. Current densities of -2 mA cm^{-2} at -0.2 V vs NHE electrode were obtained for the new p-WSe_2/Mo_xS_y photocathode. Besides developing high electro-catalytic activity, the Mo complexes films were shown to display ability to heal surface defects. The respective contributions in catalytic and healing effects observed experimentally for the various molecular Mo complexes involved strong adsorption on point defects of the 2D WSe_2 substrate of Mo complexes such as $(MoS_4)^{2-}$, $(MoOS_3)^{2-}$ and $(Mo_2S_6O_2)^{2-}$. The Mo complexes films spontaneously formed at well-defined pH were demonstrated to present n-semi-conducting behaviour and band engineering formed with p-WSe_2 showed to be suitable for ensuring charge separation and efficient migration of the photo-induced electrons for the Hydrogen Evolution Reaction, thus representing an example of multicomponent passivation layer exhibiting multiple properties.

A second strategy focus in the nanostructure optimization of WSe_2 with high specific surface area and pore walls composed of few layers. Nanostructured WSe_2 films of high surface area and good charge carrier collection were obtained by co-assembling WSe_2 nanosheets and reduced graphene oxide (rGO) nanosheets with an optimal rGO/WSe_2 nanosheet ratio. After deposition of co-catalyst thin layer, the new layered nanojunctions of rGO-WSe_2/Mo_xS_y exhibited photocurrents up to -5 mA cm^{-2} at -0.2 V vs NHE. Incident-photon-to-current efficiency conversion of 10% were achieved for WSe_2 nanoflakes of 70 nm thickness in presence of rGO and Mo_xS_y co-catalyst.

The potential of our self-assembly process in the presence of TMDC and rGO nanosheets has been illustrated with the obtention of optimized microstructures of p-MoS_2, p-WSe_2 and p-WS_2. In a long-term perspective, photoelectrodes based on TMDC nanosheets are interesting candidates for the design of tandem cells offering modular band-gap (E_g) values and hydrogen onset potentials

Keywords: photocatalysis, 2D TMDC materials, solar energy, H_2 evolution

Résumé

Le stockage de l'énergie solaire en énergie chimique est une approche hautement souhaitable pour résoudre le défi énergétique. Les cellules photo-électrochimiques combinent la collecte de l'énergie solaire et la décomposition de l'eau. Les nanofeuillets semiconducteur 2D de di-chalcogenures de métaux de transition (TMDC) sont considérés comme des matériaux attrayants pour l'élaboration de photocatalyseur efficace pour la conversion de l'énergie solaire en hydrogène. Malgré les propriétés optoélectroniques uniques des TMDC, la passivation de défauts de surface présents en concentration élevée est un défi important pour le développement de cette classe de matériaux. Dans ce contexte, le présent travail a concerné l'élaboration d'un photocatalyseur 2D TMDC pour la photo-décomposition de l'eau. Le développement de photocatalyseurs de haute performance a été examiné suivant deux axes principaux.

Un premier axe de recherche consiste à passiver les défauts de surface des nanofeuillets 2D p-WSe_2 à l'aide de complexes Mo-S pour diminuer la recombinaison des porteurs de charge photo-générés et améliorer l'activité photocatalytique. Nous avons démontré que des couches ultra minces de complexes thio et oxo-thio-Mo moléculaires représentent une classe idéale de catalyseurs, bien adaptée pour fonctionnaliser les matériaux 2D car ils sont stables dans des environnements aqueux, bon marché, respectueux de l'environnement. Des densités de courant de -2 mA cm^{-2} à -0.2 V par rapport à l'électrode d'hydrogène (NHE) ont été obtenues pour la nouvelle photocathode p-WSe_2/ Mo_xS_y. En plus d'offrir une activité électro-catalytique élevée, les films complexes Mo se sont révélés capables de guérir les défauts de surface. Les contributions respectives aux effets catalytiques et cicatrisants obse rvées expérimentalement pour les divers complexes moléculaires de Mo impliquaient la forte adsorption sur les défauts ponctuels du substrat 2D WSe_2 de complexes de Mo tels que $(MoS_4)^{2-}$, $(MoOS_3)^{2-}$ et $(Mo_2S_6O_2)^{2-}$. Il a été démontré que ces couches de co-catalyseur Mo-S formés à un pH bien défini présentent un comportement n-semi-conducteur et l'ingénierie des bandes formées avec p-WSe_2 s'est révélée appropriée pour assurer la séparation des charges et la migration efficace des électrons photo-induits pour la RDH, représentant un exemple de couche de passivation multi-composant avec de multiples propriétés.

Un deuxième axe de travail concerne l'optimisation de la nanostructure du film de WSe_2 comme objectif l'obtention d'une surface spécifique élevée et des parois de pores composées de quelques monofeuillets. Des films de WSe_2 nanostructurés de haute surface et à bonne collecte de porteurs de charge ont été obtenus par co-assemblage des nanofeuillets de WSe_2 et des nanofeuillets d'oxyde de graphène réduit (rGO) avec un rapport de nanofeuillets rGO/WSe_2 optimal. Après dépôt de la couche ultra mince de co-catalyseur les nouvelles nanojunctions de rGO-WSe_2/Mo_xS_y ont présenté des photocourants jusqu'à -5 mA cm^{-2} à -0.2 V vs NHE. Des rendements quantiques d'environ 10% ont été obtenus pour des films de nanoplaquettes de WSe_2 de 70 nm d'épaisseur en présence de rGO et catalyseur Mo_xS_y.

Le potentiel de notre procédé d'auto-assemblage en présence de nanofeuillets de TMDC et de rGO a été illustré avec l'obtention de microstructure optimisée de films de p-MoS_2, p-WSe_2 et p-WS_2. Dans une perspective à plus long terme, les photoelectrodes basées sur des nanofeuillets de TMDC sont des candidats intéressants pour la conception de cellules tandem offrant des valeurs de band-gap (E_g) et présentant des potentiels de dégagement d'hydrogène modulables.

Mots-clefs : photocatalyse, matériaux 2D TMDC, énergie solaire, génération d'H_2